

**Transmissielijnmodellering van verlieshebbende interconnecties
via de Dirichlet-Neumann operator**

**Transmission Line Modeling of Lossy Interconnects
with the Dirichlet to Neumann Boundary Operator**

Thomas Demeester

Promotor: prof. dr. ir. D. De Zutter
Proefschrift ingediend tot het behalen van de graad van
Doctor in de Ingenieurswetenschappen: Elektrotechniek

Vakgroep Informatietechnologie
Voorzitter: prof. dr. ir. D. De Zutter
Faculteit Ingenieurswetenschappen
Academiejaar 2009 - 2010



ISBN 978-90-8578-312-1
NUR 959, 928
Wettelijk depot: D/2009/10.500/70

Dankwoord

De zon schijnt. Dat gebeurt wel eens in de herfst. Ik zit op de trein. Zoals steeds zit deze vol starende mensen, moe van de werkdag en storend stil. Maar gelukkig schijnt de zon. Ik droom even weg, denkend aan vanalles en nog wat, maar kom onherroepelijk terecht bij dit doctoraat. Gelukkig, want ik ben van plan om hier, ergens tussen Brussel en Gent, de meest gelezen pagina's van dit hele werk te produceren. Ik moet hier wel bij vermelden dat het vervolg zo'n tweehonderd maal meer 'werk per pagina' heeft gevraagd dan dit dankwoord. Mocht de Dirichlet-Neumann operator u dus ongemeen interesseren, of u kan de slaap niet vatten, raad ik u alvast een hoofdstukje of twee aan.

Vier jaar geleden kwam ik thuis van een fantastisch Erasmus-jaar in Zürich. Terwijl ik daar zat, had Daniël De Zutter mij een doctoraatsbeurs geregeld, dus toen ik terug was, kon ik onmiddellijk beginnen met het 'wetenschappelijk onderzoek'. Die Forschung hatte ich schon in Zürich kennengelernt, und hat mir dank Dirk, Christophe und Rhiüdiger ganz viel Spaß gemacht. Vroeger kon ik mij bij dat onderzoek nooit veel voorstellen, maar 't had er altijd 'wijs' uitgezien, afgaande op verhalen van opa, nonkel Piet en nonkel Jo. Na ongeveer een jaar ben ik enigszins de weg kwijtgeraakt, maar gelukkig heeft Daniël mij weer op het goede spoor gezet. Daniël is een opmerkelijk promotor. Zijn vermogen om ogenblikkelijk en volledig geconcentreerd om te schakelen tussen alle zaken die hij aan zijn hoofd heeft, is verbluffend. En van die hoofd-zaken waren er steeds vele, als hoofd van onze onderzoeksgroep en als decaan van de faculteit of voorzitter van de vakgroep. Steeds was er wel een gaatje in zijn overvolle agenda, tussen de vergaderingen en de schilderijen in. Ik moest mij trouwens steeds haasten om hem mijn werk eerder af te geven dan ik het verbeterd terugkreeg. Dit zou de causaliteit in het gedrang hebben gebracht, zoals u begrijpt. Het is motiverend om een promotor te hebben die actief is geïnteresseerd in het onderzoek en naast een bijzonder scherpe geest ook een brede en gezonde kijk heeft op het vakgebied. Bedankt Daniël, het was op alle vlak een waar genoegen!

Het gebrek aan zonlicht in onze duistere bureau werd, behalve door de befaamde bureaulampjes, meer dan goedgemaakt door de warme sfeer tussen ons allen, intec'ers én telin'ers, hoewel beide partijen beweren dat het bureau eigenlijk hen toebehoort. Meer dan eens viel er een deuntje muziek te horen, van zwaar klassiek tot lichte jazz, en soms zelfs live. Eerder dan wiskundige formules, verschenen er op ons whiteboard krachtige Italiaanse termen (non preoccuparti, Luigi, manteniamo la discrezione) of fijnheden in het Nederlands. Literaire thema's passeerden de revue, maar evenzeer

de nieuwste uitspattingen van Silvio B., of het verloop van deze quiz. Wouter, Luigi, Koen, Carla - jij die de stilte doorbrak, Frederick, Sofian, Patrick, Francesco: het was bijzonder aangenaam. Jullie zijn van mij nog niet af, ik spring wel weer eens binnen!

De voorbije jaren in het Technicum op verdieping -T met zijn openstaande deuren waren bijzonder aangenaam. Met dank hiervoor aan de professoren Daniël, Luc, Femke - die ons te vroeg heeft verlaten, Hendrik, Tom, Ann, en uiteraard professor Van Bladel, onze collectieve wetenschappelijke peetvader. Evenzeer bedankt aan alle collega's voor een aantal onvergetelijke conferenties, discussies in de gang, poolavonden, Brug- of park-middagen, twaalfurenloop- en (EM)-café-momenten: Annelies, Bart, Ben, Celina, Damiano, Dieter, Dirk, Dong, Dries, Freek, Gunther, Ignace, Jan, Joris, Jürgen, Kristof, Lei, Luc, Maria Lucia, Peter, Pieterjan, Roald, Sara, Wouter. Een speciaal woord van appreciatie en dank is gericht aan Isabelle, die mij met een onverklaarbaar geduld uit de administratieve penarie wist te halen, telkens ik daar achteloos in verzeild was geraakt.

Onvergetelijk zijn de vele Zondagavonden met de 'bende', vroeger vaak in Gent, met bierhuistrappisten of trappistenhuisbier, nu vaker in huiselijke kring. Bart, Hilde, Frederik, Julie, Jan, Griet, Koen en Katrien, moge deze traditie blijven bestaan! Bovendien was er nog wel eens tijd voor een verre duik of frisse fietstocht. Wim, bedankt voor het eeuwige enthousiasme! Ook de muziek bracht de nodige afwisseling van het 'thema met variaties' waarover dit doctoraat handelt. Hierbij dank ik in de eerste plaats Michael, voor meer dan enkel de fantastische lessen, en eveneens Philip en Bart, et Baudoin, pour une faveur exceptionnelle. Zum Schluß möchte ich auch ganz gerne Clemens und Fritze danken, für ihre Freundschaft und das Querflötestimulans!

Beste mama en papa, jullie onafgebroken steun, al 3³ jaren lang, was onontbeerlijk voor dit doctoraat. Ik kan te allen tijde op jullie rekenen, bedankt voor alle moeite en de vele kansen die ik kreeg! Toon, Bieke en Sven, Jan, Nele en Herbert met kleine Soetkin, jullie zijn een familie om fier op te zijn.

Tenslotte kom ik aan de persoon die eigenlijk reeds thuis hoort in alle voorgaande paragraafjes, behalve misschien in dat over 't werk. Hoewel - ik vrees dat ze wel geduldig het één en ander heeft moeten aanhoren over de 'eierdoosfuncties' (en ik beken met spijt dat op onbewaakte momenten het woord 'dirichletfuncties' ook wel eens viel), over het 'balkje', of de nabijheid van steeds een nieuwe deadline. Laure-Ann! Zonder jouw jeugdige, muzikale, medische, en liefdevolle steun zouden de laatste jaren er heel wat donkerder hebben uitgezien. Voor het steeds opengaan deurluikje in de Burvenichstraat, de gastvrijheid van je familie, jouw inspiratie tot muziek, je medelijden met de studenten die ik examen gaf, voor meer dan ik hier kan opsommen: bedankt, merci!

Bijna ter bestemming, en nog steeds schijnt de zon...

Thomas Demeester
ergens tussen Brussel en Gent
16 oktober 2009

In grateful memory of my grandfather

GERARD DEMEESTER

a noble man

Contents

Samenvatting	vii
Summary	xi
List of Abbreviations	xv
List of Symbols	xvii
List of Publications	xix
Introduction	3
1 A Quasi-TM Multi-Conductor Transmission Line Model	13
1.1 Introduction	14
1.2 Geometry of the Problem and Field Equations	15
1.3 Coupled Transmission Line Model	17
1.4 The Capacitance Problem	19
1.4.1 Theoretical Analysis	19
1.4.2 Numerical Solution	23
1.5 The Inductance Problem	26
1.6 Numerical Results	29
1.6.1 MIS Microstrip Line	30
1.6.2 MIS Coplanar Waveguide	32
1.6.3 Multi-Conductor Line Structure	33
1.7 Conclusions	39
2 Composite Conductors	43
2.1 Modeling the Broadband Inductive and Resistive Behavior	44
2.1.1 Introduction	44
2.1.2 Inductance and Resistance Model	44
2.1.3 Determination of the Current Density	46
2.1.4 Numerical Results	47
2.1.5 Conclusions	50
2.2 Internal Impedance Calculations	51
2.2.1 Introduction	51
2.2.2 Internal Impedance of an Inhomogeneous Conductor	52

2.2.3	Numerical Results	58
2.2.4	Conclusions	64
3	Construction and Applications of the DtN Operator	69
3.1	Introduction	70
3.2	Construction of the DtN Operator	71
3.2.1	Rectangular Cross-Section	72
3.2.2	General Cross-Sections	76
3.3	Applications of the DtN Operator	78
3.3.1	Internal Impedance Calculations	78
3.3.2	Transmission Line Modeling	78
3.4	Conclusion	82
4	The Dirichlet to Neumann Operator for Triangles	85
4.1	Introduction	86
4.2	Determination of the DtN Operator in a Triangle	88
4.2.1	Geometry of the Problem and Expansion of e_z	89
4.2.2	Discretization of ψ_c and Iterative Procedure	92
4.2.3	Normal Derivative Calculation	96
4.3	Elimination of the Gibbs Effect	98
4.4	Numerical Results	99
4.4.1	Numerical Accuracy and Convergence Properties	99
4.4.2	Characterization of a Single Conductor	103
4.4.3	Multiconductor Line with Trapezoidal Conductors	104
4.4.4	Micromachined Coplanar Waveguide	106
4.5	Conclusion	108
5	Fields at a Finite Conducting Wedge	115
5.1	Introduction	115
5.2	Investigation of the Edge Effect	117
5.2.1	The Equivalent Surface Current Density	118
5.2.2	The Electric Boundary Potential ϕ_c	122
5.2.3	The Electric Field Distribution Inside the Wedge	124
5.2.4	A Local Surface Impedance Approximation	126
5.2.5	Influence on the Resistance and Inductance	128
5.3	Conclusions	130
6	Conclusions and Future Research	135
6.1	Development of a New Transmission Line Model	135
6.2	The Dirichlet to Neumann Operator	137
6.3	Conductor Modeling	138
6.4	Further Research on Interconnections	138

Appendices	145
A Conference Papers	147
A.1 Design of On-Chip Transmission Line Pairs	147
A.1.1 Introduction	147
A.1.2 Design of a Differential Pair	148
A.1.3 Conclusion	151
A.2 The DtN Operator of Polygonal Conductors	153
A.2.1 Introduction	153
A.2.2 The Dirichlet to Neumann Operator of a Convex Polygon	154
A.2.3 Numerical Results	157
A.2.4 Conclusion	158
B Analytical Calculation of Interaction Integrals	163
B.1 Introduction	163
B.2 Interaction Integrals	164
B.3 Determination of K_{00}	165
B.3.1 Branch cut horizontal or vertical	167
B.3.2 Branch cut through a corner of S	168
B.3.3 Branch cut through two opposite sides	170
B.3.4 Branch cut through two adjacent sides	170
B.4 Determination of K_{01} , K_{10} , and K_{11}	171
B.4.1 Auxiliary functions for K_{01}	171
B.4.2 Auxiliary functions for K_{10}	172
B.4.3 Auxiliary functions for K_{11}	172
C The Surface Admittance of a 3-D Conductor	177
C.1 Introduction	177
C.2 Field Expansions in a PEC Waveguide	178
C.2.1 Electric and Magnetic Eigenvectors	179
C.2.2 Field Expansions	180
C.3 Discretization of \mathbf{e}_t	183
C.4 Weighting of $\mathbf{u}_n \times \mathbf{h}$	184
C.5 Further Procedure for a Rectangular Parallelepiped	186
C.5.1 Eigenfunctions of the Rectangular Cross-Section	186
C.5.2 Discretization of \mathcal{A}	187
C.5.3 Discretization of \mathcal{Y}	187

Samenvatting

Het onderwerp van deze doctoraatsthesis kadert in het onderzoek naar metallische interconnecties in de elektronica. Doordat de kloksnelheden in moderne digitale systemen steeds verder toenemen, treden steeds vaker complexe elektromagnetische verschijnselfen op. Deze zorgen ervoor dat de conventionele simulatoren voor elektronische circuits niet meer voldoen voor een betrouwbaar ontwerp, en moeten aangevuld worden met een meer diepgaande elektromagnetische analyse. Deze elektromagnetische analyse is zowel noodzakelijk voor de interconnecties die de signalen verdelen als voor de voedingsnetwerken. Op elektronische printplaten, waar de connecties vaak ‘elektrisch lang’ zijn, komen de elektromagnetische effecten sterk tot uiting onder de vorm van golfverschijnselfen die de signaalkwaliteit kunnen aantasten, waaronder tijdsvertraging, vervorming, reflecties en demping. De vaak aanzielijke demping wordt voornamelijk veroorzaakt door hoogfrequente verliezen die optreden als gevolg van het stroomverdringingseffect in de geleiders. Ook in geïntegreerde schakelingen (chips) geven de connectiestructuren aanleiding tot ongewenste effecten. Deze worden tegenwoordig steeds belangrijker door de sterke miniaturisatie en de toenemende complexiteit van de systemen. Overspraak, of de interferentie tussen verschillende signalen, is hier het voornaamste fenomeen. Deze overspraak wordt veroorzaakt door capacitieve en inductieve koppeling tussen geleiders, die bovendien soms nog wordt versterkt door conductieve koppeling in het halfgeleidersubstraat.

Om deze parasitaire effecten te kunnen voorspellen, wordt gebruik gemaakt van elektromagnetische simulatieprogramma’s. Deze laten toe om, uitgaande van de beschouwde interconnecties, hun zogenaamde transmissielijnparameters te bepalen, die dan worden in rekening gebracht bij de simulaties van de totale circuits. Een aantal reeds bestaande transmissielijnmodellen kunnen moeilijk overweg met elektrische verliesfenomenen. Ze zullen bijvoorbeeld de metallische geleiders als ‘perfect’ (dus verliesloos) onderstellen, wat niet langer aanvaardbaar is, of komen in de moeilijkheden indien het substraat sterk geleidend is. De wetenschappelijke stand van zaken op het gebied van tweedimensionale transmissielijnmodellen omvatte bij de start van het huidige doctoraatsonderzoek (i) exacte multigeleidermodellen die echter enkel perfecte geleiders en lage substraatverliezen aankunnen, (ii) een model voor slechts een enkele signaalgeleider, dat nu wel willekeurige substraatverliezen in rekening brengt, en (iii) een nieuwe simulatietechniek voor rechthoekige geleiders, die d.m.v. een accu-

rate randintegraalformulering toelaat om heel nauwkeurig de verliezen te modelleren, in het bijzonder bij de hoogste frequenties waarbij de stroom zich bevindt in een dun laagje onder het geleideroppervlak. Deze nieuwe methode is gebaseerd op de oppervlakte-admittantie operator, die zorgt voor een verband tussen het tangentieel elektrisch en magnetisch veld aan de geleiderrand. Ze is recent ontwikkeld aan de onderzoeksgroep Elektromagnetisme van de Vakgroep Informatietechnologie aan de Universiteit Gent. Dankzij een aantal gunstige eigenschappen die te maken hebben met de zogenaamde Dirichlet-Neumann operator, ligt deze techniek aan de grondslag van dit werk. De modellen (ii) en (iii) zijn gebaseerd op een benadering van de vergelijkingen van Maxwell, met name de onderstelling dat in de dwarse richting van de geleiders geen golfffenomenen optreden. In de meeste praktische situaties houdt deze benadering stand, zowel op printplaten als in chips, en daarom wordt ze ook hier gebruikt.

Het eerste hoofdstuk beschrijft de ontwikkeling van een uitgebreid tweedimensionaal transmissielijnmodel met geleiders in een diëlektrisch en/of halfgeleidend substraat. Het bestaande model (ii) kan worden uitgebreid tot een multigeleider model, indien het reciprociteitsprincipe wordt gehanteerd, in plaats van het behoud van energie. De gegeven numerieke voorbeelden tonen duidelijk dat het model zowel de geleider- als de substraatverliezen correct in rekening brengt (met o.m. het trage-golf effect). Doordat de berekening van de Dirichlet-Neumann operator enkel kan gebeuren voor een rechthoek, zijn alle materialen combinaties van rechthoeken, maar dit is geen essentiële beperking van het model zelf.

In de daaropvolgende hoofdstukken worden een aantal aanverwante onderwerpen gedetailleerd besproken. Eerst wordt aangetoond dat het voorgestelde model ook samengestelde geleiders aankan, via de studie van gelaagde en gecoate geleiders. Bovendien blijkt de Dirichlet-Neumann operator van pas te komen bij de berekening van de inwendige impedantie van geleiders. Dit onderwerp wordt met de nodige omzichtigheid behandeld, want het betreft een fel besproken thema in eerdere literatuur. Verder wordt ook een nieuwe berekeningswijze voor de Dirichlet-Neumann operator voorgesteld, die niet enkel veel sneller is, maar tevens, naast de oorspronkelijke toepassing op goede geleiders, toelaat om diëlektrische en halfgeleidende materialen te modelleren. Deze methode is gebaseerd op een ontbinding in de modi van parallelle-plaat golfgeleiders, in plaats van de Dirichlet eigenfuncties, zoals voordien.

Hoofdstukken vier en vijf behandelen de berekening van de Dirichlet-Neumann operator voor driehoeken, waardoor het transmissielijnmodel nu ook combinaties van veelhoekige geometrieën toelaat. De voorgestelde methode laat toe om het even welke veldverdeling binnen in de driehoek te ontbinden in de bijdragen van drie incomplete sets van modi van parallelle-plaat golfgeleiders. De convergentie-eigenschappen van de iteratieve methode worden onder de loep genomen, en via een aantal voorbeelden wordt getoond dat de methode correcte resultaten oplevert. In één van de voorbeelden worden trapeziumvormige geleiders bestudeerd. Aangezien de resultaten toch signifi-

cant afwijken van deze voor rechthoekige geleiders, gaan we dieper in op het gedrag van de velden nabij geleiderhoeken. De nabije elektromagnetische velden en een aantal afgeleide veldgrootheden op het oppervlak worden onderzocht als functie van de frequentie en de grootte van de hoek. Om het veldgedrag te onderzoeken en te vergelijken met dat van perfecte geleiders, wordt de nieuwe iteratieve techniek aangewend. Tenslotte wordt ook het verband tussen de velden aan de hoeken en de globale circuitparameters kort uitgewerkt.

In het laatste hoofdstuk formuleren we een aantal conclusies, en besluiten met een aantal suggesties voor verder onderzoek in de lijn van het gepresenteerde doctoraatsonderzoek.

Een eerste appendix bundelt twee conferentiepapers die achtereenvolgens gaan over het design van een differentiële lijn en de uitbreiding van de berekeningswijze voor de Dirichlet-Neumann operator van driehoeken naar convexe veelhoeken. In een tweede appendix staan nieuwe formules voor het berekenen van quasi-statische Greense-functie-interacties, gebaseerd op een directe integratie van de logaritmische functie, met een correctieterm die de ongewenste bijdrage van de snede in het complexe vlak wegwerkt. De derde en laatste appendix geeft een afleiding van de exacte driedimensionale uitbreiding van de oppervlakte-admittantie operator, gebaseerd op een superpositie van de modi van rechthoekige golfgeleiders.

Summary

The work presented in this doctoral thesis is situated in the field of interconnect modeling. Due to the ever higher operating frequencies, a number of high-frequency electromagnetic phenomena form the reason why conventional circuit simulation tools are nowadays insufficient for a reliable design and must be complemented with electromagnetic field analyses. The main culprit is the interconnect network, used to distribute both power and signals. This is the case on printed circuit boards, where the interconnects are often electrically long, resulting in wave phenomena such as signal delays, distortion, and reflections, as well as an important high-frequency attenuation due to skin effect losses in the conductors. Also in integrated circuits (chips), the interconnects give rise to signal integrity problems, and the undesired effects are becoming a real issue, due to the present miniaturization and increase in complexity. The main effect is due to ‘crosstalk’, interference between several signal conductors, related to capacitive and inductive coupling effects and sometimes reinforced by conductive coupling in the semiconductor substrate.

Electromagnetic simulation tools are needed to predict these parasitic effects. They can extract the so-called transmission line parameters from the physical interconnect configurations, which can then be plugged into circuit simulation software. A number of transmission line models that were developed in the past have difficulties with the accurate simulation of losses. For example, they often consider the signal lines as perfect (lossless) conductors, which is no longer acceptable, or they cannot deal with high-loss substrates. The state of the art in transmission line modeling for two-dimensional metallic interconnect structures, by the start of the presented Ph. D. included (i) full-wave multiconductor transmission line models that assume perfect conductors and low-loss layered substrates, (ii) a single-conductor model when taking semiconductor substrate effects into account, and (iii) a new simulation technique for rectangular conductors, to deal with losses up to skin effect frequencies by means of a very accurate boundary integral formulation. This new technique is based on the surface admittance operator, which constitutes a relationship between the tangential electric and magnetic fields along the rectangle’s boundary. It was recently developed in the electromagnetics group of the Department of Information Technology at Ghent University, and is at the basis of this work, because it has some favourable properties, related to the use of the so-called Dirichlet to Neumann boundary operator. The

models (ii) and (iii) are based on an approximation of Maxwell's equations, assuming there are no wave phenomena in the transverse direction of the considered interconnects. This condition is fulfilled for most practical configurations, both on-chip and on-board, and is therefore assumed for the model developed in this thesis as well.

In the first chapter, a full-fledged two-dimensional multiconductor transmission line model in the presence of conductors with a finite conductivity and a semiconducting and/or dielectric substrate is developed. The existing single-conductor model (ii) can be extended in a consistent way to a multiconductor model, by invoking mode reciprocity, rather than the conservation of power. The shown numerical examples clearly demonstrate the model's capability to deal with the conductor and substrate losses (including slow-wave effects). As the calculation of the Dirichlet to Neumann operator is limited to rectangular shapes, all materials are combinations of rectangles, but this is no essential restriction of the model itself.

In the next few chapters, a number of related topics are examined in detail. First, it is shown that the developed method is capable of simulating composite conductors, and some characteristics of layered and coated conductors are explored. Furthermore, the Dirichlet to Neumann operator turns out to be a useful tool for the calculation of the internal impedance of conductors, a topic that is treated with due care, as it is a highly debated topic in previous literature. A new calculation method for the Dirichlet to Neumann operator as used in the transmission line model is presented as well, extending its original possibilities as a conductor modeling tool to dielectric and semiconducting materials, and allowing a much faster calculation. The method is based on an expansion in parallel-plate waveguide modes instead of, originally, on a Dirichlet eigenfunction expansion inside the considered rectangle.

The fourth and fifth chapter deal with the calculation of the Dirichlet to Neumann operator for triangles, enlarging the range of possible simulation configurations for the transmission line model to combinations of polygonal geometries. The presented method is based on an expansion in three incomplete sets of parallel-plate waveguide modes, which together allow to represent any possible field pattern inside the considered triangle. The convergence properties of the iterative method are examined and some numerical examples demonstrate its correctness. One of the included simulations investigates the behavior of trapezoidal conductors. In response to the obtained results that display a significant difference with the rectangular conductor case, the field behavior near conductor corners is investigated in more detail. The electric and magnetic field, as well as related field quantities on the surface, are carefully investigated as a function of the frequency and the wedge angle. The new iterative simulation method is successfully applied, to inquire into the field behavior at the edge, and for a comparison with perfect conductors. Finally, the direct relationship between the fields near the corners and the overall circuit characteristics is briefly worked out.

The final chapter formulates some overall conclusions and gives several suggestions for further research, following the line of work presented in this thesis.

In a first appendix, two conference papers are reproduced, which deal with, respectively, the design of an on-chip differential conductor pair, and the extension of the calculation method for the Dirichlet to Neumann operator for triangles to convex polygons. The second appendix gives new formulas to be used for the calculation of quasi-static Green's function interactions, based on a direct integration of the logarithmic function, with a correction term to compensate for the superfluous branch-cut contribution. Finally, the third appendix gives a derivation of the full-wave three-dimensional equivalent of the surface admittance operator, based on the superposition of rectangular waveguide modes.

List of Abbreviations

AC	Alternating Current
CPW	Coplanar Waveguide
DC	Direct Current (static regime)
DtN	Dirichlet to Neumann
EM	Electromagnetic
EMI	Electromagnetic Interference
FEM	Finite Element Method
IC	Integrated Circuit
ICWM	Iterative Combined Waveguide Modes (Method)
LC	Inductance-Capacitance
l.h.s.	left-hand side
MIS	Metal Insulator Semiconductor
MoL	Method of Lines
MoM	Method of Moments
MTL	Multiconductor Transmission Line
PCB	Printed Circuit Board
PEC	Perfect Electric Conductor
PEEC	Partial Element Equivalent Circuit
PI	Power-Current
p.u.l.	per unit of length
PV	Power-Voltage
RC	Resistance-Capacitance
RF	Radio Frequency
r.h.s.	right-hand side
RLCG	Resistance-Inductance-Capacitance-Conductance
SWF	Slow-Wave Factor
TE	Transverse Electric
TEM	Transverse Electric and Magnetic
TM	Transverse Magnetic
VLSI	Very-Large-Scale-Integration
2-D	two-dimensional
3-D	three-dimensional

List of Symbols

The list below gives an overview of the most important symbols used in this dissertation. Basic mathematical operations which are standard are not included, and neither are some of the symbols that are rarely used (e.g., in an appendix). In that situation, or if a symbol is used in a slightly different context than given here, its meaning is clearly indicated in the text itself.

Electromagnetic Field Analysis

r	2-D position vector
\mathbf{u}	Unit vector
∇_t	Transverse nabla operator (in the (x, y) plane)
$\mathbf{v}_t, \mathbf{v}_{tan}$	Transverse, resp., tangential component of vector \mathbf{v}
z	Coordinate along the longitudinal direction
j	Imaginary unit ($j^2 = -1$)
\mathbf{e}, \mathbf{E}	Electric field (V/m)
\mathbf{h}, \mathbf{H}	Magnetic field (A/m)
\mathbf{j}, \mathbf{J}	Surface current density (A/m)
\mathbf{a}, \mathbf{A}	Magnetic vector potential (Vs/m)
ϕ	Scalar electric potential (V)
ρ	Surface charge density (p.u.l. in z -direction) (C/m ²)
G_0	Green's function of free space (often the quasi-static approximation)
t	Time (s)
f	Frequency (Hz)
ω	Pulsation (1/s)
λ	Wavelength (m)
k	Wavenumber (1/m)
β	Complex propagation factor in z -direction (1/m)
α	Attenuation factor in z -direction (1/m)
ν	Singularity exponent
ϵ_r	Relative permittivity
μ_r	Relative permeability
σ	Conductivity (S/m)
c	Speed of light in the vacuum (299 792 458 m/s)
μ_0	Permeability of the vacuum ($4\pi 10^{-7}$ H/m)
ϵ_0	Permittivity of the vacuum ($1/\mu_0 c^2$ C/m)

Transmission Line Modeling

S	Generic material cross-section
c	Generic material boundary
N	Number of signal conductors; number of modes
a_m	modal representation of quantity a , for mode m
R	Resistance matrix (Ω/m)
L	Inductance matrix (H/m)
G	Conductance matrix (S/m)
C	Capacitance matrix (C/m)
\tilde{L}	Complex inductance matrix (H/m)
\tilde{C}	Complex capacitance matrix (C/m)
\mathbf{i}	Current vector (A)
\mathbf{v}	Voltage vector (V)
i, I	Current (A)
v, V	Voltage (V)
P	Power (W)
Z_c	Characteristic impedance (Ω)
Z_{in}	Internal impedance (Ω/m)
L_{in}	Internal inductance (H/m)
R_{in}	Internal resistance (Ω/m)

Numerical Techniques

A_n, \mathbf{A}	Coefficient n , resp., all coefficients in vector notation
\mathcal{D}, D	Dirichlet to Neumann operator, resp., matrix
\mathcal{Y}, Y	Surface Admittance operator, resp., matrix
ξ_m	Dirichlet eigenfunction
ψ_m	Neumann eigenfunction
k_m^2	Dirichlet eigenvalue, or, Neumann eigenvalue
ψ	A generic function, satisfying $\nabla_t^2 \psi = -k^2 \psi$
ψ_0	A generic function, satisfying $\nabla_t^2 \psi_0 = 0$
s	Normalized coordinate
$f_n(s), A_n$	A generic expansion function, resp., coefficient
c_i	Side i of a polygon
N_i	Number of expansion functions for side c_i
$t_{c_i, m}$	Basis function m on side c_i
$\Psi_{c_i, m}$	Discrete coefficients of ψ for side c_i
$\Gamma_{c_i, m}$	Discrete coefficients of $\partial\psi/\partial n$ for side c_i

List of Publications

International Science Citation Index Journals

- T. Demeester and D. De Zutter, “Modeling the broadband inductive and resistive behavior of composite conductors,” *IEEE Microwave and Wireless Components Letters*, vol. 18, no. 4, pp. 230-232, Apr. 2008.
- T. Demeester and D. De Zutter, “Quasi-TM transmission line parameters of coupled lossy lines based on the Dirichlet to Neumann boundary operator,” *IEEE Transactions on Microwave Theory and Techniques*, vol. 56, no. 7, pp. 1649-1660, July 2008.
- T. Demeester and D. De Zutter, “Internal impedance of composite conductors with arbitrary cross section,” *IEEE Transactions on Electromagnetic Compatibility*, vol. 51, no. 1, pp. 101-107, Feb. 2009.
- T. Demeester and D. De Zutter, “Construction of the Dirichlet to Neumann boundary operator for triangles and applications in the analysis of polygonal conductors,” *IEEE Transactions on Microwave Theory and Techniques*, accepted for publication.
- T. Demeester and D. De Zutter, “Fields at a finite conducting wedge and applications in interconnect modeling,” submitted to the *IEEE Transactions on Microwave Theory and Techniques*.

Other International Journals

- T. Demeester and D. De Zutter, “Construction and applications of the Dirichlet to Neumann operator in transmission line modeling,” *ELEKTRIK, Turkish Journal of Electrical Engineering and Computer Sciences*, accepted for publication (invited paper).

Articles in conference proceedings

- T. Demeester and D. De Zutter, “Modeling of the resistive and inductive behaviour of layered and coated conductors,” in *Proceedings of the 16th IEEE*

Topical Meeting on Electrical Performance of Electronic Packaging, Atlanta, USA, pp. 223-226, 29-31 Oct. 2007.

- T. Demeester and D. De Zutter, “Determination of the broadband transmission line parameters of lossy lines using the Dirichlet to Neumann operator,” in *Proceedings of the 16th IEEE Topical Meeting on Electrical Performance of Electronic Packaging*, Atlanta, USA, pp. 267-270, 29-31 Oct. 2007.
- D. De Zutter and T. Demeester, “Transmission line modeling of coupled lines in a semiconducting substrate,” in *Proceedings of the 6th Iberian Meeting on Computational Electromagnetics*, Chiclana, Spain, Oct. 2008.
- T. Demeester and D. De Zutter, “Applications of the Dirichlet to Neumann boundary operator in transmission line modeling,” in *Proceedings of the 20th International Zurich Symposium on Electromagnetic Compatibility*, Zurich, Switzerland, pp. 45-48, 12-16 Jan. 2009.
- T. Demeester and D. De Zutter, “Modeling the broadband resistive and inductive behavior of polygonal conductors,” in *Proceedings of the International Conference on Electromagnetics in Advanced Applications*, Torino, Italy, 14-18 Sep. 2009.

Conference Abstracts

- T. Demeester and D. De Zutter, “Development of a general lossy transmission line model,” in *Proceedings of the 8th FirW Ph.D. Symposium*, Ghent, Belgium, 5 Dec. 2007.
- T. Demeester and D. De Zutter, “Design and simulation of on-chip lossy transmission line pairs,” in *Proceedings of the 12th IEEE Workshop on Signal Propagation on Interconnects*, Avignon, France, 12-15 May 2008.
- T. Demeester and D. De Zutter, “Conductor modeling with the surface admittance operator of triangles,” in *Proceedings of the 13th IEEE Workshop on Signal Propagation on Interconnects*, Strasbourg, France, 12-15 May 2009.

Scientific Award

- Third place in the Student Paper Prize Competition for the paper entitled “Applications of the Dirichlet to Neumann boundary operator in transmission line modeling,” at the *20th International Zurich Symposium on Electromagnetic Compatibility*, Zurich, Switzerland, 12-16 Jan. 2009.

**TRANSMISSION LINE MODELING OF LOSSY
INTERCONNECTS WITH THE DIRICHLET TO
NEUMANN BOUNDARY OPERATOR**

Introduction

The modeling of high-speed interconnects

From the middle of the 20th century onwards, a number of important inventions in the field of electronics have drastically changed our everyday life. A first milestone was the invention of the transistor, a semiconducting device acting as an amplifier or a switch, first used for military radio applications, and which is still one of the most fundamental electronic building blocks. A further step forward was the development of the printed circuit board (PCB), which is, basically, a mechanical support containing electronic components (transistors, resistors, capacitors, ...). These are connected by means of conductive traces, which are etched from copper sheets, laminated onto a non-conductive substrate. Finally, perhaps the most important invention, the integrated circuit (IC) was developed, which allowed to embed several transistors and passive components on the surface of a thin substrate of semiconductor material. This announced the start of a rapid evolution in the miniaturization and complexity of electronic circuits, ranging from tens of transistors in the early sixties to tens of billions of transistors in nowadays very-large-scale-integration (VLSI) circuits. IC's are often digital devices, designed to process binary signals, but can also be analog devices such as operational amplifiers, or even combinations that process or convert both continuous (analog) and digital signals.

Numerous electronic devices that are part of everyday life, such as mobile phones, gps, digital hi-fi equipment, computers, and many others, contain IC's mounted on printed circuit boards. Modern semiconductor technologies allow speeds of 40 GBit/s and higher. At such high frequencies, the chip designer can no longer consider the IC as a network of discrete ('lumped') elements, but needs to take into account a number of electromagnetic effects that would otherwise degrade the quality of the electrical signals, to the point where errors would occur in digital data streams, such that the whole system would become unreliable or even fail. Most of these 'signal integrity' issues [1–3] are related to the electrical performance of the interconnections between the different electronic devices. Especially if the signals are transmitted over long distances and at high bit rates, all kinds of wave effects deteriorate their quality.

Signal integrity problems can occur on-chip, as well as on the PCB. A discussion of the different mechanisms would fall outside the scope of this work, and therefore only a few examples are given here, directly related to the topics covered in the next chapters. On a PCB, the dimensions of the interconnects with respect to the bit rate,

are often such that the metallic traces are operated in the skin effect mode, which results in an important high-frequency attenuation. The lengths of the lines often give rise to wave phenomena and, hence, signal delays. Moreover, the microstrip traces are dispersive, which might cause a distortion of the wave forms. This is due to the losses (both in the conductors and in the dielectric substrate) and to the electromagnetic field pattern that tends to concentrate in the substrate for increasing frequencies, corresponding to a gradually decreasing phase velocity.

In digital IC's, crosstalk is one of the most important signal integrity issues. It basically means that signals are affected by other, nearby, signals. Capacitive and inductive coupling phenomena are very often at the origin of crosstalk. Another possible mechanism is conductive coupling of different signal lines through the lossy (semiconducting) substrate.

For high-speed systems, design engineers often use the technique of differential signaling. This signifies that the information is transmitted in two complementary signals over a double interconnection, and the receiver only takes into account the difference between both received signals. The major advantages of this technique are a higher immunity for fluctuations in the ground potential or the common mode, a higher noise immunity, and a better protection against electromagnetic interference (EMI) or crosstalk. However, to ensure an optimal performance of these interconnections, they have to be carefully designed. The shielding against outside noise, e.g., becomes better for a smaller spacing between the differential lines (allowing also a higher trace density), but then their capacitive coupling increases, together with the attenuation. Also, the value of their differential characteristic impedance has to be accurately known for the termination of the lines, in order to prevent from reflections.

A lot of research is being performed on high-speed interconnects, and on packaging in general, in order to keep up with the miniaturization of IC's according to Moore's law, and the increase in operating frequencies. A challenging new on-chip application, e.g., are the so-called *multiband RF-interconnects* [4] which use electrically long on-chip transmission lines, as a fast and powerful alternative to the traditional RC-limited interconnects.

In all the mentioned examples, both on the PCB and on-chip, and regarding either signal integrity issues, or for direct design purposes, the frequency-dependent *transmission line parameters* of the considered interconnects are of a vital importance. The resistance, inductance, capacitance, and conductance of the lines per unit of length (p.u.l.) lead to all required parameters, such as the phase velocity, the attenuation factor, and the characteristic impedance. For coupled lines, there exist several fundamental modes, with different propagation characteristics, which can all be found as the solution of an eigenvalue problem, once the basic p.u.l. parameters are determined. For one differential pair, e.g., not only for the so-called 'differential mode' (used for signal propagation), a correct impedance matching is required, but also for

the ‘common’ mode¹ (in a perfectly symmetric configuration only excited by noise coupled into the circuit), in order to avoid EMI problems. The required transmission line model should be able to deal with *multiple coupled conductors*, each with a *finite conductivity*, and should be capable of dealing with *current crowding effects* up to skin effect frequencies. Furthermore, it is important that *conductive coupling* through semiconducting substrates is taken into account as well.

In the past, a lot of research on multiconductor transmission line models has already been done. The existing theories are not repeated here, as there is a lot of excellent literature on the subject, e.g., in [5] and [6]. These books provide an in-depth overview of and a comparison between many techniques that have been and are used for multiconductor line analysis. In general terms, the models presented in [5] and [6] deal with full-wave solutions of Maxwell’s equations for two-dimensional multiconductor structures, containing perfect electric conducting (PEC) signal lines, and mostly low-loss dielectric substrates. Important to mention is the fact that the laws of electromagnetics do not unambiguously lead to a transmission line equivalent. This is only true for low frequencies, the so-called quasi-TEM (transverse electric and magnetic) case. This issue is extensively described in [6], together with the different types of transmission line models that can be extracted from Maxwell’s equations. Each possible model is based on a, not entirely arbitrary, ‘extra’ condition, such as the requirement that all modes in the actual interconnect configuration and in the model propagate the same complex power, or, that the model remains reciprocal if no non-reciprocal materials are present.

A further advance in the field was made with [7], in which the current crowding as a function of frequency, including the strong skin effect regime, for conductors with finite conductivity was taken into account. The method was superior with respect to already existing, volume-discretization based methods, because it makes use of a boundary integral equation only, hence more accurately capturing the skin effect with less unknowns. It extends the principle of the asymptotic *local* surface admittance of a conductor at very high frequencies to a *global* (i.e., on the conductor’s surface) surface admittance. The starting point is an *equivalent surface current density source* in free space (or embedded in any other background medium such as a substrate), replacing the original conductor, but exciting the original fields outside of it. The relationship that determines this equivalent surface current anywhere on the conductor as a function of the tangential electric field everywhere on the surface, called the *surface admittance operator*, is constructed by means of the Dirichlet to Neumann (DtN) operator. Mathematically the DtN operator needed in this work is defined as follows. A scalar function $f(x, y)$ satisfies the two-dimensional wave equation $\nabla_t^2 f + k^2 f = 0$ over a surface S with boundary c . When $k = 0$ this equation reduces to the Laplace

¹Design engineers are used to call it the ‘differential’ and the ‘common’ mode, whereas people in electromagnetics refer to it as the ‘odd’, respectively, the ‘even’ mode. Throughout this thesis, the latter designation is used.

equation and when it takes a purely imaginary value it reduces to a diffusion equation. For any prescribed value of the function f on the boundary c , the DtN operator maps this value onto the corresponding normal derivative $\partial f / \partial n$ on c . However, the method presented in [7] only deals with conductors in homogeneous space, and, as opposed to the full-wave methods mentioned earlier, is only valid in the quasi-TM (transverse magnetic) frequency range². However, for many practical interconnect applications, the quasi-TM validity range completely covers the frequency band of interest. Because of its major advantages in the modeling of non-perfect conductors, the DtN operator is the basic building block of the work presented in this doctoral thesis, which deals with the more general transmission line problems as mentioned earlier.

Outline of this thesis

The main research result presented in this dissertation is a new reciprocity-based lossy multi-conductor transmission line model in the quasi-TM frequency range. However, in parallel with the development of the transmission line model itself, some additional research was performed in the field of conductor modeling, and a new algorithm was proposed to improve the calculation efficiency and to extend the possibilities of the DtN operator. These results are also presented in this work. The successive chapters do not reflect the chronological order of the research. Instead, the thesis starts with a global description of the transmission line model, and then one by one covers these additional research topics. As the work of the past three years has resulted in a number of papers published in or submitted to international journals, and which precisely cover the mentioned topics, the text of these papers is entirely reproduced in the different chapters. Only on certain locations in the text, by means of footnotes, a few comments are given to further clarify the covered topic, or to make a link with other chapters. This approach has the advantage that the chapters are relatively self-consistent and very readable. However, this means there often is some overlap between chapters, in particular in their introduction, as all the papers and hence chapters of this thesis are situated in the context of high-speed interconnect modeling, as already treated in this introductory chapter.

The following paragraphs provide an overview of the different chapters and appendices, briefly summarized and situated among the rest of the presented research.

Chapter 1

The first chapter (see [8]) presents a new transmission line model. A lot of attention is devoted to explaining why and how a reciprocal model is obtained, by carefully defining the signal currents in the model. Next, consistent with the defined reciprocal

²Notice the difference with respect to the *quasi-TEM* models mentioned above. In *quasi-TM* models, the longitudinal component of the electric field inside the conductors and semiconductors with a finite conductivity is taken into account.

model, a capacitance-conductance and an inductance-resistance problem are formulated, to be solved with the Method of Moments (MoM). The model is valid within the quasi-TM frequency range, as is also explained with care, and deals with metallic signal conductors in the presence of both semiconducting and dielectric substrates. In the numerical examples, the emphasis is in the first place on the validation of the method, by comparing the results with data that are available in literature for single line configurations. Other important aspects in the numerical results are the modal analysis of multi-line configurations, and the influence of the semiconducting substrate (with the so-called slow-wave behavior). In this chapter, all simulated configurations only consist of conductors, dielectrics and semiconductors with a rectangular shape or composed of rectangles. In Chapter 4, the DtN operator is determined for triangular shapes, such that a whole range of more complex geometries can be treated, but for which the presented transmission line model remains of course valid.

Chapter 2

The second chapter focusses on *composite conductors*, covering two different applications. In the first part [9], the broadband resistive and inductive behavior of layered and coated conductors is investigated. The main purpose of this contribution is to demonstrate the model's capability of handling thick conductors over a broad frequency range. In the theoretical section, the formulas that are required to treat composite conductors are again written down, but for the one-conductor case only. Naturally, the more general formulation of Chapter 1 remains valid (which is used to handle the more complex numerical examples). In addition, it is shown how the internal current density can be calculated by means of an expansion in Dirichlet eigenfunctions.

In the second part [10] of the chapter, the *internal impedance* of conductors is investigated. A new derivation allows to determine the internal impedance from the knowledge of the surface admittance operator only, which in the special case of a homogeneous rectangular conductor is identical with a definition already available in literature. The new technique allows to directly calculate the internal impedance of composite conductors or of conductors with a complicated conductor shape. However, since the issue has been a topic of discussion in previous papers and as an alternative definition for the internal impedance is also generally accepted, a boundary integral form of that alternative definition was developed as well, in order to compare our definition to the existing one. In the examples, not only the difference between both definitions is compared, but the influence of the conductor corners also receives some attention, further investigated in Chapter 6 as the 'edge effect'.

Chapter 3

This chapter (see [11]) deals with the discretization of the DtN operator for a rectangle, as used in the transmission line model presented in Chapter 1. The theory is however given only at this point, as the approach and notations are very similar

and therefore helpful to grasp to the more complicated case presented in Chapter 4 for triangles. It is briefly described how the electric field inside a conductor (or the electric potential inside a dielectric) is expanded in terms of parallel-plate waveguide modes, and how the numerical convergence problems at the corners are dealt with. For completeness, and as [11] is an (invited) extension of [12], the main applications of the DtN operator are briefly presented again, combined with some extra numerical examples, dealing with the internal impedance of composite conductors, and with a multi-conductor on-chip configuration.

Chapter 4

In this chapter, the Iterative Combined Waveguide Modes (ICWM) algorithm (see [13]) is introduced. It allows to calculate the DtN operator for triangular geometries. The main idea behind the method is to expand the current density or electric potential by combining three incomplete sets of parallel-plate waveguide modes, that are however each complete on one of the triangle's sides and form the exact solution on the inside. The described iterative method allows to determine the expansion coefficients, and, from the analytical expansion functions, the DtN operator. The convergence characteristics of the method and its accuracy are thoroughly investigated, and some comparison with published data confirms its correctness. The presented numerical examples involve trapezoidal conductors and, as a demonstration of the ICWM technique applied to dielectric triangles, a coplanar waveguide with a non-planar substrate.

Chapter 5

The focus in this chapter is on the field behavior near a conducting wedge (see [14]). The known singular field behavior is verified and a comparison is made with perfect conductors, using results obtained with the ICWM algorithm. Furthermore, the electric field inside the conductor and near the edge is visualized, this time by means of the parallel-plate waveguide expansion introduced in Chapter 4 (as opposed to the Dirichlet expansion employed in Chapter 2). The behavior of the fields (including the equivalent current density) is in particular investigated as a function of the wedge angle, which has an important impact on the circuit parameters. As a side result, the DtN operator leads to a new local surface impedance approximation for conductors, primarily meant to demonstrate the physical properties of the equivalent surface current density. Throughout the text, the quasi-TM approximations are reconsidered with care, now focussing on the behavior near corners, and on the validity of a constant boundary potential voltage excitation of conductors with edges. Finally, a link is made between the tangential magnetic field at a conductor's boundary, and the p.u.l. circuit resistance and inductance of that conductor.

Chapter 6

The final chapter summarizes the progress made in the field of transmission line

modeling and conductor modeling, including the new techniques for DtN operator calculations. Some suggestions are listed for further research in these domains, as there are a lot of possibilities for further developments in interconnect modeling, including the specific topics covered in this work.

Appendices

The research performed in the framework of this Ph.D. dissertation, resulted in a number of contributions to the proceedings of international conferences. The technical content of most of these papers is described in much more detail in the journal papers that constitute Chapters 1 to 5, and these papers are therefore not included. Two of them, however, contain some extra data and are reproduced in Appendix A. The first paper [15] refers to the model presented in [8] and gives simulation results for an on-chip interconnect configuration, focussing on some design aspects of a differential conductor pair, including an example of a finite length configuration with a specific source and load. The second paper [16] presents a direct extension of the ICWM algorithm theory of Chapter 4, which was, although perhaps obvious, included as well, for the sake of completeness.

Appendix B presents a new analytical calculation of the quasi-static interaction integrals in free space, for an arbitrary position and orientation of the considered integration segments. A direct implementation of the presented formulas was used for the simulations presented in Chapter 5 (including the last example of Chapter 4). The method is based on a direct integration of the logarithmic function, with a compensation term to cancel possible incorrect contributions from integrating over the branch cut in the complex plane.

Finally, Appendix C gives the field expansions and describes the procedure to discretize the full-wave surface admittance operator on the surface of a homogeneous rectangular parallelepiped, by means of an expansion in the modes of three rectangular waveguides.

Bibliography

- [1] H. W. Johnson and M. Graham, *High-speed digital design: a handbook of black magic.* Prentice-Hall, Inc., 1993.
- [2] S. H. Hall, G. W. Hall, and J. A. McCall, *High-Speed Digital System Design: A Handbook of Interconnect Theory and Design Practices.* Wiley - IEEE press, 2000.
- [3] M. Peng Li, *Jitter, Noise, and Signal Integrity at High-Speed.* Prentice-Hall, Inc., 2007.
- [4] M.-C. Chang, “Multiband RF-interconnect for CMP inter-core communications,” in *9th International Conference on Solid-State and Integrated-Circuit Technology*, Oct. 2008, pp. 1811–1814.
- [5] N. Fache, F. Olslager, and D. De Zutter, *Electromagnetic and Circuit Modeling of Multiconductor Transmission Lines.* New York: Oxford University Press Inc., 1993.
- [6] F. Olyslager, *Electromagnetic Waveguides and Transmission Lines.* Oxford, U.K.: Oxford University Press Inc., 1999.
- [7] D. De Zutter and L. Knockaert, “Skin effect modeling based on a differential surface admittance operator,” *IEEE Trans. Microw. Theory Tech.*, vol. 53, no. 8, pp. 2526–2538, Aug. 2005.
- [8] T. Demeester and D. De Zutter, “Quasi-TM transmission line parameters of coupled lossy lines based on the Dirichlet to Neumann boundary operator,” *IEEE Trans. Microw. Theory Tech.*, vol. 56, no. 7, pp. 1649–1660, Jul. 2008.
- [9] ——, “Modeling the broadband inductive and resistive behavior of composite conductors,” *IEEE Microw. Wireless Compon. Lett.*, vol. 18, no. 4, pp. 230–232, Apr. 2008.
- [10] ——, “Internal impedance of composite conductors with arbitrary cross section,” *IEEE Trans. Electromagn. Compat.*, vol. 51, no. 1, pp. 101–107, Feb. 2009.
- [11] ——, “Construction and applications of the Dirichlet to Neumann operator in transmission line modeling,” *J. Elec. Eng. Comp. Sci.*, accepted for publication.

- [12] ——, “Applications of the Dirichlet to Neumann boundary operator in transmission line modeling,” presented at the 20th International Zurich Symposium on Electromagnetic Compatibility, Jan. 2009.
- [13] ——, “Construction of the Dirichlet to Neumann boundary operator for triangles and applications in the analysis of polygonal conductors,” *IEEE Trans. Microw. Theory Tech.*, recommended for publication.
- [14] ——, “Fields at a finite conducting wedge and applications in interconnect modeling,” *IEEE Trans. Microw. Theory Tech.*, submitted for publication.
- [15] ——, “Design and simulation of on-chip lossy transmission line pairs,” in *12th IEEE Workshop on Signal Propagation on Interconnects*, Avignon, France, May 2008.
- [16] ——, “Modeling the broadband resistive and inductive behavior of polygonal conductors,” in *International Conference on Electromagnetics in Advanced Applications, Torino, Italy*, Torino, Italy, Sep. 2009.

CHAPTER 1

Quasi-TM Transmission Line Parameters of Coupled Lossy Lines Based on the Dirichlet to Neumann Boundary Operator

Thomas Demeester and Daniël De Zutter

Published in the *IEEE Transactions on Microwave Theory and Techniques*,
vol. 56, no. 7, July 2008.



We present a new multiconductor transmission line model for general two-dimensional lossy configurations, based on mode reciprocity. Particular attention is devoted to elucidate the validity of the quasi-TM model and the approximations that have to be invoked to obtain this model. A new derivation of the complex capacitance matrix is given, especially taking into account the presence of semiconductors. This derivation automatically leads to a non-classical circuit signal current definition and demands for a formulation of the complex inductance problem consistent with that definition. The relevant RLGC circuit matrices are obtained by solving boundary integral equations only, making use of the Dirichlet to Neumann boundary operator for the different materials. This allows to simulate complex MIS-structures, as shown in the numerical examples.

1.1 Introduction

Due to the increase in operating frequencies, signal integrity issues become more and more critical, not only on the package and board level but also at the chip level. In nowadays very-large-scale-integration (VLSI) circuits, lumped resistance-capacitance (RC) models no longer suffice for adequate signal analysis but are replaced by transmission line models. In the past much attention has been paid to the analysis of metal-insulator-semiconductor or MIS transmission lines. A very good overview of this work is given in the introduction of [1] and will not be repeated here. Using a variety of numerical techniques, these papers analyze the fundamental mode behavior as a function of frequency and semiconductor resistivity, revealing the existence of dielectric, slow-wave and skin-effect modes. Additional data based on quasi-analytical approaches and measurements can e.g. be found in [2–4]. It is interesting to draw the attention to a series of papers dealing with semiconductor substrate noise coupling, see [5] and the references therein. These papers use and/or discuss the validity of electroquasistatic RC-modeling to predict noise coupling and in this way also deal with the question of approximating the full Maxwell equations in the presence of semiconductors. Furthermore, an efficient quasi-TEM analysis for lossy lines, using a Finite Element approach and its full-wave extension to semiconductor traveling-wave devices, including self-consistent carrier transport, have been presented in [6] and [7].

In [1] the quasi-TM model proposed in [8] is extended to include non-perfectly conducting metallic conductors. As shown e.g. in [9] and [10] these conductor losses can become dominant for narrow strip configurations. The transmission line model developed in [1] is obtained by carefully defining the meaning of voltage and current, remaining compatible with the complex power concept [11,12]. To obtain the complex capacitance and inductance per unit of length (p.u.l), the quasi-static electric potential and the longitudinal current density are determined numerically using a combination of the Method of Lines (MoL) and the Method of Moments (MoM).

In this paper the quasi-TM analysis of [1] is extended to the multiconductor case. Section 1.2 discusses the general geometry of the considered problem together with the relevant field equations. Contrary to what one might expect, the multiconductor case does not turn out to be a straightforward extension of the single line case. Section 1.3 shows that a coupled transmission line model with each modal voltage-current (\mathbf{v}, \mathbf{i}) solution corresponding to a modal field (\mathbf{e}, \mathbf{h}) solution must be based on mode orthogonality properties. Hence, the power orthogonality definition used in [1] must be replaced by a reciprocity based approach [13] as modal fields are not power orthogonal in the presence of lossy media. It must be noted that the approach in [11] is not the only one to enforce reciprocity. As originally presented in [14] and later extended to more complex configurations in [15] and [16], one can also choose to enforce power conservation for each mode separately, whereby modal reciprocity is still invoked to ensure the reciprocity of the resulting circuit model. Section 1.4.1

presents the theoretical analysis leading to the definition of the capacitance matrix and to the meaning of voltages and currents. A lot of attention is devoted to clarify the various approximations that must be invoked to come to a quasi-TM analysis and to show under which conditions this quasi-TM analysis remains valid. Similar to the single line case, it turns out that the meaning of current must be interpreted with due care. To define the complex capacitance matrix, mode orthogonality and hence reciprocity must again be invoked. Section 1.4.2 is devoted to the numerical solution of the capacitance problem. For this numerical solution the contrast currents and the corresponding contrast surface charges are introduced. These charges and the corresponding potential distribution in the cross-section are then determined by solving an appropriate boundary integral equation with the MoM. To solve this integral equation, a relationship between the normal derivative of the potential and the potential itself at the boundary of the different media is needed. This relationship is obtained by extending the surface admittance approach of [17], based on the Dirichlet to Neumann boundary operator, to the electroquasistatic case. Section 1.5 discusses the inductance problem. Starting from the longitudinal component of the contrast current, it is shown that the longitudinal currents and the complex inductance matrix elements can also be determined by solving a boundary integral equation essentially using the differential surface admittance approach of [17] (again taking advantage of the Dirichlet to Neumann boundary operator). To correctly describe the problem in the presence of semiconductors, the theory of [17] and [18] has been reformulated as to carefully include the wave behavior in the longitudinal direction and the non-constant potential in the cross-section. The potential obtained from the capacitance problem remains necessary to solve the inductance problem. In contrast to the approach in [1], using a combination of the MoM and the MoL, the inductance problem is solved by using a surface integral equation only. The major advantage of such an approach, as opposed to volume discretization methods, is the considerably reduced number of unknowns when simulating large configurations (such as e.g. the example presented in Section 1.6.3). Especially for the simulation of strong skin-effect behavior, boundary element methods tend to have a lower computational cost. However, as soon as more complicated semiconductor models are used as in [7], volume discretization methods are indispensable. Section 1.6 discusses a series of numerical examples, including some single-conductor reference examples and the full modal analysis of an on-chip interconnect structure with four coupled signal pairs. Finally, Section 1.7 provides some conclusions.

1.2 Geometry of the Problem and Field Equations

Fig. 1.1 shows the general cross-section of the considered multiconductor transmission line (MTL). It consists of piecewise homogeneous, non-magnetic materials embedded in a lossless homogeneous background medium. In Fig. 1.1 a single PEC

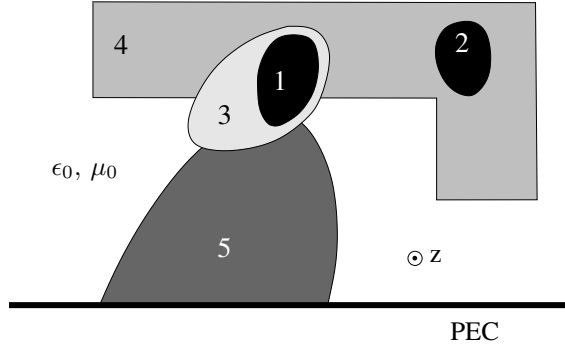


Figure 1.1: General two-dimensional cross-section to be considered. 1, 2: signal conductors ($\sigma \gg \omega\epsilon$), 3: lossless dielectrics (ϵ), 4: lossy dielectrics ($\sigma \ll \omega\epsilon$), 5: semiconductors (σ, ϵ).

(Perfectly Electric Conducting) ground plane is also shown, but its presence is not mandatory. In the sequel a distinction is made between three types of materials: signal conductors such as 1 and 2 in Fig. 1.1, for which $\sigma \gg \omega\epsilon$ over the considered frequency range (for a PEC $\sigma \rightarrow \infty$), lossless or lossy dielectrics such as 3 and 4 in Fig. 1.1 for which $\sigma = 0$ or $\sigma \ll \omega\epsilon$ and semiconductors such as 5. For simplicity, the homogeneous background medium is taken to be free space (ϵ_0, μ_0), but the analysis remains valid for any other dielectric background medium. An $e^{j\omega t}$ time-dependence is assumed. The total number of signal conductors is N . Maxwell's curl equations can be cast into the following form

$$\nabla_t e_z - \frac{\partial \mathbf{e}_t}{\partial z} = -j\omega\mu_0 (\mathbf{u}_z \times \mathbf{h}_t) \quad (1.1)$$

$$\nabla_t \times \mathbf{e}_t = -j\omega\mu_0 h_z \mathbf{u}_z \quad (1.2)$$

$$\nabla_t h_z - \frac{\partial \mathbf{h}_t}{\partial z} = (\sigma + j\omega\epsilon) (\mathbf{u}_z \times \mathbf{e}_t) \quad (1.3)$$

$$\nabla_t \times \mathbf{h}_t = (\sigma + j\omega\epsilon) e_z \mathbf{u}_z, \quad (1.4)$$

where the index “t” stands for the transverse (x, y) components. In the sequel we will also use the divergence equation

$$\nabla_t \cdot \mathbf{e}_t + \frac{\partial e_z}{\partial z} = 0. \quad (1.5)$$

We want to obtain a transmission line model for the fundamental modes propagating along the z -axis. The number of fundamental modes N is equal to the number of signal conductors (i.e. two in the case of Fig. 1.1). The z -dependence of mode m ($m = 1, 2, \dots, N$) is given by $e^{-j\beta_m z}$. In the absence of a PEC reference conductor, one of the conductors must be chosen as the reference conductor and in that case only $N - 1$ fundamental modes are needed. In the most general case, a full-wave

analysis is needed to determine the modal wavenumbers β_m and the corresponding modal field distributions. In this paper a quasi-TM approximation is proposed, based on the assumption that even at the highest frequency of interest no wave phenomena occur in the transverse plane. This implies that the wavelength $\lambda_m = 2\pi/\text{Re}(\beta_m)$ of each propagating mode remains significantly larger than the relevant diameter of the cross-section. Restricting ourselves to the fundamental modes, any solution of (1.1-1.4) for the transverse fields can be expressed as a superposition of these modes as [12]

$$\mathbf{e}_t(\mathbf{r}, z) = \sum_{m=1}^N \mathbf{E}_{tm}(\mathbf{r}) (K_m^+ e^{-j\beta_m z} + K_m^- e^{j\beta_m z}) \quad (1.6)$$

$$\mathbf{h}_t(\mathbf{r}, z) = \sum_{m=1}^N \mathbf{H}_{tm}(\mathbf{r}) (K_m^+ e^{-j\beta_m z} - K_m^- e^{j\beta_m z}). \quad (1.7)$$

\mathbf{E}_{tm} and \mathbf{H}_{tm} are the transverse modal field patterns, K_m^+ and K_m^- are the complex amplitudes of the modes respectively propagating in the positive and in the negative z -direction and $\mathbf{r} = x\mathbf{u}_x + y\mathbf{u}_y$.

1.3 Coupled Transmission Line Model

The circuit transmission line model we want to determine, describes the field problem in terms of voltages, currents, the complex capacitance matrix $\tilde{\mathbf{C}} = \mathbf{C} + \mathbf{G}/j\omega$ and the complex inductance matrix $\tilde{\mathbf{L}} = \mathbf{L} + \mathbf{R}/j\omega$ as

$$\frac{\partial \mathbf{i}}{\partial z} = -j\omega \tilde{\mathbf{C}} \mathbf{v} \quad (1.8)$$

$$\frac{\partial \mathbf{v}}{\partial z} = -j\omega \tilde{\mathbf{L}} \mathbf{i}, \quad (1.9)$$

with $\mathbf{v}(z)$ and $\mathbf{i}(z)$ the $N \times 1$ voltage and current vectors associated with the N signal conductors. In the absence of a PEC reference conductor, only $N-1$ currents and voltages are needed. A large body of literature, see [12], has been dedicated to investigate the mapping of the field problem onto a circuit description. One possible approach is to invoke power conservation together with a precise definition for either the current (PI-model) or the voltage (PV-model). The latter approach was also adopted in [1] for the single line case. The PI- and PV-model will only yield (almost) identical results in the (quasi-)TEM case. For the multiconductor case discussed here, a different approach based on reciprocity and mode orthogonality will be adopted, as explained and motivated in the sequel. For a general discussion on the differences between power based and reciprocity based models, we refer the reader to [12]. It has to be remarked that for lossless structures, both types of models are identical as the modal fields can

be chosen to be real.

Just as for the fields in (1.6) and (1.7), the voltages and currents in (1.8) and (1.9) can be expressed in terms of eigenmodes as

$$\mathbf{v}(z) = \sum_{m=1}^N \mathbf{v}_m (K_m^+ e^{-j\beta_m z} + K_m^- e^{j\beta_m z}) \quad (1.10)$$

$$\mathbf{i}(z) = \sum_{m=1}^N \mathbf{i}_m (K_m^+ e^{-j\beta_m z} - K_m^- e^{j\beta_m z}). \quad (1.11)$$

The voltage and current eigenmodes \mathbf{v}_m and \mathbf{i}_m are solutions to the following equations

$$j\beta_m \mathbf{i}_m = j\omega \tilde{\mathbf{C}} \mathbf{v}_m \quad (1.12)$$

$$j\beta_m \mathbf{v}_m = j\omega \tilde{\mathbf{L}} \mathbf{i}_m. \quad (1.13)$$

The reader will remark that the eigenvalues β_m are identical in all field and circuit equations. This property of the model is quite obvious as we require the modal signal speeds to be identical for the actual fields and for their circuit representation. Furthermore, the modal excitation coefficients K_m^+ and K_m^- are also *identical* in the modal field and modal circuit description. In general, this is only possible in reciprocity based models by requiring that the following equality holds

$$\iint_S (\mathbf{e}_t \times \mathbf{h}_t) \cdot \mathbf{u}_z dS = \mathbf{v}^T \cdot \mathbf{i}, \quad (1.14)$$

with S the total cross-section and with the superindex T indicating the transpose of the vector. Expression (14) differs from the one used in power based models in which the complex conjugate of \mathbf{h}_t and \mathbf{i} are used. As a consequence of the fundamental modal field orthogonality property [12] stating that

$$\iint_S (\mathbf{E}_{ti} \times \mathbf{H}_{tj}) \cdot \mathbf{u}_z dS = 0, \quad i \neq j, \quad (1.15)$$

for any modal fields \mathbf{E}_{ti} and \mathbf{H}_{tj} , (1.14) also remains valid on a mode per mode basis, i.e.

$$\iint_S (\mathbf{E}_{tm} \times \mathbf{H}_{tm}) \cdot \mathbf{u}_z dS = \mathbf{v}_m^T \cdot \mathbf{i}_m \quad (1.16)$$

and this property will be needed in the sequel. In the lossy case, using a power based model, this property is lost because the modes are no longer power orthogonal as in the lossless case.

In the next sections, starting from the above general description of the field prob-

lem and its circuit equivalent, we turn to the solution of the quasi-TM problem and to the determination of the complex capacitance and inductance matrix.

1.4 The Capacitance Problem and the Meaning of Voltages and Currents in the Transmission Line Equivalent

1.4.1 Theoretical Analysis

Due to the fact that $\sigma \gg \omega\epsilon$ for signal conductors, the *cross-sectional* tangential electric field \mathbf{e}_{tan} at the conductor's surface must be zero. If this would not be the case, the presence of such a field would very quickly (i.e. within a few times the relaxation time ϵ/σ) lead to a redistribution of the surface charges such that \mathbf{e}_{tan} becomes zero. \mathbf{e}_{tan} can be expressed in terms of the vector potential \mathbf{a} and the scalar potential ϕ as $\mathbf{e}_{tan} = -(\partial\phi/\partial tan)\mathbf{u}_{tan} - j\omega\mathbf{a}_{tan}$. Outside the good conductors¹, \mathbf{a}_t is of order ω , and hence in the quasi-TM approximation, $\omega\mathbf{a}_t$ is neglected with respect to $\nabla_t\phi$ (which corresponds to neglecting h_z with respect to \mathbf{h}_t). The continuity of \mathbf{a}_{tan} at the conductor's boundary implies therefore that $\mathbf{e}_{tan} \approx -(\partial\phi/\partial tan)\mathbf{u}_{tan}$. This in turn shows that, for a fixed value of z , ϕ takes a constant value on all signal conductors' boundaries, allowing to *define* the circuit voltages \mathbf{v} in (1.9) as these constant potential values².

We will now derive a general expression for the capacitance matrix and from this infer a meaning for the circuit currents \mathbf{i} . Cross multiplying (1.3) with \mathbf{e}_t and taking

¹Inside the good conductors, however, the quasi-TM approximation $\mathbf{e}_t \approx -\nabla_t\phi$ is not valid (at least within the skin-effect frequency range). The normal component a_n of the magnetic vector potential at the boundary is generally not continuous, hence no conclusions about its amplitude inside the conductor can be drawn, compared to its value on the outer side of the boundary. \mathbf{e}_t does not have a zero'th order frequency component inside the conductor (as it has on the outside), and hence $j\omega\mathbf{a}_t$ cannot be neglected with respect to \mathbf{e}_t . Note that $|\mathbf{e}_t| \ll |e_z|$ inside the conductor, but in order to accurately describe the capacitive properties of the line, see Chapter 5, \mathbf{e}_t itself cannot be neglected.

A detailed argumentation to support the fact that $\mathbf{e}_t \not\approx -\nabla_t\phi$ inside a conductor, is the following. If $j\omega\mathbf{a}_t$ could be neglected, then the surface charge ρ_c could be written as $\rho_c \approx -(\sigma/j\omega)\partial\phi^-/\partial n$, with $\partial\phi^-/\partial n$ the outward normal derivative of the electric potential, evaluated just inside the conductor. As soon as the skin depth is significantly smaller than the transverse dimensions of the conductor, $(1/j\omega)\partial\phi^-/\partial n$ becomes proportional to $\omega^{-1/2}$ (for a constant boundary excitation $\phi_c = V$, and with $\nabla_t\phi^2 = j\omega\mu_0\sigma\phi$ inside the conductor). This can be easily shown for some simple conductor configurations, such as a long slab or a circle. However, the surface charge on a good conductor is, within the quasi-TM frequency range, independent of the frequency (apart from a possible influence from a neighboring semiconducting substrate, as is shown further in this chapter). We can come to this conclusion by formulating an equivalent problem in free space, in which the equivalent surface charge is related to the electric potential through the quasi-static Green's function G_0 of free space. The result is independent of the frequency, if no moderately conducting semiconductors are around. This shows that the initial assumption about the surface charge is wrong.

²The fact that the electric potential takes a constant value on a signal conductor's boundary, at least within the quasi-TM limit, is further argued in Chapter 5, especially near sharp boundary edges.

advantage of (1.2) shows that

$$\mathbf{e}_t \times \frac{\partial \mathbf{h}_t}{\partial z} = -(\sigma + j\omega\epsilon)(\mathbf{e}_t \cdot \mathbf{e}_t) \mathbf{u}_z - j\omega\mu_0 h_z^2 \mathbf{u}_z - \nabla_t \times (h_z \mathbf{e}_t). \quad (1.17)$$

Integrating this over the cross-section S leads to the approximate result

$$\iint_S \left(\mathbf{e}_t \times \frac{\partial \mathbf{h}_t}{\partial z} \right) \cdot \mathbf{u}_z dS = - \iint_S (\sigma + j\omega\epsilon) \mathbf{e}_t \cdot \mathbf{e}_t dS. \quad (1.18)$$

To obtain (1.18) the contribution of the higher-order term in h_z^2 was neglected. The $\nabla_t \times ()$ term reduces to a vanishing boundary integral at infinity or to a zero contribution on the surface of a PEC conductor, when present. We now insert expansions (1.6) and (1.7) into the left hand side of (1.18), invoke the mode orthogonality (1.15) and use (1.8), (1.10) and (1.11) to show that

$$-\mathbf{v}^T \cdot \frac{\partial \mathbf{i}}{\partial z} = \mathbf{v}^T \cdot (j\omega \tilde{\mathbf{C}}) \cdot \mathbf{v} = \iint_S (\sigma + j\omega\epsilon) \mathbf{e}_t \cdot \mathbf{e}_t dS. \quad (1.19)$$

Note that using the power conservation and reciprocity approach of [14–16] does not allow to obtain (1.19). It would be interesting to investigate how to modify the present theory to accommodate this alternative approach, but this falls outside the scope of the present paper. The total cross-section S consists of three parts: signal conductors, semiconductors and dielectrics (including the background medium). For the dielectrics the approximation $\mathbf{e}_t = -\nabla_t \phi$ holds as the contribution from the vector potential $-j\omega \mathbf{a}_t$ is of higher order in ω . For the semiconductors, the following reasoning can be adopted. For the frequency range in which σ remains much larger than $\omega\epsilon$, the potential ϕ on the boundary of the semiconductor will remain constant, just as for a signal conductor. For these frequencies for which this no longer holds, the semiconductor will behave as a complex dielectric. The potential will not be constant on its boundary but now (just as for the lossy dielectrics) it is allowed to state that the approximation $\mathbf{e}_t = -\nabla_t \phi$ holds. The neglected term $-j\omega \mathbf{a}_t$ is very small in the quasi-TM range, and is therefore negligible with respect to the term $-\nabla_t \phi$. In the case of a constant boundary potential, this approximation is no longer valid, but then the *total* transverse electric field itself becomes very small. The numerical results in Section 1.6 will confirm that the semiconductor behavior can be captured as described above.

To further transform the r.h.s. of (1.19), following the above reasoning, the cross-section S is subdivided in two parts S_1 and S_2 . S_1 encompasses the signal conductors and those semiconductors for which, at the considered frequency, the potential is constant on their boundary. S_2 is the remaining part of S and here $\mathbf{e}_t = -\nabla_t \phi$ holds. Taking into account the divergence law (1.5), the contribution from S_2 to the r.h.s. of

(1.19) becomes

$$\begin{aligned} & \iint_{S_2} (\sigma + j\omega\epsilon) \mathbf{e}_t \cdot \mathbf{e}_t dS \\ &= - \iint_{S_2} (\sigma + j\omega\epsilon) \left(\nabla_t \cdot (\phi \mathbf{e}_t) + \phi \frac{\partial e_z}{\partial z} \right) dS \quad (1.20) \\ &= \int_{c_2} (\sigma + j\omega\epsilon) \phi \mathbf{u}_n \cdot \mathbf{e}_t dc - \iint_{S_2} (\sigma + j\omega\epsilon) \phi \frac{\partial e_z}{\partial z} dS. \quad (1.21) \end{aligned}$$

The boundary c_2 of S_2 consists of (i) a contribution at infinity, which drops out, (ii) possible contributions of dielectrics and/or semiconductors touching each other, but due to the continuity of $(\sigma + j\omega\epsilon) \mathbf{u}_n \cdot \mathbf{e}_t$ these contributions also drop out and (iii) contributions at the boundaries between these materials and the signal conductors and semiconductors with a constant surface potential. In the sequel, the term “relevant” is used to indicate these semiconductors. In (1.21) the normal \mathbf{u}_n is directed outwards w.r.t. the good conductors, explaining the change in sign in going from (1.20) to (1.21). In these remaining contributions (iii), the constant potential can be put in front of the integration, the continuity of $(\sigma + j\omega\epsilon) \mathbf{u}_n \cdot \mathbf{e}_t$ can again be invoked and the divergence theorem combined with (1.5), but now for the cross-sections of the signal conductors and the relevant semiconductors, lead to the following expression for the first term in (1.21)

$$\int_{c_2} (\sigma + j\omega\epsilon) \phi \mathbf{u}_n \cdot \mathbf{e}_t dc = - \sum_j \phi_j \frac{\partial}{\partial z} \iint_{S_j} \sigma e_z dS \quad (1.22)$$

$$= - \sum_j \phi_j \frac{\partial I_j}{\partial z} \quad (1.23)$$

$$= j\omega \sum_j \phi_j q_j. \quad (1.24)$$

The summation in (1.24) now runs over all signal conductor cross-sections *and* relevant semiconductor cross-sections, ϕ_j is the constant potential, I_j is the total longitudinal current and q_j the total surface charge associated with cross-section j . To avoid confusion with the circuit currents \mathbf{i} introduced in (1.8) and (1.9), we use capital I 's here. To obtain (1.24) and in line with previous approximations, displacement currents in good conducting materials were neglected with respect to conduction currents. We now turn back to (1.19) and write it with (1.21) and (1.24) as

$$\mathbf{v}^T \cdot (j\omega \tilde{\mathbf{C}}) \cdot \mathbf{v} = j\omega \sum_j \phi_j q_j - \iint_{S_2} (\sigma + j\omega\epsilon) \phi \frac{\partial e_z}{\partial z} dS + \iint_{S_1} \sigma \mathbf{e}_t \cdot \mathbf{e}_t dS. \quad (1.25)$$

To keep our approximations consistent, comparing (1.22) and the remaining integral over S_2 in (1.25), we see that we have to drop this term because the longitudinal conduction and displacement currents in S_2 are much smaller than the currents in the signal conductors. Moreover, the last term of (1.25) stands for the contribution from transverse currents in the good conducting materials and these remain negligible as compared to the contribution of the longitudinal currents represented by the second term. Hence, from (1.25), we finally arrive at

$$\mathbf{v}^T \cdot \tilde{\mathbf{C}} \cdot \mathbf{v} = [\mathbf{v}^T \quad \mathbf{v}_{sc}^T] \cdot \begin{bmatrix} \mathbf{q} \\ \mathbf{q}_{sc} \end{bmatrix} \quad (1.26)$$

with \mathbf{q} and \mathbf{q}_{sc} column vectors containing the charges respectively on each signal conductor and on each relevant semiconductor and with \mathbf{v} and \mathbf{v}_{sc} the corresponding voltages. The voltages \mathbf{v}_{sc} depend linearly on \mathbf{v} .

According to (1.26), the capacitance matrix can be obtained solving an almost classical capacitance problem. We will come back to that problem in the next subsection. Suffices to say here that two distinct situations can occur. Either one of the relevant semiconductors touches a signal conductor such that its potential becomes equal to that of the signal conductor, or, the semiconductor stands free, but in that case its total charge must remain zero. Together with Laplace's equation for the potential this will suffice to determine $\tilde{\mathbf{C}}$. Using (1.8), (1.26) can also be rewritten as

$$\mathbf{v}^T \cdot \frac{\partial \mathbf{i}}{\partial z} = [\mathbf{v}^T \quad \mathbf{v}_{sc}^T] \cdot \begin{bmatrix} \frac{\partial \mathbf{I}}{\partial z} \\ \frac{\partial \mathbf{I}_{sc}}{\partial z} \end{bmatrix} \quad (1.27)$$

From the above equation we can now derive the following interpretation for the circuit currents \mathbf{i} in our reciprocity based, quasi-TM model. Suppose that signal conductor n is put at the non-zero potential v_n while all other signal conductor potentials remain zero. From (1.27) we see that

$$i_n = I_n + \sum_p \frac{v_{sc,p}}{v_n} I_{sc,p} \quad (1.28)$$

This shows that the circuit current i_n associated with signal conductor n must be interpreted as the actual current running through that conductor increased by suitably weighted currents running through some of the relevant semiconductors. From the semiconductors taken into account as good conductors, only those remain present in the summation over p provided they touch the considered signal conductor, such that $v_{sc,p} = v_n$. In all other cases their contribution remains zero either because they touch a signal conductor at zero potential $v_{sc,p} = 0$, or are standing free, in which case $I_{sc,p} = 0$. Above, a lot of, but consistent, approximations have been introduced. Such approximations are inevitable when trying to come up with a quasi-TM analysis.

In [1], for the single signal conductor case, $N = 1$, power conservation was in-

voked to derive an expression for the circuit current i associated with a voltage excitation v , leading to a current expression (eqn. 27 of [1]) differing from the traditional conduction current found in the quasi-TEM approximation:

$$i = i_c + \iint_{S_{\text{semicond.}}} J_z \frac{\phi^*}{v^*} dS. \quad (1.29)$$

The current i is the sum of the total longitudinal current i_c flowing in the signal conductor and a, by the normalized complex conjugate potential ϕ^*/v^* of the semiconductors, weighted contribution of the longitudinal currents flowing in the semiconducting layers. Remark that if we keep the potential under the integral sign in the contribution of the semiconductors in (1.25), a similar result is obtained. For the examples considered in [1], our numerical results (see Section 1.6) are identical. This is a consequence of (i) the fact that the semiconductor contributions to (1.29) are indeed negligible when their potential is not constant, and (ii) the fact that their contribution is identically zero when the potential is constant, because in the numerical examples in [1] all semiconductors touch the ground conductor and/or the surrounding metallic box which are kept at zero potential.

1.4.2 Numerical Solution

The capacitance problem formulated above can numerically be solved by various techniques. Here we opt for a surface integral equation solution combined with the Dirichlet to Neumann operator presented in [17], but specifically tailored to the capacitance problem. To this end all materials are replaced by their equivalent unknown contrast current source $\mathbf{j}_c = (\sigma + j\omega(\epsilon - \epsilon_0)) \mathbf{e}$. These sources reside in the homogeneous background medium and generate the original fields. The z -component of this contrast current will serve as the starting point for solving the inductance problem in Section 1.5, and the transverse component is essential for the capacitance problem.

As all media are piecewise homogeneous, the divergence of \mathbf{j}_c is zero and no volume contrast charges are present. However, at each interface between a material and the background medium, a contrast surface charge density ρ_{eq} , given by

$$\rho_{\text{eq}} = -\frac{j_{c,n}}{j\omega} = -\left(\epsilon - \epsilon_0 + \frac{\sigma}{j\omega}\right) e_n \quad (1.30)$$

must be taken into account, with $j_{c,n}$ and e_n representing the normal components with regard to the outward pointing unit normal \mathbf{u}_n . The equivalent surface charge ρ_{eq} in (1.30) consists of the actual surface charge and of the so-called polarization surface charge with respect to the homogeneous background medium. In reality, more complex situations such as the interface between a dielectric and a signal conductor or semiconductor will occur. In these cases, two contrast surface densities ρ_{eq}^+ and ρ_{eq}^-

are introduced, each defined as in (1.30) with respect to the outward pointing normal. The sum of ρ_{eq}^+ and ρ_{eq}^- yields the correct total contrast surface charge. Neglecting $\epsilon - \epsilon_0$ with respect to $\frac{\sigma}{j\omega}$ in (1.30) at good conductors and relevant semiconductors (completely in line with the reasoning in section 1.4.1), we immediately see that the total contrast surface charges on these constant potential surfaces are those needed in (1.26).

Now consider the potential ϕ_{eq} due to all introduced contrast surface charge densities. This potential differs from the potential ϕ introduced in Section 1.4.1 but throughout the cross-section of each good conductor or relevant semiconductor, ϕ_{eq} assumes the same constant value as ϕ on its boundary. As the contrast charges reside in a homogeneous background medium, ϕ_{eq} satisfies Laplace's equation everywhere and can hence be expressed as:

$$\phi_{\text{eq}}(\mathbf{r}) = -\frac{1}{\epsilon_0} \int_{\Sigma c} \rho_{\text{eq}}(\mathbf{r}') G_0(\mathbf{r}|\mathbf{r}') dc(\mathbf{r}'). \quad (1.31)$$

The integration runs over all the boundaries c on which contrast charges were introduced. The Green's function G_0 satisfies

$$\nabla_t^2 G_0(\mathbf{r}|\mathbf{r}') + (k_0^2 - \beta^2) G_0(\mathbf{r}|\mathbf{r}') = \delta(\mathbf{r} - \mathbf{r}'), \quad (1.32)$$

with k_0 the wavenumber of the background medium. The term $-\beta^2 G_0(\mathbf{r}|\mathbf{r}')$ stands for the second order derivative with respect to z , and as long as the quasi-TM assumption holds, it is negligible with respect to each of the transverse second order derivatives in $\nabla_t^2 G_0(\mathbf{r}|\mathbf{r}')$. As k_0^2 has the same order of magnitude as β^2 , it is neglected as well and (1.32) reduces to

$$\nabla_t^2 G_0(\mathbf{r}|\mathbf{r}') = \delta(\mathbf{r} - \mathbf{r}'). \quad (1.33)$$

The quasi-static Green's function G_0 is equal to $(1/2\pi) \ln |\mathbf{r} - \mathbf{r}'|$ for free space. If we consider a half-plane on top of a PEC ground, an image source term $-\delta(\mathbf{r} - \mathbf{r}'')$ (with \mathbf{r}'' the mirror image of \mathbf{r}' with respect to the PEC ground) is added to the r.h.s. of (1.32) and (1.33), and G_0 becomes $(1/2\pi) \ln(|\mathbf{r} - \mathbf{r}'| / |\mathbf{r} - \mathbf{r}''|)$. For \mathbf{r} on c in (1.31) a surface integral equation for ρ_{eq} is obtained.

The relevant semiconductors can be subdivided into two groups, whether or not they are attached to a signal conductor. The potential of those that touch a signal conductor is equal to that of the signal conductor (i.e. zero for a semiconductor touching a PEC reference conductor). The total charge on each of the signal conductors and the total charge of the attached relevant semiconductors, is denoted as $(\mathbf{q} + \mathbf{q}_{sc,A})$. The charge and potential of the relevant semiconductors that stand free are written as

$\mathbf{q}_{sc,F}$, resp. $\mathbf{v}_{sc,F}$. With this notation, (1.26) can be transformed into

$$\mathbf{v}^T \cdot \tilde{\mathbf{C}} \cdot \mathbf{v} = \begin{bmatrix} \mathbf{v}^T & \mathbf{v}_{sc,F}^T \end{bmatrix} \cdot \begin{bmatrix} \mathbf{q} + \mathbf{q}_{sc,A} \\ \mathbf{q}_{sc,F} \end{bmatrix} \quad (1.34)$$

To obtain all the elements of the capacitance matrix, we one by one put $\phi_{eq} = 1$ on the boundary of a signal conductor and its touching constant surface potential semiconductors, as well as on the relevant semiconductors that are standing free, while keeping $\phi_{eq} = 0$ on all the other ones, each time solving (1.31). In this way the extended capacitance matrix $\tilde{\mathbf{C}}_{ext}$, defined as

$$\begin{bmatrix} \mathbf{q} + \mathbf{q}_{sc,A} \\ \mathbf{q}_{sc,F} \end{bmatrix} = \tilde{\mathbf{C}}_{ext} \cdot \begin{bmatrix} \mathbf{v} \\ \mathbf{v}_{sc,F} \end{bmatrix} \quad (1.35)$$

is obtained. Once $\tilde{\mathbf{C}}_{ext}$ is determined, the actual capacitance matrix $\tilde{\mathbf{C}}$ can be retrieved after some straightforward matrix manipulations by eliminating $\mathbf{v}_{sc,F}$ and $\mathbf{q}_{sc,F}$ from (1.35), based on the requirement that when a semiconductor stands free, its total charge remains zero, and thus $\mathbf{q}_{sc,F} = 0$. However, fixing the boundary potentials as explained above, does not suffice to solve (1.31). For this, additional relationships between the potentials and the charges on the remaining boundaries are needed, more specifically on the boundaries of the dielectrics and the semiconductors which behave as lossy dielectrics. We focus our attention to such a single homogeneous semiconductor with cross-section S_i and boundary c_i . In this case the original potential ϕ in S_i approximately satisfies $\nabla_t^2 \phi = j\omega\mu_0\sigma\phi$. The diffusion term is present if σ becomes significantly larger than $\omega\epsilon$, even when not yet high enough for ϕ to become constant on the boundary. In this case, as explained in section 1.4.1, the approximation $\mathbf{e}_t = -\nabla_t\phi$ (i.e., dropping the higher order contribution $-j\omega\mathbf{a}_t$ of the vector potential) is still valid, as is the case for dielectrics. Let us now expand ϕ in terms of the normalized Dirichlet eigenfunctions ξ_m of S_i which themselves satisfy

$$\nabla_t^2 \xi_m(\mathbf{r}) + k_m^2 \xi_m(\mathbf{r}) = 0, \quad \mathbf{r} \in S_i \quad (1.36)$$

with $\xi_m = 0$ on the boundary c_i of S_i and with k_m^2 the corresponding Dirichlet eigenvalues. It is easily derived that the normal derivative $\frac{\partial\phi}{\partial n}$ can be expressed as

$$\frac{\partial\phi(\mathbf{r})}{\partial n} = -\frac{\partial}{\partial n} \sum_{\forall m} \frac{\xi_m(\mathbf{r})}{k_m^2 + j\omega\mu_0\sigma} \oint_{c_i} \phi(\mathbf{r}') \frac{\partial\xi_m(\mathbf{r}')}{\partial n} d\mathbf{c}(\mathbf{r}') \quad (1.37)$$

with $\mathbf{r} \in c_i$. For lossless dielectrics the term $j\omega\mu_0\sigma$ is not present. Relationship (1.37) between $\frac{\partial\phi}{\partial n}$ and ϕ is a Dirichlet to Neumann boundary operator. Going back to (1.30) and approximating e_n by $-\frac{\partial\phi}{\partial n}$, (1.30) and (1.37) yield a relationship between

the contrast charge density and the potential on c_i . Discretization of this relationship³ and of (1.31) with the MoM yields the wanted charge distributions and the elements of $\tilde{\mathcal{C}}_{ext}$.

Note that the integral equation (1.31) combines the *equivalent* potential ϕ_{eq} with the contrast charge density. In the r.h.s. of (1.37), ϕ is therefore replaced by ϕ_{eq} . This is allowed on all boundaries with good conductors (with constant potential $\phi = \phi_{eq}$ on the outer boundary), and on all boundaries with dielectrics (where $\phi = \phi_{eq}$ as well). On internal boundaries between two adjacent semiconductors that both exhibit an important conductivity, ϕ is subject to diffusion, whereas ϕ_{eq} is not, and hence $\phi_{eq} \neq \phi$. However, if the potential is not yet constant on the outer boundary, the diffusion is still limited and the small difference between ϕ and ϕ_{eq} has very little influence on the solution to the integral equation.

At this point we will not discuss the numerical method in further detail. It suffices to mention that the relation between ρ_{eq} and ϕ_{eq} on the boundaries is discretized in an analogous way as the differential surface admittance operator \mathcal{Y} in [17], although here, piecewise linear basis functions were used to discretize both quantities, whereas [17] uses pulse functions.

1.5 The Inductance Problem

To solve the inductance problem, we will only need the longitudinal part of the contrast current, i.e. $j_{c,z} = (\sigma + j\omega(\epsilon - \epsilon_0)) e_z = (k_0^2 - k^2) e_z / j\omega\mu_0$ with e_z the as yet unknown longitudinal electric field and k the wavenumber of the considered material. First, we will restrict the reasoning to a particular mode m and afterwards extend the result to an arbitrary superposition of modes. To distinguish between the single mode problem and the general one, capital letters will be used for the modal problem. The scalar vector potential A_{zm} for the equivalent contrast current problem is

$$-j\omega A_{zm}(\mathbf{r}) = \iint_{\Sigma S_i} \left((k_0^2 - \beta_m^2) - (k^2 - \beta_m^2) \right) \cdot E_{zm}(\mathbf{r}') G_0(\mathbf{r}|\mathbf{r}') dS(\mathbf{r}'). \quad (1.38)$$

³This discretization is not as straightforward as could be expected from [17]. A direct use of (1.37) introduces important Gibbs phenomena over the total boundary c_i , on which the Dirichlet expansion does not converge since $\phi_{c_i} \neq 0$, whereas $\xi_{c_i} \equiv 0$. Instead of (1.37), a slightly different expansion is used in practice, not based directly on the Dirichlet eigenfunctions of S_i themselves, but on a well-chosen combination of parallel-plate waveguide modes. This restricts the numerical inaccuracies to the corner points, where they can be cancelled out by using a number of additional expansion functions. This is explained in more detail in Chapter 3 for a rectangular cross-section, and in Chapter 4 for triangles, with a direct extension to polygons in Appendix A.2.

The integration runs over all the cross-sections S_i of the different materials. The longitudinal electric field E_{zm} satisfies the wave equation

$$\nabla_t^2 E_{zm} + (k^2 - \beta_m^2) E_{zm} = 0 \quad (1.39)$$

and can be written in terms of the potentials, as

$$E_{zm}(\mathbf{r}) = j\beta_m \phi_{eq,m}(\mathbf{r}) - j\omega A_{zm}(\mathbf{r}), \quad (1.40)$$

where $\phi_{eq,m}$ is the equivalent scalar potential for mode m and with ϕ_{eq} the same equivalent potential as already introduced in Section 1.4.2. Judicious manipulations of (1.38) and (1.40), invoking (1.32) and (1.39) in conjunction with Green's theorem, lead to

$$j\beta_m \phi_{eq,m}(\mathbf{r}) = - \int_{\Sigma c_j} \left(\frac{\partial E_{zm}(\mathbf{r}')}{\partial n} G_0(\mathbf{r}|\mathbf{r}') - E_{zm}(\mathbf{r}') \frac{\partial G_0(\mathbf{r}|\mathbf{r}')}{\partial n} \right) dc(\mathbf{r}'). \quad (1.41)$$

Next, we introduce the fictitious field E_{z0m} within each subregion S_i , defined as a solution to the homogeneous wave equation (i.e. without the contrast current source-term) in the background medium, i.e.,

$$\nabla_t^2 E_{z0m} + (k_0^2 - \beta_m^2) E_{z0m} = 0 \quad (1.42)$$

and which takes the same value $E_{z0m} = E_{zm}$ on the boundary and only on the boundary c_i of S_i as the E_{zm} field we want to determine. This allows to write (1.41) for any observation point \mathbf{r} , again using (1.32), as

$$E_{z0m}(\mathbf{r}) = j\beta_m \phi_{eq,m}(\mathbf{r}) + \int_{\Sigma c_j} \left(\frac{\partial E_{zm}(\mathbf{r}')}{\partial n} - \frac{\partial E_{z0m}(\mathbf{r}')}{\partial n} \right) G_0(\mathbf{r}|\mathbf{r}') dc(\mathbf{r}'). \quad (1.43)$$

In the quasi-TM limit, the integration runs over all boundaries c_j of conductors and semiconductors. The dielectrics yield no contribution, because E_{zm} and E_{z0m} have the same boundary value and satisfy Laplace's equation, which amounts to neglecting the dielectric displacement currents in (1.38) as compared to the conductors' currents. Physically, as introduced in [17], (1.43) means that the inductance problem can be described in terms of equivalent so-called differential surface currents on each boundary c_j , given by

$$J_{sm,j}(\mathbf{r}') = \frac{1}{j\omega\mu_0} \left(\frac{\partial E_{zm}(\mathbf{r}')}{\partial n'} - \frac{\partial E_{z0m}(\mathbf{r}')}{\partial n'} \right), \quad (1.44)$$

with $\mathbf{r}' \in c_j$. It has also been shown in [17] that the following differential surface admittance operator $\mathcal{Y}(\mathbf{r}', \mathbf{r}'')$ can be introduced

$$J_{sm,j}(\mathbf{r}') = \oint_{c_j} \mathcal{Y}_j(\mathbf{r}', \mathbf{r}'') E_{zm,j}(\mathbf{r}'') d\mathbf{c}(\mathbf{r}''), \quad \mathbf{r}' \in c_j, \quad (1.45)$$

expressing a relationship between the differential surface current on boundary c_j and the longitudinal electric field on that same boundary. Note that in the quasi-TM limit the operator \mathcal{Y} does *not* depend on β_m as in this limit we approximate $(k^2 - \beta_m^2)$ in (1.39) by $-j\omega\mu_0\sigma$ and neglect the term $(k_0^2 - \beta_m^2) E_{z0m}$ in (1.42) with respect to both terms in $\nabla_t^2 E_{z0m}$. Integrating $J_{sm,j}$ over c_j leads to an expression for the longitudinal current I_j through the cross-section S_j

$$I_{jm} = \oint_{c_j} J_{sm,j}(\mathbf{r}') d\mathbf{c}(\mathbf{r}'). \quad (1.46)$$

Until now the reasoning was restricted to a particular mode, meaning that the signal conductor potentials ϕ_{eq} take their respective modal values on each of the signal conductors. To extend (1.43) to a general superposition of modes, we start from (1.13) and consider an arbitrary superposition of modes corresponding to a set of voltages \mathbf{v} used to excite the signal conductors, to arrive at

$$\tilde{\mathbf{L}}^{-1} \sum_m \alpha_m \mathbf{v}_m = \tilde{\mathbf{L}}^{-1} \mathbf{v} = j\omega \sum_m \alpha_m \frac{\mathbf{i}_m}{j\beta_m}. \quad (1.47)$$

The α_m are modal amplitudes. If we now define the following quantities:

$$\hat{e}_{z0} = \sum_m \alpha_m \frac{E_{z0m}}{j\beta_m} \quad (1.48)$$

$$\phi_{eq} = \sum_m \alpha_m \phi_{eq,m} \quad (1.49)$$

$$\hat{i}_p = \sum_m \alpha_m \frac{i_{m,p}}{j\beta_m} \quad (1.50)$$

(1.45), (1.43) and (1.46) can be rewritten as

$$\hat{j}_{s,j}(\mathbf{r}') = \oint_{c_j} \mathcal{Y}_j(\mathbf{r}', \mathbf{r}'') \hat{e}_{z0}(\mathbf{r}'') d\mathbf{c}(\mathbf{r}'') \quad (1.51)$$

$$\hat{e}_{z0}(\mathbf{r}) = \phi_{eq}(\mathbf{r}) + j\omega\mu_0 \oint_{\Sigma c_j} \hat{j}_{s,j}(\mathbf{r}') G_0(\mathbf{r}|\mathbf{r}') d\mathbf{c}(\mathbf{r}') \quad (1.52)$$

$$\hat{I}_j = \oint_{c_j} \hat{j}_{s,j} d\mathbf{c} \quad (1.53)$$

We now turn back to (1.47) and put signal conductor n on potential v_n with all other signal conductors on zero potential, leading to

$$[\tilde{\mathbf{L}}^{-1}]_{pn} = \frac{j\omega}{v_n} \hat{i}_p. \quad (1.54)$$

To obtain the wanted elements of the inverse of the inductance matrix, the knowledge of the weighted circuit currents \hat{i}_p suffices. In Section 1.4, these circuit currents (1.28) were found as a suitable combination of the currents I_n running through the signal conductors and those, $I_{sc,p}$, running through the semiconductors. From (1.51-1.53) the various currents can be determined by solving the integral equation which follows directly from (1.52) by putting the observation point \mathbf{r} on the boundary of one of the conductors or semiconductors (and on which $\hat{e}_{z0} = \hat{e}_z$). For a correct solution, it is important not only to take into account those semiconductors that behave as good conductors and whether or not contribute to the circuit currents, but also those for which σ is significant, even though ϕ_{eq} is not constant yet. The required value of ϕ_{eq} can be found as a side result from the solution of the capacitance problem. Integral equation (1.52) is of the same form as the one obtained in [17] and can be solved using the MoM, together with the MoM discretization of (1.51) and the explicit calculation of \mathcal{Y}_j again using the Dirichlet to Neumann operator. Knowledge of the β_m is not necessary. Note however that once the capacitance and inductance matrix have been determined, the β_m^2/ω^2 -values can be obtained as the eigenvalues of $\tilde{\mathbf{L}}\tilde{\mathbf{C}}$.

1.6 Numerical Results

To validate the proposed theoretical model for the semiconductors' behavior in interconnect structures, a number of single-conductor lines are investigated. A more complicated example for a multi-conductor line structure is given as well, modeling four coupled differential pair transmission lines in a realistic high-frequency chip technology.

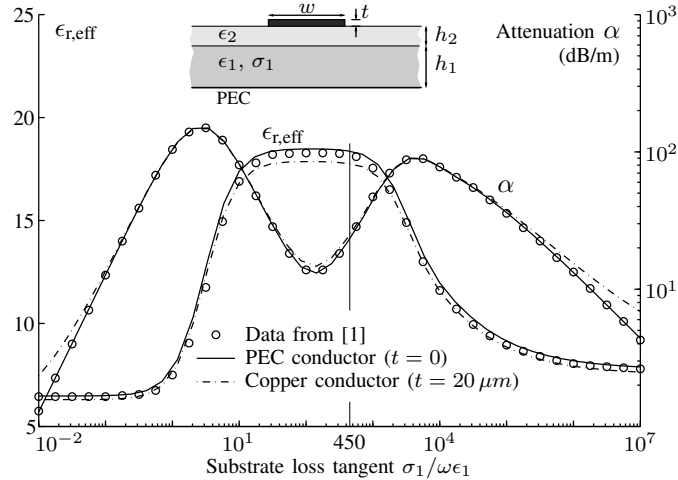


Figure 1.2: Effective relative permittivity $\epsilon_{r,\text{eff}}$ and attenuation factor (dB/m) for the fundamental mode of the shown MIS microstrip line at 1 GHz, as a function of the loss tangent $\sigma_1/\omega\epsilon_1$ of the lower substrate. $w = 600 \mu\text{m}$, $h_1 = 500 \mu\text{m}$, $h_2 = 135 \mu\text{m}$, and $\epsilon_1 = \epsilon_2 = 9.7 \epsilon_0$. The vertical line indicates where $\sigma_1 = 450 \omega\epsilon_1$.

1.6.1 MIS Microstrip Line

As a first example, consider the open MIS microstrip line, shown on the inset of Fig. 1.2. The line consists of a $h_1 = 500 \mu\text{m}$ thick lossy substrate with conductivity σ_1 , separated from a thin signal conductor by a lossless dielectric layer with thickness $h_2 = 135 \mu\text{m}$. All materials are non-magnetic (as will be the case in all the examples). Simulations were performed at 1 GHz, for increasing values of σ_1 , such that the fundamental mode evolves from a dielectric mode, over the slow-wave range, to a skin effect mode. In [1], an infinitely thin and perfect electric conducting (PEC) signal line was used. Our simulation of the PEC line (full line in Fig. 1.2) yields identical results for the attenuation factor⁴ α . Yet, a small difference in the

⁴ For completeness, a number of basic definitions are given here, that are not always explicitly written in the text itself. In the case of a single line along the z -axis, the fields behave as $e^{-j\beta z+j\omega t}$, or, for a multiconductor structure, each fundamental mode with mode number β_m behaves according to

$$e^{-j\beta_m z+j\omega t} = (e^{\beta_m^I z}) e^{-j\beta_m^R (z - \frac{\omega}{\beta_m^R} t)},$$

with $\beta_m = \beta_m^R + j\beta_m^I$. In this expression, we can identify the modal speed or phase velocity, given by $v_m = \omega/\beta_m^R$, and the attenuation factor ($e^{\beta_m^I z}$), in which $\beta_m^I \leq 0$ if $\beta_m^R > 0$, for a wave travelling along $+z$. In this thesis, the attenuation factor is mostly shown in decibels per unit of length (dB/m), written as

$$\alpha = (20/z) (-\log_{10} e^{\beta_m^I z}) = -20 \beta_m^I \log_{10} e$$

or multiplied with a factor 0.001 when the scale is (dB/mm). The modal slow wave factor (SWF) and effective relative permittivity $\epsilon_{r,\text{eff},m}$ are defined in relation to the modal phase velocity (with $c = 299\,792\,458 \text{ m/s}$ the speed of light in vacuum) as $v_m = c/\text{SWF} = c/\sqrt{\epsilon_{r,\text{eff},m}}$ such that the

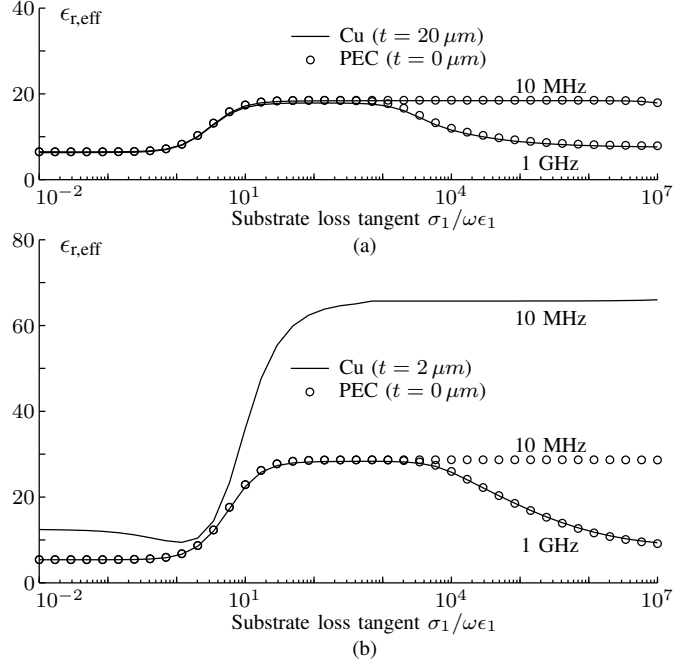


Figure 1.3: $\epsilon_{r,\text{eff}}$ at 10 MHz and 1 GHz for (a) the configuration as in Fig. 1.2 ($h_1 = 500 \mu\text{m}$, $h_2 = 135 \mu\text{m}$, $w = 600 \mu\text{m}$), and (b) a modified configuration with smaller conductor ($h_1 = 500 \mu\text{m}$, $h_2 = 13.5 \mu\text{m}$, $w = 60 \mu\text{m}$)

effective relative permittivity $\epsilon_{r,\text{eff}}$ is noticeable because the results shown here were obtained by leaving away the top side of the box surrounding the structure in [1], resulting in a small shift of the inductance and hence the observed difference in $\epsilon_{r,\text{eff}}$. The difference is very small though, and the large box described in [1] allows a good approximation of the open line structure. Simulating the signal line as a copper conductor ($\sigma_{\text{Cu}} = 58 \text{ MS/m}$) of the same width and with finite thickness ($w = 600 \mu\text{m}$, $t = 20 \mu\text{m}$) only slightly affects the results, as shown in Fig. 1.2 (dash-dot lines).

The transition between the regions in which a different semiconductor model is applied, is for all examples chosen to be $\sigma_1 = 450 \omega\epsilon_1$. For lower values of σ_1 , the substrate is treated as a lossy dielectric, and for higher σ_1 as a conductor with constant surface potential. As can be seen from Fig. 1.2, our approach leads to correct and continuous results, as predicted by our theory.

SWF is actually an effective refraction index (because only non-magnetic materials are considered). We finally find, with k_0 the propagation constant of free space given by $k_0 = \omega\sqrt{\epsilon_0\mu_0} = \omega/c$, that

$$\text{SWF} = \frac{\beta_m^R}{k_0} \quad \text{and} \quad \epsilon_{r,\text{eff},m} = \left(\frac{\beta_m^R}{k_0} \right)^2.$$

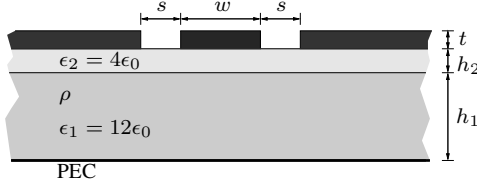


Figure 1.4: MIS Coplanar Waveguide structure (Example 1.6.2)

As an illustration of the frequency-dependency, the same configuration was simulated both for the PEC and the copper signal line, at the frequencies 10 MHz and 1 GHz. Fig. 1.3 (a) shows that the resulting $\epsilon_{r,\text{eff}}$ -values are very similar, be it that at 10 MHz the skin effect mode is never reached (current crowding would only occur for a loss tangent, higher than 10^7). In both cases, there is virtually no difference in $\epsilon_{r,\text{eff}}$ between the copper and the PEC conductor. However, now consider an analogous configuration, but with a smaller conductor, closer to the substrate ($h_2 = 13.5 \mu\text{m}$, $w = 60 \mu\text{m}$, and $t = 2 \mu\text{m}$ for the copper strip). The thickness of the lower substrate and the material parameters remain unchanged. Fig. 1.3 (b) shows that at 1 GHz, the finite conductivity of the line still has no influence on the propagation constant. The main difference between both configurations at 1 GHz, is the different value of $\epsilon_{r,\text{eff}}$ in the slow-wave range of the fundamental mode. In Fig. 1.3 (b), $\epsilon_{r,\text{eff}}$ at 1 GHz is higher than in Fig. 1.3 (a), because the lower substrate has a higher internal inductance (as it was not scaled together with the line), whereas the capacitance remains unchanged as soon as $\sigma_1 > \omega\epsilon_1$. At 10 MHz, $\epsilon_{r,\text{eff}}$ is much larger in Fig. 1.3 (b) than in Fig. 1.3 (a), although only for the copper conductor. By decreasing the dimensions of the line, the resistance R increases with respect to the inductance L and the point where $R \approx \omega L$ shifts towards higher frequencies. At 10 MHz the line in Fig. 1.3 (b) operates in the so-called *RC-range*⁵, where $R > \omega L$.

1.6.2 MIS Coplanar Waveguide

Another single line structure, used to verify the validity of our method, is the MIS CPW presented in Fig. 1.4. This structure has previously been analyzed in [19] with the full-wave Method of Lines (MoL) technique and in [1] with a quasi-TM approach (MoM/MoL). The resulting slow-wave factor (SWF) and the attenuation, obtained

⁵One has to be careful not to draw any wrong conclusions from the presented results in the RC-range. In this frequency range, $\epsilon_{r,\text{eff}} \propto 1/\omega$, but this does not mean the line behaves dispersively. The reason for this is, that for these frequencies the line rather acts as a lumped RC circuit, or an attenuator, instead of as a transmission line. In the RC-range, the imaginary part β_I of the mode number β has the same order of magnitude as the real part β_R . A phase difference of, e.g., $\pi/2$ would imply a power attenuation with a factor $e^{-\pi} \approx -0.043$. In a more realistic situation, such a line with an acceptable loss would be much smaller than a quarter wavelength. Its phase delay would therefore be negligible in the RC-range (despite its strongly frequency-dependent effective permittivity).

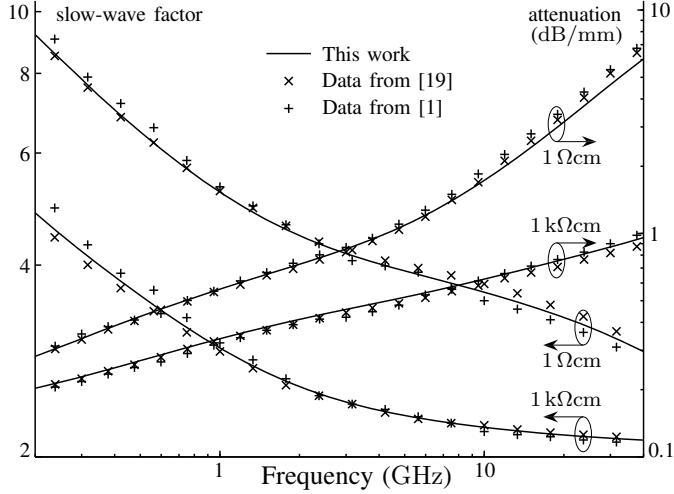


Figure 1.5: Slow-wave factor and attenuation for the fundamental mode in the MIS CPW of Fig. 1.4, with dimensions $h_1 = 480$, $h_2 = 1$, $t = 0.8$, $s = 5$, $w = 10$, all in micrometers. Top conductors: $\sigma = 27$ MS/m. Results are shown for a very weakly doped ($\rho = 1\text{ k}\Omega\text{cm}$) and a weakly doped ($\rho = 1\text{ }\Omega\text{cm}$) substrate.

for a very weakly and a weakly doped substrate ($\rho = 1\text{ k}\Omega\text{cm}$, resp. $\rho = 1\text{ }\Omega\text{cm}$), corresponding to a dielectric and a slow-wave fundamental mode, are presented in Fig. 1.5 together with the results from [19] and [1]. For the heavily doped case, the characteristic impedance is shown in Fig. 1.6 and compared with measured values from [10], with a satisfying match.

1.6.3 Multi-Conductor Line Structure

In the final example of Fig. 1.7, a transmission line system of 8 coupled lines is analyzed. The dimensions are based on a currently used semiconductor technology. Four identical pairs of conductors (c_1 to c_8) and a reference conductor (c_R), all with conductivity $\sigma_{\text{sig}} = 40$ MS/m, are embedded in a dielectric layer above a thick semiconducting substrate, on top of a PEC plane. The substrate conductivity $\sigma_{\text{sub}} = 2$ S/m, unless indicated differently (as for Fig. 1.9 and 1.10). Locally (underneath c_1 and c_2), the substrate has been heavily doped ($\sigma_{\text{dop}} = 0.03$ MS/m). Permittivities are $\epsilon_{\text{diel}} = 4\epsilon_0$ and $\epsilon_{\text{sub}} = 12\epsilon_0$. The dimensions, in micrometers, are indicated in the cross-section (not shown in proportion). The structure is enclosed between two PEC ‘mirror’ walls at the left and right side, in order to imitate a wide slab (as was done in [1] as well).

In Fig. 1.8, the modal voltages on each signal conductor are presented for the 8 fundamental modes, at a frequency of 10 GHz and for a substrate conductivity

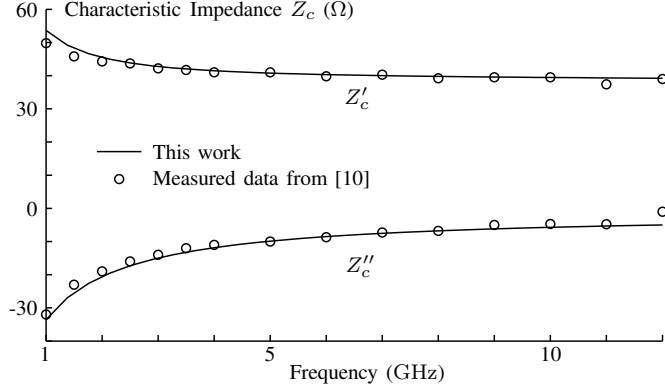


Figure 1.6: Real part Z'_c and imaginary part Z''_c of the characteristic impedance for the fundamental mode in the MIS CPW from Fig. 1.4, with heavily doped substrate ($\rho = 0.0125 \Omega\text{cm}$). Dimensions are $h_1 = 530$, $h_2 = 0.53$, $t = 1$, $s = 6$, $w = 4.2$ (all in micrometers). Top conductors: $\sigma = 33.3 \text{ MS/m}$.

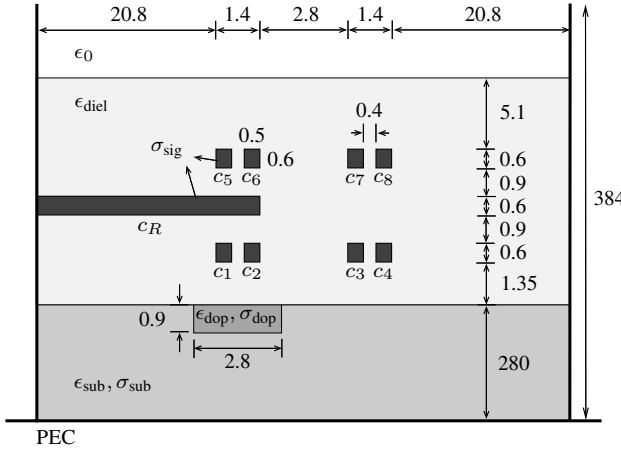


Figure 1.7: Cross-section of the multi-conductor line structure of Example 1.6.3. All indicated dimensions are in micrometers.

$\sigma_{\text{sub}} = 2 \text{ S/m}$. For a clear graphical presentation of the modes, each normalized modal voltage V is presented with a modified amplitude $V_0 = |V| \cdot \text{sign}(\text{Re}(V))$ and a phase ϕ , such that $V = V_0 e^{-j\phi}$. The modes fall apart into two groups: the modes (m_1-m_4), in which both conductors of each pair have more or less the same excitation, and those (m_5-m_8), with an opposite excitation of both conductors of each pair. In the next paragraphs, they are resp. called the *even* and the *odd* modes.

The behavior of the SWF and attenuation as a function of the substrate loss factor $\sigma_{\text{sub}}/\omega\epsilon_{\text{sub}}$ is shown in Fig. 1.9. There is a large difference in the behavior of the

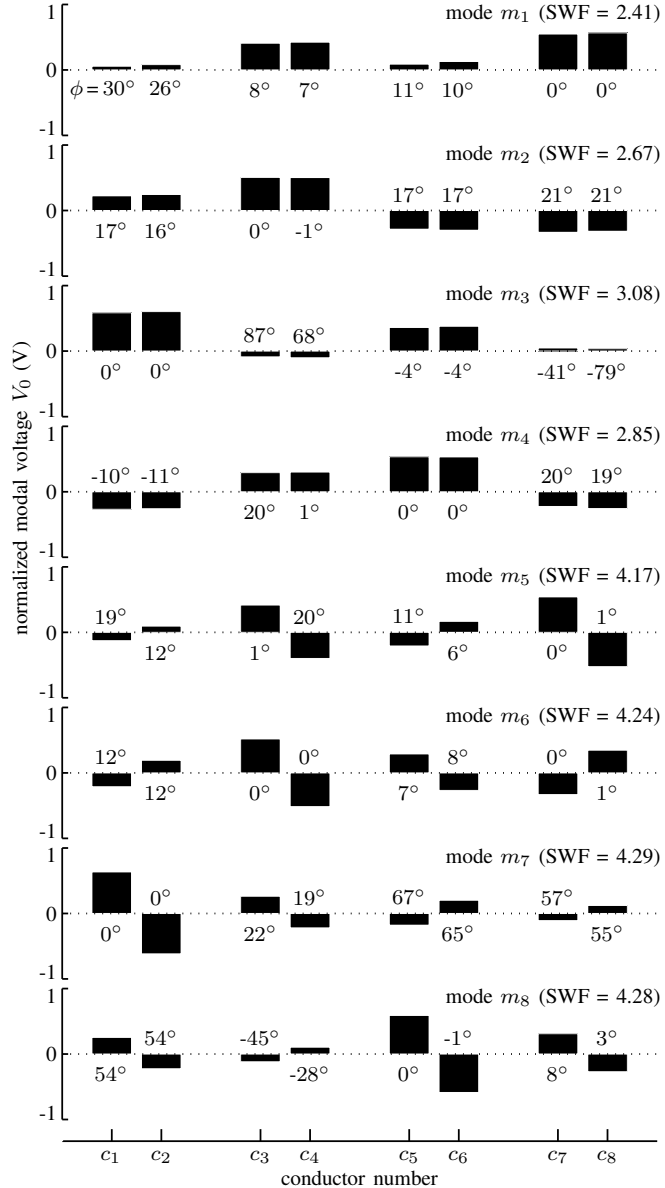


Figure 1.8: Modal voltages for the configuration of Fig. 1.7, at 10 GHz, and with $\sigma_{\text{sub}} = 2 \text{ S/m}$. The complex modal voltages V are found as $V = V_0 e^{-j\phi}$, with V_0 shown as bars and ϕ (expressed in degrees) at the corresponding bar. The modes can be split up into a quasi ‘even’ excitation of each of the conductor pairs (mode m_1 to m_4), and a quasi ‘odd’ excitation (mode m_5 to m_8). For each mode, the SWF is indicated as well.

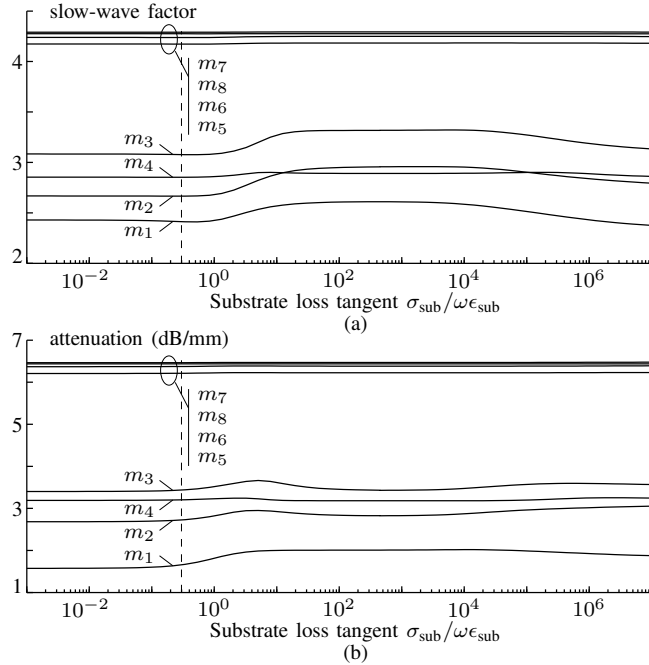


Figure 1.9: Slow-wave factor (a) and attenuation factor (b) for each of the fundamental modes of the multi-conductor structure of Fig. 1.7 at 10 GHz, as a function of the substrate loss tangent (ranging from 10^{-3} to 10^7). The vertical dashed lines indicate where $\sigma_{\text{sub}} = 2 \text{ S/m}$, i.e. for which the modal voltages are shown in Fig. 1.8.

even and the odd modes, which can be explained as follows. Each pair can roughly be approximated as a symmetric line pair in its own respect. For such a line, the two fundamental modes β_{even} and β_{odd} are found from

$$\begin{aligned} \beta_{\text{even}}^2 &= - (j\omega(C_s - |C_m|) + (G_s + G_m)) \\ &\quad \cdot (j\omega(L_s + L_m) + (R_s + R_m)) \\ \beta_{\text{odd}}^2 &= - (j\omega(C_s + |C_m|) + (G_s - G_m)) \\ &\quad \cdot (j\omega(L_s - L_m) + (R_s - R_m)) \end{aligned} \quad (1.55)$$

in which the indices s and m denote the diagonal, resp. the off-diagonal elements from the (2×2) circuit matrices associated with each line pair. As an illustration, Fig. 1.10 shows the relevant elements of the complex matrices \tilde{C} and \tilde{L} , associated with the conductor pair c_3-c_4 . The elements C_{33} and C_{44} correspond to C_s from (1.55) (the small difference between them due to the actual non-symmetry of the configuration), whereas C_{34} corresponds to C_m . From Fig. 1.10 (a), it becomes clear that the factor $(j\omega C_s + G_s)$ in (1.55) is dominated by the capacitance term and the numerical results

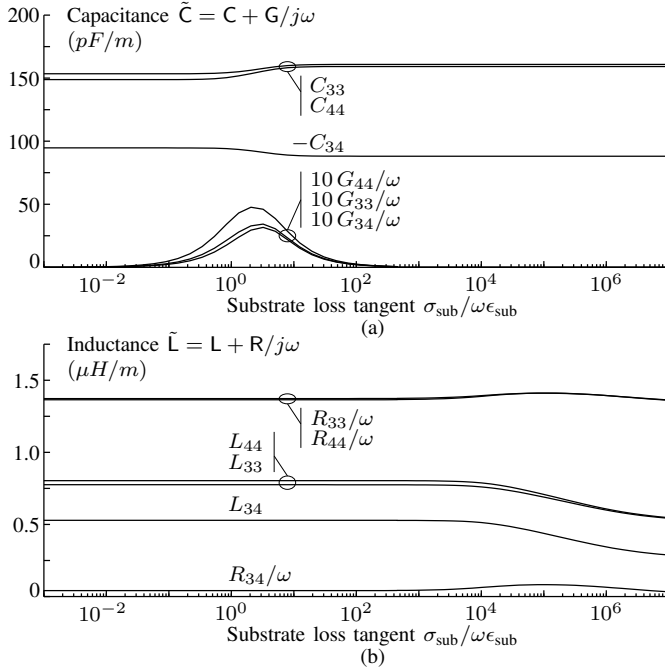


Figure 1.10: Elements of complex capacitance matrix $\tilde{\mathbf{C}}$ and inductance matrix $\tilde{\mathbf{L}}$ for the structure of Fig. 1.7 at 10 GHz, as a function of the substrate loss factor. (a) Entries of $\text{Re}(\tilde{\mathbf{C}}) = \mathbf{C}$, compared to $-\text{Im}(\tilde{\mathbf{C}}) = \mathbf{G}/\omega$ (scaled by a factor 10 for clearness), and (b) elements of $\text{Re}(\tilde{\mathbf{L}}) = \mathbf{L}$, compared to $-\text{Im}(\tilde{\mathbf{L}}) = \mathbf{R}/\omega$.

confirm this is also the case for the other line pairs. For all line pairs, both C_s (positive) and C_m (negative) are influenced in the same way by the charge on the substrate's surface. As soon as the loss tangent becomes larger than about 1, an increasing σ_{sub} leads to a higher C_s , whereas $|C_m|$ decreases. For the odd mode, depending on $C_s + |C_m|$, the influence of σ_{sub} is cancelled out, whereas it is reinforced for the even mode. This explains the flat behavior of the SWF in Fig. 1.9 (a) around $\sigma_{\text{sub}}/\omega\epsilon_{\text{sub}} \approx 1$ for the odd modes, and the increase for the even modes. This effect is not very pronounced for mode m_4 , although an 'even' mode. This is due to the reference conductor, shielding c_5 and c_6 from the substrate. The reason why m_3 has the highest and m_1 the lowest SWF from the even modes, is readily explained as well. The influence of the reference conductor and the doped part (σ_{dop}) in the substrate lead to higher capacitance elements associated with the conductors on the left (c_1, c_2, c_5 and c_6 , strongly excited in mode m_3) than for those on the right (excited in mode m_1). At higher values of σ_{sub} , when the magnetic field can no longer fully penetrate the substrate, an analogous argumentation based on the inductance and resistance coefficients, explains the different σ_{sub} -dependence of the odd and the even modes.

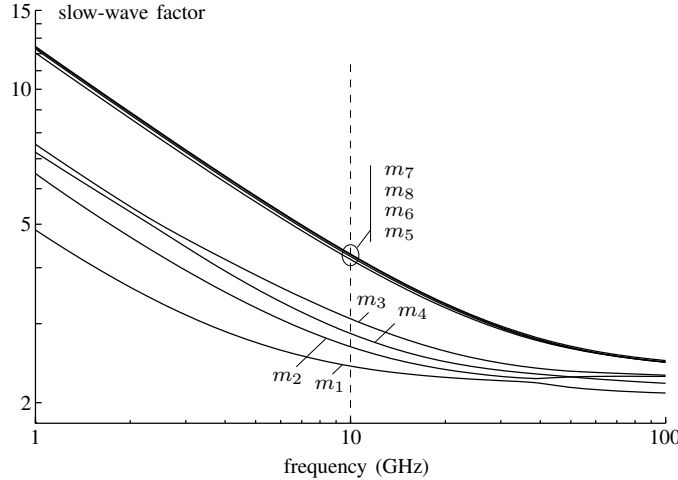


Figure 1.11: Slow-wave factor as a function of frequency for the fundamental modes m_1 to m_8 of Fig. 1.7 (with $\sigma_{\text{sub}} = 2 \text{ S/m}$). The dotted line denotes the frequency at which the modal voltages are shown in Fig. 1.3.

Fig. 1.9 also shows that the overall odd mode SWF is higher than for the even modes. As both conductors of each pair are close to one another, $|C_m|$ is of the same order of magnitude as C_s and $(C_s + |C_m|)$ is hence considerably larger than $(C_s - |C_m|)$. Furthermore, $|j\omega L_s + R_s|$ is considerably higher than $|j\omega L_m + R_m|$, due to the large line resistance R_m , see Fig. 1.10 (b). Going back to (1.55), the above considerations immediately lead to the observed difference in magnitude of the SWF of the even and odd modes.

Similar reasonings can be put forward to explain the attenuation factors. The main effect is here that the odd modal currents, opposite in both conductors of each pair, tend to repel each other, and hence flow through a smaller effective area of the conductors than the currents of the even modes, resulting in a higher attenuation.

The conductance coefficients G_{33} , G_{34} and G_{44} shown on Fig. 1.10 (a), clearly demonstrate the semiconductor's behavior. For a very low conductivity σ_{sub} , e_t must be taken into account but the transverse currents $\sigma_{\text{sub}} e_t$ are still negligible. When σ_{sub} increases, the transverse currents and the G -values also increase. However, as soon as the loss tangent becomes considerably higher than 1, charge relaxation reduces e_t . This effect outweighs the increase in σ_{sub} and hence the G -values decrease again and in the end become negligible as soon as the substrate's surface potential has become constant.

Finally, the frequency-dependency of the SWF is shown in Fig. 1.11, for a substrate conductivity $\sigma_{\text{sub}} = 2 \text{ S/m}$. The transition from the RC- to the LC-range takes place around 20 GHz. This frequency is quite high because the conductors' cross-

sections are small, resulting in large R -values.

1.7 Conclusions

A new multiconductor transmission line model has been developed, valid for general 2-D lossy line configurations within the quasi-TM frequency range.

A careful theoretical analysis proves that, within the quasi-TM limit, semiconductors can be accurately modeled by only considering two different regimes as a function of their loss factor. For highly doped semiconductors the boundary potential becomes constant, and their longitudinal current is taken into account. Lowly doped semiconductors can be treated as lossy dielectrics. In the quasi-TM limit these two regimes suffice to obtain accurate and continuous results as a function of conductivity and frequency.

We have also shown how an existing quasi-TM model for a single line can be extended to coupled lines. For this a reciprocity based approach as compared to a power based one proved to be necessary, leading to a non-conventional definition of the circuit modal currents (as compared to classical quasi-TEM models in the sole presence of low loss dielectrics). To obtain the RLGC circuit matrices, solving two boundary integral equations (one for the complex capacitance problem and one for the complex inductance problem) combined with the Dirichlet to Neumann boundary operator for the different materials, turned out to be sufficient.

A number of single conductor lines were simulated, showing excellent agreement with results already available in literature and the possibilities of the method were further explored by considering an 8-line multiconductor example of an on-chip configuration.

Bibliography

- [1] G. Plaza, R. Marques, and F. Medina, “Quasi-TM MoL/MoM approach for computing the transmission-line parameters of lossy lines,” *IEEE Trans. Microw. Theory Tech.*, vol. 54, no. 1, pp. 198–209, Jan. 2006.
- [2] E. Groteluschen, L. S. Dutta, and S. Zaage, “Quasi-analytical analysis of the broadband properties of multiconductor transmission lines on semiconducting substrates,” *IEEE Trans. Compon., Packag., Manuf. Technol. B*, vol. 17, no. 3, pp. 376–382, Aug. 1994.
- [3] H. Ymeri, B. Nauwelaers, K. Maex, and D. De Roest, “Influence of a lossy silicon substrate on conductance and capacitance of coupled interconnects,” *Journal of Microwaves and Optoelectronics*, vol. 3, no. 3, pp. 49–53, Dec. 2003.
- [4] U. Arz, H. Grabinski, and D. F. Williams, “Influence of the substrate resistivity on the broadband propagation characteristics of silicon transmission lines,” in *ARFTG Conference Digest-Spring, 54th*, vol. 36, Dec. 1999, pp. 65–70.
- [5] G. Manetas, V. N. Kourkoulos, and A. C. Cangellaris, “Investigation on the frequency range of validity of electroquasistatic RC models for semiconductor substrate coupling modeling,” *IEEE Trans. Electromagn. Compat.*, vol. 49, no. 3, pp. 577–584, Aug. 2007.
- [6] F. Bertazzi, G. Ghione, and M. Goano, “Efficient quasi-tem frequency-dependent analysis of lossy multiconductor lines through a fast reduced-order fem model,” *IEEE Trans. Microw. Theory Tech.*, vol. 51, no. 9, pp. 2029–2035, Sep. 2003.
- [7] F. Bertazzi, F. Cappelluti, S. Guerrieri, F. Bonani, and G. Ghione, “Self-consistent coupled carrier transport full-wave em analysis of semiconductor traveling-wave devices,” *IEEE Trans. Microw. Theory Tech.*, vol. 54, no. 4, pp. 1611–1618, Jun. 2006.
- [8] J. Aguilera, R. Marques, and M. Horro, “Improved quasi-static spectral domain analysis of microstrip lines on high-conductivity insulator-semiconductor substrates,” *IEEE Microw. Guided Wave Lett.*, vol. 9, no. 2, pp. 57–59, Feb. 1999.
- [9] J. J. Kucera and R. J. Gutmann, “Effect of finite metallization and inhomogeneous dopings on slow-wave-mode propagation,” *IEEE Trans. Microw. Theory Tech.*, vol. 45, no. 10, pp. 1807–1810, Oct. 1997.

- [10] Y. R. Kwon, V. M. Hietala, and K. S. Champlin, “Quasi-TEM analysis of ‘slow-wave’ mode propagation on coplanar microstructure MIS transmission lines,” *IEEE Trans. Microw. Theory Tech.*, vol. 35, no. 6, pp. 545–551, Jun. 1987.
- [11] F. Olyslager and D. De Zutter, “Rigorous boundary integral equation solution for general isotropic and uniaxial anisotropic dielectric waveguides in multilayered media including losses, gain and leakage,” *IEEE Trans. Microw. Theory Tech.*, vol. 41, no. 8, pp. 1385–1392, Aug. 1993.
- [12] F. Olyslager, *Electromagnetic Waveguides and Transmission Lines*. Oxford, U.K.: Oxford University Press Inc., 1999.
- [13] F. Olyslager, D. de Zutter, and A. T. de Hoop, “New reciprocal circuit model for lossy waveguide structures based on the orthogonality of the eigenmodes,” *IEEE Trans. Microw. Theory Tech.*, vol. 42, no. 12, pp. 2261–2269, Dec. 1994.
- [14] L. Wiemer and R. H. Jansen, “Reciprocity related definition of strip characteristic impedance of multiconductor hybrid-mode transmission lines,” *Microwave Optical Tech. Lett.*, vol. 1, no. 1, pp. 22–25, Mar. 1988.
- [15] G. Cano, F. Medina, and M. Horno, “Efficient spectral domain analysis of generalized multistrip lines in stratified media including thin, anisotropic, and lossy substrates,” *IEEE Trans. Microw. Theory Tech.*, vol. 40, no. 2, pp. 217–227, Feb. 1992.
- [16] F. Mesa, G. Cano, F. Medina, R. Marques, and M. Horno, “On the quasi-tem and full-wave approaches applied to coplanar multistrip on lossy dielectric layered media,” *IEEE Trans. Microw. Theory Tech.*, vol. 40, no. 3, pp. 524–531, Mar. 1992.
- [17] D. De Zutter and L. Knockaert, “Skin effect modeling based on a differential surface admittance operator,” *IEEE Trans. Microw. Theory Tech.*, vol. 53, no. 8, pp. 2526–2538, Aug. 2005.
- [18] D. De Zutter, H. Rogier, L. Knockaert, and J. Sercu, “Surface current modelling of the skin effect for on-chip interconnections,” *IEEE Trans. Compon., Packag., Manuf. Technol. B*, vol. 30, no. 2, pp. 342–349, May 2007.
- [19] K. Wu and R. Vahldieck, “Hybrid-mode analysis of homogeneously and inhomogeneously doped low-loss slow-wave coplanar transmission lines,” *IEEE Trans. Microw. Theory Tech.*, vol. 39, no. 8, pp. 1348–1360, Aug. 1991.

CHAPTER 2

Composite Conductors

Thomas Demeester and Daniël De Zutter

2.1 : Published in the *IEEE Microwave and Wireless Components Letters*,
vol. 18, no. 4, Apr. 2008.

2.2 : Published in the *IEEE Transactions on Electromagnetic Compatibility*,
vol. 51, no. 1, Feb. 2009.



Accurately modeling interconnect structures is an important issue in high-frequency chip design. Conductors have a finite thickness and conductivity, and are often composed of different metals. In a first part of this chapter, it is shown that the Dirichlet to Neumann technique can be used to model the inductive and resistive behavior of such structures, up to high frequencies at which the skin effect is well-developed. It is furthermore demonstrated how the method can be used for the accurate and fast calculation of their longitudinal current distribution.

The second part of this chapter presents a new method to calculate the internal inductance and resistance per unit of length for the considered composite conductors, also based on the Dirichlet to Neumann operator. The method is formulated in such a way, that the physical meaning of the internal impedance is clarified, as obtained by disregarding the external magnetic field. A comparison is made with the definitions known in literature to determine the internal impedance. In a number of numerical examples, the differences between those definitions and ours are elucidated, and some physical properties of the internal impedance are investigated.

2.1 Modeling the Broadband Inductive and Resistive Behavior of Composite Conductors

2.1.1 Introduction

Due to the continually increasing clock rates, it becomes necessary to take into account the wave character of on-chip interconnect structures, as is already the case for high-frequency printed circuit board design. Predicting signal delay, attenuation, and dispersion on these interconnects demands the accurate determination of the circuit parameters, i.e. capacitance, inductance, conductance and resistance per unit length (p.u.l.). It is particularly important to take into account the finite thickness and conductivity of signal conductors over a broad frequency range, see e.g. [1,2]. Recent developments in chip technologies involve the use of composite conductors, composed of metals with a different conductivity [3]. In this paper, the resistance-inductance (RL) problem for such composite conductors is treated (Section 2.1.2). The approach adopted in [1] is extended for composite conductors, and leads to the derivation of an expression for the conductors' current distribution (Section 2.1.3). In Section 2.1.4, the method is illustrated with some examples of coated and layered conductors.

Commercial EM codes are not well suited to accurately model broadband skin effect in thick layered conductors. This is either due to the large number of discretisations needed in volume methods or to the non-exact boundary impedance conditions imposed at the conductors' surface.

2.1.2 Inductance and Resistance Model

Fig. 2.1 shows the 2-D cross-section of the considered configuration. It consists of a single non-magnetic composite conductor. The conductor's cross-section S (with boundary c) is composed of N conductors with cross-section S_i (with boundary c_i) and conductivity σ_i ($i = 1, \dots, N$). The fundamental mode propagating along the line has an $e^{-j\beta z+j\omega t}$ field dependence.

The considered frequency range is limited by the requirement that the relevant transverse diameter of the structure remains much smaller than the modal wavelength $2\pi/\text{Re}(\beta)$. This leads to a quasi-TM description (see e.g. [4]) of the problem and in that case the non-magnetic dielectric background in which the conductor is embedded does not influence the solution of the RL-problem. Semiconducting media are excluded as they require a much more complex analysis¹.

For conciseness, the theory below is restricted to the single line case. Following the analysis in [1], this theory can be readily extended to the multiple line case as illustrated by the differential line example in Section 2.1.4.

¹In order to include semiconductors, the theory as explained in Chapter 1 should be applied. The current paper however studies the properties of layered and coated conductors as opposed to homogeneous conductors, and hence the influence of the substrate is not immediately relevant here.

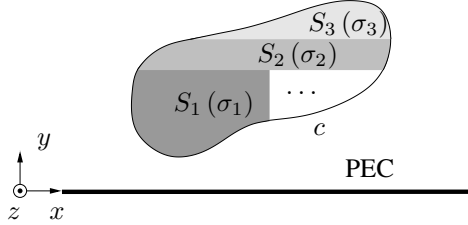


Figure 2.1: Composite conductor above a PEC ground plane.

The RL-behavior of the line can be described by the transmission line equation

$$j\beta v = (R + j\omega L)i, \quad (2.1)$$

in which the circuit voltage v is defined as the constant value of the electric potential ϕ on c and the circuit current i is the total longitudinal current flowing through the composite conductor. R and L are themselves frequency-dependent. In the absence of a PEC plane, at least two conductors must be present, one of which serves as the zero potential reference.

In the quasi-TM limit, the wave equation for E_z can be simplified to the diffusion equation inside and to Laplace's equation outside the conductor

$$\nabla_t^2 E_z(\mathbf{r}) = \begin{cases} j\omega\mu_0\sigma_i E_z(\mathbf{r}) & \mathbf{r} \in S_i \\ 0 & \mathbf{r} \notin S. \end{cases} \quad (2.2a)$$

$$(2.2b)$$

Each cross-section S_i of the conductor is now replaced by its corresponding contrast current $\sigma_i E_z$, neglecting dielectric displacement currents. The resulting configuration is that of a set of unknown currents $\sigma_i E_z$ residing in free space. The fields in this equivalent configuration remain unaffected, but the electric potential ϕ inside the conductor now satisfies Laplace's equation instead of the diffusion equation and assumes the constant value v throughout S . Decomposing E_z on S in terms of the electric scalar potential and the z -component of the magnetic vector potential yields, for $\mathbf{r} \in S$

$$E_z(\mathbf{r}) = j\beta v + j\omega\mu_0 \iint_{\Sigma S_i} G_0(\mathbf{r}|\mathbf{r}') \sigma_i E_z(\mathbf{r}') dS', \quad (2.3)$$

in which $G_0(\mathbf{r}|\mathbf{r}') = (1/2\pi) \ln(|\mathbf{r} - \mathbf{r}'|/|\mathbf{r} - \mathbf{r}''|)$ is the quasi-static half-space Green's function with $\mathbf{r}' = (x' \mathbf{u}_x + y' \mathbf{u}_y)$ and $\mathbf{r}'' = (x' \mathbf{u}_x - y' \mathbf{u}_y)$. G_0 satisfies

$$\nabla_t^2 G_0(\mathbf{r}|\mathbf{r}') = \delta(\mathbf{r} - \mathbf{r}') - \delta(\mathbf{r} - \mathbf{r}''). \quad (2.4)$$

For each S_i , we now introduce a fictitious field E_i which satisfies $\nabla_t^2 E_i = 0$ throughout S_i and is equal to E_z on the boundary c_i of S_i . Substituting E_z from (2.2a) into

(2.3), using (2.4) and Green's theorem, leads to

$$\frac{E_i(\mathbf{r})}{j\beta} = v + j\omega\mu_0 \oint_{\Sigma c_i} G_0(\mathbf{r}|\mathbf{r}') \left[\frac{J_s(\mathbf{r}')}{j\beta} \right] dc', \quad \mathbf{r} \in S_i \quad (2.5)$$

in which the equivalent surface current density J_s on each boundary c_i is defined by

$$J_s(\mathbf{r}') = \frac{1}{j\omega\mu_0} \left(\frac{\partial E_z(\mathbf{r}')}{\partial n'} - \frac{\partial E_i(\mathbf{r}')}{\partial n'} \right), \quad \mathbf{r}' \in c_i. \quad (2.6)$$

Moreover, integrating (2.6) over c_i easily leads to $i_i = \oint_{c_i} J_s dc$, i.e. the total surface current on c_i is identical to the bulk current flowing through S_i . Equation (2.5) is evaluated on all boundaries c_i , where $E_i = E_z$, and, together with (2.6), forms an integral equation that can be solved with the Method of Moments (MoM), leading for any voltage excitation v to the corresponding value of $[J_s/j\beta]$ on all boundaries c_i . The Dirichlet to Neumann technique as introduced in [1], is used to discretize (2.6). From (2.1) and the resulting $[J_s/j\beta]$, the resistance and inductance p.u.l. are determined by

$$(R + j\omega L)^{-1} = \frac{(i/j\beta)}{v} = \frac{1}{v} \oint_{\Sigma c_i} \left(\frac{J_s}{j\beta} \right) dc. \quad (2.7)$$

In order to determine $\beta = \sqrt{-j\omega C(j\omega L + R)}$, we still need the capacitance C . Its value can easily be determined by solving, e.g., again with the MoM, a classical potential problem $\nabla_t^2 \phi = 0$ everywhere, with the boundary c at the constant potential v . Of course, here the dielectric properties of the (layered) background medium must be taken into account.

2.1.3 Determination of the Current Density

To determine the complete current distribution inside the composite conductor we start from

$$\nabla_t^2 (E_z(\mathbf{r}) - E_i(\mathbf{r})) = j\omega\mu_0\sigma_i E_z(\mathbf{r}), \quad \mathbf{r} \in S_i. \quad (2.8)$$

As $(E_z - E_i)$ is zero on the complete boundary c_i of S_i , it is allowed to expand that quantity in the Dirichlet eigenfunctions $\xi_{m,i}$ of S_i , such that

$$E_z(\mathbf{r}) = E_i(\mathbf{r}) + \sum_{\forall m} c_{m,i} \xi_{m,i}(\mathbf{r}), \quad \mathbf{r} \in S_i, \quad (2.9)$$

with coefficients $c_{m,i}$ determined by

$$c_{m,i} = \frac{j\omega\mu_0\sigma_i}{k_{m,i}^2 (k_{m,i}^2 + j\omega\mu_0\sigma_i)} \oint_{c_i} E_i(\mathbf{r}') \frac{\partial \xi_{m,i}(\mathbf{r}')}{\partial n'} dc', \quad (2.10)$$

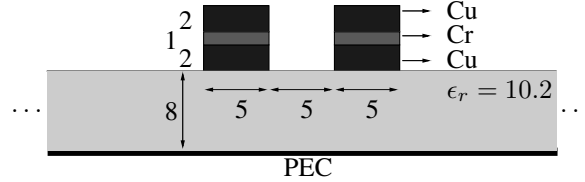


Figure 2.2: Symmetrical pair with layered conductors (copper/chromium/copper), with resistivities $\rho_{\text{Cu}} = 1.7 \mu\Omega\text{cm}$, and $\rho_{\text{Cr}} = 12.9 \mu\Omega\text{cm}$. All dimensions are in micrometers.

in which $k_{m,i}^2$ is the eigenvalue corresponding to the Dirichlet eigenfunction $\xi_{m,i}$, for which

$$\nabla_t^2 \xi_{m,i}(\mathbf{r}) + k_{m,i}^2 \xi_{m,i}(\mathbf{r}) = 0, \quad \mathbf{r} \in S_i. \quad (2.11)$$

The fictitious field E_i follows from (2.5), and combined with (2.9) and (2.10), the internal longitudinal electric field E_z and hence the current density can be calculated.

2.1.4 Numerical Results

Layered Conductors

Consider the differential microstrip pair from Fig. 2.2, in which the copper signal lines each have a horizontal chromium middle layer with a lower conductivity. In Fig. 2.3, the modal behavior of this configuration ('Cu - Cr - Cu') is compared with the case with homogeneous copper conductors ('homog. Cu'). The mode numbers β are found from the eigenvalues β^2 of $-j\omega\tilde{\mathbf{C}}(\mathbf{R} + j\omega\mathbf{L})$ (\mathbf{C} being the capacitance, \mathbf{R} the resistance, and \mathbf{L} the inductance matrix). The shown effective relative permittivity $\epsilon_{r,\text{eff}}$ and attenuation factor α are defined by $\beta = k_0\sqrt{\epsilon_{r,\text{eff}}} - j\alpha$, with k_0 the free space wave number.

For the lower frequencies (the so-called *RC-range*), $\epsilon_{r,\text{eff}}$ and α are slightly higher for the layered conductors, due to the higher DC-resistance. At skin-effect frequencies, $\epsilon_{r,\text{eff}}$ is independent of the chromium layer, and the same conclusion can be drawn for the inductance matrix. This is not surprising, as there is no more relevant internal inductance. The difference in attenuation between both configurations is smaller than in the RC-range. This is explained by the lower chromium/copper ratio of the currents flowing near the surface. The circuit parameters for this structure are presented in [5].

In Fig. 2.4, the E_z field for a frequency 100 GHz is shown on different depths at the right side of the left conductor (left conductor kept at zero potential, right conductor at 1V). The field decays exponentially toward the inside of the conductor, but penetrates deeper into the chromium layer than into the copper.

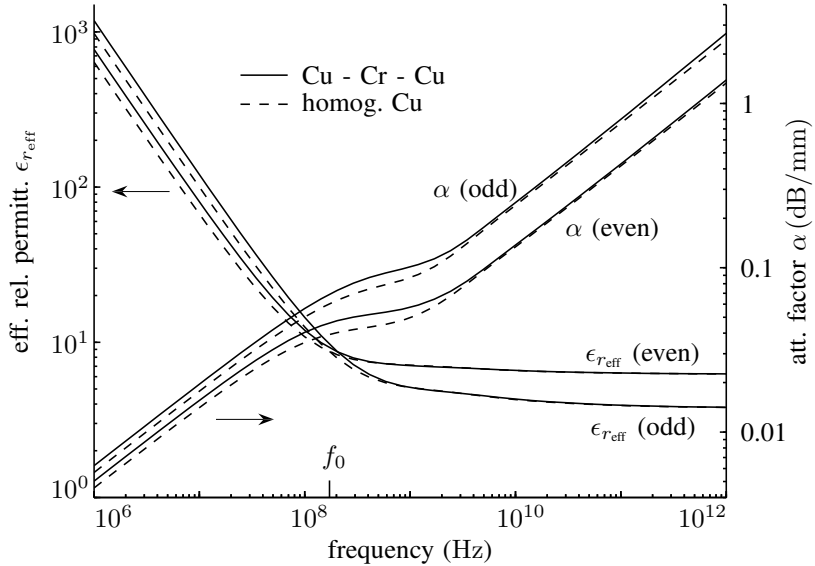


Figure 2.3: Effective relative permittivity $\epsilon_{r\text{eff}}$ and attenuation α (dB/mm) for the odd and even propagation mode of the configuration ('Cu - Cr - Cu') in Fig. 2.2, compared to the case with homogeneous copper conductors ('homog. Cu'). f_0 denotes the frequency at which the skindepth in copper equals the conductor thickness ($5 \mu\text{m}$).

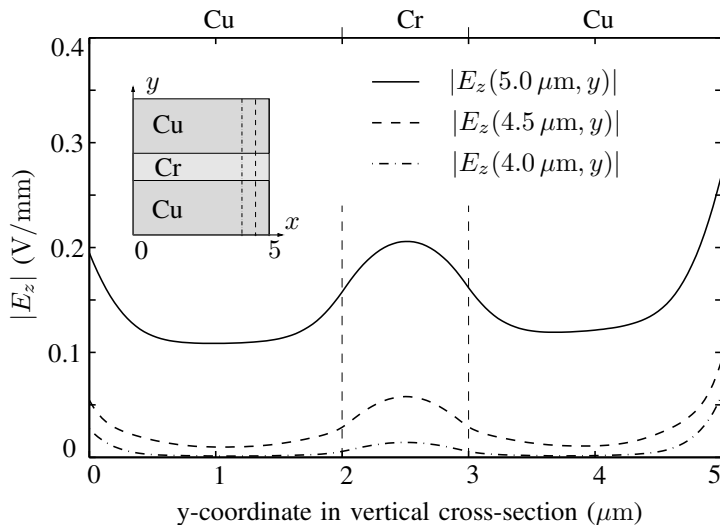


Figure 2.4: Electric field E_z at 100 GHz, along vertical lines at different depths on the right side of the left conductor from Fig. 2.2.

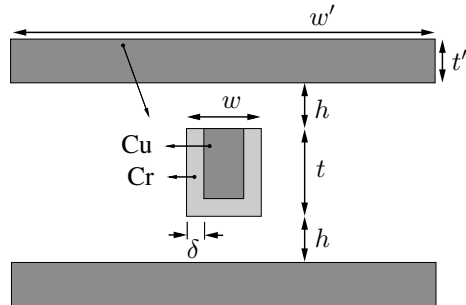


Figure 2.5: Transmission line system with two copper reference conductors and a coated signal conductor (inside: Cu with resistivity $\rho_{Cu} = 1.7 \mu\Omega\text{cm}$; coating: Cr with $\rho_{Cr} = 12.9 \mu\Omega\text{cm}$). The dimensions are: $w = 238$, $t = t' = 500$, $h = 450$, $w' = 3117$, $\delta = 10$, all in nanometers.

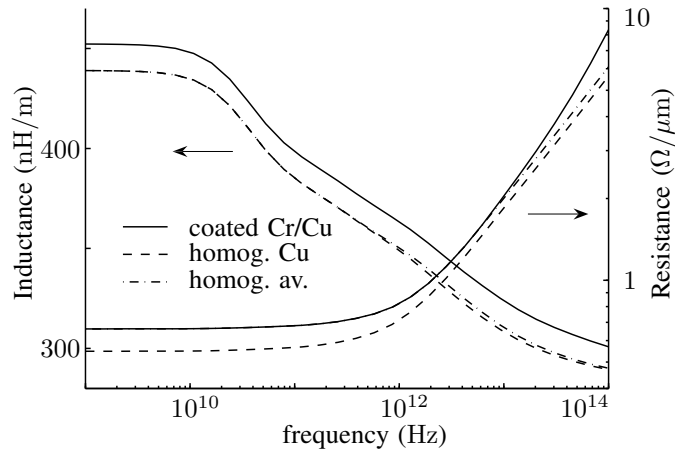


Figure 2.6: Resistance and Inductance p.u.l. for the configuration of Fig. 2.5.

Coated Conductor

As a second example, the coated conductor shown in Fig. 2.5 is modeled. The circuit inductance and resistance p.u.l. presented in Fig. 2.6 show that the RL-behavior of the coated conductor is quite different from that of a homogeneous copper conductor with the same dimensions. For skin-effect frequencies, the resistance increases more rapidly for the coated conductor, given that a gradually larger part of the current flows within the less conducting coating. A better approximation for the actual resistance is obtained by a homogeneous conductor with a resistivity $\rho_{av} = 2.06 \mu\Omega\text{cm}$, found as the weighted average of ρ_{Cu} and ρ_{Cr} such that the same DC-resistance as the coated conductor is obtained.

The configuration of Fig. 2.5 was taken from [6], in which a substitution of the

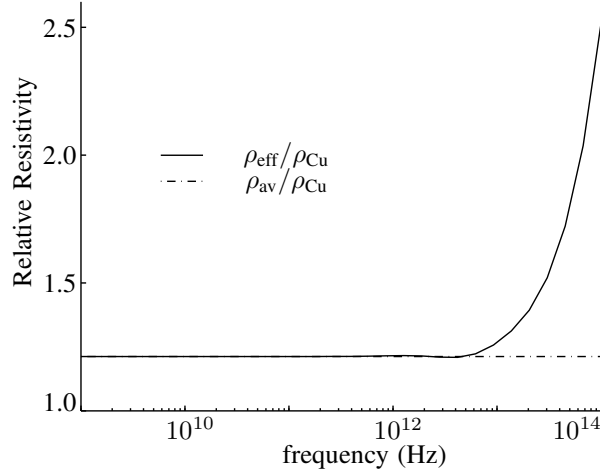


Figure 2.7: Relative resistivities $\rho_{\text{eff}}/\rho_{\text{Cu}}$ and $\rho_{\text{av}}/\rho_{\text{Cu}}$, producing the resistance, resp. only the DC-resistance of the coated conductor of Fig. 2.5.

composite conductor by a homogeneous conductor with an unknown *effective resistivity* ρ_{eff} is proposed. With the developed techniques it is now possible to actually calculate $\rho_{\text{eff}}(f)$. Fig. 2.7 shows this effective value as a function of frequency normalized on ρ_{Cu} . For low frequencies ρ_{eff} coincides with ρ_{av} as defined above. The difference between ρ_{eff} and ρ_{av} at higher frequencies clearly illustrates the effect of the coating. The DC-value ρ_{av} is a good approximation for $\rho_{\text{eff}}(f)$, up to the frequencies at which the skindepth $\sqrt{\rho_{\text{av}}/\pi\mu_0 f}$ becomes comparable with the coating thickness, which is far beyond the relevant frequencies in current chip technologies.

2.1.5 Conclusions

The Dirichlet to Neumann technique is perfectly suited for the description of the resistive and inductive behavior of multi-conductor transmission line systems with composite conductors. Additionally, the technique allows an elegant and accurate calculation of the current profile in the conductors, up to high frequencies.

2.2 Internal Impedance of Composite Conductors with Arbitrary Cross Section

2.2.1 Introduction

In the past, many different techniques were developed to predict the high-frequency behavior of conductors, both on printed circuit boards (PCB) and, more recently, within very-large-scale-integration (VLSI) circuits on chip. Due to the increase in operating frequencies, it is no longer possible to model interconnects on PCB's as lossless perfect electric conductors (PEC) only, or to neglect the on chip wave phenomena by only taking resistance and capacitance per unit of length (p.u.l.) into account. Consequently, an accurate description of the inductive and resistive behavior of interconnect conductors is needed. The p.u.l. *internal* impedance Z_{in} of a conductor is a widely used parameter for this purpose, see e.g. [7], or, for an overview of available literature, the introduction in [8]. Z_{in} describes the behavior of a conductor, disregarding the influence of the external magnetic field. Internal resistance and inductance can be calculated from the Joule losses, respectively, the magnetic energy density within the conductor. This can be done either by means of a volume discretization of the conductor as in [8], or, by using a surface discretization as used in [9] to calculate the circuit resistance and inductance.

Some aspects involving the difference between the real and the imaginary part of Z_{in} for rectangular conductors at skin-effect frequencies, and the influence on Z_{in} of the shape of the conductors and in particular its corners, remained a topic for discussion (see [8, 10, 11]), and will be further treated in the examples in this paper. More recently in [12], the Thévenin theorem applied to a small section Δz of a conductor extending along the z -direction allowed to derive an expression for the internal impedance by relating the voltage drop over this section to the longitudinal current through that section. An exact expression for Z_{in} in a rectangular conductor was derived, thus settling the discussion.

In Section 2.2.2, the internal impedance concept is extended to inhomogeneous conductors with arbitrary cross-sectional geometry. An expression for Z_{in} , valid in the quasi-transverse-magnetic (quasi-TM) frequency range, is derived directly from the surface admittance operator [1]. The result for the homogeneous rectangular conductor case is identical to the result from [12]. A comparison with the definition of Z_{in} from [8] is made, as it in fact appears to be different from the one used in [12]. It is also shown how the internal impedance as defined in [8] can be calculated from the boundary value of the longitudinal electric field, in conjunction with the Dirichlet to Neumann operator. Some numerical examples are given in Section 2.2.3, mainly focussing on the differences between several definitions of Z_{in} , and on the use of Z_{in} vs. a direct calculation of the circuit parameters. Finally, section 2.2.4 formulates some conclusions.

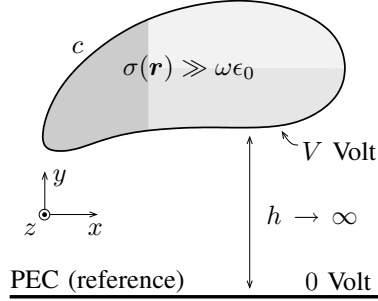


Figure 2.8: General conductor, for which the internal impedance is determined.

2.2.2 Internal Impedance of an Inhomogeneous Conductor

General Derivation

Fig. 2.8 shows the two-dimensional cross section of the nonmagnetic conductors for which the internal impedance will be determined. Within the conductor, it is assumed that $\sigma(\mathbf{r}) \gg \omega\epsilon_0$ (with $\mathbf{r} = x\mathbf{u}_x + y\mathbf{u}_y$), such that the electric potential ϕ is constant on the boundary c of the transverse conductor's cross section S . By definition, this constant value is taken to be the line voltage V in the equivalent transmission line model. The considered frequency validity range is restricted by the quasi-TM conditions. These quasi-TM conditions on the one hand imply that $|\mathbf{h}_t| \gg |\mathbf{h}_z|$ outside the conductors, such that $\mathbf{e}_t = -\nabla_t \phi$, using index t to denote the transverse (x, y) -plane. On the other hand, the relevant transverse dimensions are much smaller than the longitudinal wavelength, such that the second order z -derivative in the general wave equation can be neglected with respect to the transverse second order derivatives. Within the conductor, the field quantities therefore satisfy the diffusion equation, which for e_z becomes (with an $e^{j\omega t}$ time dependence of the fields)

$$\nabla_t^2 e_z(\mathbf{r}) = j\omega\mu_0\sigma(\mathbf{r}) e_z(\mathbf{r}), \quad \mathbf{r} \in S. \quad (2.12)$$

It is assumed that the conductivity $\sigma(\mathbf{r})$ is a piecewise continuous function of \mathbf{r} . The total longitudinal current I through S is written as

$$I = \iint_S \sigma(\mathbf{r}') e_z(\mathbf{r}') dS(\mathbf{r}') \quad (2.13)$$

$$= \oint_c \frac{1}{j\omega\mu_0} \frac{\partial e_z(\mathbf{r}')}{\partial n'} dc(\mathbf{r}') \quad (2.14)$$

$$= \oint_c \frac{1}{j\omega\mu_0} \left(\frac{\partial e_z(\mathbf{r}')}{\partial n'} - \frac{\partial e_{z0}(\mathbf{r}')}{\partial n'} \right) dc(\mathbf{r}'). \quad (2.15)$$

Splitting up (2.13) into integrations over the different areas S_i in which $\sigma(\mathbf{r})$ is continuous and invoking Gauss' law yields a sum of surface integrals along all boundaries c_i of S_i . On the internal boundaries $c_{i_{in}}$ of discontinuity in $\sigma(\mathbf{r})$, the quasi-TM tangential magnetic field can be simplified as

$$h_{tan} \approx \frac{1}{j\omega\mu_0} \left(\frac{\partial e_z}{\partial n} - \frac{1}{\sigma} \frac{\partial^2 h_z}{\partial z \partial \tan} \right) \approx \frac{1}{j\omega\mu_0} \frac{\partial e_z}{\partial n}, \quad (2.16)$$

because in the quasi-TM approximation $(1/\sigma) \partial^2 h_z / \partial z \partial \tan$ is negligible with respect to $\partial e_z / \partial n$ on $c_{i_{in}}$, or at least (if $\partial e_z / \partial n$ on $c_{i_{in}}$ itself is very small) with respect to $\partial e_z / \partial n$ on the outer boundary. Consequently, the continuity of h_{tan} allows for the continuity requirement of $\partial e_z / \partial n$ on these $c_{i_{in}}$. Hence, the contributions of the internal boundaries drop out, such that the integration (2.14) over the outer boundary c remains. The fictitious field quantity e_{z0} in (2.15) has the same value as e_z on the boundary c of S , but satisfies Laplace's equation $\nabla_t^2 e_{z0} = 0$ within S , such that its contribution to (2.15) is zero. With the introduction of e_{z0} , however, the integrand of (2.15) becomes the equivalent differential surface current density j_s , as introduced in [1]. The surface admittance operator \mathcal{Y} defined by

$$j_s(\mathbf{r}' \in c) = \frac{1}{j\omega\mu_0} \left(\frac{\partial e_z(\mathbf{r}')}{\partial n'} - \frac{\partial e_{z0}(\mathbf{r}')}{\partial n'} \right) \quad (2.17)$$

$$= \oint_c \mathcal{Y}(\mathbf{r}', \mathbf{r}'') e_z(\mathbf{r}'') d\mathbf{c}(\mathbf{r}'') \quad (2.18)$$

relates j_s to $e_z = e_{z0}$ on c . For the important case of completely homogeneous conductors, the surface admittance matrix \mathbf{Y} (i.e. the discretized form of \mathcal{Y}) can be found by expanding $(e_z - e_{z0})$ over S into the Dirichlet eigenfunctions of the cross section [1]. Only for simple geometries (rectangle, circle), the Dirichlet eigenfunctions can be written down analytically. In more general configurations, \mathbf{Y} can be obtained, for example, from integral methods as in [13]. Using (2.18), expression (2.15) for the current is rewritten as

$$I = \oint_c d\mathbf{c}(\mathbf{r}') \oint_c \mathcal{Y}(\mathbf{r}', \mathbf{r}'') e_z(\mathbf{r}'') d\mathbf{c}(\mathbf{r}''). \quad (2.19)$$

In (2.19), I is determined by \mathcal{Y} (which accounts for the geometry and material properties of the conductor) and by the boundary value of e_z ,

$$e_z(\mathbf{r}) = -\frac{\partial V}{\partial z} - j\omega a_z(\mathbf{r}), \quad \mathbf{r} \in c \quad (2.20)$$

with $V(z)$ the constant boundary value of the electric potential ϕ on c and a_z the longitudinal component of the magnetic vector potential. The total circuit impedance

is found as $Z = R + j\omega L = -(\partial V/\partial z)/I$. In order to define an internal impedance Z_{in} , the total current I is subdivided into two contributions I_{in} and $I - I_{\text{in}}$, such that Z_{in} becomes

$$Z_{\text{in}} = -(\partial V/\partial z)/I_{\text{in}}. \quad (2.21)$$

To determine I_{in} , the following reasoning can be adopted. The part of the current through S that is induced by any magnetic field due to external currents, should not be included in I_{in} . We therefore assume that there are no currents outside S (or rather that the PEC reference conductor is infinitely far away, see Fig. 1 for $h \rightarrow \infty$), such that the so-called *proximity* effect is not present and such that \mathbf{h}_t both inside and outside S completely follows from the current distribution over S . Further, we want to extract from I the part that is related to the external magnetic field, which is, in accordance with the quasi-TM approximations, found as

$$\mu_0 \mathbf{h}_t(\mathbf{r}) = -\mathbf{u}_z \times \nabla_t a_z(\mathbf{r}), \quad \mathbf{r} \in S, \quad (2.22)$$

with S the area outside the conductor, where a_z satisfies Laplace's equation. The external magnetic field would only vanish if a_z outside the conductor were constant or, hence, zero, because on the reference at infinity $a_z = 0$. The a_z -value on c would then be zero as well. Consequently, in order to determine I_{in} , a_z is set to zero in (2.20), such that the influence of the external magnetic field is omitted, and hence from (2.19)

$$I_{\text{in}} = -\frac{\partial V}{\partial z} \oint_c dc(\mathbf{r}') \oint_c \mathcal{Y}(\mathbf{r}', \mathbf{r}'') dc(\mathbf{r}''). \quad (2.23)$$

The constant boundary value $\partial V/\partial z$ was put in front of the integration. Hence, (2.21) and (2.23) lead to

$$Z_{\text{in}}^{-1} = \oint_c dc(\mathbf{r}') \oint_c \mathcal{Y}(\mathbf{r}', \mathbf{r}'') dc(\mathbf{r}'') \quad (2.24)$$

showing that \mathcal{Y} uniquely determines Z_{in} .

Homogeneous Conductors

For a homogeneous conductor, [1] shows how $(e_z - e_{z0})$ can be expanded into a series of the Dirichlet eigenfunctions ξ_ν of S , which leads to

$$j_s(\mathbf{r}) = \sigma \sum_\nu \frac{1}{k_\nu^2(j\omega\mu_0\sigma + k_\nu^2)} \frac{\partial \xi_\nu(\mathbf{r})}{\partial n} \oint_c e_z \frac{\partial \xi_\nu}{\partial n} dc, \quad \mathbf{r} \in c, \quad (2.25)$$

with k_ν^2 the eigenvalue corresponding to the Dirichlet eigenfunction ξ_ν . Combining (2.18), (2.24) and (2.25), yields

$$Z_{\text{in}}^{-1} = \sigma \sum_{\nu} \frac{\left(\oint_c \frac{\partial \xi_\nu}{\partial n} dc \right)^2}{k_\nu^2(j\omega\mu_0\sigma + k_\nu^2)}. \quad (2.26)$$

For the rectangular region $-a \leq x \leq a$ and $-b \leq y \leq b$, the Dirichlet eigenfunctions ξ_{mn} and the eigenvalues k_{mn}^2 satisfying $\nabla_t^2 \xi_{mn} + k_{mn}^2 \xi_{mn}^2 = 0$, are given by

$$\xi_{mn} = \frac{1}{\sqrt{ab}} \sin\left(\frac{m\pi(x-a)}{2a}\right) \sin\left(\frac{n\pi(y-b)}{2b}\right) \quad (2.27)$$

$$k_{mn}^2 = \left(\frac{m\pi}{2a}\right)^2 + \left(\frac{n\pi}{2b}\right)^2 \quad (2.28)$$

such that, after some manipulations, (2.26) becomes

$$Z_{\text{in}}^{-1} = \frac{16\sigma}{ab} \sum_{m=1}^{\infty} \sum_{n=1}^{\infty} \frac{\left(\frac{(m-1/2)\pi}{a}\right)^2 + \left(\frac{(n-1/2)\pi}{b}\right)^2}{\left(\frac{(m-1/2)\pi}{a}\right)^2 \left(\frac{(n-1/2)\pi}{b}\right)^2} \times \frac{1}{\left(\frac{(m-1/2)\pi}{a}\right)^2 + \left(\frac{(n-1/2)\pi}{b}\right)^2 + j\omega\mu_0\sigma}. \quad (2.29)$$

This result is identical to eqn. 10 of [12] and demonstrates the correctness of the presented method.

Further Discussion on the Meaning of Z_{in}

It is important to realize that, even though the boundary value on c of the contribution $j\omega a_z$ to e_z fully determines the magnetic field outside the conductor, the inside and the outside magnetic fields are inextricably linked, due to the connection between the $-\partial\phi/\partial z$ and $-j\omega a_z$ parts of the internal e_z field, as enforced by Ampère's law. Extracting Z_{in} (as defined in this paper) from the total impedance Z , is based on the solution of the diffusion equation inside the conductor, by eliminating the influence of the outside of the conductor by means of the nonphysical boundary condition $a_z = 0$.

The authors of [12] present two different ways to excite the conductor, (i.e. an *internal* and an *external* excitation) which both lead to exactly the same Z_{in} . In both cases they presume that on the outer boundary c of the conductor the e_z field equals the voltage drop per unit length $-\partial V/\partial z$, hence they also assume $a_z = 0$ on c . Calculating the current with the boundary condition $a_z = 0$ on c therefore yields I_{in} and hence the internal impedance given by (2.24), as confirmed by (2.29).

Another way to define Z_{in} is the method used in [8]. The conductor is placed in free space, so as to eliminate the proximity effect, and the current distribution is

determined with the help of the quasi-static free space Green's function. The correct (nonconstant) value of a_z on c and the corresponding current distribution over S are determined and then used to calculate Z_{in} . The longitudinal electric field e_z on c is not constant, but especially at the higher frequencies e_z gets stronger near the corners, due to the external magnetic field. The solution to the diffusion equation for the current density in the conductor is hence different from the one obtained for $a_z = 0$, except at DC or for an isolated circular conductor, where both solutions are identical.

We don't pretend to know whether the definition for Z_{in} used in [8] or the one proposed in [12] is the more correct or apt one. Both definitions eliminate the proximity effect. The former one seems more physically acceptable in the sense that it uses the current due to the total magnetic field to determine R_{in} , and only uses the internal magnetic field to determine L_{in} . The latter one is based on the elimination of the effect of the external magnetic field to calculate both R_{in} and L_{in} . It accounts for the influence of the surface voltage excitation only, sometimes referred to as the *impressed* electric field $E_0 = -\partial V/\partial z$, although this impressed field cannot be physically separated from the total electric field.

Both the internal electric and magnetic field in a realistic configuration are subject to the proximity effect, i.e. the presence of the nearby currents. None of the above definitions for Z_{in} can therefore be used to accurately take into account the finite conductivity of a conductor, by adding Z_{in} to the circuit impedance obtained for the perfect conductor case, see also [11] and the examples in Section 2.2.3.

Calculation of Z_{in} Based on Energy Considerations

In the numerical examples of Section 2.2.3, a comparison is made between the different methods to calculate the internal impedance. To obtain the numerical data, a boundary integral equation method is used [14], and consequently, the definition of the internal inductance according to [8],

$$|I|^2 L_{in} = \mu_0 \iint_S |\mathbf{h}_t|^2 dS \quad (2.30)$$

needs to be transformed into an integral over the boundary of the considered conductor. Using a power conservation argument, a suitable expression for Z_{in} (including both inductance and resistance) will be derived. It can be applied for a conductor in free space (and corresponds as such to the definition used in [8]), but can also be used for a signal conductor in a more realistic configuration, such as a microstrip. In Section 2.2.3, the difference between both situations will be used to visualize the proximity effect. The method described underneath leads to an expression for Z_{in} as a function of the boundary e_z field and its normal derivative. A similar result for the circuit inductance and resistance matrices was obtained in [9].

In order for the transmission line to transmit the same complex power as its circuit

equivalent (with current I and voltage V),

$$VI^* = \iint_{S_{\text{tot}}} (\mathbf{e}_t \times \mathbf{h}_t^*) \cdot \mathbf{u}_z dS \quad (2.31)$$

is invoked, with S_{tot} the total transverse cross section. The fundamental laws of Faraday and Ampère (assuming an $e^{-j\beta z}$ dependence)

$$\nabla_t e_z + j\beta \mathbf{e}_t = -j\omega \mu_0 \mathbf{u}_z \times \mathbf{h}_t, \quad (2.32)$$

$$\nabla_t \times \mathbf{h}_t = (\sigma + j\omega \epsilon) e_z \mathbf{u}_z \quad (2.33)$$

together with the telegrapher's equation $j\beta V = ZI$, are used to write (2.31) as

$$Z|I|^2 = \iint_{S_{\text{tot}}} (\sigma + j\omega \epsilon)^* |e_z|^2 dS + j\omega \iint_{S_{\text{tot}}} \mu_0 |\mathbf{h}_t|^2 dS. \quad (2.34)$$

The internal impedance of the signal conductor with area S is consequently defined (with $\sigma \gg \omega \epsilon_0$) as

$$Z_{\text{in}}|I|^2 \stackrel{\text{def}}{=} \iint_S \sigma |e_z|^2 dS + j\omega \iint_S \mu_0 |\mathbf{h}_t|^2 dS. \quad (2.35)$$

Invoking (2.32) and (2.12), (2.35) is rewritten, with $Z_{\text{in}} = R_{\text{in}} + j\omega L_{\text{in}}$, as

$$(R_{\text{in}} + j\omega L_{\text{in}})|I|^2 = \iint_S \left(\sigma |e_z|^2 - \frac{|\nabla_t e_z|^2}{j\omega \mu_0} \right) dS - p_{\text{rest}} \quad (2.36)$$

$$\approx -\frac{1}{j\omega \mu_0} \oint_c e_z \frac{\partial e_z^*}{\partial n} dc. \quad (2.37)$$

All contributions of the internal boundaries of discontinuity in $\sigma(r)$ are cancelled out because of the continuity of e_z and h_{\tan} . The remaining integral encompasses, again, only the outer boundary of the conductor. In order to obtain (2.37), the term p_{rest} was neglected, based on a number of quasi-TM approximations. p_{rest} is determined by

$$\begin{aligned} j\omega \mu_0 p_{\text{rest}} &= 2 \operatorname{Re} \left(\beta^2 \iint_S |e_z|^2 dS + j\beta \sum_i \oint_{c_i} e_n e_z^* dc \right) \\ &\quad + |\beta|^2 \iint_S |\mathbf{e}_t|^2 dS, \end{aligned} \quad (2.38)$$

in which the first term can be neglected w.r.t. the first term on the r.h.s. of (2.36), because $|\beta|^2 / \omega \mu_0 \ll \sigma$. Furthermore, because the fields vary much faster in the trans-

verse direction than along z , and because the longitudinal electric field e_z is much larger than the transverse field \mathbf{e}_t , $|\beta\mathbf{e}_t| \ll |\nabla_t e_z|$ within S . For the same reasons, $|\beta e_n|$ (with e_n the normal component of the electric field) on all boundaries c_i is much smaller than $|\partial e_z / \partial n|$ on the conductor's boundary c . The other terms on the r.h.s. of (2.38) can hence be neglected as well. The boundary value of e_z , for use in (2.37), is calculated as

$$e_z(\mathbf{r}) = j\beta V + j\omega\mu_0 \sum_i \oint_{c_i} G_0(\mathbf{r}|\mathbf{r}') j_s(\mathbf{r}') d\mathbf{c}', \quad \mathbf{r} \in c \quad (2.39)$$

in which $G_0(\mathbf{r}|\mathbf{r}')$ is the quasi-static free space Green's function and j_s is the equivalent differential surface current density on the boundaries of the subregions S_i (with continuous conductivity), following from the solution of the complex capacitance and inductance problem. If the electric and magnetic energy density are integrated over the cross section of a conductor in an inhomogeneous environment (e.g., above a semiconducting substrate, and in the vicinity of other conductors), (2.39) has to be modified. The reader is referred to [14] for further details. The value of $\partial e_z / \partial n$ along c , also required in (2.37), can be calculated with the help of the Dirichlet to Neumann operator, mapping the boundary value of e_z to its normal derivative.

2.2.3 Numerical Results

In a number of numerical examples, both presented methods to calculate the internal impedance, (2.24) and (2.37), will be compared. First, these expressions are applied to a homogeneous rectangular conductor, and the results are verified with data from [8] and [12]. As a next example, a composite conductor is considered. Next, the influence of rectangular corners on a conductor's internal resistance is investigated, so as to further clarify one of the subjects of discussion in [10] and [11]. In a final simulation, the difference between the *incremental* inductance, as proposed in [11], and the *internal* inductance is examined.

Throughout the next paragraphs, the lower index ' in ' denotes the internal impedance quantities, for example, Z_{in} , as opposed to the global circuit impedance Z . The lower index ' \mathcal{Y} ' as in $Z_{\text{in},\mathcal{Y}}$ indicates the use of (2.24) to calculate the internal impedance, i.e. by means of the surface admittance operator \mathcal{Y} of the conductor, based on the condition $e_z = \text{const}$ on c . The internal impedance calculated with (2.37), by integration of the internal magnetic and electric energy density, is denoted with the lower index ' \mathcal{E} '. $Z_{\text{in},\mathcal{E}}$ is calculated for the considered conductor in free space, omitting the proximity effect.

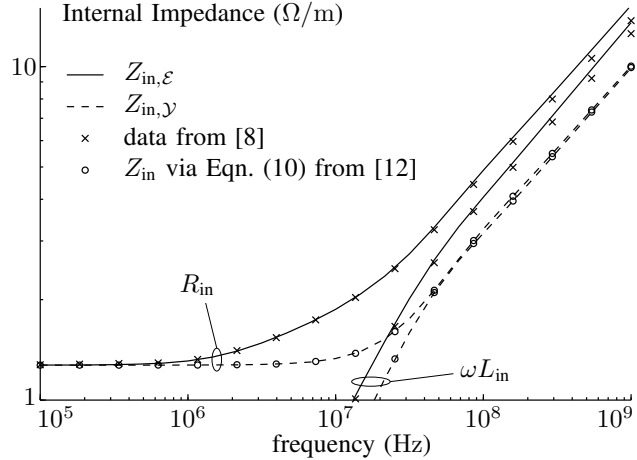


Figure 2.9: Internal impedance $Z_{in} = (R_{in} + j\omega L_{in})$ of a rectangular copper conductor (dimensions 15 mil \times 1.4 mil, conductivity $\sigma = 58$ MS/m). Different calculation methods: $Z_{in,\epsilon}$ via (2.37), and $Z_{in,y}$ via (2.24); verification using [8] and [12].

Internal Impedance of a Homogenous Rectangular Conductor

Consider an isolated rectangular copper conductor with dimensions 15 mil \times 1.4 mil (or $381 \mu m \times 35.56 \mu m$). Fig. 2.9 presents the real part (R_{in}) and imaginary part (ωL_{in}) of the internal impedance of the conductor.

The results obtained with (2.37), by integrating the energy density over the conductor's cross-section, are compared with data from [8]. The agreement is good, except for a small deviation at the highest frequencies. In [8], the conductor was discretized into 172×16 subrectangles, such that at 1 GHz the skin depth roughly equals one discretization interval. The discretization used in our simulation (225 intervals along the length and 21 along the width of the conductor) is only slightly finer, but the method is based on boundary quantities only (due to the surface admittance operator) and hence more apt to be used at skin effect frequencies. It was verified that reducing the number of discretization intervals by a factor of three (and along the length of the conductor even more), still produces very good results.

The internal impedance $Z_{in,y}$, calculated using the surface admittance matrix, produces identical results as Eqn. (10) from [12], as indicated by (2.29). The large difference between $Z_{in,y}$ and $Z_{in,\epsilon}$ is due to the non-constant component of e_z on the conductor's boundary, more in particular the increase around the corners, as will be further discussed in some of the following examples.

The difference in the behavior of $R_{in,\epsilon}$ and $R_{in,y}$ is very pronounced due to the shape of the conductor and is worth some comments. In $R_{in,y}$, only the skin effect plays a role (for a constant boundary value of e_z), and it becomes clearly visible when

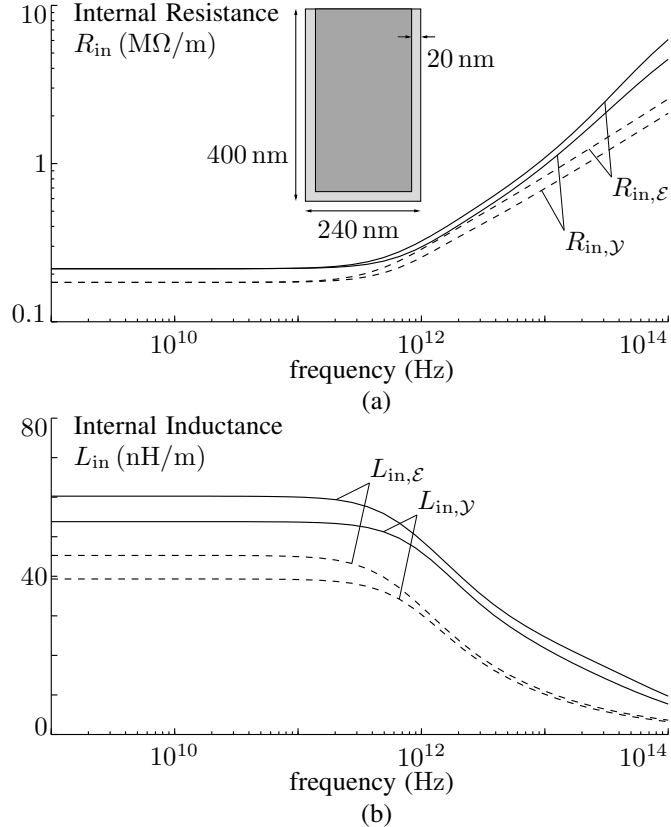


Figure 2.10: Full lines: (a) internal resistance and (b) internal inductance for the coated conductor shown in the inset of (a), with $\sigma_{bulk} = 58.8 \text{ MS/m}$, and $\sigma_{coating} = 7.7 \text{ MS/m}$. Dashed lines: analogously, but for $\sigma_{coating} = \sigma_{bulk} = 58.8 \text{ MS/m}$.

the smallest dimension of the block (1.4 mil) gets larger than about two skin depths (around 14 MHz). $R_{in,\varepsilon}$ additionally comprises the influence of the non-uniformity in the boundary value of e_z , which becomes important as soon as the largest dimension of the conductor (15 mil) becomes a few skin depths long, which happens at much lower frequencies.

Internal Impedance of a Composite Conductor

The conductor in the inset of Fig. 2.10 consists of copper ($\sigma = 58.8 \text{ MS/m}$), with a chromium coating ($\sigma = 7.7 \text{ MS/m}$) along three sides. Its internal resistance and inductance are shown, respectively, in Fig. 2.10 (a) and (b). The obtained R_{in} and L_{in} (full lines) are compared with those, calculated for a homogeneous copper conductor with the same area (dashed lines). At skin-effect frequencies, as long as the

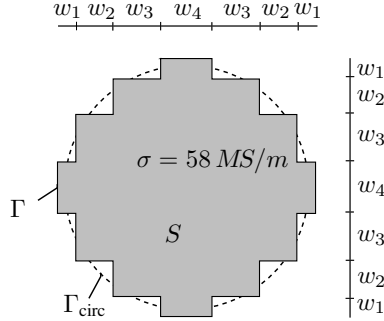


Figure 2.11: Copper conductor Γ , used to investigate the influence of corners. The total area S is $2500 \mu\text{m}^2$, and $w_1 = 4.64 \mu\text{m}$, $w_2 = 8.29 \mu\text{m}$, $w_3 = 10.94 \mu\text{m}$, $w_4 = 11.93 \mu\text{m}$.

current is not flowing entirely within the coating (which is the case up to approximately 10^{14} Hz), the resistance for the coated conductor increases faster than $\propto \sqrt{f}$, because a relatively larger part of the current goes through the less conducting coating. The inductances are also higher for the coated than for the homogeneous conductor, due to the difference in the current distribution. The differences between both ways to calculate Z_{in} can readily be explained as well. $R_{\text{in},\mathcal{E}} > R_{\text{in},\mathcal{Y}}$ at skin effect frequencies, because an increased e_z at the corners forces a larger part of the current through a smaller area, hence, resulting in a higher resistance. The contribution of the (nonconstant) boundary value of a_z for the calculation of $L_{\text{in},\mathcal{E}}$ leads to $L_{\text{in},\mathcal{E}} > L_{\text{in},\mathcal{Y}}$.

Contrary to what one might expect, the low-frequency limit of the internal inductance is not the same for both discussed methods. The contribution to Z_{in} that remains as $f \rightarrow 0$, is only its real part, the DC resistance $R_{\text{in,DC}}$, related to the total ‘impressed’ current, and therefore identical for both methods. The imaginary part $\omega L_{\text{in,DC}}$, however, is different in both methods. It is related to that part of the total current that is induced by (the change in time of) the magnetic field generated by the ‘impressed’ part of the current (and is therefore proportional to the frequency). That magnetic field is not uniform, both inside the conductor as along its boundary. Its exponential decrease inside the conductor causes current crowding at higher frequencies but is barely noticeable at low frequencies (as it is $\propto f$). This phenomenon is comprised in both $\omega L_{\text{in},\mathcal{Y}}$ and $\omega L_{\text{in},\mathcal{E}}$. The magnetic field’s (variable) boundary value, related to the outside magnetic field, causes the boundary variation of a_z and hence a second contribution to $\omega L_{\text{in},\mathcal{E}}$, not comprised in $\omega L_{\text{in},\mathcal{Y}}$. This explains the difference $L_{\text{in,DC},\mathcal{E}} > L_{\text{in,DC},\mathcal{Y}}$. The authors would like to stress that this difference is only due to the different definitions used in (2.24) and (2.37) for the *internal* inductance. For the *total* inductance, there is one unique value, independent of the way it is calculated.

Influence of Corners on the Internal Resistance

Consider the copper conductor Γ shown in Fig. 2.11. On the one hand, $R_{\text{in},\mathcal{E}}$ is calculated from (2.37). The result equals the circuit resistance of the isolated conductor Γ in free space (obtained by means of the techniques described in [15]), and hence corresponds to the definition of R_{in} as used in [8]. On the other hand, $R_{\text{in},\mathcal{Y}}$ is calculated from (2.24), in accordance to the definition of [12]. The total surface admittance matrix was determined by means of the Dirichlet to Neumann operator.

To investigate the influence of the corners on R_{in} , we will compare Γ to the circular conductor Γ_{circ} with the same area S , also shown in Fig. 2.11. For Γ_{circ} , both definitions yield the same R_{in} [7], i.e. $R_{\text{in},\mathcal{Y}} = R_{\text{in},\mathcal{E}} = R_{\text{in}}$.

Fig. 2.12 shows that all the low-frequency internal resistances equal the DC resistance of a copper conductor with cross-sectional area S . At skin-effect frequencies, $R_{\text{in},\mathcal{Y}}$ for Γ is lower than for the circular conductor Γ_{circ} because its perimeter L_a is longer than the circumference L_c of the circle. Fig. 2.12 shows how $R_{\text{in},\mathcal{Y}}$ approaches the high-frequency limit of, respectively, $1/(\sigma L_a \delta)$ for Γ and $1/(\sigma L_c \delta)$ for Γ_{circ} , with δ the skin depth. The convergence to this limit is a bit slower for Γ , because the corners disturb the local plane wave character of the internal field distribution. Calculating $R_{\text{in},\mathcal{E}}$ for Γ results in a *higher* value than for Γ_{circ} , even though its perimeter is longer and the skin-effect is already well-developed at the highest frequencies ($\delta \approx w_1/10$ at 20 GHz). Due to the increased e_z field associated with the important external magnetic field near the corners, a larger part of the current² flows in smaller areas near these corners, which explains why $R_{\text{in},\mathcal{E}}$ is significantly higher than $R_{\text{in},\mathcal{Y}}$.

Internal vs. Incremental Inductance

As a final example, the internal inductance of a single microstrip line (Fig. 2.13) is investigated. The dielectric layer between the signal line and the ground plane was chosen quite thin, such as to clearly demonstrate the effect of the magnetic field generated by the return currents. The caret symbol “^” denotes impedance quantities for the *total* microstrip configuration, as opposed to placing the conductor in free space. A number of different results for the internal inductance are presented in Fig. 2.14. $(\hat{L} - \hat{L}_{\text{PEC}})$ is the *incremental* inductance, defined by the total inductance of the microstrip configuration minus the inductance obtained for a perfectly electric conducting (PEC) line. $(L - L_{\text{PEC}})$ is the incremental inductance in case the conductor is standing on its own in free space. Further, $\hat{L}_{\text{in},\mathcal{E}}$ and $L_{\text{in},\mathcal{E}}$ denote the internal inductance obtained by integration of the magnetic energy density over the conductor’s cross section, respectively, for the microstrip line and for the isolated conductor case. Finally, $L_{\text{in},\mathcal{Y}}$ is the internal inductance, obtained for a constant surface value of e_z .

²A more precise analysis (see Chapter 5), shows that in the vicinity of the corners, there is not only an increase of the current density, but also a phase shift with respect to the ‘plane wave’-like behavior away from the corners, which leads to the increased line resistance.

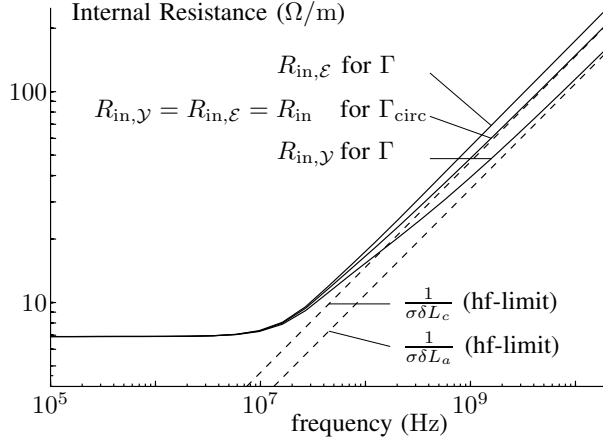


Figure 2.12: Internal resistance for conductor Γ (see Fig. 2.11) and the circular conductor Γ_{circ} with the same cross-sectional area S .

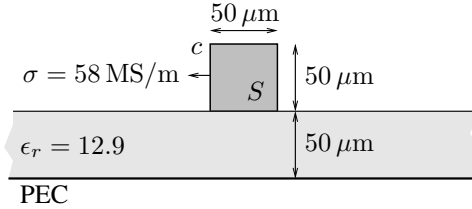


Figure 2.13: Single microstrip configuration.

For the lowest frequencies, the magnetic field fully penetrates the conductor and all inductance values in Fig. 2.14 are constant, whereas for skin effect frequencies they all decrease as $1/\sqrt{f}$. $L_{\text{in},y}$ is lower than the other internal inductances, because a part of the total magnetic flux inside the conductor is omitted. Firstly, the magnetic flux generated by external currents is left out. This flux is responsible for the proximity-effect, which is also the reason why $(\hat{L} - \hat{L}_{\text{PEC}}) > (L - L_{\text{PEC}})$ and $\hat{L}_{\text{in},\epsilon} > L_{\text{in},\epsilon}$. Secondly, $L_{\text{in},y}$ doesn't contain the internal flux generated by that part of the current that is related to the external magnetic field. It is also observed that $(\hat{L} - \hat{L}_{\text{PEC}}) > \hat{L}_{\text{in},\epsilon}$ and $(L - L_{\text{PEC}}) > L_{\text{in},\epsilon}$. This means that the magnetic energy p.u.l. *outside* the copper conductor, for a unit current flowing through the line, is higher than the total magnetic energy p.u.l. for the PEC conductor case. The difference in the external magnetic field is due to the difference between a uniform current density and a surface current distribution. Consequently, the determination of L_{in} by integration of the magnetic energy inside the conductor, leads to a result which deviates from the incremental inductance, especially at low frequencies.

The real and imaginary part of $Z_{\text{in},\epsilon}$ and $Z_{\text{in},y}$ up to very high frequencies are

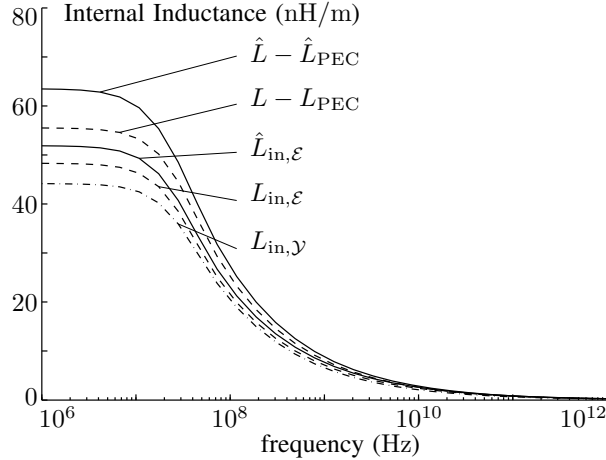


Figure 2.14: Incremental and internal inductance for the configuration of Fig. 2.13.

shown in Fig. 2.15. At skin-effect frequencies, $R_{in,E}$ remains slightly higher than $R_{in,Y}$, due to the increased electric field near the corners.

2.2.4 Conclusions

In this paper, the authors tried to clarify the meaning of a conductor's internal resistance and inductance p.u.l., by carefully formulating the proper definitions and elucidating some aspects that were leading to discussions in previous papers. The surface admittance boundary operator appears to be a useful tool to describe the conductor's behavior. In its integrated form, it directly leads to the inverse of the internal impedance (in accordance to one of the definitions used in literature). Yet neither of the presented techniques to calculate the internal impedance produces an accurate approximation of the incremental impedance, mainly due to the influence of the return current on internal current distributions in a realistic configuration. Furthermore, the numerical cost of a simulation with realistic conductors, even for more complicated composite conductors, is no longer much higher than for PEC conductors, e.g., when the effect of the conductor is represented by a fully equivalent differential surface current and its corresponding surface admittance operator. The authors therefore believe that the importance of internal impedance calculations will decline, in favour of simulations which directly take into account the correct finite conductivity of the conductors.

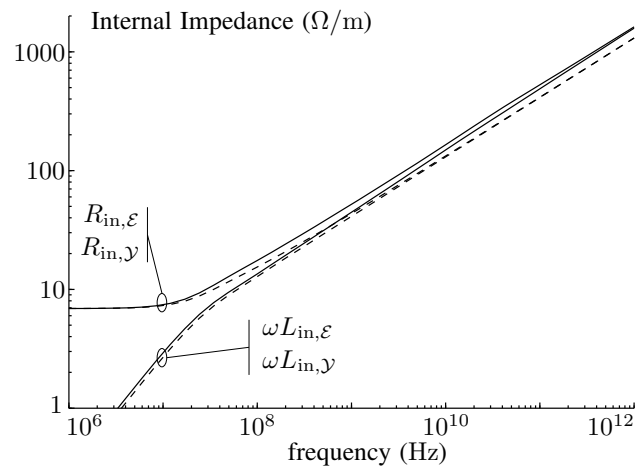


Figure 2.15: Internal impedance $Z_{\text{in}} = (R_{\text{in}} + j\omega L_{\text{in}})$ of the conductor in Fig. 2.13, calculated from the internal energy (subscript ϵ , solid lines), respectively, with constant e_z on the boundary (subscript γ , dashed lines).

Bibliography

- [1] D. De Zutter and L. Knockaert, “Skin effect modeling based on a differential surface admittance operator,” *IEEE Trans. Microw. Theory Tech.*, vol. 53, no. 8, pp. 2526–2538, Aug. 2005.
- [2] G. Plaza, R. Marques, and F. Medina, “Quasi-TM MoL/MoM approach for computing the transmission-line parameters of lossy lines,” *IEEE Trans. Microw. Theory Tech.*, vol. 54, no. 1, pp. 198–209, Jan. 2006.
- [3] Int. technol. roadmap for semiconductors. [Online]. Available: <http://public.itrs.net>
- [4] J. Aguilera, R. Marques, and M. Horro, “Improved quasi-static spectral domain analysis of microstrip lines on high-conductivity insulator-semiconductor substrates,” *IEEE Microw. Guided Wave Lett.*, vol. 9, no. 2, pp. 57–59, Feb. 1999.
- [5] T. Demeester and D. De Zutter, “Modeling of the resistive and inductive behaviour of layered and coated conductors,” in *IEEE 16th Conf. Elect. Performance Electron. Packag.*, Atlanta, USA, Oct. 2007.
- [6] (2008) Compact modeling of on-chip passive structures at high frequencies. IST World. IST-2001-34058. [Online]. Available: <http://www.magwel.com/codestar/codestar>
- [7] S. Ramo, J. R. Whinnery, and T. Van Duzer, *Fields and Waves in Communication Electronics*, 2nd ed. New York: Wiley, 1984.
- [8] G. Antonini, A. Orlandi, and C. Paul, “Internal impedance of conductors of rectangular cross section,” *IEEE Trans. Microw. Theory Tech.*, vol. 47, no. 7, pp. 979–985, Jul. 1999.
- [9] M. Tsuk and J. Kong, “A hybrid method for the calculation of the resistance and inductance of transmission lines with arbitrary cross sections,” *IEEE Trans. Microw. Theory Tech.*, vol. 39, no. 8, pp. 1338–1347, Aug. 1991.
- [10] W. Heinrich, “Comments on internal impedance of conductors of rectangular cross section,” *IEEE Trans. Microw. Theory Tech.*, vol. 49, no. 3, pp. 580–581, Mar. 2001.

- [11] F. Medina, R. Marques, G. Antonini, A. Orlandi, and C. Paul, “Comments on internal impedance of conductors of rectangular cross section [and author’s reply],” *IEEE Trans. Microw. Theory Tech.*, vol. 49, no. 8, pp. 1511–1513, Aug. 2001.
- [12] A. Rong and A. Cangellaris, “Note on the definition and calculation of the per-unit-length internal impedance of a uniform conducting wire,” *IEEE Trans. Electromagn. Compat.*, vol. 49, no. 3, pp. 677–681, Aug. 2007.
- [13] L. Knockaert, D. De Zutter, G. Lippens, and H. Rogier, “On the Schur complement form of the Dirichlet-to-Neumann operator,” *Wave Motion*, vol. 45, no. 3, pp. 309–324, Jan. 2008.
- [14] T. Demeester and D. De Zutter, “Quasi-TM transmission line parameters of coupled lossy lines based on the Dirichlet to Neumann boundary operator,” *IEEE Trans. Microw. Theory Tech.*, vol. 56, no. 7, pp. 1649–1660, Jul. 2008.
- [15] ——, “Modeling the broadband inductive and resistive behavior of composite conductors,” *IEEE Microw. Wireless Compon. Lett.*, vol. 18, no. 4, pp. 230–232, Apr. 2008.

CHAPTER 3

Construction and Applications of the Dirichlet to Neumann Operator in Transmission Line Modeling

Thomas Demeester and Daniël De Zutter

Accepted for publication in *ELEKTRIK*,
Turkish Journal of Electrical Engineering and Computer Sciences,
invited paper



The Dirichlet to Neumann (DtN) operator is a useful tool in the characterization of interconnect structures. In combination with the Method of Moments, it can be used for the calculation of the per unit length transmission line parameters of multi-conductor interconnections, or to directly determine the internal impedance of conductors. This paper presents a new and fast calculation method for the DtN boundary operator in the important case of rectangular structures, based on the superposition of parallel-plate waveguide modes. Especially for its non-differential form, some numerical issues need to be addressed. It is further explained how the DtN operator can be determined for composite geometries. The theory is illustrated with some numerical examples.

3.1 Introduction

For accurate signal integrity simulations of on-chip interconnect structures, a broad-band transmission line model is required. In the near future, systems with speeds of 40 Gbit/s and higher will be developed, for which undesired effects as cross-talk, losses, and wave propagation on interconnects will play an important role. On printed circuit boards (PCB) at these frequencies, the skin effect is strongly developed, leading to highly increased losses, and taking into account wave propagation effects is eminently important for signal integrity predictions. Sources and loads should therefore be carefully matched, up to the highest frequencies. In order to predict all these effects, an advanced transmission line model is required, rigorously taking into account the material properties and geometry of the considered structures.

In [1], such a 2-D multi-conductor transmission line model is developed for the determination of the quasi-TM resistance, inductance, capacitance and conductance matrices of the system. All homogeneous materials (including dielectrics, conductors and semiconductors) are replaced by an equivalent contrast current source in free space. These sources can be transformed into surface sources, resulting in a boundary integral equation formulation of the problem. Essential herein, is the use of the Dirichlet to Neumann boundary operator (as introduced below), which allows to deal with a large variation in geometry parameters, see Section 3.3.2. The boundary formulation is advantageous with respect to other methods that are based on a volume discretization, such as the single-conductor model presented in [2], based on a combination of the Method of Moments and the Method of Lines.

In [1], the transmission line characterization is split up into two parts. For the resistance-inductance (RL) problem, the contrast currents are transformed into differential surface currents j_s on the boundary of conductors and semiconductors, defined for an $e^{j\omega t}$ -dependence of the fields, as [3]

$$j_s(\mathbf{r}) = \frac{1}{j\omega\mu_0} \left(\frac{\partial e_z(\mathbf{r})}{\partial n} - \frac{\partial e_{z0}(\mathbf{r})}{\partial n} \right), \quad \mathbf{r} \in c \quad (3.1)$$

with $\partial/\partial n$ the outward normal derivative with respect to the boundary c of the considered material S . e_z satisfies the diffusion equation $\nabla_t^2 e_z = j\omega\mu_0\sigma e_z$ (with the index t denoting the transverse xy -plane), whereas e_{z0} is defined with the same boundary value on c , but in free space, and satisfies Laplace's equation $\nabla_t^2 e_{z0} = 0$ inside S . For the capacitance-conductance (CG) problem, the contrast sources lead to the surface charge on the conductors, and an equivalent surface charge ρ_s

$$\rho_s(\mathbf{r}) = (\epsilon - \epsilon_0 + \sigma/j\omega) \frac{\partial \phi(\mathbf{r})}{\partial n}, \quad \mathbf{r} \in c \quad (3.2)$$

on the boundaries of dielectrics and semiconductors. ϕ is the scalar electric potential, satisfying Laplace's equation or the diffusion equation in, respectively, dielectrics

and semiconductors. Consequently, the transformed problem only uses frequency-dependent surface currents and charges in free space, and can be directly solved with the Method of Moments (MoM). For further details, the reader is referred to [1].

The DtN operators \mathcal{D} and \mathcal{D}_0 are essential in both the RL and the CG problem and are defined, for $\mathbf{r} \in c$, by

$$\frac{\partial\psi(\mathbf{r})}{\partial n} = \oint_c \mathcal{D}(\mathbf{r}, \mathbf{r}') \psi(\mathbf{r}') d\mathbf{c}', \quad \mathbf{r} \in c \quad (3.3)$$

$$\frac{\partial\psi_0(\mathbf{r})}{\partial n} = \oint_c \mathcal{D}_0(\mathbf{r}, \mathbf{r}') \psi_0(\mathbf{r}') d\mathbf{c}', \quad \mathbf{r} \in c \quad (3.4)$$

with

$$\nabla_t^2 \psi(\mathbf{r}) = j\omega\mu_0\sigma \psi(\mathbf{r}) \quad \text{and} \quad \nabla_t^2 \psi_0(\mathbf{r}) = 0, \quad \mathbf{r} \in S \quad (3.5)$$

Hence (3.1) and (3.2) can be written concisely as

$$j\omega\mu_0 j_{s,c} = \oint_c (\mathcal{D} - \mathcal{D}_0) e_z d\mathbf{c} \quad (3.6)$$

$$\rho_{s,c} = (\epsilon - \epsilon_0 + \sigma/j\omega) \oint_c \mathcal{D} \phi d\mathbf{c}. \quad (3.7)$$

with lower index c to denote evaluation on the considered boundary.

Section 3.2 deals with the discretization of $(\mathcal{D} - \mathcal{D}_0)$, in the sequel called the *differential* DtN operator, and \mathcal{D} , the *non-differential* DtN operator, on the boundary of a rectangular area, with an extension to arbitrary shapes which are composed of rectangular blocks. In section 3.3 some applications are discussed, including internal impedance calculations and transmission line modeling. Finally, some conclusions are formulated in Section 3.4.

3.2 Construction of the DtN Operator

In [3], a method to calculate the matrix $(\mathcal{D} - \mathcal{D}_0)$ as the MoM discretization of $(\mathcal{D} - \mathcal{D}_0)$ for the rectangular area S is proposed, based on the following strategy. A general boundary function ψ expanded in piecewise constant basis functions is projected on a basis of the Dirichlet eigenfunctions of S , resulting for a rectangle in a double summation of sines functions. Next, the normal derivative of each Dirichlet function is calculated, and the double summation is again weighted with the original basis functions, resulting in an expression for $\partial\psi/\partial n$. For the contribution of ψ on one side, to $\partial\psi/\partial n$ on the same or the opposite side, the remaining double summation can be transformed into a single sum. For the interaction between adjacent sides however, a double infinite summation remains, each to be judiciously truncated. The proposed

method in this paper directly leads to a single summation for all interactions, and, hence, a much faster calculation. Another reason to introduce the new calculation method presented in this paper, is the need for the non-differential DtN operator for the CG problem, which was not required for the RL problem treated in [3]. The function $e_z - e_{z0}$, the Dirichlet expansion of which is needed to discretize (3.6), is zero on c , and the Dirichlet functions of S are indeed only complete on S including its boundary, for the expansion of a function with a zero boundary value. The Dirichlet expansion of ψ with a non-zero boundary value, needed for (3.7), would lead to an important Gibbs phenomenon on the *total* boundary c , leading to highly inaccurate results. This problem is circumvented with the new method, as will be shown in the next paragraphs.

3.2.1 Rectangular Cross-Section

Consider region $S \leftrightarrow x \in [0, x_0], y \in [0, y_0]$, with boundary c and sides $c_1(y = 0)$, $c_2(x = x_0)$, $c_3(y = y_0)$ and $c_4(x = 0)$. The aim is to determine the discretized (matrix) form D of operator \mathcal{D} , for which

$$\frac{\partial \psi(\mathbf{r})}{\partial n} = \oint_c D(\mathbf{r}, \mathbf{r}') \psi(\mathbf{r}') d\mathbf{c}(\mathbf{r}'), \quad \mathbf{r} \in c \quad (3.8)$$

$$\nabla_t^2 \psi(\mathbf{r}) = -k^2 \psi(\mathbf{r}), \quad \mathbf{r} \in S \quad (3.9)$$

with $\mathbf{r} = x\mathbf{u}_x + y\mathbf{u}_y$ the position vector in the chosen (x, y) system. First, an expansion of ψ is constructed from the knowledge of its boundary value ψ_c and based on (3.9). The contribution of each side is treated separately, by splitting up ψ as

$$\psi(x, y) = \sum_{i=1}^4 \psi^{(i)}(x, y) \quad (3.10)$$

in which $\psi^{(i)}$ takes the actual boundary value of ψ on side c_i , and is zero on the other sides. Expanding ψ on c_1 (written as ψ_{c_1}) into sines immediately leads to

$$\psi^{(1)}(x, y) = \sum_{n=1}^{N_1} A_n^{(1)} \sin\left(\frac{n\pi x}{x_0}\right) f_n^-(y/y_0) \quad (3.11)$$

with $f_n^-(s)$, for $s \in [0, 1]$, defined as

$$f_n^-(s) = \frac{e^{j\beta_n y_0 s} - e^{j\beta_n y_0 (2-s)}}{1 - e^{j\beta_n 2y_0}} \quad \text{and} \quad f_n^+(s) = \frac{e^{j\beta_n y_0 s} + e^{j\beta_n y_0 (2-s)}}{1 - e^{j\beta_n 2y_0}}. \quad (3.12)$$

The function f_n^+ is introduced as well, as it will be needed in the sequel. The upper limit N_1 in (3.11) is taken high enough, such that the truncated sine expansion on c_1 is

a good approximation of the actual boundary value of ψ_1 . The β_n in (3.12) are found from

$$\beta_n^2 = k^2 - \left(\frac{n\pi}{x_0} \right)^2 \quad (3.13)$$

and the square root is chosen such, that $\operatorname{Re}(j\beta_n) < 0$. As required, (3.11) satisfies (3.9), reduces to

$$\psi_{c_1}^{(1)} = \sum_{n=1}^{N_1} A_n^{(1)} \sin \left(\frac{n\pi x}{x_0} \right) \quad (3.14)$$

on c_1 , and is zero on the other sides. Expansion (3.11) can be seen as an expansion in the modes of a parallel-plate waveguide with c_2 and c_4 as its plates, more specifically these modes that are zero on c_3 . The functions $\psi^{(i)}$ ($i = 2, 3, 4$) are defined analogously to (3.11), but with the sine expansions on the corresponding sides c_i , respectively, and with an analogous interpretation in terms of an expansion in waveguide modes.

Along each side, we will use the normalized coordinate $s \in [0, 1]$ (in counter-clockwise direction), such that the sides are determined by

$$c_1 \leftrightarrow \{x = s x_0, y = 0\} \quad (3.15)$$

$$c_2 \leftrightarrow \{x = x_0, y = s y_0\} \quad (3.16)$$

$$c_3 \leftrightarrow \{x = (1 - s) x_0, y = y_0\} \quad (3.17)$$

$$c_4 \leftrightarrow \{x = 0, y = (1 - s) y_0\} \quad (3.18)$$

In order to discretize ψ on c_1 , this side is divided into M_1 segments, using the discretization points x_m , ($m = 1, \dots, M_1 + 1$), not necessarily chosen uniformly along c_1 , and with x_1 and x_{M_1+1} the corner points. The normalized coordinates of these discretization points are $s_m = x_m/x_0$, such that $s_1 = 0$ and $s_{M_1+1} = 1$. An analogous discretization is performed for the other sides, with the segments numbered in counter-clockwise direction. On side c_i ($i = 1, 2, 3, 4$), ψ_{c_i} can hence be approximated by

$$\psi_{c_i}(s) \simeq \sum_{m=1}^{M_i} \Psi_{c_i,m} t_{c_i,m}(s), \quad 0 \leq s \leq 1. \quad (3.19)$$

The basis functions $t_{c_i,m}(s)$, with $m = 1, \dots, M_i$, can be a constant pulse on the interval $[s_m, s_{m+1}]$ (corresponding, e.g. on c_1 , to $x \in [x_m, x_{m+1}]$), a piecewise linear ‘hat’ function on $[s_{m-1}, s_{m+1}]$, or any other basis function. The coefficients $\Psi_{c_i,m}$ are taken together into one column vector Ψ_c as

$$\Psi_c = \begin{bmatrix} \Psi_{c_1} \\ \Psi_{c_2} \\ \Psi_{c_3} \\ \Psi_{c_4} \end{bmatrix} \quad (3.20)$$

in which $[\Psi_{c_i}]_m = \Psi_{c_i,m}$. In a first step, the expansion coefficients $A_n^{(1)}$ from (3.11) (and grouped in the vector $\mathbf{A}^{(1)}$) are determined from the coefficients $\Psi_{c_1,m}$. By inserting (3.15) in (3.11), we find with (3.19)

$$\psi_{c_1}^{(1)} \simeq \sum_{m=1}^{M_1} \Psi_{c_1,m} t_{c_1,m}(s) \simeq \sum_{n=1}^{N_1} A_n^{(1)} \sin(n\pi s) \quad (3.21)$$

and, by weighting with the set $\{2 \sin n\pi s\}$,

$$\mathbf{Q}_1 \cdot \Psi_{c_1} = \mathbf{A}^{(1)} \quad (3.22)$$

The $N_1 \times M_1$ matrix \mathbf{Q}_1 is given by

$$[\mathbf{Q}_1]_{n,m} = 2 \int_0^1 t_{c_1,m}(s) \sin n\pi s \, ds. \quad (3.23)$$

The knowledge of the coefficients $A_n^{(1)}$ determines the normal derivative of $\psi^{(1)}$ on each side of S . We find from (3.11), invoking (3.12) and (3.15)-(3.18),

$$\frac{\partial \psi_{c_1}^{(1)}(s)}{\partial n} = \sum_{n=1}^{N_1} -j\beta_n f_n^+(0) \sin n\pi s A_n^{(1)} \quad (3.24)$$

$$\frac{\partial \psi_{c_2}^{(1)}(s)}{\partial n} = \sum_{n=1}^{N_1} \frac{n\pi}{x_0} (-1)^n f_n^-(s) A_n^{(1)} \quad (3.25)$$

$$\frac{\partial \psi_{c_3}^{(1)}(s)}{\partial n} = \sum_{n=1}^{N_1} j\beta_n f_n^+(1) \sin n\pi(1-s) A_n^{(1)} \quad (3.26)$$

$$\frac{\partial \psi_{c_4}^{(1)}(s)}{\partial n} = \sum_{n=1}^{N_1} -\frac{n\pi}{x_0} f_n^-(1-s) A_n^{(1)} \quad (3.27)$$

The normal derivative $\partial \psi^{(1)} / \partial n$ is discretized on side c_i , as

$$\frac{\partial \psi_{c_i}^{(1)}(s)}{\partial n} \simeq \sum_{m=1}^{M_i} \Gamma_{c_i,m}^{(1)} t_{c_i,m}(s) \quad (3.28)$$

and weighting (3.24-3.27) with the basis functions $t_{c_i,m}(s)$ on the corresponding sides, leads with (3.28) to

$$\mathbf{B}_i \cdot \Gamma_{c_i}^{(1)} = \mathbf{T}_{i1} \cdot \mathbf{A}^{(1)}, \quad \text{with } i = 1, \dots, 4 \quad (3.29)$$

with the $M_i \times M_i$ weighting matrices B_i given by

$$[B_i]_{m,\tilde{m}} = \int_0^1 t_{c_i,m}(s) t_{c_i,\tilde{m}}(s) ds \quad (3.30)$$

and the $M_i \times N_1$ submatrices T_{i1} given by

$$[T_{11}]_{\tilde{m},n} = -j\beta_n f_n^+(0) \int_0^1 \sin n\pi s t_{c_1,\tilde{m}}(s) ds \quad (3.31)$$

$$[T_{21}]_{\tilde{m},n} = \frac{n\pi}{x_0} (-1)^n \int_0^1 f_n^-(s) t_{c_2,\tilde{m}}(s) ds \quad (3.32)$$

$$[T_{31}]_{\tilde{m},n} = j\beta_n f_n^+(1) \int_0^1 \sin n\pi(1-s) t_{c_3,\tilde{m}}(s) ds \quad (3.33)$$

$$[T_{41}]_{\tilde{m},n} = -\frac{n\pi}{x_0} \int_0^1 f_n^-(1-s) t_{c_4,\tilde{m}}(s) ds. \quad (3.34)$$

Finally, with (3.22) and (3.29),

$$\Gamma_c^{(1)} = D^{(1)} \cdot \Psi_{c_1} \quad (3.35)$$

for

$$\Gamma_c^{(1)} = \begin{bmatrix} \Gamma_{c_1}^{(1)} \\ \Gamma_{c_2}^{(1)} \\ \Gamma_{c_3}^{(1)} \\ \Gamma_{c_4}^{(1)} \end{bmatrix} \quad \text{and} \quad D^{(1)} = \begin{bmatrix} B_1^{-1} T_{11} \\ B_2^{-1} T_{21} \\ B_3^{-1} T_{31} \\ B_4^{-1} T_{41} \end{bmatrix} \cdot Q_1 \quad (3.36)$$

The matrix $D^{(1)}$ maps the boundary value of $\psi^{(1)}$, i.e., the actual value of ψ on c_1 and zero on the other sides, onto its normal derivative $\partial\psi_c^{(1)}/\partial n$. A similar procedure yields the matrices $D^{(2)}$, $D^{(3)}$, and $D^{(4)}$ to account for the boundary value of ψ on sides c_2 , c_3 , and c_4 . The total DtN matrix D can hence be constructed, with (3.20), as

$$D = [D^{(1)} \quad D^{(2)} \quad D^{(3)} \quad D^{(4)}] \quad (3.37)$$

The calculation as described above for the non-differential matrix D (or D_0), raises an accuracy problem in the corners of the rectangle. The sine expansion on each side is actually the Fourier series of the “odd extension” of ψ on that side, and hence discontinuous in case the corner values are non-zero. This causes a Gibbs phenomenon that is reinforced in the calculation of $\partial\psi/\partial n$, and leads to an inaccurate D . However, a well-chosen mathematical manipulation allows to circumvent this problem. Let us first discuss the calculation of the non-differential matrix D_0 . A part $\tilde{\psi}_0 = p_1xy + p_2x + p_3y + p_4$ is beforehand subtracted from the total ψ_0 , as it obviously satisfies Laplace’s equation, and with the coefficients p_i chosen such, that in the four corners $\tilde{\psi}_0 = \psi_0$ (assuming ψ continuous along the boundary, which is indeed

the case for both the electric scalar potential and for the longitudinal electric field). The normal derivative of $\tilde{\psi}_0$ is known analytically, and the technique described above is then used for the calculation of $\partial(\psi_0 - \tilde{\psi}_0)/\partial n$, immune to Gibbs phenomena as the corner values are identically zero.

The differential DtN matrix ($D - D_0$) is also calculated with the procedure explained in this section, but with the submatrices $(T_{ij} - T_{0,ij})$ instead of only T_{ij} . A careful calculation of these submatrices allows to take into account the fact that $\psi_c - \psi_{0,c} = 0$, such that no Gibbs phenomenon will be present, and $(D - D_0)$ is accurate.

Finally, D can be calculated by adding D_0 to $(D - D_0)$. Alternatively, D can be calculated *directly* as well. There always exists an analytically known function $\tilde{\psi}$ which has the same corner values as ψ itself, and satisfies the diffusion equation (3.9) inside S , for any value of k^2 . Such a function $\tilde{\psi}$ can be formed as a linear combination of four functions $\tilde{\psi}^{p_i}$ ($i = 1, \dots, 4$), which are 1 in corner p_i but zero in all the other corners, and satisfy (3.9) inside S . Such a function is, e.g., for corner $p_1(0, 0)$

$$\tilde{\psi}^{p_1}(x, y) = \cos\left(\frac{\pi x}{2x_0}\right) \left(\frac{e^{j\beta y} - e^{j\beta(2y_0-y)}}{1 - e^{j\beta 2y_0}} \right) \quad (3.38)$$

with $\beta^2 = k^2 - (\pi/2x_0)^2$, and analogous for the other corners. The numerical procedure to determine the DtN operator can then be correctly applied to $\psi - \tilde{\psi}$, and the normal derivative of $\tilde{\psi}$ can be calculated separately, again leading to the correct DtN operator.

An example is given to illustrate the explained ideas. Fig. 3.1 shows the normal derivative of a harmonic function ψ_0 of the form

$$\psi_0(x, y) = \alpha_1 (\cos cx + \alpha_2 \sin cx) (e^{cy} + \alpha_3 e^{-cy}) + \alpha_4, \quad (3.39)$$

on the boundary of rectangle S , shown in the inset of Fig. 3.1. The coefficients α_1 to α_4 can be determined from the arbitrarily chosen value $c = 3\pi/2$, together with the indicated corner values of ψ_0 in Fig. 3.1. A fine discretization was used (horizontally 100 intervals and 1000 sines, vertically 30 intervals and 300 sines). The analytical normal derivative, $\partial\psi_0/\partial n$, is compared to the result with the compensation for non-zero boundary values of ψ_0 , indicated in Fig. 3.1 as “ ψ_0 indirect”, and the results are indistinguishable. Conversely, the method without compensation, denoted “ ψ_0 direct”, exhibits, as expected, an important Gibbs phenomenon in the three corners where $\psi_0 \neq 0$.

3.2.2 General Cross-Sections

The following paragraphs describe how the matrix D_{tot} , i.e., the discretized form of the operator \mathcal{D}_{tot} , can be calculated for a general shape that consists of parts for which

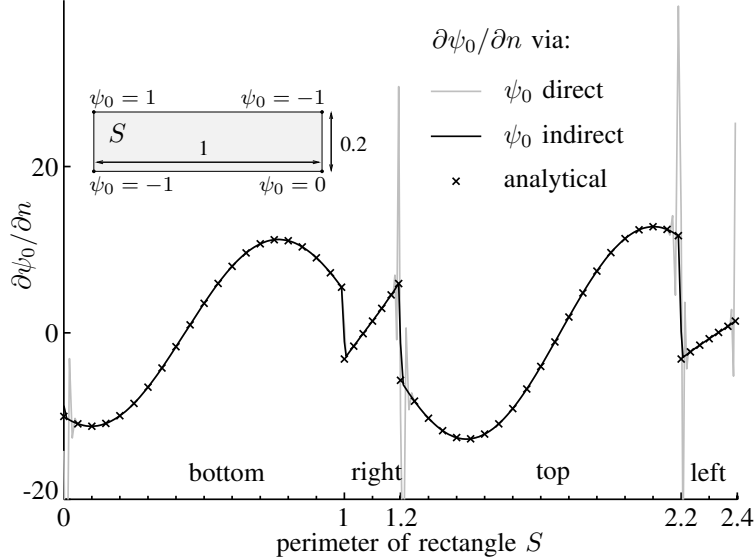


Figure 3.1: Normal derivative of a harmonic function ψ_0 . For “ ψ_0 direct”, $\partial\psi_0/\partial n$ was calculated as $\oint_c \mathcal{D}_0 \psi_0 \, dc$, whereas for “ ψ_0 indirect”, as $\partial\psi_0/\partial n + \oint_c \mathcal{D}_0 (\psi_0 - \psi_0) \, dc$, avoiding Gibbs phenomena.

the matrix D is known. A distinction has to be made between the discretization of $\partial e_z/\partial n$ (for conductors) and $\partial\phi/\partial n$ (for dielectrics), with e_z the longitudinal electric field, and ϕ the scalar electric potential.

In the case of a composite conductor, the matrix D_{tot} can be obtained from the matrices $D^{(i)}$ of the different parts of the conductor (for which the conductivity $\sigma^{(i)}$ is assumed constant) by elimination of the internal boundaries. To that end, two additional conditions have to be imposed, i.e., the continuity of both e_z and $\partial e_z/\partial n$ on the internal boundaries. In the quasi-TM approximation $\partial e_z/\partial n$ is continuous, due to the continuity of the cross-sectional tangential magnetic field

$$h_{\tan} \approx \frac{1}{j\omega\mu_0} \left(\frac{\partial e_z}{\partial n} - \frac{1}{\sigma} \frac{\partial^2 h_z}{\partial z \partial \tan} \right) \approx \frac{1}{j\omega\mu_0} \frac{\partial e_z}{\partial n}. \quad (3.40)$$

For the determination of the differential surface admittance matrix $Y_{\text{tot}} = (D_{\text{tot}} - D_{0,\text{tot}})/j\omega\mu_0$ of a composite conductor [4], D_{tot} and $D_{0,\text{tot}}$ need to be determined separately from the corresponding matrices of the different parts. The reason is that e_z (satisfying the diffusion equation) and e_{z0} (satisfying Laplace’s equation) are not the same on the inner boundaries of the total conductor (although they need to be identical on the outer boundary, by definition).

In order to calculate the discretized form of $\partial\phi/\partial n$ for composite (lossy) dielectrics, the continuity of ϕ needs to be invoked, as well as the continuity of $(\epsilon +$

$\sigma/j\omega) \partial\phi/\partial n$, because for these materials $\mathbf{e}_t \approx -\nabla_t\phi$ within the quasi-TM approximation [1].

3.3 Applications of the DtN Operator

3.3.1 Internal Impedance Calculations

Consider a conductor above a reference plane, situated infinitely far away (in order to exclude proximity effects). The current I through the conductor can be written, because e_z inside the conductor satisfies the diffusion equation, as

$$I = \iint_S \sigma e_z dS = \frac{1}{j\omega\mu_0} \oint_c \frac{\partial e_z}{\partial n} dc = -\frac{1}{j\omega\mu_0} \oint_c dc \oint_c \mathcal{D} \left(\frac{\partial V}{\partial z} + j\omega a_z \right) dc \quad (3.41)$$

in which V is the constant boundary value of the electric scalar potential ϕ , and a_z the longitudinal component of the magnetic vector potential. In order to determine the *internal* impedance, the magnetic field *outside* the conductor should be made zero, or, $a_z = \text{const} = 0$ because on the reference at infinity $a_z = 0$. It is physically not possible to have a non-zero current without an external magnetic field. The above reasoning is merely a way to conclude that the influence of the external magnetic field is omitted from (3.41) by setting $a_z = 0$ on c . The remaining part I_{in} of the current is related to the internal impedance Z_{in} by $\partial V/\partial z = -Z_{\text{in}} I_{\text{in}}$, such that Z_{in} can be identified as

$$Z_{\text{in}}^{-1} = \frac{1}{j\omega\mu_0} \oint_c dc \oint_c \mathcal{D} dc. \quad (3.42)$$

Hence, the DtN operator directly leads to the internal impedance of a conductor. It can be proven that, for the case of a homogeneous rectangular conductor, (3.42) is identical to the result obtained in [5]. For more details, and a comparison with an alternative calculation method for the internal impedance, the reader is referred to [6].

Consider the layered conductor shown in the inset of Fig. 3.2. The circuit behavior of such a conductor in a microstrip configuration was described in [4]. It is now possible to investigate the influence of the inhomogeneity, by determining Z_{in} . To that end, the total DtN operator for the composite conductor is calculated, and then with (3.42) the internal impedance $Z_{\text{in}} = R_{\text{in}} + j\omega L_{\text{in}}$. The result is shown in Fig. 3.2, where the layered conductor is compared to a homogeneous copper conductor with the same geometry.

3.3.2 Transmission Line Modeling

A complete on-chip transmission line configuration is shown in Fig. 3.3. Two pairs of parallel traces, (c_1, c_2) and (c_3, c_4) , are embedded in a dielectric material above a

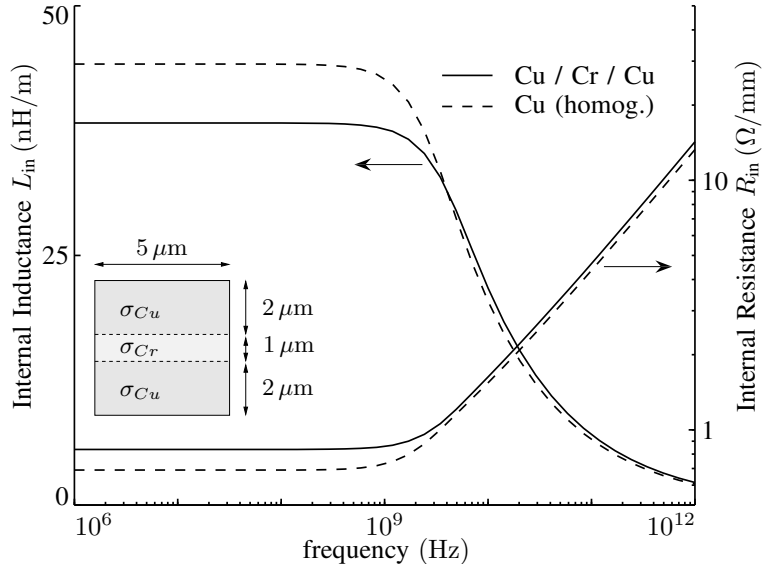


Figure 3.2: Internal inductance L_{in} and internal resistance R_{in} for a layered conductor ($\sigma_{Cu} = 58 \text{ MS/m}$, $\sigma_{Cr} = 7.75 \text{ MS/m}$), compared to a homogeneous copper conductor.

semiconducting substrate. The DtN operator is used to replace conductors, semiconductors and dielectrics by surface sources in free space, from which the transmission line parameters are determined.

Some elements of the resulting transmission line matrices per unit length (the inductance L , resistance R , capacitance C , and conductance G) are shown in Fig. 3.4. In Fig. 3.4 (a), the inductance elements show that at the highest frequencies the magnetic field is for the greater part forced out of the conductors. This corresponds to the current crowding effect, resulting in an increased resistance R_{11} . The skin effect is not yet fully developed though, as at 100 GHz the skin depth equals the conductors' height. Fig. 3.4 (b) shows the capacitance and conductance elements. As motivated in [1], a material is considered a good conductor as long as its conductivity $\sigma \gg \omega\epsilon$. If that is the case for the semiconducting substrate, i.e., if the frequency is low enough, a surface charge exists on top of the substrate. At 100 MHz, this surface charge is still considerable ($\sigma_s \simeq 30\omega\epsilon$, with $\sigma_s = 2 \text{ S/m}$ and $\epsilon = 12\epsilon_0$), but at 3 GHz, $\sigma_s \simeq \omega\epsilon$, and from higher frequencies onwards, the substrate behaves as a dielectric. The presence of this low-frequency surface charge on the substrate increases the self-capacitance C_{11} but at the same time has a decoupling effect on the nearby conductors. This explains why $|C_{12}|$ and $|C_{23}|$ increase when the substrate starts to behave as a dielectric. It is also observed that the self-conductance G_{11} increases once the dielectric behavior of the substrate becomes dominant, because then a transverse electric field is built up inside the substrate, causing the conductance losses.

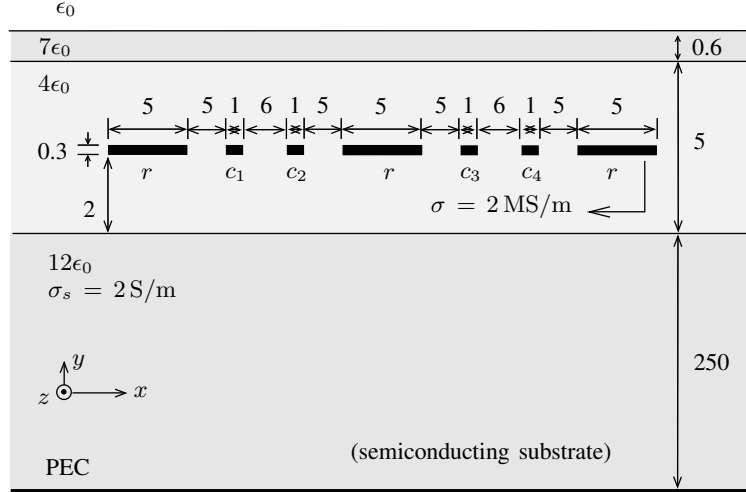


Figure 3.3: Cross section (not drawn to scale) of a four-line configuration (conductors c_1 to c_4), with 3 reference lines (indicated as r). All dimensions are in micrometer.

It is now investigated how the signal line pairs of Fig. 3.3 are coupled, when they are excited with perfectly differential currents. Both signal pairs are separated by a reference conductor r (kept on zero potential). A reference conductor is placed on both sides of the signal lines as well, so as to guarantee as good as possible the symmetry of the configuration, avoiding the excitation of the common modes. First, consider only the conductor pair (c_1, c_2) , designed for a high-frequency differential characteristic impedance of 175Ω (in the absence of other conductors). The separation of $6 \mu\text{m}$ between c_1 and c_2 is chosen quite large to keep the mutual capacitance low, and as such minimize the attenuation and maximize the propagation speed of the differential mode. The separation cannot become too large, however, to keep the sensitivity with respect to outside noise low.

Suppose two such pairs are used for a $500 \mu\text{m}$ long on-chip interconnection, but only little space is available, such that c_2 and c_3 can be separated by a distance of $15 \mu\text{m}$ only, to keep the lines far enough away from other circuits. The inset of Fig. 3.5 shows how the lines are used to connect a source with a differential load impedance of 175Ω . The results in Fig. 3.5 show the output voltages $|v_{12}|$ and $|v_{34}|$ for a unit current excitation of signal pair (c_1, c_2) and with the current source on the other pair switched off. The configuration of Fig. 3.3 is compared with the case in which the three reference conductors are left out. The coupling of both lines for a differential excitation is, as expected, smaller when the reference conductors r shield the signal lines. Yet the coupling is in both cases very weak (considering the factor 10 in the graphical presentation of $|v_{43}/i_s|$). What's more, the presence of the conductors r

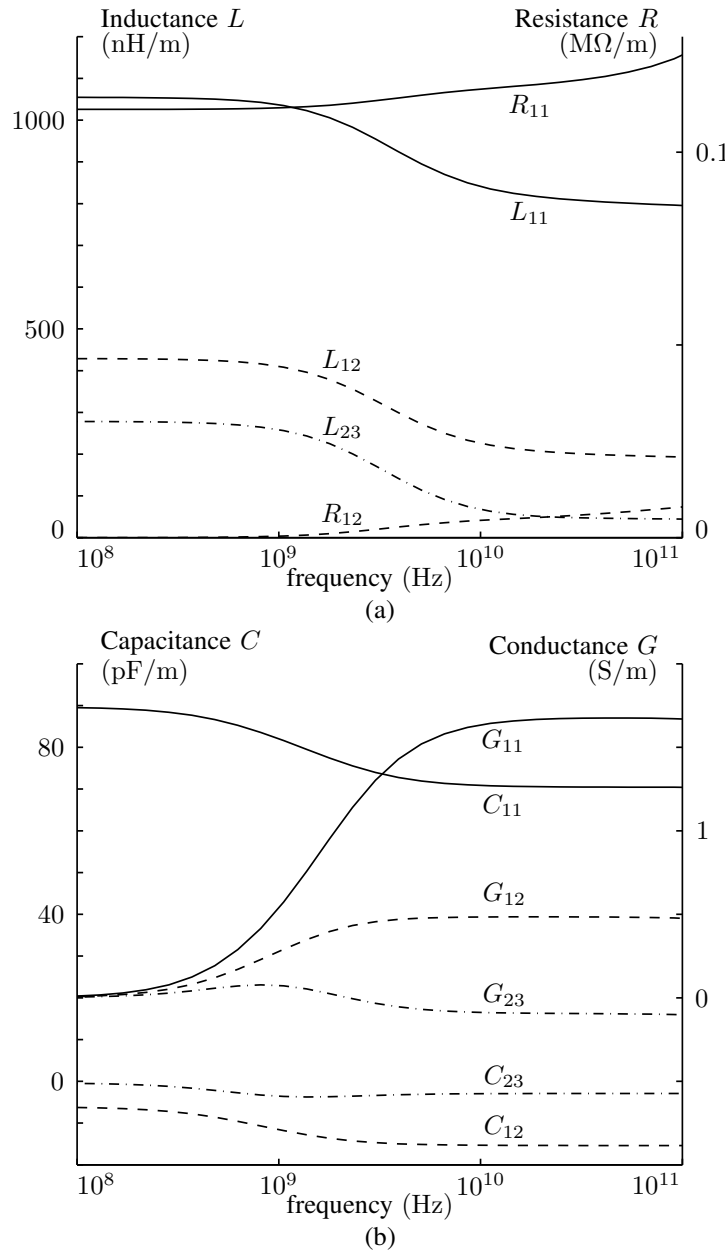


Figure 3.4: Elements of the transmission line matrices (a) L (inductance) and R (resistance), and (b) C (capacitance) and G (conductance), for the structure of Fig. 3.3.

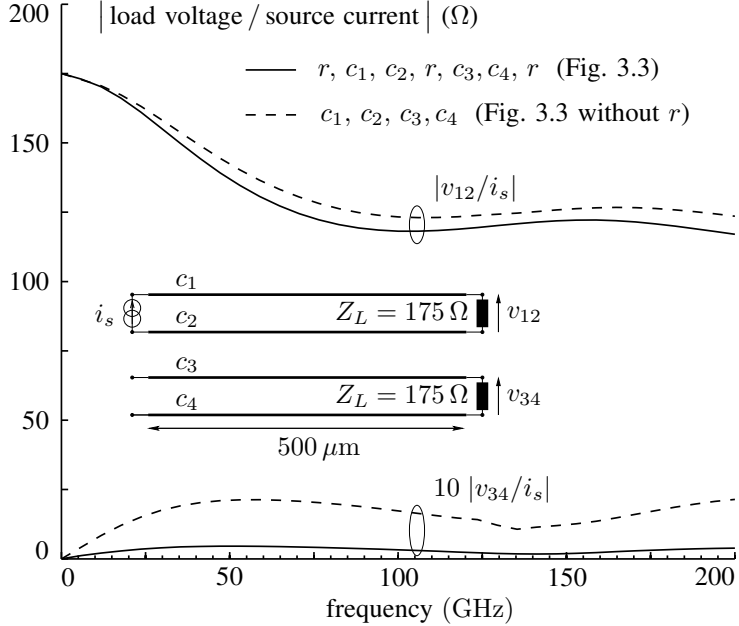


Figure 3.5: Source-interconnect-load configuration and load voltages, comparing the configuration of Fig. 3.3 with the case in which the reference conductors r are left away.

increases the capacitance of the signal lines. As a result, see $|v_{12}/i_s|$ in Fig. 3.5, the attenuation gets higher, and the lines become electrically longer, such that wave effects become important from slightly lower frequencies onwards.

3.4 Conclusion

This paper presents a new and efficient way to calculate the differential Dirichlet to Neumann boundary operator for rectangular blocks. Unlike the original calculation method [3], the new method allows to calculate the non-differential DtN operator as well, which is needed on the one hand for capacitance calculations and, on the other hand, to calculate the DtN operator for more complicated shapes. Some numerical examples demonstrate the practical use of the DtN operator for internal impedance calculations and, especially, for accurate transmission line modeling.

Bibliography

- [1] T. Demeester and D. De Zutter, “Quasi-TM transmission line parameters of coupled lossy lines based on the Dirichlet to Neumann boundary operator,” *IEEE Trans. Microw. Theory Tech.*, vol. 56, no. 7, pp. 1649–1660, Jul. 2008.
- [2] G. Plaza, R. Marques, and F. Medina, “Quasi-TM MoL/MoM approach for computing the transmission-line parameters of lossy lines,” *IEEE Trans. Microw. Theory Tech.*, vol. 54, no. 1, pp. 198–209, Jan. 2006.
- [3] D. De Zutter and L. Knockaert, “Skin effect modeling based on a differential surface admittance operator,” *IEEE Trans. Microw. Theory Tech.*, vol. 53, no. 8, pp. 2526–2538, Aug. 2005.
- [4] T. Demeester and D. De Zutter, “Modeling the broadband inductive and resistive behavior of composite conductors,” *IEEE Microw. Wireless Compon. Lett.*, vol. 18, no. 4, pp. 230–232, Apr. 2008.
- [5] A. Rong and A. Cangellaris, “Note on the definition and calculation of the per-unit-length internal impedance of a uniform conducting wire,” *IEEE Trans. Electromagn. Compat.*, vol. 49, no. 3, pp. 677–681, Aug. 2007.
- [6] T. Demeester and D. De Zutter, “Internal impedance of composite conductors with arbitrary cross section,” *IEEE Trans. Electromagn. Compat.*, vol. 51, no. 1, pp. 101–107, Feb. 2009.

CHAPTER 4

Construction of the Dirichlet to Neumann Boundary Operator for Triangles and Applications in the Analysis of Polygonal Conductors

Thomas Demeester and Daniël De Zutter

Accepted for publication in the
IEEE Transactions on Microwave Theory and Techniques



This paper introduces a fast and accurate method to investigate the broadband inductive and resistive behavior of conductors with a non-rectangular cross-section. The presented Iterative Combined Waveguide Modes (ICWM) algorithm leads to an expansion of the longitudinal electric field inside a triangle, using a combination of parallel-plate waveguide modes in three directions, each perpendicular to one of the triangle sides. This expansion is used to calculate the triangle's Dirichlet to Neumann boundary operator. Subsequently, any polygonal conductor can be modeled as a combination of triangles. The method is especially useful to investigate current crowding effects near sharp conductor corners. In a number of numerical examples, the accuracy of the ICWM algorithm is investigated, and the method is applied to some polygonal conductor configurations.

4.1 Introduction

To adequately address broadband signal integrity for board and package level interconnections, fully fledged RLGC transmission models are required. For the highest clock rates this is now also the case for on-chip interconnections as argued in [1]. The influence of the finite conductivity of the conductors and the associated frequency dependent skin effect losses and internal inductance (the so-called current crowding phenomenon) has received considerable attention in literature, see e.g. [2] and [3] and the many references in these papers. In [4] a single lossy line in the presence of a semiconducting substrate is analysed in the quasi-TM limit. The conductor losses can even become dominant for narrow strip configurations [5]. In [6] this quasi-TM analysis is extended to multiconductor lines in the presence of a semiconducting substrate.

To this end we introduced the Dirichlet to Neumann (DtN) operator [7] to capture the current crowding phenomenon inside a good conductor. The frequency ranges from DC to tens of GHz, at which point the skin-effect is fully developed and can be described by the familiar scalar surface impedance Z_s

$$Z_s = \frac{1+j}{\sigma\delta} \quad (4.1)$$

with σ the conductivity, and δ the skin depth. The DtN operator is used to obtain a surface admittance relationship $\mathcal{Y}(\mathbf{r}, \mathbf{r}')$ between the longitudinal electric field $e_z(\mathbf{r}')$ and the differential surface current $j_s(\mathbf{r})$, with \mathbf{r}' and \mathbf{r} on the circumference of the conductor's cross-section. To determine the per unit length inductance and resistance of a particular transmission line configuration, it now suffices to replace the conductors by their equivalent differential surface currents placed in the background medium. These differential, or so-called 'equivalent' surface currents are determined such, that they exactly give rise to the original fields outside the conductor when this conductor is made transparent by replacing its material properties by those of the background medium. Combining this with an integral equation solution for the fields generated by these currents, directly leads to the desired L and R matrices. In the quasi-TM approximation this approach can be extended to the determination of the capacitance and conductance matrices C and G by again invoking the DtN operator but now to obtain a relationship between the potential ϕ on the circumference of each dielectric and semiconductor, and its normal derivative $\partial\phi/\partial n$. Invoking an integral equation for the potential as a function of the equivalent surface charges in combination with this relationship between ϕ and $\partial\phi/\partial n$, and by exciting the conductors' boundaries with a constant potential, allows for a determination of C and G as demonstrated in [6] for coupled lines in the presence of semiconducting media.

Although the DtN operator theory can in principle be applied to conductors with an arbitrary cross-section, its practical application remained restricted to a rectangular cross-section. This is due to the fact that the analytical determination of the DtN

operator was based on its expansion in terms of the Dirichlet eigenfunctions. These functions are only known for the rectangle and the circle and because at least a few thousands of them are needed for a correct broadband analysis, their numerical determination for other shapes is excluded. However, more complex conductor shapes, provided they are formed by combining rectangles, can be handled as demonstrated in [8] and [9], e.g., to examine the effect of layered on-chip conductors.

Effects such as underetching or electrolytical growth in the integrated circuit manufacturing process, lead to conductors that are trapezoidal rather than rectangular. In [10], such lines are investigated using a combination of the Finite Element Method (FEM) and the Method of Lines (MoL). To investigate trapezoidal conductors, or more generally, the influence of sharp or obtuse conductor corners on the current crowding, by means of the fast boundary integral equation method presented in [6], the knowledge of the DtN operator for a triangular cross-section is of paramount importance. Combining triangular cross-sections with rectangular ones, as in [9] for rectangular cross-sections, then allows one to approximate almost any cross-sectional shape.

In section 4.2 and 4.3 the DtN operator for the triangle is determined by a new method not depending on the Dirichlet eigenfunctions. As argued and demonstrated in [6] and [7], for piecewise homogeneous media, the use of the DtN operator allows to reformulate the complete problem in terms of a set of coupled boundary integral equations only requiring the discretization of the unknowns on the boundaries of the different subdomains. The use of the proper Green's functions for each subdomain, leads to the additional advantage that the skin-effect can be captured in a very accurate way.

First, the e_z field on the circumference of the triangle is discretized, e.g., by using piecewise constant or linear basis functions. Inside the triangle e_z satisfies the diffusion equation. Next, we choose to expand e_z inside the triangle in terms of three sets of parallel-plate waveguide modes, each set with one of the triangle's sides as the waveguide's height. In theory using only a single complete set of parallel-plate waveguide modes would suffice, but the extra waveguide modes are introduced to avoid numerical inaccuracies as will be carefully substantiated at the end of Section 4.2.1. This in turn leads to a numerically very stable determination of the normal derivative of e_z on the circumference, as a function of its original discretized representation.

In section 4.4, some numerical examples demonstrate the accuracy of the method and the convergence properties of the iterative process to determine the DtN operator. Furthermore, the resistance of a single conductor composed of triangles is determined for different conductor shapes. For a rectangle, results are compared with data available in literature. Next, the resistive and inductive properties of a multiconductor line with trapezoidal conductors are investigated and compared to the rectangular conductor case. Finally, a coplanar waveguide above a non-planar substrate is simulated and its characteristic impedance is compared with reference data.

4.2 Determination of the DtN Operator in a Triangle

As introduced in [7] and further elaborated in [6], the required relationship between e_z on a triangle's boundary c and the differential surface current j_s is given by

$$j_s(\mathbf{r}) = \frac{1}{j\omega\mu_0} \left(\frac{\partial e_z(\mathbf{r})}{\partial n} - \frac{\partial e_{z,0}(\mathbf{r})}{\partial n} \right), \quad \mathbf{r} \in c \quad (4.2)$$

$$= \frac{1}{j\omega\mu_0} \oint_c (\mathcal{D}(\mathbf{r}, \mathbf{r}') - \mathcal{D}_0(\mathbf{r}, \mathbf{r}')) e_z(\mathbf{r}') d\mathbf{c}(\mathbf{r}') \quad (4.3)$$

with $(\mathcal{D} - \mathcal{D}_0)$ the *differential* DtN operator. The actual electric field e_z and the fictitious field $e_{z,0}$ have the same boundary value on c , but inside triangle T , e_z satisfies the diffusion equation, whereas $e_{z,0}$ satisfies Laplace's equation

$$\nabla_t^2 e_z(\mathbf{r}) = j\omega\mu_0\sigma e_z(\mathbf{r}), \quad \mathbf{r} \in T \quad (4.4)$$

$$\nabla_t^2 e_{z,0}(\mathbf{r}) = 0, \quad \mathbf{r} \in T \quad (4.5)$$

as dictated by the quasi-TM approximations [6]. For a rectangular area, (4.3) was discretized by means of the Dirichlet expansion of $(e_z - e_{z,0})$, which is zero on the boundary c .

For the complex capacitance problem $C + G/j\omega$, the required relationship between the equivalent surface charge ρ_s and the electric potential ϕ_c on the boundary of dielectrics and semiconductors is given by

$$\rho_s(\mathbf{r}) = (\epsilon - \epsilon_0 + \sigma/j\omega) \frac{\partial \phi(\mathbf{r})}{\partial n}, \quad \mathbf{r} \in c \quad (4.6)$$

$$= (\epsilon - \epsilon_0 + \sigma/j\omega) \oint_c \mathcal{D}(\mathbf{r}, \mathbf{r}') \phi(\mathbf{r}') d\mathbf{c}(\mathbf{r}') \quad (4.7)$$

in which ϕ satisfies the diffusion equation in the semiconductors, and Laplace's equation in the dielectrics. The discretization of (4.7) requires the determination of the *non-differential* DtN operator \mathcal{D} . Because a Dirichlet expansion cannot be used to represent a non-zero boundary function, an alternative expansion was used to discretize (4.7) on a rectangle [11], based on the superposition of the modal fields that exist in two perpendicular parallel-plate waveguides. A similar approach will be used here, but the contributions from the three parallel-plate waveguides, each perpendicular to one of the sides of the triangle, will interfere with one another, which was not the case for the rectangle.

The algorithm introduced in this paper will lead to the DtN matrix D , the discretized form of the non-differential operator \mathcal{D} , defined for triangle T with boundary c by

$$\frac{\partial \psi(\mathbf{r})}{\partial n} = \oint_c \mathcal{D}(\mathbf{r}, \mathbf{r}') \psi(\mathbf{r}') d\mathbf{c}(\mathbf{r}'), \quad \mathbf{r} \in c \quad (4.8)$$

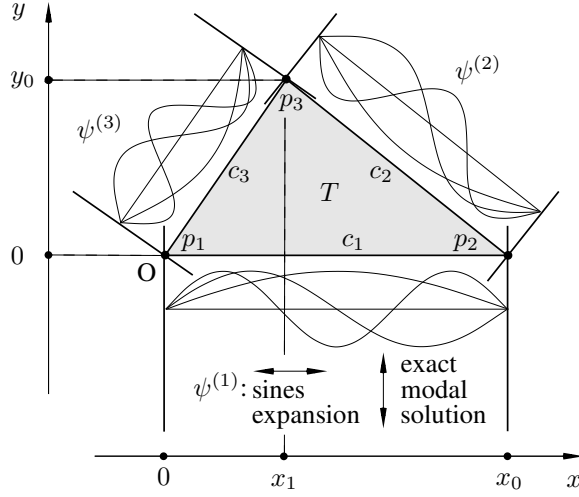


Figure 4.1: Triangle T , with corners $\{p_i\}$ and sides $\{c_i\}$ ($i = 1, 2, 3$), placed in a cartesian coordinate system with origin O and axes (x, y) , and with a schematic indication of the way ψ on T is split up into $\psi^{(1)}$, $\psi^{(2)}$, and $\psi^{(3)}$, according to parallel-plate waveguide modes in three directions.

for ψ satisfying

$$\nabla_t^2 \psi(\mathbf{r}) = -k^2 \psi(\mathbf{r}), \quad \mathbf{r} \in T. \quad (4.9)$$

4.2.1 Geometry of the Problem and Expansion of e_z

Consider triangle T , shown in Fig. 4.1, defined by its corner points $p_1(0, 0)$, $p_2(0, x_0)$ and $p_3(x_1, y_0)$. Along the sides c_1 , c_2 and c_3 , we will use the normalized coordinate s ranging from 0 to 1 in counter-clockwise direction along boundary c of triangle T , such that

$$c_1 \leftrightarrow \{x = s x_0, y = 0\} \quad (4.10)$$

$$c_2 \leftrightarrow \{x = x_0 + s(x_1 - x_0), y = s y_0\} \quad (4.11)$$

$$c_3 \leftrightarrow \{x = (1 - s)x_1, y = (1 - s)y_0\} \quad (4.12)$$

The outward pointing normal unit vectors on each side are needed in the sequel as well. They are given by

$$\mathbf{u}_1 = \left[0, -1 \right], \quad \mathbf{u}_2 = \left[\frac{y_0}{l_2}, \frac{x_0 - x_1}{l_2} \right], \quad \mathbf{u}_3 = \left[-\frac{y_0}{l_3}, \frac{x_1}{l_3} \right] \quad (4.13)$$

with l_1 , l_2 and l_3 the lengths of the respective sides.

The function $\psi(x, y)$ inside T is split up into three subfunctions

$$\psi(x, y) = \psi^{(1)}(x, y) + \psi^{(2)}(x, y) + \psi^{(3)}(x, y) \quad (4.14)$$

with

$$\psi^{(1)}(x, y) = \sum_{n=1}^{N_1} A_{c_1, n} f_{c_1, n}(x, y) \quad (4.15)$$

$$\psi^{(2)}(x, y) = \sum_{n=1}^{N_2} A_{c_2, n} f_{c_2, n}(x, y) \quad (4.16)$$

$$\psi^{(3)}(x, y) = \sum_{n=1}^{N_3} A_{c_3, n} f_{c_3, n}(x, y) \quad (4.17)$$

The functions $f_{c_1, n}(x, y)$ are given by

$$f_{c_1, n}(x, y) = \left(e^{j\beta_n y} - e^{-j\beta_n(y-2y_0)} \right) \sin \frac{n\pi x}{x_0} \quad (4.18)$$

with $\beta_n^2 = k^2 - (n\pi/x_0)^2$ and its square root β_n chosen such, that $\text{Re}(j\beta_n) < 0$. The upper limit N_1 in (4.15) is the number of sine functions used to expand the x -dependence of $\psi^{(1)}$.

The function $\psi^{(1)}$ can, with (4.15) and (4.18), be seen as an expansion of a longitudinal electric field into the eigenmodes of a parallel-plate waveguide, filled with the medium with wave number k and directed vertically with the plates through corners p_1 and p_2 of triangle T . The y -dependence in (4.18) is the exact solution to (4.9) for each term in the sine expansion along x , and is chosen such, that its contribution at $y = y_0$ (and hence at p_3) becomes zero.

The functions $f_{c_2, n}(x, y)$ and $f_{c_3, n}(x, y)$ can be written in a similar way, but it is unnecessary to explicitly write them down in the same coordinate system used for $f_{c_1, n}(x, y)$. Instead, a different set of axes is associated with each side c_i of the triangle. It has corner p_i as its origin, and side c_i as its x -axis. The same triangle in three different orientations and for each of these coordinate systems, is shown in Fig. 4.2.

By this judicious choice of the axes, we only need (4.18) to express the contributions of the parallel-plate waveguides associated with sides c_2 and c_3 , in the sense that

$$f_{c_2, n}(x, y) = f'_{c_1, n}(x', y') \quad (4.19)$$

$$f_{c_3, n}(x, y) = f''_{c_1, n}(x'', y'') \quad (4.20)$$

This means that, e.g., for $f_{c_2, n}(x, y)$, the same form as (4.18) is used, but with x, y, x_0, x_1, y_0 replaced by x', y', x'_0, x'_1, y'_0 , and with $N'_1 = N_2$ terms in the expansion

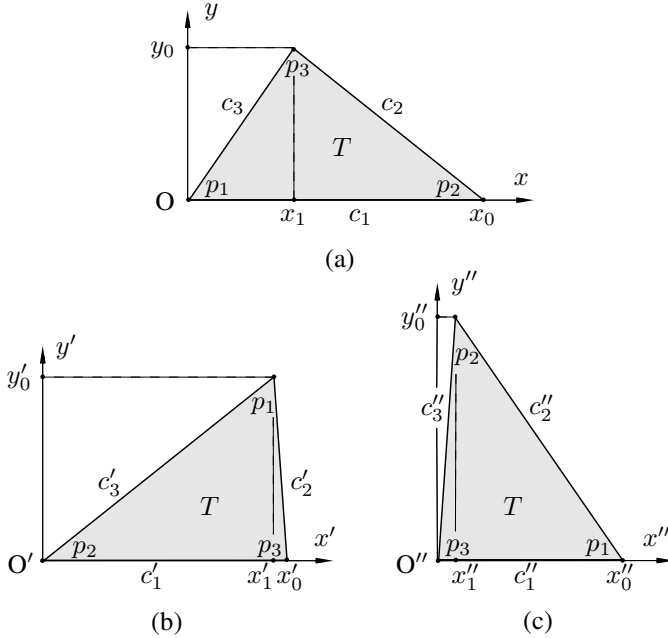


Figure 4.2: Three different axes sets, each associated with a different orientation of triangle T . (a) unprimed, with c_1 underneath, (b) primed, with c_2 underneath ($c_1' = c_2$, $c_2' = c_3$, $c_3' = c_1$), (c) double primed, with c_3 underneath ($c_1'' = c_3$, $c_2'' = c_1$, $c_3'' = c_2$).

of $\psi^{(2)}$.

The sine expansion $\{\sin(n\pi x/x_0)\}$ in (4.18) for $\psi^{(1)}$ forms (theoretically, for $N_1 \rightarrow \infty$) a complete set on c_1 , except for the corner points where all sine functions are zero. This problem and some related issues will be addressed in Section 4.3. An analogous argumentation is valid for $\psi^{(2)}$ and $\psi^{(3)}$. Due to the specific form of (4.15) and (4.18), with a single multiplicative degree of freedom for each basis function $f_{c_1,n}$ (its coefficient $A_{c_1,n}$), $\psi^{(1)}$ is fully determined over the complete triangle, once its boundary value on c_1 is fixed, and so are $\psi^{(2)}$ for side c_2 and $\psi^{(3)}$ for c_3 . It would, alternatively, be possible to determine the coefficients $\tilde{A}_{c_1,n}$ and $\tilde{B}_{c_1,n}$ of only one *complete* set of waveguide modes, written as

$$\tilde{\psi}(x, y) = \sum_{n=1}^{N_1} \left(\tilde{A}_{c_1,n} e^{j\beta_n y} - \tilde{B}_{c_1,n} e^{-j\beta_n y} \right) \sin \frac{n\pi x}{x_0} \quad (4.21)$$

and such that $\tilde{\psi}$, taking the place of ψ in (4.14), satisfies prescribed boundary values on c_1 , c_2 and c_3 (in principle this is only true for $N_1 \rightarrow \infty$). However, our method uses the combination of three sets of expansion functions, which are, on their own, only sufficient to represent a prescribed boundary value on one of the sides, but altogether

on the three sides. Although the introduction of two extra sets of waveguide modes is at first glance unnecessary, our method has the advantage that we can enforce $\psi^{(1)}$ to be zero at p_3 , in this way avoiding the exponential terms in (4.18) to become large (and analogously for $\psi^{(2)}$ and $\psi^{(3)}$). If, instead, (4.21) would be used, the exponential behavior of the parallel-plate waveguide modes in the direction perpendicular to c_1 would lead to ill-conditioning and completely inaccurate results.

As for each boundary excitation there exists a unique solution for the expansion coefficients $A_{c_i,n}$, it should be possible to construct a set of equations that can be solved directly for these coefficients. This procedure needs to be repeated as many times as there are discretization segments, and would lead to very long calculations. Therefore, the authors have opted for an iterative approach to determine the unknown entries of the DtN matrix. This method has two major advantages. First of all, it is possible to construct a very good initial guess to start the iteration (assuming at first there is no interaction between the sides), and furthermore, the iterative method has an exponential convergence behavior (as explained in the sequel), which leads to an accurate solution within a very limited number of iteration steps.

4.2.2 Discretization of ψ_c and Iterative Procedure

The following paragraphs describe the iterative procedure to determine the expansion coefficients $A_{c_i,n}$ of (4.14-4.17), which in the sequel will be called the Iterative Combined Waveguide Modes (ICWM) algorithm. Before giving some more mathematical details, we start with a brief physical description of the method. On each side, the unknown function ψ is first expanded in a set of non-uniform basis functions, typically pulses or hat functions. The complex amplitudes of these functions are collected in a column vector Ψ_c . Next, this representation is recast in the form (4.15-4.18) necessitating the introduction of a mapping matrix W between Ψ_c and the A -coefficients in (4.15-4.17) collected in the column vector A . To be able to determine W , three additional matrix operations are needed, i.e. Q , D and P . D and Q transform the original basis expansion on each side into Fourier series expansions. Then P matrices are defined that project the Fourier series coefficients from one side of the triangle onto another side. These matrices account for the “overlap”, i.e. for the way in which the three sets of parallel-plate waveguide modes influence each other. For a better readability of this text, the explicit form of several of these matrices is not given, but can be found in the Appendix.

The proposed method is based on improving an initial guess for the expansion coefficients, by cycling through the sides until the required accuracy is reached. Suppose we start from side c_1 . The expansion of ψ_{c_1} in sine functions yields a first approximation $\psi^{(1),\langle 1 \rangle}$ for $\psi^{(1)}$. The notation $\langle n \rangle$ will be used to denote a certain value after iteration cycle n . Subtracting the contribution of $\psi^{(1),\langle 1 \rangle}$ on c_2 from the actual boundary value ψ_{c_2} , and expanding this result in sines, i.e., calculating the coeffi-

cients $\{A_{c_2}^{(1)}\}$, yields $\psi^{(2),\langle 1 \rangle}$. For the third side, the contributions of both $\psi^{(1),\langle 1 \rangle}$ and $\psi^{(2),\langle 1 \rangle}$ are subtracted from ψ_{c_3} , before expanding it into sines, yielding $\psi^{(3),\langle 1 \rangle}$. This is the end of the first iteration cycle. From now on, both previous contributions from the expansions on two of the sides to the third side are subtracted from the actual boundary value, and the remainder is expanded into sines. In each iteration cycle, the contribution of the three $\psi^{(i),\langle n \rangle}$ on each of the sides constitute a continually better approximation of the actual boundary value ψ_{c_i} . In Section 4.4, the convergence properties of the method are numerically illustrated. We now first go into some of the mathematical details.

In order to discretize the function ψ on side c_1 , the side is divided into segments, using a number of discretization points x_m , ($m = 1, \dots, M_1 + 1$), with x_1 and x_{M_1+1} the corner points. A uniform distribution of these points along the sides is not required. They can be chosen at will, so as to assure an optimal representation of the continuous function ψ_{c_1} . The normalized discretization points s_m on side c_1 are defined by $x_m = s_m l_1$, and analogously on the other sides. With these, we get for side c_i (with $i = 1, 2, 3$)

$$\psi_{c_i}(s) \simeq \sum_{m=1}^{M_i} \Psi_{c_i,m} t_{c_i,m}(s), \quad 0 \leq s \leq 1. \quad (4.22)$$

The functions $t_{c_i,m}(s)$, with $m = 1, \dots, M_i$, can be a constant pulse on the interval $[s_m, s_{m+1}]$ (corresponding, e.g. on c_1 , to $x \in [x_m, x_{m+1}]$), a piecewise linear ‘hat’ function on $[s_{m-1}, s_{m+1}]$, or any other basis function.

The coefficients $\Psi_{c_i,m}$ are taken together into one column vector Ψ_c as

$$\Psi_c = \begin{bmatrix} \Psi_{c_1} \\ \Psi_{c_2} \\ \Psi_{c_3} \end{bmatrix} \quad (4.23)$$

in which $[\Psi_{c_i}]_m = \Psi_{c_i,m}$. The expansion coefficients $A_{c_i,n}$ from (4.15-4.17) are taken together into column vectors A_{c_i} . The purpose of the ICWM algorithm is the determination of the $N_i \times M$ matrices W_{c_i} (with $M = M_1 + M_2 + M_3$), defined by

$$A_{c_i} = W_{c_i} \Psi_c. \quad (4.24)$$

Once these matrices are known, the expansion (4.14-4.17) is fully determined for any boundary function ψ_c , and $\partial\psi/\partial n$ can be determined from the normal derivative of the functions $f_{c_1,n}$, $f_{c_2,n}$, and $f_{c_3,n}$.

In order to calculate the matrices W_{c_i} , two different types of interactions have to be worked out. On the one hand, we need to transform the coefficients of a discretized function on c_i into its sine expansion. On the other hand, we need to determine the expansion coefficients that result from expanding subfunction $\psi^{(j)}$, but evaluated on side c_i ($i \neq j$), into sines on side c_i .

In order to simplify the notations used in the sequel, some auxiliary functions are defined here, related to the evaluation of $f_{c_1}(x, y)$ and its derivatives on sides c_2 and c_3 .

$$\gamma_n^-(s) \stackrel{\text{def}}{=} \left(e^{j\beta_n y_0(1-s)} - e^{j\beta_n y_0(1+s)} \right) \quad (4.25)$$

$$\gamma_n^+(s) \stackrel{\text{def}}{=} \left(e^{j\beta_n y_0(1-s)} + e^{j\beta_n y_0(1+s)} \right) \quad (4.26)$$

$$\zeta_{2,n}(s) \stackrel{\text{def}}{=} \frac{n\pi}{x_0} (x_0 + s(x_1 - x_0)) \quad (4.27)$$

$$\zeta_{3,n}(s) \stackrel{\text{def}}{=} \frac{n\pi}{x_0} ((1-s)x_1) \quad (4.28)$$

These functions will be used frequently in the sequel, without each time referring to (4.25-4.28), though. For example, $\psi^{(1)}$ evaluated on c_3 can now be compactly written as

$$\psi_{c_3}^{(1)}(s) = \sum_{n=1}^{N_1} A_{c_1,n} \gamma_n^-(s) \sin \zeta_{3,n}(s). \quad (4.29)$$

First, the transformation matrices Q_i and the scaling matrices D_i are defined. They transform the coefficients $\Psi_{c_i,m}^{(i)}$, with the superscript (i) indicating the contribution of $\psi^{(i)}$ only, into its sine expansion coefficients A_{c_i} . The expansion of $\psi^{(1)}$ on side c_1 ,

$$\psi_{c_1}^{(1)}(s) \simeq \sum_{m=1}^{M_1} \Psi_{c_1,m}^{(1)} t_{c_1,m}(s) \quad (4.30)$$

$$\simeq \sum_{n=1}^{N_1} A_{c_1,n} \gamma_n^-(1) \sin n\pi s, \quad (4.31)$$

is weighted with the set $\{2 \sin n\pi s, n = 1, \dots, N_1\}$. Taking the coefficients together in the vectors $\Psi_{c_1}^{(1)}$ and A_{c_1} , leads to

$$Q_1 \Psi_{c_1}^{(1)} = D_1^{-1} A_{c_1} \quad (4.32)$$

with the explicit form of the $N_1 \times M_1$ matrix Q_1 and the $N_1 \times N_1$ diagonal matrix D_1 given in the Appendix.

For the other sides c_2 and c_3 , the primed and double primed quantities can be used, as indicated in (4.19) and (4.20). We schematically write this as

$$Q_2 = Q'_1, \quad D_2 = D'_1, \quad (4.33)$$

$$Q_3 = Q''_1, \quad D_3 = D''_1. \quad (4.34)$$

The expansion matrices P_{ij} are used to calculate the coefficients $C_{c_i,n}^{(j)}$ in the sine

expansion on c_i of subfunction $\psi^{(j)}$, defined by its coefficients $A_{c_j,n}$. Evaluating $\psi^{(1)}$ on c_2 and on c_3 and expanding it into sines on these sides, yields, with (4.11), (4.12), (4.15) and (4.18),

$$\psi_{c_2}^{(1)}(s) \simeq \sum_{n_2=1}^{N_2} C_{c_2,n_2}^{(1)} \sin n_2 \pi s \quad (4.35)$$

$$\simeq \sum_{n_1=1}^{N_1} A_{c_1,n_1} \gamma_{n_1}^-(1-s) \sin \zeta_{2,n_1}(s) \quad (4.36)$$

$$\psi_{c_3}^{(1)}(s) \simeq \sum_{n_3=1}^{N_3} C_{c_3,n_3}^{(1)} \sin n_3 \pi s \quad (4.37)$$

$$\simeq \sum_{n_1=1}^{N_1} A_{c_1,n_1} \gamma_{n_1}^-(s) \sin \zeta_{3,n_1}(s). \quad (4.38)$$

Weighting (4.35) and (4.36) with the set $\{2 \sin n_2 \pi s\}$, and (4.37) and (4.38) with the set $\{2 \sin n_3 \pi s\}$, yields

$$C_{c_2}^{(1)} = P_{21} A_{c_1} \quad (4.39)$$

$$C_{c_3}^{(1)} = P_{31} A_{c_1} \quad (4.40)$$

with the $N_2 \times N_1$ matrix P_{21} and the $N_3 \times N_1$ matrix P_{31} specified in the Appendix.

Performing the same operations for the rotated geometries shown in Fig. 4.2 (b) and (c), leads to the other required matrices

$$P_{12} = P'_{31}, \quad P_{32} = P'_{21} \quad (4.41)$$

$$P_{13} = P''_{21}, \quad P_{23} = P''_{31}. \quad (4.42)$$

The ICWM procedure as outlined above is an iterative procedure to determine the W_{c_i} matrices. Initially, all three matrices are supposed zero. We now describe cycle n of the iteration. Suppose after $n-1$ iteration cycles, we want to determine the coefficients $A_{c_1}^{\langle n \rangle}$ from $A_{c_2}^{\langle n-1 \rangle}$ and $A_{c_3}^{\langle n-1 \rangle}$. Evaluation of (4.14) with the l.h.s. discretized using (4.22), evaluated on c_1 with (4.10), and with the insertion of expansion (4.15) and (4.18), gives

$$\begin{aligned} & \sum_{m=1}^{M_1} \Psi_{c_1,m} t_{c_1,m}(s) - (\psi_{c_1}^{(2),\langle n-1 \rangle} + \psi_{c_1}^{(3),\langle n-1 \rangle}) \\ &= \sum_{n=1}^{N_1} A_{c_1,n}^{\langle n \rangle} \gamma_n^-(1) \sin n \pi s. \end{aligned} \quad (4.43)$$

Weighting (4.43) with the set $\{2 \sin n\pi s\}$ yields

$$Q_1 \Psi_{c_1} - (C_{c_1}^{(2),\langle n-1 \rangle} + C_{c_1}^{(3),\langle n-1 \rangle}) = D_1^{-1} A_{c_1}^{\langle n \rangle}. \quad (4.44)$$

The analogous relationships as (4.39), but involving P_{12} and P_{13} , allow to write (4.44) as

$$A_{c_1}^{\langle n \rangle} = D_1 (Q_1 \Psi_{c_1} - P_{12} A_{c_2}^{\langle n-1 \rangle} - P_{13} A_{c_3}^{\langle n-1 \rangle}). \quad (4.45)$$

Define the matrix

$$\tilde{Q}_1 = [Q_1, 0_{N_1 \times M_2}, 0_{N_1 \times M_3}], \quad (4.46)$$

using the notation $0_{N_i \times M_j}$ for a $N_i \times M_j$ zero matrix. Inserting the relationships (4.24) leads from (4.45) to

$$W_{c_1}^{\langle n \rangle} = D_1 (\tilde{Q}_1 - P_{12} W_{c_2}^{\langle n-1 \rangle} - P_{13} W_{c_3}^{\langle n-1 \rangle}). \quad (4.47)$$

Analogous calculations show that

$$W_{c_2}^{\langle n \rangle} = D_2 (\tilde{Q}_2 - P_{21} W_{c_1}^{\langle n \rangle} - P_{23} W_{c_3}^{\langle n-1 \rangle}) \quad (4.48)$$

$$W_{c_3}^{\langle n \rangle} = D_3 (\tilde{Q}_3 - P_{31} W_{c_1}^{\langle n \rangle} - P_{32} W_{c_2}^{\langle n \rangle}) \quad (4.49)$$

with

$$D_2 = D'_1, \quad \tilde{Q}_2 = [0_{N_2 \times M_1}, Q_2, 0_{N_2 \times M_3}] \quad (4.50)$$

$$D_3 = D''_1, \quad \tilde{Q}_3 = [0_{N_3 \times M_1}, 0_{N_3 \times M_2}, Q_3]. \quad (4.51)$$

The update equations (4.47), (4.48) and (4.49) form the core of the n 'th iteration cycle of the ICWM procedure.

4.2.3 Normal Derivative Calculation

The outward pointing normal derivative $\partial \psi_c / \partial n$ is discretized on side i as

$$\frac{\partial \psi_{c_i}(s)}{\partial n} \simeq \sum_{m=1}^{M_i} \Gamma_{c_i, m} t_{c_i, m}(s). \quad (4.52)$$

The purpose is to determine the $\Gamma_{c_i, m}$ coefficients, taken together per side i into the vector Γ_{c_i} , such that

$$\Gamma_{c_i} = \sum_{j=1}^3 \Gamma_{c_i}^{(j)} = \sum_{j=1}^3 T_{ij} A_{c_j} \quad (4.53)$$

in which $\Gamma_{c_i}^{(j)}$ contains the coefficients $\Gamma_{c_i}^{(j)}$ in the contribution from $\psi^{(j)}$ to the total normal derivative on c_i . Hence, with (4.24) and by grouping the vectors Γ_{c_i} into Γ_c ,

we find

$$\Gamma_c = D \Psi_c \quad (4.54)$$

with

$$D = \begin{bmatrix} T_{11} W_{c_1} + T_{12} W_{c_2} + T_{13} W_{c_3} \\ T_{21} W_{c_1} + T_{22} W_{c_2} + T_{23} W_{c_3} \\ T_{31} W_{c_1} + T_{32} W_{c_2} + T_{33} W_{c_3} \end{bmatrix} \quad (4.55)$$

which is the discretized form of (4.8), i.e., the matrix-representation of the DtN operator, mapping ψ_c onto $\partial\psi_c/\partial n$. The matrices T_{ij} are determined by calculating the outward normal derivative of $\psi^{(j)}$ on side c_i , and weighting the result with the basis functions $t_{c_i}(s)$ along that side. On c_1 , $\partial\psi^{(1)}/\partial n$ is written as

$$\frac{\partial\psi_{c_1}^{(1)}(s)}{\partial n} \simeq \sum_{m=1}^{M_1} \Gamma_{c_1,m}^{(1)} t_{c_1,m}(s) \quad (4.56)$$

$$\simeq - \sum_{n=1}^{N_1} A_{c_1,n} j\beta_n \gamma_n^+(1) \sin n\pi s \quad (4.57)$$

and leads to

$$\Gamma_{c_1}^{(1)} = T_{11} A_{c_1}. \quad (4.58)$$

On c_2 , the normal derivative of $\psi^{(1)}$ becomes, with (4.13),

$$\frac{\partial\psi_{c_2}^{(1)}(s)}{\partial n} = \mathbf{u}_2 \cdot [\nabla\psi^{(1)}]_{c_2} \quad (4.59)$$

$$\simeq \sum_{m=1}^{M_2} \Gamma_{c_2,m}^{(1)} t_{c_2,m}(s) \quad (4.60)$$

$$\begin{aligned} &\simeq \sum_{n=1}^{N_1} A_{c_1,n} \left(\frac{y_0}{l_2} \gamma_n^-(1-s) \frac{n\pi}{x_0} \cos \zeta_{2,n}(s) \right. \\ &\quad \left. + \frac{x_0 - x_1}{l_2} j\beta_n \gamma_n^+(1-s) \sin \zeta_{2,n}(s) \right). \end{aligned} \quad (4.61)$$

Weighting (4.60) and (4.61) with the basis functions $t_{c_2,m}(s)$ on c_2 leads to

$$\Gamma_{c_2}^{(1)} = T_{21} A_{c_1}. \quad (4.62)$$

Analogously, $\partial\psi_{c_3}^{(1)}/\partial n$ becomes

$$\frac{\partial\psi_{c_3}^{(1)}(s)}{\partial n} = \mathbf{u}_3 \cdot [\nabla\psi^{(1)}]_{c_3} \quad (4.63)$$

$$\simeq \sum_{m=1}^{M_3} \Gamma_{c_3,m}^{(1)} t_{c_3,m}(s) \quad (4.64)$$

$$\begin{aligned} &\simeq \sum_{n=1}^{N_1} A_{c_1,n} \left(-\frac{y_0}{l_3} \gamma_n^-(s) \frac{n\pi}{x_0} \cos \zeta_{3,n}(s) \right. \\ &\quad \left. + \frac{x_1}{l_3} j\beta_n \gamma_n^+(s) \sin \zeta_{3,n}(s) \right) \end{aligned} \quad (4.65)$$

and leads to

$$\Gamma_{c_3}^{(1)} = T_{31} A_{c_1}. \quad (4.66)$$

The $M_i \times N_1$ matrices T_{i1} are defined in the Appendix. For the remaining T_{ij} matrices, we can immediately write

$$T_{12} = T'_{31}, \quad T_{22} = T'_{11}, \quad T_{32} = T'_{21} \quad (4.67)$$

$$T_{13} = T''_{21}, \quad T_{23} = T''_{31}, \quad T_{33} = T''_{11}. \quad (4.68)$$

4.3 Elimination of the Gibbs Effect

For the non-differential DtN operator as defined by (4.8), the Gibbs phenomena at the corners of the triangle are considerable, due to the expansion functions $f_{c_i,n}$ which are zero in the corner points, and hence not apt to represent a non-zero corner value.

As will become clear in Section 4.4 from the numerical data, this Gibbs phenomenon corrupts the solution along the complete boundary. An accurate elimination of the Gibbs effect is therefore required for an arbitrary value of k^2 . The solution for the Gibbs effect presented in [11] for a rectangular cross-section, only deals with $k^2 = 0$. Below, a generalization is presented. This generalization is only valid provided the boundary value of ψ_c is continuous, but this is indeed the case, both for the scalar electric potential and for the longitudinal electric field.

The DtN operator (4.55) is only correct provided all corner values are zero. A function satisfying this requirement is obtained by subtracting from ψ three analytically known functions $\hat{\psi}^{p_i}$, that satisfy (4.9), have a non-zero corner value at p_i , and are zero on the other corners. We start at corner p_1 . The proposed function $\hat{\psi}^{p_1}$ is defined by

$$\hat{\psi}^{p_1}(x, y) = \hat{\alpha}^{p_1} \cos \frac{\pi x}{2x_0} \left(e^{j\hat{\beta}y} - e^{j\hat{\beta}(2y_0-y)} \right), \quad (4.69)$$

with $\hat{\beta}^2 = k^2 - (\pi/2x_0)^2$. It reaches its maximal amplitude at p_1 , and is, as required,

zero at p_2 and p_3 . Analogous functions are defined, associated with p_2 and p_3 . We now have to determine a matrix \hat{D}^{p_1} , which transforms Ψ_c into the normal derivative of $\hat{\psi}^{p_1}$, with a correctly determined coefficient $\hat{\alpha}^{p_1}$. Secondly, a matrix \hat{R}^{p_1} is needed, to reduce the original boundary coefficients Ψ_c to those without the contribution of $\hat{\psi}^{p_1}$. The same argumentation can be followed to treat corners p_2 and p_3 , with the introduction of analogous matrices. This results in

$$\Gamma_c = D_{\text{tot}} \Psi_c \quad (4.70)$$

with

$$D_{\text{tot}} = \left(D \hat{R}^{p_3} \hat{R}^{p_2} \hat{R}^{p_1} + \hat{D}^{p_3} \hat{R}^{p_2} \hat{R}^{p_1} + \hat{D}^{p_2} \hat{R}^{p_1} + \hat{D}^{p_1} \right) \quad (4.71)$$

Compared to the original discretized form D (4.55) of the DtN operator, D_{tot} is its modified form which does no longer suffer from the Gibbs phenomenon. The expressions for \hat{D}^{p_i} and \hat{R}^{p_i} ($i = 1, 2, 3$) can be found in the Appendix.

4.4 Numerical Results

A few numerical simulations are presented, to investigate the convergence and accuracy properties of the method, including an illustration of the effectiveness of the Gibbs phenomenon elimination as described in Section 4.3. In a few further examples, the inductive and resistive behavior of trapezoidal conductors is investigated. All simulations were done with a uniform, piecewise constant approximation of the longitudinal electric field on the triangles, except for the last one, where we used a piecewise linear discretization on the boundaries.

4.4.1 Numerical Accuracy and Convergence Properties

In order to illustrate the effectiveness of the method described in Section 4.3 to eliminate the Gibbs effect at the triangles' corners, we compare the normal derivative $\partial\psi/\partial n$ of a function $\psi(x, y)$, along the boundary of a triangle T_1 without and with the use of the correction formula (4.71) instead of (4.55).

Triangle T_1 is shown in the inset of Fig. 4.3 (a), and has side lengths of, respectively, $c_1 = 4$ mm and $c_2 = c_3 = 2.5$ mm. The boundary value ψ_c is chosen to be continuous along its boundary, and linear on each side, with corner values $\psi_{p_1} = 0$, $\psi_{p_2} = -1$, and $\psi_{p_3} = 1$. For a high resolution of the displayed results along the boundary, the number of discretization intervals is chosen to be 300 along c_1 , and 188 along c_2 and c_3 . Obviously, for most applications the results will be accurate enough with a coarser discretization. The number of sine functions used along each side amounts to 400 along c_1 , and 250 along c_2 and c_3 .

Fig. 4.3 (a) displays the results for the dielectric case (neglecting the displacement currents in the quasi-TM case), with ψ satisfying Laplace's equation in T_1 . Without the Gibbs effect compensation, i.e., using only (4.55), the oscillations are huge and not even restricted to the corner areas. Note that corner p_1 does not introduce any Gibbs effect, because ψ_c is exactly zero at p_1 . With (4.71), the numerical result is almost indistinguishable from the exact $\partial\psi/\partial n$, namely -1000 on c_1 , 650 on c_2 and 950 on c_3 . An analogous comparison is made in Fig. 4.3 (b), for the same boundary value ψ_c , but with ψ satisfying the diffusion equation (4.4) in T_1 , for a conductivity $\sigma = 57.2 \text{ MS/m}$ and at 100 kHz . The Gibbs effect is especially strong near the corners now, but again totally eliminated by using (4.71).

A peculiarity of the results in Fig. 4.3 (b) is the behavior near the corners. This is worth some additional comments, given its general validity and importance for the high-frequency current distribution near an edge. At 100 kHz , the skin depth $\delta \approx 0.21 \text{ mm}$. Based on a local plane wave approximation, ψ will be exponentially damped, proportional to $e^{-n/\delta}$, with n the coordinate in the normal direction n from a boundary point p towards the inside of the triangle. This approximation does not hold, if the distance along n to the opposite side is smaller than a few times the skin depth. If, e.g., p lays on c_1 at a distance $\delta/2$ from the corner point p_2 , then the distance from p to the adjacent side c_2 (in the normal direction with respect to c_1) is $3\delta/8$ (for a corner of 36.9°). If p starts to approach p_2 even closer, the diffusion term no longer plays a role, and we should therefore get the same result as in Fig. 4.3 (a). The boundary interval of length δ centered around p_2 is indicated by the dashed vertical lines in Fig. 4.3 (b). The normal derivative $\partial\psi/\partial n$ in this interval is indeed very similar to the corresponding solution of Fig. 4.3 (a), indicated in dash-dot lines. This phenomenon is clearly visible for the sharp corners p_1 and p_2 . For the obtuse corner p_3 however, this is not the case. The reason for that is, that for any boundary point p close to p_3 , the diffusion term still plays a role, because in the normal direction, the adjacent side is not reached, let alone that this distance becomes $\ll \delta$ near the corner¹.

In a second numerical experiment, the convergence of the iterative method is investigated. As explained in Section 4.2.3, the normal derivative $\partial\psi/\partial n$ is determined analytically from the expansion of ψ itself. The correctness of $\partial\psi/\partial n$ is hence limited by the accuracy of the expansion of ψ in T_1 and more specifically on its boundary, as each term in the expansion exactly satisfies the governing equation (4.9) inside T_1 . Therefore, it is investigated how the boundary value $\psi_c^{(n)}$ of the expansion after n iteration steps becomes a better approximation of the exact ψ_c for increasing n . Again consider the function $\psi(x, y)$ over triangle T_1 , but now with a constant boundary value $\psi_c = \psi_0$. Fig. 4.4 displays the relative error of $\psi_c^{(n)}$ with respect to ψ_0 , for (a) ψ satisfying Laplace's equation, and (b) the diffusion equation, as in Fig. 4.3. As for $\partial\psi/\partial n$,

¹This important phenomenon plays a major role in the so-called *edge effect*, which has a noticeable influence on the circuit characteristics of the considered lines. The edge effect is therefore investigated in detail in Chapter 5, on the one hand by means of a series expansion of the fields near a wedge, and on the other hand, using the ICWM algorithm.

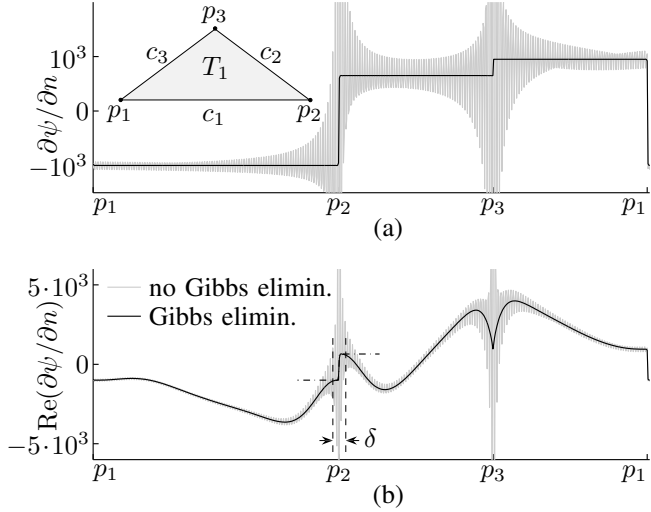


Figure 4.3: Normal derivative $\partial\psi/\partial n$ along the boundary of triangle T_1 (see inset of (a), $c_1 = 4$ mm, $c_2 = c_3 = 2.5$ mm) both without and with elimination of the Gibbs effect, for ψ linear along the sides of T_1 , and with $\psi_{p_1} = 0$, $\psi_{p_2} = -1$, $\psi_{p_3} = 1$. The simulations were performed at 100 kHz, for (a) T_1 as a dielectric, and (b) T_1 as a conductor with $\sigma = 57.2$ MS/m, with only $\text{Re}(\partial\psi/\partial n)$ shown.

the Gibbs effect in the calculation of ψ_c is taken care of by subtracting an analytical part with the same corner values as ψ_c , and then using the matrices $W_{c_1}^{(n)}$, $W_{c_2}^{(n)}$, and $W_{c_3}^{(n)}$ to calculate the expansion coefficients for the sine expansions on each side of the remaining part of ψ , which now has zero corner values.

It is clearly visible in both Fig. 4.4 (a) and (b) that the error rapidly decreases with each iteration step. After a certain number of iteration steps (about 8 in this case, and earlier on side c_2 and c_3), the relative error will no longer further decrease (but is already much smaller than 1/1000). This is not due to the limited accuracy of the expansion coefficients, as will be shown in a further numerical experiment. It is caused by the limited accuracy in the estimation of the corner values of ψ , that are further processed for Gibbs effect elimination.

The convergence behavior of the iterative procedure to find the expansion of ψ depends much stronger on the triangle's shape than on the diffusion coefficient k^2 in (4.9). It is expected that the scheme converges slower, the sharper a corner of the triangle becomes, due to the increased interaction between the corresponding adjacent sides. Consider the triangular conductor T_2 (shown in the inset of Fig. 4.5), with conductivity $\sigma = 57.2$ MS/m., and at 100 kHz. The area of the isosceles triangle T_2 is kept to 1 mm², whereas the top angle is varied from 60° to 3.75°. The convergence of matrix $W_{c_2}^{(n)}$ is presented in Fig. 4.5 by means of the normalized Frobenius norm

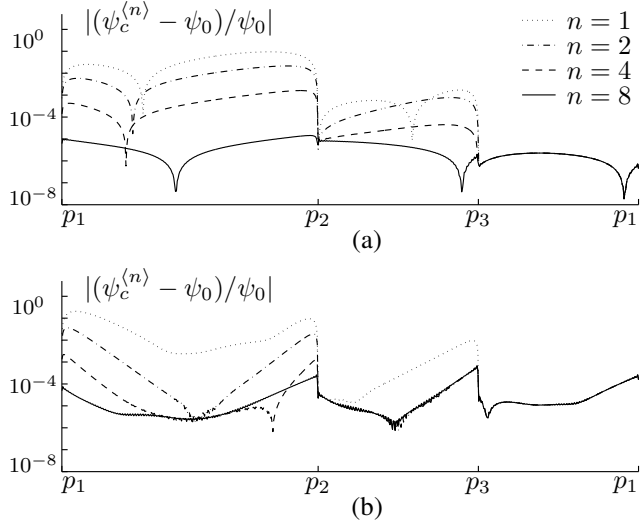


Figure 4.4: Relative error after n iterations, in the estimation $\psi_c^{(n)}$ of a constant boundary value $\psi_c = \psi_0$, for triangle T_1 (see Fig. 4.3 (a)). The simulations were performed at 100 kHz, for (a) T_1 as a dielectric, and (b) T_1 as a conductor with $\sigma = 57.2$ MS/m.

of the difference between two consecutive matrices $W_{c_2}^{(n-1)}$ and $W_{c_2}^{(n)}$, i.e., by

$$\frac{\|W_{c_2}^{(n)} - W_{c_2}^{(n-1)}\|}{\|W_{c_2}^{(n)}\|} = \frac{\sqrt{\sum_{i,j} \left| [W_{c_2}^{(n)}]_{i,j} - [W_{c_2}^{(n-1)}]_{i,j} \right|^2}}{\sqrt{\sum_{i,j} \left| [W_{c_2}^{(n)}]_{i,j} \right|^2}} \quad (4.72)$$

For $\alpha = 60^\circ$, the accuracy is only limited by the floating point precision within less than 20 iteration steps. The smaller α becomes, the slower the iterative procedure converges, but even for $\alpha = 3.75^\circ$ the difference between steps $n-1$ and n decreases exponentially. In this example we used 228 parallel-plate waveguide modes per side.

After these convincing examples of the convergence behavior of the ICWM algorithm, the authors would like to add a few comments to indicate that the scheme will *always* converge. This is indeed the case, at least within the validity range of the quasi-TM analysis. The reason is, that $\text{Re}(j\beta_n)$, with β_n defined as for (4.18), is strictly negative. The function $f_{c_1,n}$ will consequently only have a small contribution to sides c_2 and c_3 , compared to its function value on c_1 . Generally speaking, a correction of the coefficients $A_{c_i,n}$ of the functions $f_{c_i,n}$ of side c_i will result in a smaller required correction of the coefficients $A_{c_j,n}$ on the other sides c_j ($j \neq i$), due to the fact, mentioned above, that $f_{c_i,n}$ has only an exponentially small contribution on the other sides c_j ($j \neq i$). As this is true for all sides $i = 1, 2, 3$, the iterative procedure

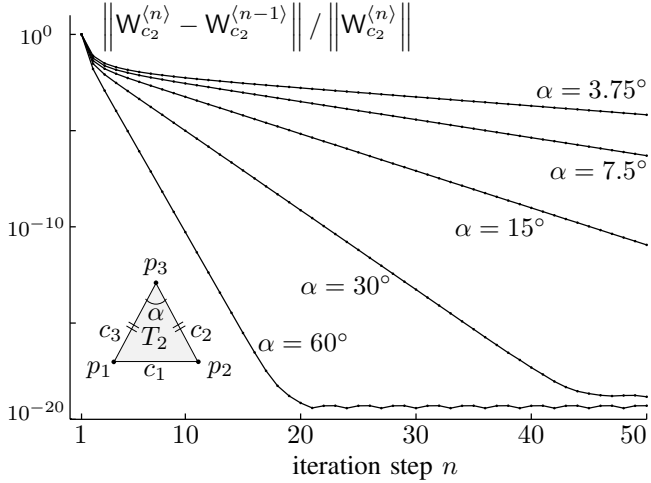


Figure 4.5: Convergence behavior of matrix $W_{c2}^{(n)}$ as a function of the number of iteration steps n for the isosceles triangle T_2 with surface 1 mm^2 (see inset). Simulations were performed at 100 kHz and with $\sigma = 57.2 \text{ MS/m}$.

can be expected to converge exponentially and this is what is indeed observed numerically. This explains why, even within the first iteration cycle $n = 1$ on Fig. 4.4, the approximation of ψ on the boundary will be better on side c_3 than on side c_2 , which in turn is better than on c_1 .

A more rigorous convergence analysis could be carried out by investigating the behavior of the matrices P_{ij} , or by considering the contribution of one expansion function $f_{c1,n}$ on sides c_2 and c_3 , for the case of the highest possible coupling with side c_1 (in other words, for the slowest exponential decrease of $f_{c1,n}$). This ‘worst case scenario’ is found for the *first order mode* $f_{c1,1}$, for a *dielectric* material (with $k^2 = 0$ within the quasi-TM approximation), and for *sharp corners* adjacent to c_1 . Even if the exponential decline is slow and can be approximated by a linear function, the contribution of $f_{c1,1}$ to c_2 and c_3 will still remain small enough to ensure a good convergence, because its function value is forced to zero on p_3 .

4.4.2 Characterization of a Single Conductor

As a verification of the surface admittance matrix for triangles, the p.u.l. resistance of a square copper conductor composed of two triangles is simulated, and compared to data available in literature [7]. The conductor is placed in free space, and has a side length of 4.62 mm and a conductivity $\sigma = 57.2 \text{ MS/m}$. The result is shown in Fig. 4.6. Exactly the same resistance is obtained with the square conductor composed of two triangles, as the result from [7], determined with the surface admittance matrix of the square. To investigate the influence of the conductor’s shape, the resistance of a

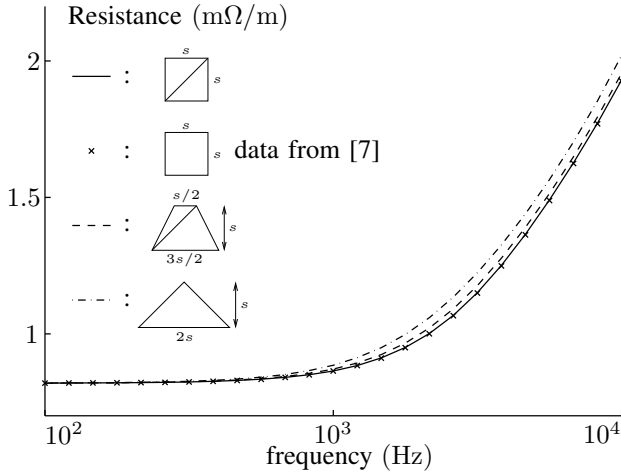


Figure 4.6: Resistance ($\text{m}\Omega/\text{m}$) for a square copper conductor ($s = 4.62 \text{ mm}$, $\sigma = 57.2 \text{ MS/m}$) formed by two triangles (solid line) vs. the result from [7] (in x-markers), and compared to a trapezoid (dashed line) and a triangle (dash-dot line) with the same area.

trapezoid (composed of two triangles, shown in the legend of Fig. 4.6) and a triangular conductor are shown in Fig. 4.6 as well. All conductors have the same area, and hence exactly the same low-frequency resistance. At 10 kHz, the skin depth δ in copper is about 0.665 mm, and the major part of the current flows within a layer with thickness δ underneath the surface. One would therefore expect a resistance, roughly inversely proportional to the circumference, but this is not yet the case within the investigated frequency range. The trapzoid's circumference $L = (2 + \sqrt{5})s$ is higher than the square's ($L = 4s$), yet the latter one has the lowest high-frequency resistance. A similar effect is noticeable for the triangular conductor, with $L = (2 + \sqrt{8})s$ and a still higher resistance. The reason is that the *effective* length of the skin layer where the current flows, is shortened due to the corner effect at the sharp corners. It is expected that at still higher frequencies, the corner effect becomes less pronounced. A fully detailed investigation of the field behavior at the corners is investigated in the next chapter.

4.4.3 Multiconductor Line with Trapezoidal Conductors

In a next numerical example, the inductive and resistive characteristics of a multiconductor line are investigated. The purpose is to get a better understanding of the (coupling) behavior of trapezoidal conductors, rather than to simulate a more realistic structure, with a substrate. The structure under investigation is shown in Fig. 4.7 and consists of two line pairs (1 – 2 and 3 – 4), with an opposite orientation with respect to the nearby perfect electric conducting (PEC) ground plane. All conductors have the

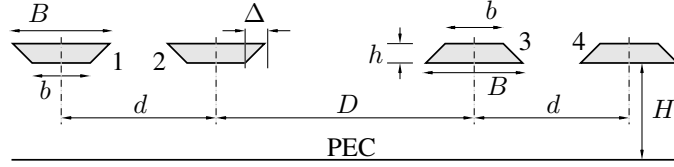


Figure 4.7: Structure with 4 trapezoidal copper conductors ($\sigma = 57.2 \text{ MS/m}$) above a PEC ground plane (shown *on scale*). Dimensions are $B = 1.5$, $b = 0.9$, $h = 0.3$, $\Delta = 0.3$, $d = 2.4$, $D = 4$, and $H = 1.5$, all in millimetres.

conductivity of copper, $\sigma = 57.2 \text{ MS/m}$, and the dimensions are indicated in Fig. 4.7.

The resistance matrix R and the inductance matrix L of the structure are determined over a frequency range from 1 kHz (at with the skin depth $\delta \approx 2 \text{ mm}$), up to 100 MHz (where $\delta \approx 0.0067 \text{ mm}$). The configuration of Fig. 4.7 is compared to an analogous configuration with rectangular conductors with the same area (with height h , width $(b + B)/2$, separated by the same distances d , resp. D , and on the same height H above the ground plane). The results for the trapezoidal conductors are presented in Fig. 4.8 with full lines, whereas dashed lines are used for the rectangular conductor case. resistance- and inductance-values pertaining to the rectangular case will be denoted by \hat{R} and \hat{L} .

Fig. 4.8 (a) displays the self inductance elements L_{11} , \hat{L}_{11} , L_{44} and \hat{L}_{44} , and the resistance elements R_{11} , \hat{R}_{11} , R_{44} and \hat{R}_{44} . At the lowest frequencies, there is no difference between the resistance elements (as all conductors have the same area), but towards the higher frequencies, the trapezoidal conductors display a higher resistance, in accordance with the result from Fig. 4.6, except for the highest simulated frequencies, for which the corner effect becomes negligible. The difference between the self-inductance elements are the result of the detailed current distribution in the conductors which are influenced by the corner behavior which is clearly different for sharp and obtuse corners, by the position of these corners w.r.t. the ground plane, and by the proximity effect of the corners. The inductance values for the respective configurations but with perfect electric conductors, are indicated as well (with the superscript *PEC*). A good convergence to this limit is observed for the high-frequency inductance of the copper lines.

Fig. 4.8 (b) shows the inductive and resistive coupling between lines 1 and 2, respectively, 3 and 4, again compared with the rectangular conductor case. The mutual resistance elements are negative, but very small with respect to the resistance elements shown in (a), such that the resistance matrix remains positive-definite. The mutual inductance elements are important, due to the close vicinity of the conductors.

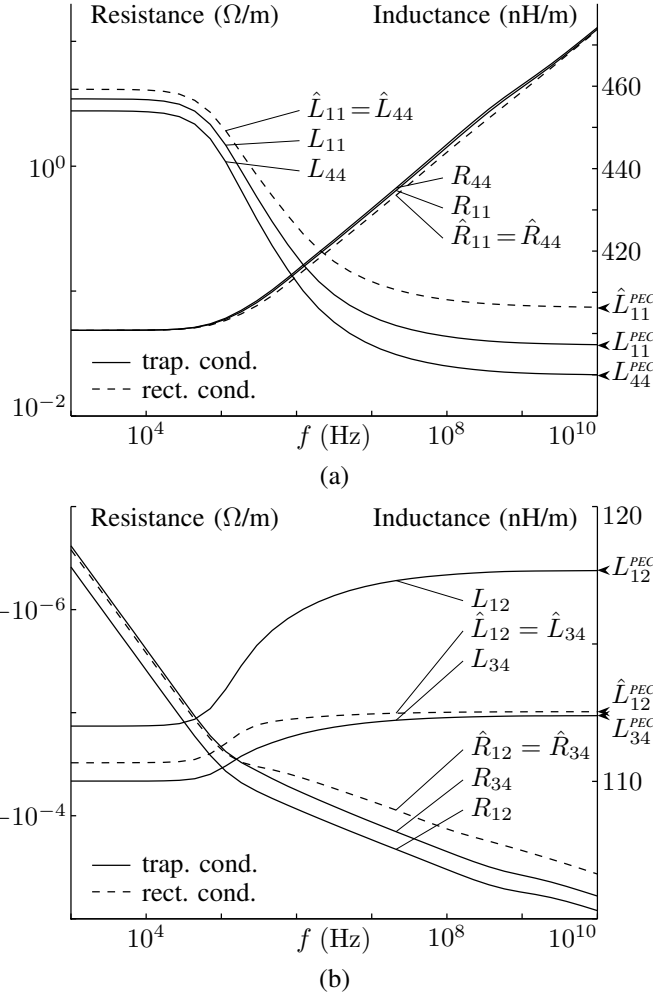


Figure 4.8: Elements of the resistance matrix \mathbf{R} and inductance matrix \mathbf{L} for the configuration of Fig. 4.7. Full lines, with trapezoidal conductors; dashed lines, with rectangular conductors. (a) self-inductance and resistance, (b) coupling between the lines of each signal pair (1 – 2, and 3 – 4).

4.4.4 Micromachined Coplanar Waveguide

The final presented example treats the coplanar waveguide (CPW) structure shown in Fig. 4.9. As a result of the etching process during the manufacturing of the CPW, the silicon substrate material ($\epsilon_r = 11.7$) is partly removed underneath the separation between the signal line and the reference conductors. The structure was taken from [10], where it was simulated for PEC conductors. The characteristic impedance of the line

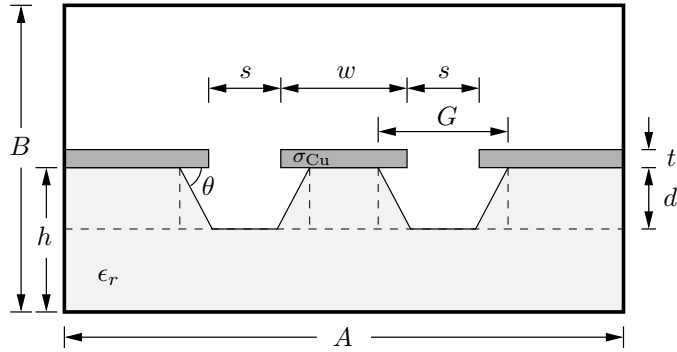


Figure 4.9: Coplanar waveguide structure, enclosed by a PEC box (not shown *on scale*). The dimensions are $A = 320$, $B = 500$, $h = 300$, $w = 50$, $s = 45$, $t = 1$, all in micrometers. Furthermore, $\theta = 54.7^\circ$, $\epsilon_r = 11.7$, and $\sigma_{\text{Cu}} = 57.2 \text{ MS/m}$.

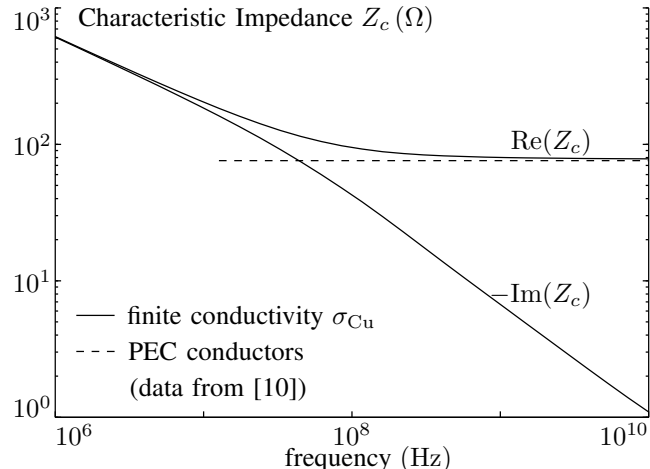


Figure 4.10: The characteristic impedance Z_c of the structure shown in Fig. 4.9.

for the copper conductor case ($\sigma_{\text{Cu}} = 57.2 \text{ MS/m}$) is shown Fig. 4.10, and at the highest frequencies approaches the PEC limit obtained from [10]. As claimed in the Introduction, this example shows that the DtN operator combined with the integral equation techniques of [6] can handle non-planar substrates including very thin conducting slabs. The dashed lines shown on the substrate in Fig. 4.9 denote its division in subregions for which the DtN operator is determined separately, i.e., 4 rectangles and 3 triangles. Of course, it was also necessary to determine the DtN operator for the three rectangular copper conductors.

4.5 Conclusion

The presented Iterative Combined Waveguide Modes algorithm leads to the Dirichlet to Neumann operator for an arbitrary triangle, which can be used to calculate the multi-conductor transmission line parameters for polygonal conductor structures. The iterative method has good convergence properties and is accurate over a broad frequency range. As an illustration, the inductive and resistive behavior of trapezoidal conductors is investigated in a few numerical examples.

Appendix

This Appendix displays the explicit forms of the relevant expansion matrices, in the order of their introduction in Sections 4.2 and 4.3.

Submatrices Related to Expanding ψ over Triangle T

$$[Q_1]_{n,m} = 2 \int_0^1 (\sin n\pi s) t_{c_1,m}(s) ds \quad (4.73)$$

$$[D_1]_{n,n} = (\gamma_n^-(1))^{-1} \quad (\text{diagonal}) \quad (4.74)$$

$$\begin{aligned} [P_{21}]_{n_2,n_1} &= -4j \frac{x_0 - x_1}{x_0} \frac{\beta_{n_1}}{y_0} \frac{n_1\pi}{y_0} \frac{n_2\pi}{y_0} (-1)^{n_1} \\ &\times \left(2e^{j\beta_{n_1}y_0} (-1)^{n_1+n_2} \cos\left(\frac{n_1\pi x_1}{x_0}\right) - \gamma_{n_1}^+(1) \right) \\ &\times \left(\left(\frac{\pi}{y_0}\right)^2 \left(n_2 + n_1 \frac{x_0 - x_1}{x_0}\right)^2 - \beta_{n_1}^2 \right)^{-1} \\ &\times \left(\left(\frac{\pi}{y_0}\right)^2 \left(n_2 - n_1 \frac{x_0 - x_1}{x_0}\right)^2 - \beta_{n_1}^2 \right)^{-1} \end{aligned} \quad (4.75)$$

$$\begin{aligned} [P_{31}]_{n_3,n_1} &= -4j \frac{x_1}{x_0} \frac{\beta_{n_1}}{y_0} \frac{n_1\pi}{y_0} \frac{n_3\pi}{y_0} \\ &\times \left(2e^{j\beta_{n_1}y_0} \cos\left(\frac{n_1\pi x_1}{x_0}\right) - (-1)^{n_3} \gamma_{n_1}^+(1) \right) \\ &\times \left(\left(\frac{\pi}{y_0}\right)^2 \left(n_3 + n_1 \frac{x_1}{x_0}\right)^2 - \beta_{n_1}^2 \right)^{-1} \\ &\times \left(\left(\frac{\pi}{y_0}\right)^2 \left(n_3 - n_1 \frac{x_1}{x_0}\right)^2 - \beta_{n_1}^2 \right)^{-1} \end{aligned} \quad (4.76)$$

Submatrices Related to $\partial\psi/\partial n$

For the definition of T_{11} , the auxiliary matrices B_1 ($M_1 \times M_1$) and \tilde{T}_{11} ($M_1 \times N_1$) are defined as

$$[B_1]_{\tilde{m},m} = \int_0^1 t_{c_1,\tilde{m}}(s) t_{c_1,m}(s) ds \quad (4.77)$$

$$[\tilde{T}_{11}]_{\tilde{m},n} = -j\beta_n \gamma_n^+(1) \int_0^1 (\sin n\pi s) t_{c_1,\tilde{m}}(s) ds \quad (4.78)$$

and with these,

$$T_{11} = B_1^{-1} \tilde{T}_{11}. \quad (4.79)$$

With $B_2 = B'_1$ and $B_3 = B''_1$ we find

$$T_{21} = B_2^{-1} \tilde{T}_{21} \quad (4.80)$$

$$T_{31} = B_3^{-1} \tilde{T}_{31}, \quad (4.81)$$

with the $M_2 \times N_1$ matrix \tilde{T}_{21} and the $M_3 \times N_1$ matrix \tilde{T}_{31} defined as

$$\begin{aligned} [\tilde{T}_{21}]_{\tilde{m},n} &= \int_0^1 \left(\frac{y_0}{l_2} \gamma_n^-(1-s) \frac{n\pi}{x_0} \cos \zeta_{2,n}(s) \right. \\ &\quad \left. + \frac{x_0 - x_1}{l_2} j\beta_n \gamma_n^+(1-s) \sin \zeta_{2,n}(s) \right) t_{c_2,\tilde{m}}(s) ds \end{aligned} \quad (4.82)$$

$$\begin{aligned} [\tilde{T}_{31}]_{\tilde{m},n} &= \int_0^1 \left(-\frac{y_0}{l_3} \gamma_n^-(s) \frac{n\pi}{x_0} \cos \zeta_{3,n}(s) \right. \\ &\quad \left. + \frac{x_1}{l_3} j\beta_n \gamma_n^+(s) \sin \zeta_{3,n}(s) \right) t_{c_3,\tilde{m}}(s) ds \end{aligned} \quad (4.83)$$

Submatrices Related to the Gibbs Effect Elimination

The following functions are introduced

$$\hat{\gamma}^-(s) \stackrel{\text{def}}{=} \left(e^{j\hat{\beta}y_0(1-s)} - e^{j\hat{\beta}y_0(1+s)} \right) \quad (4.84)$$

$$\hat{\gamma}^+(s) \stackrel{\text{def}}{=} \left(e^{j\hat{\beta}y_0(1-s)} + e^{j\hat{\beta}y_0(1+s)} \right) \quad (4.85)$$

$$\hat{\zeta}_2(s) \stackrel{\text{def}}{=} \frac{\pi}{2x_0} (x_0 + s(x_1 - x_0)) \quad (4.86)$$

$$\hat{\zeta}_3(s) \stackrel{\text{def}}{=} \frac{\pi}{2x_0} ((1-s)x_1). \quad (4.87)$$

The $M \times M$ matrices \hat{D}^{p_i} are found from

$$\hat{D}^{p_i} = \hat{T}^{p_i} \hat{W}^{p_i} \quad (4.88)$$

for

$$\hat{W}^{p_1} = \left(\hat{\gamma}^-(1) \right)^{-1} \hat{W}_0^{p_1} \quad (4.89)$$

$$\hat{W}^{p_2} = \left(\hat{\gamma}'^-(1) \right)^{-1} \hat{W}_0^{p_2} \quad (4.90)$$

$$\hat{W}^{p_3} = \left(\hat{\gamma}''^-(1) \right)^{-1} \hat{W}_0^{p_3}. \quad (4.91)$$

with $\hat{W}_0^{p_i}$ the M -element row vector that selects from Ψ_c a good approximation of the corner value of ψ at p_i . Furthermore

$$\hat{T}^{p_1} = \begin{bmatrix} \hat{T}_{11} \\ \hat{T}_{21} \\ \hat{T}_{31} \end{bmatrix} \quad (4.92)$$

with

$$[B_1 \hat{T}_{11}]_{\tilde{m},1} = -j\hat{\beta} \gamma^+(1) \int_0^1 \cos\left(\frac{\pi s}{2}\right) t_{c_1, \tilde{m}}(s) ds \quad (4.93)$$

$$\begin{aligned} [B_2 \hat{T}_{21}]_{\tilde{m},1} &= \\ &- \frac{y_0}{l_2} \frac{\pi}{2x_0} \int_0^1 \hat{\gamma}^-(1-s) \sin \hat{\zeta}_2(s) t_{c_2, \tilde{m}}(s) ds \\ &+ \frac{x_0 - x_1}{l_2} j\hat{\beta} \int_0^1 \hat{\gamma}^+(1-s) \cos \hat{\zeta}_2(s) t_{c_2, \tilde{m}}(s) ds \end{aligned} \quad (4.94)$$

$$\begin{aligned} [B_3 \hat{T}_{31}]_{\tilde{m},1} &= \\ &\frac{y_0}{l_3} \frac{\pi}{2x_0} \int_0^1 \hat{\gamma}^-(s) \sin \hat{\zeta}_3(s) t_{c_3, \tilde{m}}(s) ds \\ &+ \frac{x_1}{l_3} j\hat{\beta} \int_0^1 \hat{\gamma}^+(s) \cos \hat{\zeta}_3(s) t_{c_3, \tilde{m}}(s) ds \end{aligned} \quad (4.95)$$

and

$$\hat{T}^{p_2} = \begin{bmatrix} \hat{T}'_{31} \\ \hat{T}'_{11} \\ \hat{T}'_{21} \end{bmatrix} \quad \text{and} \quad \hat{T}^{p_3} = \begin{bmatrix} \hat{T}''_{21} \\ \hat{T}''_{31} \\ \hat{T}''_{11} \end{bmatrix} \quad (4.96)$$

The $M \times M$ matrices \hat{R}^{p_i} are written as

$$\hat{R}^{p_i} = E - \hat{L}^{p_i} \hat{W}^{p_i} \quad (4.97)$$

with E the $M \times M$ unit matrix. Matrix \hat{L}^{p_i} is split up as

$$\hat{L}^{p_1} = \begin{bmatrix} \hat{L}_{11} \\ \hat{L}_{21} \\ \hat{L}_{31} \end{bmatrix} \quad (4.98)$$

with

$$[B_1 \hat{L}_{11}]_{\tilde{m},1} = \gamma^-(1) \int_0^1 \cos\left(\frac{\pi s}{2}\right) t_{c_1, \tilde{m}}(s) ds \quad (4.99)$$

$$[B_2 \hat{L}_{21}]_{\tilde{m},1} = \int_0^1 \hat{\gamma}^-(1-s) \cos \hat{\zeta}_2(s) t_{c_2, \tilde{m}}(s) ds \quad (4.100)$$

$$[B_3 \hat{L}_{31}]_{\tilde{m},1} = \int_0^1 \hat{\gamma}^-(s) \cos \hat{\zeta}_3(s) t_{c_3, \tilde{m}}(s) ds \quad (4.101)$$

and

$$\hat{L}^{p_2} = \begin{bmatrix} \hat{L}'_{31} \\ \hat{L}'_{11} \\ \hat{L}'_{21} \end{bmatrix} \quad \text{and} \quad \hat{L}^{p_3} = \begin{bmatrix} \hat{L}''_{21} \\ \hat{L}''_{31} \\ \hat{L}''_{11} \end{bmatrix} \quad (4.102)$$

Bibliography

- [1] G. Manetas, V. N. Kourkoulos, and A. C. Cangellaris, “Investigation on the frequency range of validity of electroquasistatic RC models for semiconductor substrate coupling modeling,” *IEEE Trans. Electromagn. Compat.*, vol. 49, no. 3, pp. 577–584, Aug. 2007.
- [2] G. Antonini, A. Orlandi, and C. Paul, “Internal impedance of conductors of rectangular cross section,” *IEEE Trans. Microw. Theory Tech.*, vol. 47, no. 7, pp. 979–985, Jul. 1999.
- [3] K. Coperich, A. Ruehli, and A. Cangellaris, “Enhanced skin effect for partial-element equivalent-circuit (PEEC) models,” *IEEE Trans. Microw. Theory Tech.*, vol. 48, no. 9, pp. 1435–1442, Sep. 2000.
- [4] G. Plaza, R. Marques, and F. Medina, “Quasi-TM MoL/MoM approach for computing the transmission-line parameters of lossy lines,” *IEEE Trans. Microw. Theory Tech.*, vol. 54, no. 1, pp. 198–209, Jan. 2006.
- [5] J. J. Kucera and R. J. Gutmann, “Effect of finite metallization and inhomogeneous dopings on slow-wave-mode propagation,” *IEEE Trans. Microw. Theory Tech.*, vol. 45, no. 10, pp. 1807–1810, Oct. 1997.
- [6] T. Demeester and D. De Zutter, “Quasi-TM transmission line parameters of coupled lossy lines based on the Dirichlet to Neumann boundary operator,” *IEEE Trans. Microw. Theory Tech.*, vol. 56, no. 7, pp. 1649–1660, Jul. 2008.
- [7] D. De Zutter and L. Knockaert, “Skin effect modeling based on a differential surface admittance operator,” *IEEE Trans. Microw. Theory Tech.*, vol. 53, no. 8, pp. 2526–2538, Aug. 2005.
- [8] T. Demeester and D. De Zutter, “Internal impedance of composite conductors with arbitrary cross section,” *IEEE Trans. Electromagn. Compat.*, vol. 51, no. 1, pp. 101–107, Feb. 2009.
- [9] ———, “Modeling the broadband inductive and resistive behavior of composite conductors,” *IEEE Microw. Wireless Compon. Lett.*, vol. 18, no. 4, pp. 230–232, Apr. 2008.

-
- [10] H.-H. Chen, “Finite-element method coupled with method of lines for the analysis of planar or quasi-planar transmission lines,” *IEEE Trans. Microw. Theory Tech.*, vol. 51, no. 3, pp. 848–855, Mar. 2003.
 - [11] T. Demeester and D. De Zutter, “Applications of the Dirichlet to Neumann boundary operator in transmission line modeling,” presented at the 20th International Zurich Symposium on Electromagnetic Compatibility, Jan. 2009.

CHAPTER 5

Fields at a Finite Conducting Wedge and Applications in Interconnect Modeling

Thomas Demeester and Daniël De Zutter

Submitted for publication in the
IEEE Transactions on Microwave Theory and Techniques



The fields at a finite conducting 2-D wedge are studied by means of the surface admittance operator, and compared to the case of a perfect conductor. This technique, applied to a number of numerical examples, allows a thorough investigation of the singular behavior of the fields near the edge, including non-singular fields such as the longitudinal current distribution. Special attention is devoted to the validity of the quasi-TM approximations, when edge singularities are taken into account. The studied field properties lead to the formulation of an approximative local surface impedance for conductors, and are finally used to show how some differences in the resistive and inductive behavior of conductors with a different geometry are due to edge effects.

5.1 Introduction

For many years, researchers have been looking for accurate descriptions of the loss mechanisms in interconnect structures. As modern technological applications in very-large-scale-integration (VLSI) circuits push the limits of speed and miniaturization, conductor losses more than ever remain an important issue, by far more relevant than

radiation or dielectric losses. Not only heat generation needs to be kept under control, the losses also have an important impact on the signal integrity, due to attenuation and dispersion.

The earliest research on interconnect losses is well-summarized in [1], mentioning for instance Wheeler's incremental inductance rule, where the magnetic field generated by the axial current flow is used to calculate the losses, assuming an equal real and imaginary part of the high-frequency internal impedance per unit length. The resistive properties of coupled lines with finite conductivity were more rigorously studied in [2] and [3], using the Method of Moments (MoM) with a boundary discretization, respectively, a volume discretization of the field quantities. Many other numerical approaches were used for analogous purposes, e.g., Finite Elements Methods [4], hybrid methods based on the 'filament technique' at low frequencies and a surface integral equation at high frequencies [5], or a combination of the MoM and the Method of Lines [6], just to mention a few. Generally, the boundary integral equation techniques appear to be more suited in terms of both computation time efficiency and accuracy, than methods based on a volume discretization of the currents, especially at the highest frequencies.

The importance of the edge effect in the current profile of polygonal (mostly rectangular) conductors became clear with the (sometimes mutually inconsistent) results that were found from internal inductance calculations [7–9], and which clearly showed an important deviation from Wheeler's rule.

In parallel with the research on the effect of the finite conductivity on the circuit level properties (resistance, inductance) of the lines, another topic of investigation was the singular field behavior at edges. In [10], and further in [11], the cases of perfectly electric conducting (PEC) wedges and wedges with dielectric contrast were treated. A more detailed analysis and further references can be found in [12]. The theory of the singularity exponent as formulated in [11] was extended to finite conducting wedges in [13].

Although the specific field behavior at conductors' edges (both in the PEC and in the finite conducting case) and the current profile (relevant to the resistive and inductive properties of the lines) are intrinsically linked, both aspects were so far not examined simultaneously. On the one hand, 'circuit oriented' papers such as, e.g., [7,14,15], concentrate on the interconnect behavior, with no specific attention devoted to edge effects and their influence on the circuit parameters. On the other hand, [11] and [13] focus on the edge singularities only, not paying particular attention to the properties of the longitudinal field components, such as the current density, as these do not exhibit a singular behavior at the edges.

This paper describes the behavior of a finite conducting wedge, as a function of its opening angle α , in combination with the longitudinal current profile. As opposed to the singularity exponent technique of [11] and [13], the applied method enables the description of the *total* edge field quantities, not restricted to the strongest singularity

only. Although the technique is a numerical approximation obtained by the MoM, it is well-suited for an accurate description of the fields near an edge from low to very high frequencies, as it makes use of a boundary integral equation formulation, in combination with a field expansion that exactly describes the current crowding phenomenon inside the conductor.

Essential in this technique is the surface admittance matrix, which relates the electric field to the equivalent surface current densities that replace the conductors. The surface admittance matrix is calculated by means of a discretization of the Dirichlet to Neumann (DtN) operator of the considered conductor's cross-section. The method was first introduced for conductors in [16] and extended to dielectrics and semiconductors in [17]. In [18] and [19], the original method for rectangular conductors was extended to general polygonal shapes.

In Section 5.2, a single wedge is considered. First, the relationship between Meixner's [11] work on field singularities and the quasi-TM approximations underlying the coupled transmission line model presented in [17] is elucidated. Next, the equivalent surface current density j_{eq} as introduced in [16] and the current profile inside the wedge are studied. Subsequently, an approximative local surface impedance model for conductors is proposed, intended to demonstrate the principle physical properties of j_{eq} . In a last subsection, the properties of the wedge current profile are used to reveal the influence of varying conductor angles on the per unit length (p.u.l.) resistance and inductance for conductors with a high but finite conductivity.

Finally, Section 5.3 summarizes the results.

5.2 Investigation of the Edge Effect

This section is intended to provide the reader with some insight into the field distribution and essential phenomena that occur near edges. Focus is on the physics of the current and field distribution near a single edge, and the validity of the quasi-TM approximations (which is confirmed by numerical results).

The considered configuration consists of one triangular metallic non-magnetic conductor S with conductivity σ , placed in free space. It is assumed that no other materials (dielectric or semiconducting substrates) are around, in order to study the edge effect in its most basic configuration, although the results are valid for more complicated structures as well. In order to avoid the proximity effect in the current distribution, the reference conductor is considered infinitely far away. All simulation results shown here are obtained by using the numerical method described in [18]. For the discretization of the boundary quantities, piecewise linear basis functions are used over a non-uniform grid. In this way a very fine grid can be used near the corner tips. When focussing on the edge effect only, the simulation frequency will be chosen sufficiently high, such that the influence of the side, opposite to the corner of interest, is negligible. In practice, this means the skin depth has to be much smaller than the

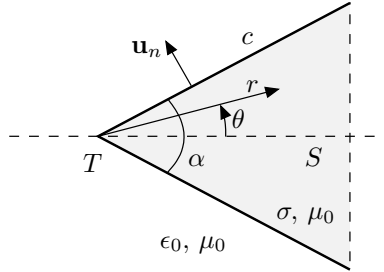


Figure 5.1: Basic configuration of a conducting wedge (as part of a triangle), placed in free space.

distance between that corner and its opposite side.

5.2.1 The Equivalent Surface Current Density

Consider the triangle shown in Fig. 5.1 with an opening angle α at corner T , with the permeability μ_0 of free space and a ‘high’ conductivity σ (such that $\sigma \gg \omega\epsilon_0$). As explained above, we are only interested in the edge effect in the neighborhood of T . As mentioned in the Introduction, the volume current flowing through S , is replaced by an equivalent surface current density source \mathbf{j}_{eq} in free space on the boundary c of S . This equivalent source is found from the requirement that outside S , it generates the original fields [16]

$$\mathbf{j}_{\text{eq}} = \mathbf{u}_n \times (\mathbf{h}^+ - \mathbf{h}_0^-) = \mathbf{u}_n \times (\mathbf{h}^- - \mathbf{h}_0^-). \quad (5.1)$$

with \mathbf{u}_n the outward pointing normal unit vector on c . The superscripts + and – are used for the outer, respectively, the inner limit of the fields at c , and the subscript ‘0’ indicates field quantities inside S in the equivalent configuration, in which the material properties of S are replaced by free space. To obtain the last part of (5.1), the continuity of the tangential magnetic field was invoked, which allows to write \mathbf{j}_{eq} in terms of boundary quantities *inside* S in the original, respectively, the equivalent configuration.

The quasi-TM approximations [17] dictate that for the determination of e_z (to determine the resistive and inductive properties), the longitudinal component $j_{\text{eq},z}$ of the total equivalent current density suffices (as briefly motivated in the Appendix). For an $e^{-j\beta z + j\omega t}$ -dependence of the fields, the transverse magnetic field \mathbf{h}_t is found from Faraday’s law

$$j\omega\mu_0 \mathbf{h}_t = j\beta \mathbf{u}_z \times \mathbf{e}_t - \nabla_t e_z \times \mathbf{u}_z. \quad (5.2)$$

in which $\nabla_t = \partial/\partial x \mathbf{u}_x + \partial/\partial y \mathbf{u}_y$. Hence, $j_{\text{eq},z}$, concisely written as j_{eq} , is given

by

$$j\omega\mu_0 j_{\text{eq}} = j\beta(e_n^- - e_{n0}^-) + \frac{\partial e_z^-}{\partial n} - \frac{\partial e_{z0}^-}{\partial n} \quad (5.3)$$

with $e_n = \mathbf{e}_t \cdot \mathbf{u}_n$ and $\partial/\partial n$ the outward normal derivative.

In [11], Meixner presents an expansion of the fields near the edge, in order to investigate the field singularities. He shows that the longitudinal fields e_z and h_z do not display a singularity at the edge, and if there is no magnetic contrast (as is the case here), the total magnetic field remains finite. The e_z field, e.g., can be expanded in polar coordinates r and θ as

$$e_z(r, \theta) = c_1(\theta)r^\nu + \dots, \quad (5.4)$$

omitting higher order terms in r , and with

$$c_1(\theta) = -\frac{j\beta}{\nu}l \cos \nu\theta. \quad (5.5)$$

with l a complex integration constant. The transverse tangential and the normal electric field components exhibit a singular term that behaves as $r^{\nu-1}$. In [13], it is shown that in the case of a good conductor, ν can be well approximated by

$$\nu = \frac{\pi}{2\pi - \alpha}. \quad (5.6)$$

which exactly dictates the singular behavior of e_n in the case of a PEC conductor.

If the field expansions from [11] are inserted in (5.3), the singular terms in $j\beta e_n^-$ and $\partial e_z^-/\partial n$ cancel each other out, as is also the case for $j\beta e_{n0}^-$ and $\partial e_{z0}^-/\partial n$. Furthermore, these expansions allow to compare the singular terms in $\partial e_z/\partial n$ and $\partial e_{z0}/\partial n$. Inside the wedge, e_z satisfies

$$\nabla_t^2 e_z = (\beta^2 - k^2) e_z \quad (5.7)$$

with $k^2 = -j\omega\mu_0(\sigma + j\omega\epsilon)$. The expansion (5.4) of e_z is substituted in (5.7) and yields

$$\left(\nu^2 c_1(\theta) + \frac{\partial^2 c_1(\theta)}{\partial \theta^2} \right) r^{\nu-2} + \dots = (\beta^2 - k^2) c_1(\theta) r^\nu + \dots \quad (5.8)$$

Setting the coefficient of $r^{\nu-2}$ to zero, confirms the θ behavior of $c_1(\theta)$ in (5.5), which is independent of the material parameters. The same remark holds for the term in $r^{\nu-1}$ in $\nabla_t^2 e_z$. In the quasi-TM limit, the right-hand side of (5.7) becomes $j\omega\mu_0\sigma e_z$, and as seen from (5.8), this diffusion term is not relevant very close to the corner tip. A

completely similar reasoning can be put forward for e_{z0} which satisfies

$$\nabla_t^2 e_{z0} = (\beta^2 - k_0^2) e_{z0} \quad (5.9)$$

with $k_0^2 = \omega^2 \epsilon_0 \mu_0$. By construction, e_{z0} has the same boundary value on c as e_z , and because replacing k^2 by k_0^2 in (5.7) has no influence on the singular behavior, the two highest order terms of the expansions of e_z and e_{z0} are identical. As a consequence, the singularity in $\partial(e_z - e_{z0})/\partial n$ is cancelled out, as well as the first higher order term ($\propto r^\nu$).

The above reasoning shows that all four field components in the right-hand side of (5.3) contain the *same* singular term. Leaving these singular terms out, thus has no influence on j_{eq} . Let us indicate the fields in (5.3) without their singular term with the caret symbol “ $\hat{\cdot}$ ”. Within the quasi-TM limit, the terms $j\beta\hat{e}_n^-$ and $j\beta\hat{e}_{n0}^-$ are both negligible with respect to $\partial\hat{e}_z^-/\partial n$ (considering the fact that $|\partial\hat{e}_z^-/\partial n| > |\partial\hat{e}_{z0}^-/\partial n|$ due to the current crowding effect). The reason for this is twofold. On the one hand, the longitudinal wavelength is much larger than a typical cross-sectional distance over which the fields extend, and therefore we can in general say that “ $j\beta \ll \partial/\partial n$ ” for a certain field quantity. On the other hand, $|\hat{e}_n^-| \ll |\hat{e}_z^-|$. Taking these two arguments into account leads to

$$j_{\text{eq}} = \frac{1}{j\omega\mu_0} \left(\frac{\partial\hat{e}_z^-}{\partial n} - \frac{\partial\hat{e}_{z0}^-}{\partial n} \right) \quad (5.10)$$

$$= \frac{1}{j\omega\mu_0} \left(\frac{\partial e_z^-}{\partial n} - \frac{\partial e_{z0}^-}{\partial n} \right). \quad (5.11)$$

This proves that in the quasi-TM approximation expression (5.11), already put forward in [16] for the z -independent TM case, still remains valid when the singular field behavior at an edge is accounted for. As not only the singular terms in $r^{\nu-1}$ in (5.11) cancel out, but also the nonsingular terms in r^ν and a possible constant term, j_{eq} will become zero at the tip T , as will be confirmed by the numerical examples.

In the sequel, j_{eq} for a finite conductor will be compared to the surface current density j_{PEC} on a PEC wedge. This is motivated by the following observation. As the fields inside the PEC conductor are zero, the inside can be substituted by free space, provided proper surface charges and surface currents are placed on the boundary. If these sources are equal to the original surface charge and current on the PEC conductor, the fields in both configurations are the same and the boundary conditions are met. j_{PEC} is hence the ‘equivalent current source’ for the PEC problem, and is in this paper compared to the finite conducting case. j_{PEC} can be obtained by solving a static potential problem, with the longitudinal magnetic vector potential $a_z = V\sqrt{\epsilon_0\mu_0}$ on c . This result is obtained from the general relationship

$$e_z = j\beta\phi - j\omega a_z, \quad (5.12)$$

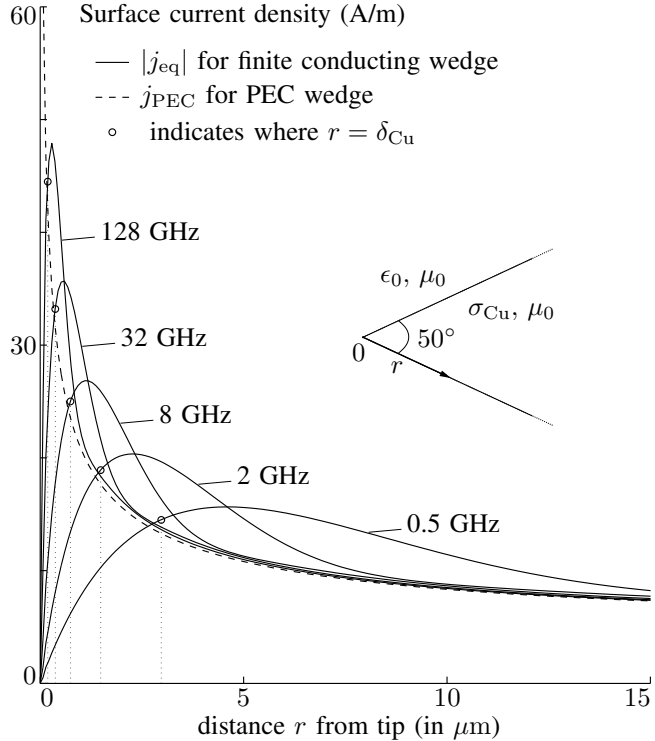


Figure 5.2: Surface current density $|j_{\text{eq}}|$ for a 50° copper wedge (see inset). Solid lines: $|j_{\text{eq}}|$ for finite conductivity ($\sigma_{\text{Cu}} = 57.2 \text{ MS/m}$), with indication of the distance δ_{Cu} from the corner top. Dashed line: $|j_{\text{PEC}}|$ for PEC wedge.

combined with $e_z = 0$, $\phi = V$ and $\beta = \omega\sqrt{\epsilon_0\mu_0}$ on the boundary of the considered perfect conductor in free space.

In Fig. 5.2, the equivalent surface current density $|j_{\text{eq}}|$ near a copper wedge of 50° is compared with the PEC case, for various frequencies. In the simulation, the wedge was the top corner of an isosceles triangle (with both legs $60 \mu\text{m}$ long, such that the edge effects of the different corners do not interfere at the shown frequencies), with the electric boundary potential put to $V = 1 \text{ V}$. To get an idea of the frequency relative to the dimensions, the point where the distance r to the corner tip equals one skindepth δ_{Cu} , is indicated as well. Notice that, as explained earlier, j_{eq} vanishes at the tip and therefore does not have j_{PEC} as its limiting case for $\omega\sigma \rightarrow \infty$, because j_{PEC} is always singular (for an wedge angle smaller than 180°). It is clear though, that more than a few skindepths away from the edge, j_{eq} and j_{PEC} become almost identical.

In Fig. 5.3, a similar wedge is treated as in Fig. 5.2, but at a fixed frequency

(10 GHz) and for a varying top angle α . In order to investigate the behavior of j_{eq} with respect to j_{PEC} for different values of α , Fig. 5.3 (a) shows the normalized current density $|j_{\text{eq}}|/j_{\text{PEC}}$ near the corner tip. As the solution of the diffusion equation only depends on the product $\omega\sigma$ instead of both factors separately, the abscis r is normalized by the skin depth in copper $\delta_{\text{Cu}} = (\pi f \mu_0 \sigma_{\text{Cu}})^{-1/2}$. The deviation of the curves in Fig. 5.3 (a) from unity shows the influence of the finite conductivity. The equivalent current density at the sharpest angles deviates more from j_{PEC} than at the wider angles. This can be explained by the diffusion at skin effect frequencies. Near the edge of a narrow wedge, the adjacent sides are more tightly coupled for a wider wedge, and the current crowding effect starts appearing further away from the tip as compared to the wide wedge case. Therefore, the edge effect is more important for narrower wedges. In [18], this phenomenon appears to be the reason for the slower convergence of the ICWM (Iterative Combined Waveguide Modes) procedure for sharper angles, where the coupling between the sides of the conductor is gradually taken into account.

As a verification of the singular behavior of j_{PEC} , Fig. 5.3 (b) shows j_{PEC} for the same wedge, normalized by a factor $C r^{\nu-1}$, with ν given by (5.6). For $\pi > \alpha > 0$, the singularity exponent $(\nu - 1)$ lays between 0 and $-1/2$, with, e.g., an $r^{-1/3}$ -behavior for a 90° angle. For each value of α , the proportionality constant C is chosen such that $(j_{\text{PEC}}/C r^{\nu-1})$ becomes one in the limit for $r = 0$.

5.2.2 The Electric Boundary Potential ϕ_c

This paragraph is intended to demonstrate the validity of the assumption that, in the quasi-TM limit, the electric potential ϕ on the boundary of a good conductor remains constant over its edges. With Meixner, the potential ϕ can be written as

$$\phi(r, \theta) = V + f_1(\theta) r^\nu + f_2(\theta) r^{\nu+1} + \dots \quad (5.13)$$

The expansions in [11] only describe the singular behavior of the fields (or their normal derivatives) and here, (5.13) is completed with a constant term V , as motivated in [20]. The coefficient $f_1(\theta)$ is found as

$$f_1(\theta) = -\frac{l \cos \nu \theta}{\nu} \quad (5.14)$$

and the term $f_1(\theta) r^\nu$ has a singular normal derivative at $r = 0$. From (5.5) and (5.12), we see that neglecting this term with respect to the total potential ϕ , corresponds to neglecting the term $c_1(\theta) r^\nu$ in e_z . This means that an excitation with a constant boundary value $\phi_c = V$, does not give rise to a singularity in $\partial e_z / \partial n$. This approximation is acceptable within the quasi-TM limit, as is briefly discussed in the Appendix.

We will demonstrate with a numerical example how accurate this approximation really is, by comparing the approximative constant voltage excitation $\phi_c = V$ with

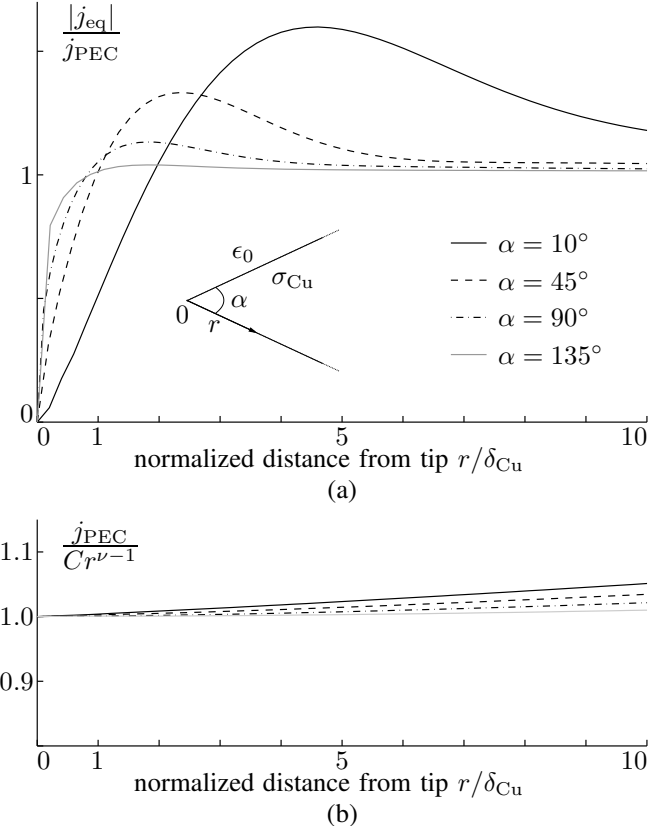


Figure 5.3: Normalized surface current densities for different angles α , and at 10 GHz. (a) $|j_{\text{eq}}|/j_{\text{PEC}}$, and (b) $j_{\text{PEC}}/Cr^{\nu-1}$, with C chosen such, that $j_{\text{PEC}}/Cr^{\nu-1}$ becomes one at $r = 0$.

the term $f_1(\theta) r^\nu = \Delta\phi_c$ on the boundary $\theta = \alpha/2$ of a wedge (see Fig. 5.1). Near the edge, where the singular term proportional to $r^{\nu-1}$ dominates the surface charge ρ_{eq} (see Appendix), e_n^- is, with the results from [11], given by

$$e_n^- \approx -l \sin \frac{\nu\alpha}{2} r^{\nu-1} \approx \frac{j\omega}{\sigma} \rho_{\text{eq}} \quad (5.15)$$

such that

$$\Delta\phi_c \approx \frac{j\omega}{\sigma} \frac{\rho_{\text{eq}}}{\nu r^{\nu-1}} \cot\left(\frac{\nu\alpha}{2}\right) r^\nu. \quad (5.16)$$

Note that ρ_{eq} is a very good approximation of the actual surface charge, even though calculated with the approximative excitation $\phi_c = V$, as it is very similar to the PEC case where $\phi_c \equiv V$ (see Appendix). Note that ρ_{eq} itself is proportional to $r^{\nu-1}$ and

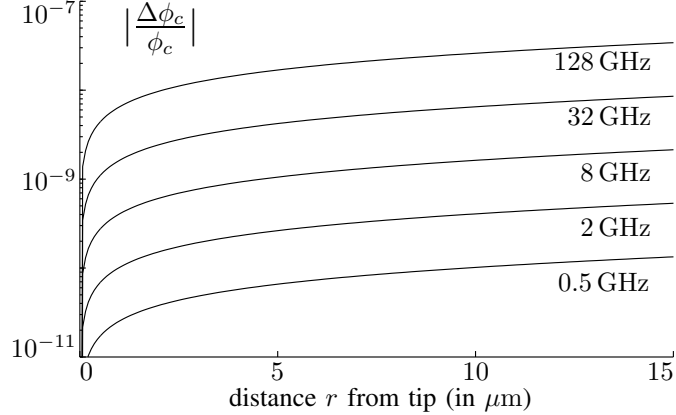


Figure 5.4: The term $\Delta\phi_c$ in the boundary potential expansion near the edge, in absolute value and normalized by ϕ_c , for the 50° wedge shown in Fig. 5.2

hence that $\Delta\phi_c$ tends to zero as r^ν .

For the copper 50° wedge from Fig. 5.2 and at the same frequencies, the term $\Delta\phi_c$ is compared with the voltage $\phi_c = V$, the constant excitation voltage used in the quasi-TM simulations. Fig. 5.4 shows the results, and it appears that even at the highest shown frequencies, $\Delta\phi_c$ remains many orders of magnitude smaller than ϕ_c , for the shown region $r \in [0, 15 \mu\text{m}]$ where the approximation (5.16) can be assumed to be valid.

5.2.3 The Electric Field Distribution Inside the Wedge

The longitudinal electric field e_z on a conductor's boundary can be found with the MoM [17], and the inside e_z field is readily determined as well, by means of an expansion in terms of parallel plate waveguide modes as described in [18]. In Fig. 5.5, the normalized longitudinal electric field distribution $|e_z/j\beta\phi_c|$ is shown inside the 50° copper wedge of Fig. 5.2 and for a radial length of $r = 15 \mu\text{m}$, at 10 MHz, 100 MHz, 1 GHz, and 10 GHz. For these frequencies, the skin depth is given, respectively, by $21 \mu\text{m}$, $6.6 \mu\text{m}$, $2.1 \mu\text{m}$ and $0.66 \mu\text{m}$.

In order to visualize the influence of the wedge angle on the current distribution, Fig. 5.6 (a) again shows the normalized electric field $|e_z/j\beta\phi_c|$, and Fig. 5.6 (b) shows the phase of e_z on c . The same geometries are used as for the simulations shown in Fig. 5.3. The increase of e_z toward the edge is much more pronounced for the sharpest angles, and almost non-existing for the obtuse angle of 135° . The phase $\arg(e_z)$ for the sharp corners displays a large deviation of the plane wave limit of 45° , over a distance of many skindepths away from the tip.

As a verification of the numerical results, the boundary value of e_z on a rectan-

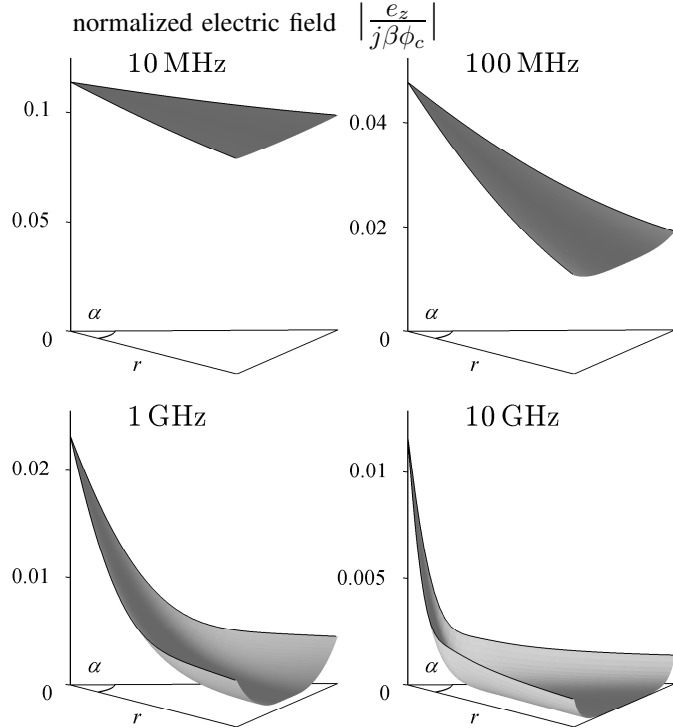


Figure 5.5: Normalized electric field $|e_z / j\beta\phi_c|$ inside a copper wedge ($\sigma_{\text{Cu}} = 57.2 \text{ MS/m}$) with an angle $\alpha = 50^\circ$, shown for $r \in [0, 15 \mu\text{m}]$.

angular conductor is compared with results found in [21]. The simulated configuration consists of a golden microstrip line above a ground plane. Fig. 5.7 shows the geometry (see inset), as well as the results calculated by means of the MoM in combination with the DtN operator in solid lines, at different frequencies. At the frequency f_0 , the reference data from [21] are indicated as well. Note that in [21], a golden ground plane was used, whereas here just a PEC ground is considered. Yet the results seem to match quite accurately. In [21], the fields were considered to be z -independent, and excited by means of the external field E_z^{ext} , which corresponds with our term $j\beta\phi_c$ in (5.12). In Fig. 5.7, the normalized field $|e_z / j\beta\phi_c|$ is given. At the lowest frequencies, $j\omega a_z \ll e_z$, such that the current distribution is almost uniform and $e_z / j\beta\phi_c \approx 1$. At skin effect frequencies, e_z decreases because the difference between $j\beta\phi$ and $j\omega a_z$ goes to zero for $\omega\sigma \rightarrow \infty$, as the fields approach the PEC field distribution with $e_z \equiv 0$.

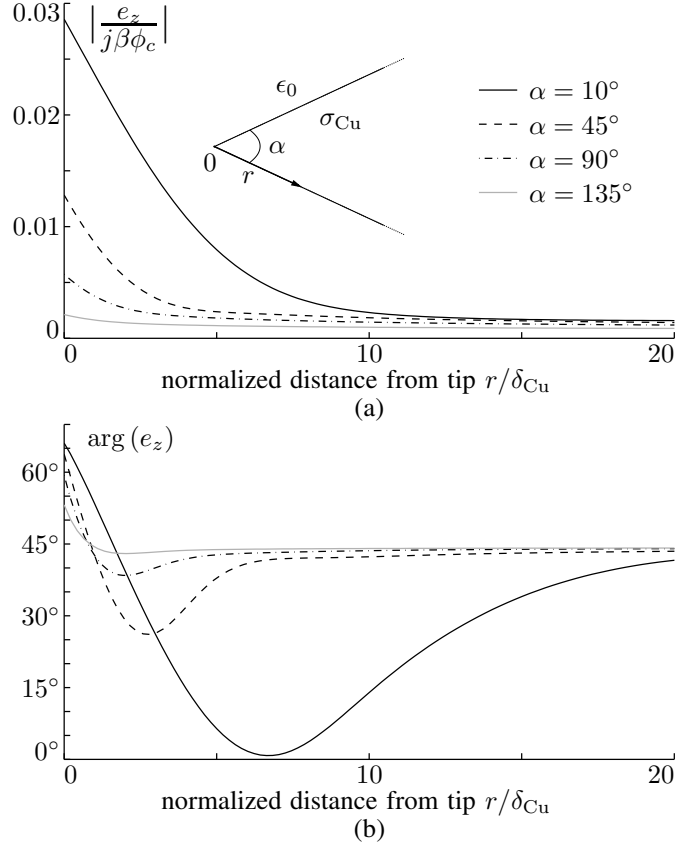


Figure 5.6: (a) The normalized electric field $|e_z/j\beta\phi_c|$ on the boundary of a copper wedge ($\sigma_{Cu} = 57.2 \text{ MS/m}$) for different angles α and at 10 GHz, and (b) the phase of the corresponding electric field e_z (for $\phi_c = 1 \text{ V}$).

5.2.4 A Local Surface Impedance Approximation

After studying j_{eq} and e_z near a wedge, we have a sufficient understanding on the wedge effects as to propose the following approximation for j_{eq} on the boundary c of an arbitrary two-dimensional conductor in free space (hence not restricted to the wedge only)

$$j_{eq} \approx \frac{1}{j\omega\mu_0} \left(e_z \frac{\partial e_1}{\partial n} \right)_c \stackrel{\text{def}}{=} j_{\text{approx}}. \quad (5.17)$$

The approximate surface current density j_{approx} contains the actual boundary value of e_z , multiplied with the normal derivative of a function e_1 which satisfies

$$\nabla_t^2 e_1 = j\omega\mu_0\sigma e_1 \quad (5.18)$$

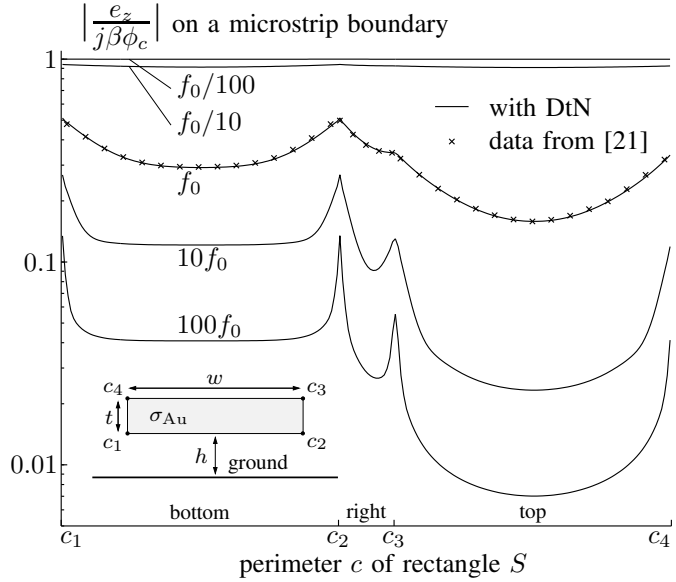


Figure 5.7: Normalized longitudinal electric field $|e_z / j\beta|$ on the boundary of the microstrip, shown in the inset, with $w = 10 \mu\text{m}$, $t = 2 \mu\text{m}$, $h = 2 \mu\text{m}$, and $\sigma_{Au} = 41 \text{ MS/m}$. The simulations were performed for different frequencies, with $f_0 = 4.367 \text{ GHz}$.

inside the conductor (as e_z itself), but is 1 on c . The idea behind this approximation is the separation of the two major phenomena that play a role. On the one hand, we have the value of e_z on c , increasing towards the corners as governed by the (outside) magnetic field, and on the other hand the current crowding phenomenon inside the conductor, which would behave like $\partial e_1 / \partial n$ if the boundary field were a constant. At the higher frequencies and far enough away from the corners, the local plane wave behavior confirms that the approximation becomes accurate. At the lower frequencies, e_z is approximately constant over the cross-section, and the approximation holds as well. With (5.17), we have therefore constructed a *local* surface impedance Z_{approx} ,

$$Z_{\text{approx}} = \frac{j\omega\mu_0}{\frac{\partial e_1}{\partial n}} \quad (5.19)$$

with the correct low- and high-frequency limits. The approximation is acceptable, because the total current I is, for any frequency, found as

$$I = \oint_c j_{\text{eq}} dc = \oint_c j_{\text{approx}} dc. \quad (5.20)$$

This can be proved by invoking Green's theorem in combination with (5.17), (5.18) and the same diffusion equation for e_z itself¹.

As a numerical verification, consider a rectangular copper conductor ($\sigma_{\text{Cu}} = 58 \text{ MS/m}$) with dimensions $200 \mu\text{m} \times 30 \mu\text{m}$ in free space. At 1 MHz, 100 MHz, and 10 GHz, the real and imaginary part of both j_{eq} and j_{approx} are shown in Fig. 5.8. For these frequencies, the skindepth in copper is, respectively, $66 \mu\text{m}$, $6.6 \mu\text{m}$, and $0.66 \mu\text{m}$. At the low and high frequencies, j_{eq} and j_{approx} are very close to one another as expected, but also at the intermediate frequency the behavior is quite similar, confirming the physical ideas behind the equivalent surface current density.

5.2.5 The Edge Effect vs. the p.u.l. Resistance and Inductance

In [18], it was found that the high-frequency resistance for trapezoidal or triangular conductors is higher than for a rectangular reference conductor with the same cross-sectional area, despite their longer circumference. In a last numerical example, the field distribution for these situations is shown in direct relationship with the corresponding circuit properties.

The starting point is the following telegrapher equation for a single line

$$j\beta V = (j\omega L + R)I = ZI. \quad (5.21)$$

Studying $e_z/j\beta V$ on the conductor's cross-section, or its normal derivative at the boundary, only yields information on Z^{-1} , not directly on the resistance and inductance of the line. Therefore, we will transform (5.21) into

$$(j\omega L + R) = j\beta \tilde{V} \oint_c \left(\frac{1}{j\omega\mu_0} \frac{\partial e_z^-}{\partial n} \right)^* dc. \quad (5.22)$$

with the excitation voltage \tilde{V} chosen real and positive, but such that $|I| = 1 \text{ A}$ (or, alternatively, $\tilde{V} = V/|I|^2$). The integrand equals the complex conjugate h_{\tan}^* of the tangential magnetic field in the quasi-TM limit. The contribution of $\partial e_{z0}/\partial n$ could be included as well, to obtain j_{eq} in the integrand (as it does not contribute to the integration), but this would make the graphical results less transparent.

The first considered configuration consists of a rectangular golden conductor with width $w = 10 \mu\text{m}$ and height $t = 2 \mu\text{m}$, placed above a PEC ground plane with a separation of $h = 2 \mu\text{m}$. This is the configuration used in Fig. 5.7, and operated at 10 GHz. Secondly, a symmetric trapezoidal golden conductor is considered, also placed above a PEC ground plane, with a bottom width $B = 12 \mu\text{m}$ and a top width

¹ Note that the integration of Z_{approx}^{-1} along the boundary of the conductor yields the inverse of the internal impedance $Z_{\text{in},y}$, introduced in Chapter 2 based on the assumption that the influence of the external magnetic field is omitted by introducing the artificial boundary condition of a constant tangential electric field. This relationship is not surprising, as e_1 does not vary along the boundary.

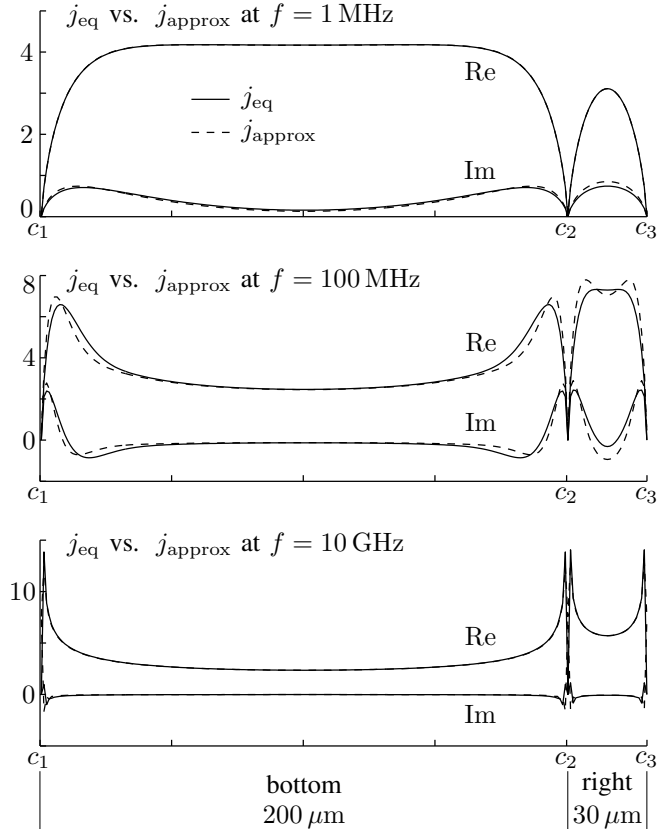


Figure 5.8: Real and imaginary part of j_{eq} and j_{approx} , at (a) 1 MHz, (b) 100 MHz, and (c) 10 GHz for a rectangular copper conductor in free space ($\sigma_{\text{Cu}} = 58 \text{ MS/m}$, width = 200 μm , height = 30 μm).

$b = 8 \mu\text{m}$, and hence the same area as its rectangular counterpart.

Fig. 5.9 shows the resistance R and the inductance L of both configurations. The inductance of the trapezoidal conductor is considerably lower than the rectangle's, and the resistance displays the opposite behavior.

According to (5.22), the circuit parameters ωL and R are obtained by integration of the quantities $\text{Im}(j\beta \tilde{V} h_{\tan}^*)$ and $\text{Re}(j\beta \tilde{V} h_{\tan}^*)$ shown in, respectively, Fig. 5.10 (a) and (b). The main difference in $j\beta \tilde{V} h_{\tan}^*$ between bottom and top side is governed by the proximity effect. There is a very close resemblance on the top side of both conductors, with a considerably lower tangential magnetic field than on the bottom side. It means that the 135° angles of the trapezoidal conductor have very little influence on the field distribution, confirming previous investigations at wedges. For the bottom sides, there is a larger deviation, primarily due to the proximity effect as well. As the

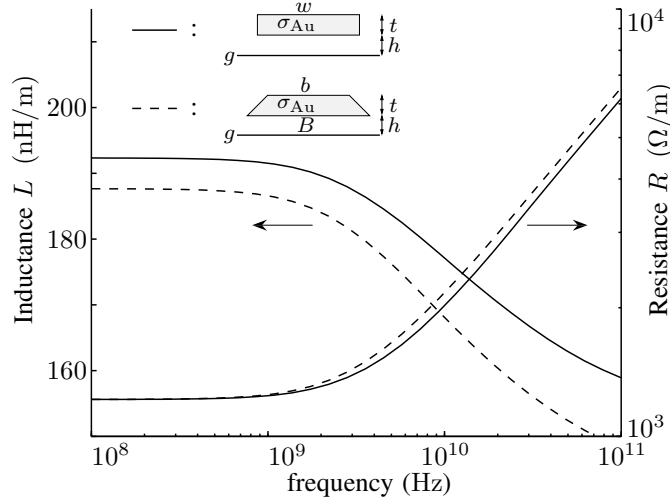


Figure 5.9: Resistance and Inductance p.u.l. for a golden conductor (solid lines: rectangular; dashed lines: trapezoidal) placed a distance $h = 2 \mu\text{m}$ above a PEC ground plane g . The dimensions are $w = 10 \mu\text{m}$, $t = 2 \mu\text{m}$, $B = 12 \mu\text{m}$, and $b = 8 \mu\text{m}$.

bottom side of the trapezoidal conductor is larger than the corresponding side for the rectangle, and given the fact that the total current flowing through both conductors remains fixed at 1 A and is primarily located in the lower part of the conductor, due to the proximity effect, the average bottom field away from the corners is smaller in the trapezoidal case as compared to the rectangular one. This translates into a lower L -value. The authors have verified that the current density distribution shows a similar behavior. However, near the sharp 45° angles, the phase shift in the current density (see also Fig. 5.6 (b)) and therefore also in the tangential magnetic field, has the effect that the resistive term $\text{Re}(j\beta \tilde{V} h_{\tan}^*)$ is no longer smaller than at the 90° angles of the rectangle, but even slightly higher, resulting in an overall higher p.u.l. resistance R at skin effect frequencies.

5.3 Conclusions

The quasi-TM techniques for modeling the resistive and inductive properties of conductors remain valid near conductor edges. The specific field behavior of a finite conducting wedge was investigated and illustrated with a number of numerical examples to clarify the underlying physical mechanisms, which led to the formulation of an approximative local surface impedance description of conductors. Finally, the studied phenomena were used to explain some differences in the (R, L) -behavior of microstrips with different geometries.

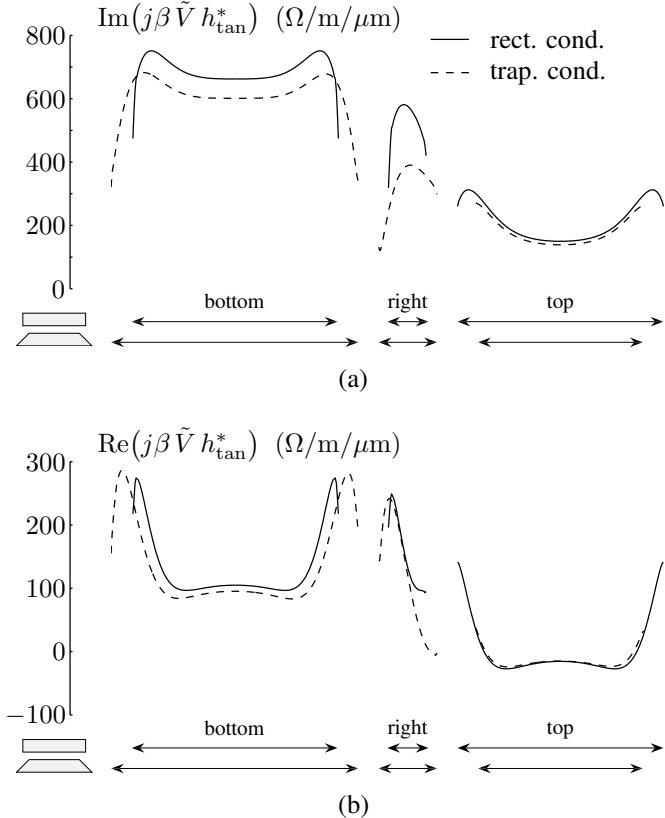


Figure 5.10: Comparison of $j\beta \tilde{V} h_{\tan}^*$ on the boundary of the rectangular vs. the trapezoidal conductor (each above a PEC ground plane), used in Fig. 5.9.

Appendix

This Appendix deals with some issues, related to the quasi-TM approximations. In the frequency range where they are valid, $|j_{\text{eq},z}| \gg |j_{\text{eq,tan}}|$. The reason is, with (5.1), that

$$|h_{\tan}| \gg |h_z| \quad (5.23)$$

(with the subscript tan denoting the transverse part of the total tangential field component), as h_{\tan} has a static contribution, whereas h_z is only of second order in ω . However, to keep the quasi-TM equations consistent, $j_{\text{eq,tan}}$ cannot be considered zero, as it is relevant for the capacitive behavior. Indeed, the surface charge ρ_{eq} , associated with the total equivalent current density is found as

$$-j\omega\rho_{\text{eq}} = \frac{\partial j_{\text{eq,tan}}}{\partial \tan} - j\beta j_{\text{eq},z}. \quad (5.24)$$

The surface charge, associated with the normal electric field, is singular at the edges, as is $\partial j_{\text{eq,tan}} / \partial \tan$, while $j\beta j_{\text{eq},z}$ remains finite. Moreover, the variation of $j_{\text{eq},z}$ in the z direction is small, compared to variations in the cross-section. Therefore, the term in $j_{\text{eq,tan}}$ is essential in (5.24). In practice, the influence of $j_{\text{eq,tan}}$ is well taken care of, if a surface charge source ρ_{eq} is *directly* imposed on the surface, together with the current source $j_{\text{eq},z}$. This charge distribution can be determined by solving a quasi-static potential problem replacing the actual conductor with a PEC one, as motivated in [17]. This approach remains valid at the edges as well, because the singular term in ρ_{eq} has an $r^{\nu-1}$ behavior, and for a good conductor, ν approximately equals its value for a PEC conductor [13].

As shown earlier, the approximation $\phi_c = V$ corresponds to omitting the term $c_1(\theta) r^\nu$ in e_z . That (finite) term keeps up for the ‘slow’ longitudinal variation of the (singular) transverse current, because the curl of the total electric field has to remain finite. The field h_z is associated with the transverse electric field (more specifically, its transverse rotation), and similarly, the much larger h_{tan} with the part of e_z without the term $c_1(\theta) r^\nu$ (by means of its normal derivative). Within the quasi-TM limit (5.23), we can therefore say that near the edge $|e_z| \gg |c_1(\theta) r^\nu|$ and hence the approximation $\phi_c = V$ is sufficiently accurate (confirmed also in Fig. 5.3).

Bibliography

- [1] E. Denlinger, “Losses of microstrip lines,” *IEEE Trans. Microw. Theory Tech.*, vol. 28, no. 6, pp. 513–522, Jun 1980.
- [2] R.-B. Wu and J.-C. Yang, “Boundary integral equation formulation of skin effect problems in multiconductor transmission lines,” *IEEE Trans. Magn.*, vol. 25, no. 4, pp. 3013–3015, Jul. 1989.
- [3] R. Faraji-Dana and Y. Chow, “The current distribution and ac resistance of a microstrip structure,” *IEEE Trans. Microw. Theory Tech.*, vol. 38, no. 9, pp. 1268–1277, Sep. 1990.
- [4] L. Olson, “Application of the finite element method to determine the electrical resistance, inductance, capacitance parameters for the circuit package environment,” *IEEE Trans. Compon., Hybrids, Manuf. Technol.*, vol. 5, no. 4, pp. 486–492, Dec. 1982.
- [5] M. Tsuk and J. Kong, “A hybrid method for the calculation of the resistance and inductance of transmission lines with arbitrary cross sections,” *IEEE Trans. Microw. Theory Tech.*, vol. 39, no. 8, pp. 1338–1347, Aug. 1991.
- [6] G. Plaza, R. Marques, and F. Medina, “Quasi-TM MoL/MoM approach for computing the transmission-line parameters of lossy lines,” *IEEE Trans. Microw. Theory Tech.*, vol. 54, no. 1, pp. 198–209, Jan. 2006.
- [7] G. Antonini, A. Orlandi, and C. Paul, “Internal impedance of conductors of rectangular cross section,” *IEEE Trans. Microw. Theory Tech.*, vol. 47, no. 7, pp. 979–985, Jul. 1999.
- [8] F. Medina, R. Marques, G. Antonini, A. Orlandi, and C. Paul, “Comments on internal impedance of conductors of rectangular cross section [and author’s reply],” *IEEE Trans. Microw. Theory Tech.*, vol. 49, no. 8, pp. 1511–1513, Aug. 2001.
- [9] W. Heinrich, “Comments on internal impedance of conductors of rectangular cross section,” *IEEE Trans. Microw. Theory Tech.*, vol. 49, no. 3, pp. 580–581, Mar. 2001.

- [10] A. Maue, “Zur formulierung eines allgemeinen beugungs-problems durch eine integralgleichung,” *Zeitschrift für Physik A Hadrons and Nuclei*, vol. 126, no. 7-9, pp. 601–618, Jul. 1949.
- [11] J. Meixner, “The behavior of electromagnetic fields at edges,” *IEEE Trans. Antennas Propag.*, vol. 20, no. 4, pp. 442–446, Jul. 1972.
- [12] J. Van Bladel, *Singular Electromagnetic Fields and Sources*. New York: Oxford University Press Inc., 1991.
- [13] J. Geisel, K.-H. Muth, and W. Heinrich, “The behavior of the electromagnetic field at edges of media with finite conductivity,” *IEEE Trans. Microw. Theory Tech.*, vol. 40, no. 1, pp. 158–161, Jan 1992.
- [14] A. Djordjevic, T. Sarkar, and S. Rao, “Analysis of finite conductivity cylindrical conductors excited by axially-independent tm electromagnetic field,” *IEEE Trans. Microw. Theory Tech.*, vol. 33, no. 10, pp. 960–966, Oct. 1985.
- [15] R. Faraji-Dana and Y. Chow, “Ac resistance of two coupled strip conductors,” *Microwaves, Antennas and Propagation, IEE Proceedings H*, vol. 138, no. 1, pp. 37–45, Feb. 1991.
- [16] D. De Zutter and L. Knockaert, “Skin effect modeling based on a differential surface admittance operator,” *IEEE Trans. Microw. Theory Tech.*, vol. 53, no. 8, pp. 2526–2538, Aug. 2005.
- [17] T. Demeester and D. De Zutter, “Quasi-TM transmission line parameters of coupled lossy lines based on the Dirichlet to Neumann boundary operator,” *IEEE Trans. Microw. Theory Tech.*, vol. 56, no. 7, pp. 1649–1660, Jul. 2008.
- [18] ———, “Construction of the Dirichlet to Neumann boundary operator for triangles and applications in the analysis of polygonal conductors,” *IEEE Trans. Microw. Theory Tech.*, recommended for publication.
- [19] ———, “Modeling the broadband resistive and inductive behavior of polygonal conductors,” in *International Conference on Electromagnetics in Advanced Applications, Torino, Italy*, Torino, Italy, Sep. 2009.
- [20] A. Omar and K. Schunemann, “Application of the generalized spectral-domain technique to the analysis of rectangular waveguides with rectangular and circular metal inserts,” *IEEE Trans. Microw. Theory Tech.*, vol. 39, no. 6, pp. 944–952, Jun. 1991.
- [21] R. Faraji-Dana and Y. Chow, “The current distribution and ac resistance of a microstrip structure,” *IEEE Trans. Microw. Theory Tech.*, vol. 38, no. 9, pp. 1268–1277, Sep. 1990.

CHAPTER 6

Conclusions and Future Research

In this work, a new and powerful multiconductor transmission line model was developed, in an attempt to meet the technological requirements for the design of present day and future high-speed metallic interconnections. In parallel with the model itself (Chapter 1), a number of related issues were studied, such as conductor modeling (Chapters 2 and 5) and the discretization of the Dirichlet to Neumann operator (Chapters 3 and 4).

This final chapter summarizes the results and the possibilities of the final model itself, along with its limitations and with some ideas for further research in the field of metallic interconnections.

6.1 Development of a New Transmission Line Model

The previous chapters describe a multi-conductor transmission line model [1–3], developed for the simulation of two-dimensional interconnect structures, consisting of signal conductors, semiconductors, and dielectric materials, all piecewise homogeneous and composed of polygonal subregions. These materials are replaced by equivalent surface sources (charges and currents), defined by the requirement that they excite the same fields as the original configuration. Two relationships can be found between these sources and the fields, (a) by relating fields and sources by means of the Green’s function of free space (or, more generally, of the background medium), and (b) by relating the free space sources for each homogeneous subregion with the original fields at the boundary surface of the material. The latter relationship is formulated by means of the Dirichlet to Neumann (DtN) operator, which can be calculated for general polygonal shapes. Two boundary integral equations are hence found, which are solved by means of the classical Method of Moments (MoM). An appropriate inte-

gration of the equivalent surface sources then leads to the circuit matrices (resistance, inductance, capacitance and conductance) of the coupled transmission line model, and hence to the characteristics of the fundamental propagation modes the configuration supports.

Applications

The model is suited for the simulation of interconnections both on printed circuit boards (PCB), as within integrated circuits (on-chip), irrespective of the different physical properties of these applications. On the PCB level, the signals transmitted over the longest interconnections are often subject to important signal delays due to wave effects, such that an accurate prediction of the p.u.l. inductance and capacitance, but also of the resistive and conductive losses, is primordial. Although the operating frequencies, and especially the highest harmonics, often correspond with a strong skin effect operation of the interconnections, these frequency-dependent parameters can be calculated very accurately, thanks to the introduction of the equivalent surface currents by means of the DtN operator, such that the exponential current profile towards the inside of the conductors is *exactly* accounted for. For on-chip interconnections, the operation frequencies with respect to the geometrical dimensions are such, that the resistive and capacitive properties of the lines dictate the overall behavior. Yet also inductive coupling effects and conductive (substrate) losses are no longer negligible in modern high-speed semiconductor technologies. The influence of high-loss substrates was investigated and incorporated in the model, requiring a reciprocity-based approach. As a result, effects such as slow-wave propagation modes are correctly taken into account.

Limitations

The highest frequencies for which the model is valid, are limited by the validity of the quasi-transverse-magnetic (quasi-TM) approximations [1]. These require that the longitudinal wavelength is considerably larger than the transverse dimensions over which the fields are relevant, and the model is, hence, not suitable if transverse wave phenomena occur. However, the highest operation frequencies relative to the lines' dimensions are often generously within the quasi-TM validity range.

Furthermore, the practical interconnections for which the 2-D model can be applied, should involve lines that are long enough and without any bends, to justify the use of a two-dimensional model. Yet, 2-D models are nowadays often used in practice by circuit designers and will in the near future gain importance with respect to traditional (often quasi-empirical) design formulas. Full 3-D interconnect simulations, especially with finite conductivities and at high frequencies, are computationally still very hard, and therefore not apt for optimization and design.

6.2 The Dirichlet to Neumann Operator

A new method has been developed to calculate the DtN operator for rectangular regions [4]. On the one hand, the original method [5] that makes use of a double summation involving the rectangle's Dirichlet eigenfunctions, is replaced by a much faster calculation method, based on an expansion in parallel-plate waveguide modes, and hence resulting in a single summation only. On the other hand, this novel method additionally allows for the calculation of the *non-differential* DtN operator at the boundary of dielectrics and semiconductors, which is required for capacitance and conductance calculations.

In a further contribution [3], the parallel-plate waveguide expansion technique was extended to the case of triangular conductors, resulting in the *Iterative Combined Waveduide Modes* (ICWM) algorithm, with an extension towards general convex polygons [6].

Extension Towards 3-D Conductors

Apart from the work on the two-dimensional transmission line model, a lot of time was invested in an extension of the surface admittance concept towards three dimensions. We started with the full-wave 3-D calculation of the surface admittance operator on the surface of a rectangular parallelepiped, as a logical extension of the 2-D rectangle. The 3-D surface admittance operator relates the tangential electric field with the equivalent surface current density, obtained from replacing the considered material by the background material. The developed method is based on the superposition of modes from a *rectangular* waveguide, leading to a double summation of modes instead of the triple summation that would result from the traditional 3-D Dirichlet eigenfunction approach [7]. In Appendix C, the basic ideas and field expansions are written down. The explicit projection matrices that result from an expansion in basis functions and the Galerkin testing procedure, are however left out here, as the expressions are quite formidable. Yet it is possible to write the interaction between the electric and magnetic tangential field components on two faces as an efficient matrix product (provided that a specific tensor-product is introduced), and to prove that the resulting surface admittance matrix is symmetric (at least theoretically, if infinite expansion series could be used).

An implementation was written for a pulse function expansion of the field quantities on the boundaries, and gave satisfactory results for internal impedance calculations as described in [8]. However, inserting the resulting matrix in a classical solution method (MoM) was not possible, because the solenoidal and the irrotational field components could not be rigorously separated for a pulse function discretization (not even by using the solenoidal and irrotational expansion functions, due to the truncation of the series expansions), and the so-called low-frequency breakdown caused unacceptable numerical inaccuracies.

This problem could have been solved by using the classical rooftop basic functions. That was however not implemented, because of another, and more fundamental problem. Imagine, e.g., a cube, roughly discretized using 15 intervals on each side. With six sides, and four field components per side, this would result in a surface admittance matrix containing almost 30 million entries. Storing and loading, and especially inversion of such a large (dense) matrix would be computationally too heavy, especially for finer discretizations, required for accurately capturing current crowding effects or to represent charge densities near corners. In other numerical methods, such as the Fast Multipole Method adapted for low-frequency problems [9], the multiplication of such a matrix with a candidate solution is calculated *directly* (without having to store the whole matrix), for use in an iterative procedure, and hence computationally less demanding.

6.3 Conductor Modeling

In the field of conductor modeling, the transmission line model research resulted in three specific contributions. First of all, as a demonstration of the model's accuracy in handling thick conductors over a broad frequency range, the properties of coated and layered on-chip conductors were investigated [2].

In another contribution [8], it was shown that the knowledge of the surface admittance operator of a conductor, containing material and frequency data but independent of the surrounding environment, suffices to investigate the conductor's internal impedance. The developed techniques allowed a careful comparison with analogous contributions found in literature, and a generalization of these results for, e.g., complicated conductor shapes or composite conductors.

Finally, the ICWM algorithm was used in a thorough investigation of the fields at sharp conductor edges, allowing to make a link with the global circuit properties of conductors, and to investigate how these are influenced by the conductor edges.

6.4 Further Research on Interconnections

In this section, a few suggestions for further research topics are listed. Some of them directly follow from the research presented in this dissertation, and others are just vague ideas, but might be relevant in the light of future advances in metallic interconnects. However, the presented ideas were not yet further explored, and neither has their feasibility been investigated, and they should therefore be approached with a fair share of scepticism.

Transmission Line Modeling

- The DtN concept for conductors or non-planar substrates could be integrated in a solver that already handles a one-dimensional layered substrate, for which the Green's function can be determined. This would highly improve the efficiency of the method, especially for on-chip applications as, e.g., the configuration in Fig. 1.7, where the computation of the DtN operator of the semiconducting substrate requires much more computation time and memory than of all the conductors together, considering its dimensions.
- For the calculation of the DtN operator itself, improvements are still possible, both when using the direct calculation method for rectangular geometries, as well as for triangular geometries by means of the ICWM algorithm. The reason is that the expansion techniques are not yet fully optimized for efficiency. The correction technique of the Gibbs effect (see Chapters 3 and 4) by means of one extra expansion function per corner (being non-zero at that corner), could be extended with additional basis functions, such that less terms are needed in the overall expansion. The coefficients of these basis functions must then be determined by solving an appropriate set of equations. For example in the case of conductors, a number of extra basis functions could be used that are each constant on one side of the considered polygon and describe the exact behavior on the inside. In order to describe the very-low-frequency case, the contributions of higher order expansion functions would hence be much smaller than by using the method as described in this work, and less terms would be required. A further increase in efficiency could perhaps be obtained by fast transform techniques for the boundary expansion coefficients.
- It would be interesting to simulate transmission line structures beyond the quasi-TM frequency range, and implement a 2-D full-wave solver. For that, the DtN operator that maps the electric field onto its normal derivative should be extended as to relate the total tangential electric and magnetic fields. To that end, specific expansion functions are needed for the different fields (i.e., analogous to Appendix C, but one dimension lower). The method could also be based on the same ideas of waveguide mode expansions (in this case of both electric and magnetic) parallel-plate waveguides). Furthermore, no longer the quasi-static Green's function (i.e., the singular logarithmic term from the full-wave Green's function), but the full-wave 2-D Green's function itself needs to be used.
- The presented two-dimensional transmission line model in the frequency domain could be transformed into a parametric state-space model, using, e.g., vector fitting techniques [10], in order to investigate time domain responses of bit streams as input signals. It would be interesting to see, how the geometry-dependent frequency-domain parameters (RLGC matrices of the lines, in com-

bination with the source and load impedances), influence the bit error rate of a realistic transmission channel, or how the inductive and capacitive coupling parameters result in cross-talk effects.

- In line with the topic mentioned above, but not necessarily in the time domain, the influence of realistic (even non-linear) source and load circuits could be investigated. It would be equally interesting to take end effects into account, i.e., the fact that the interconnect configuration can no longer be assumed two-dimensional, near its end points.

Conductor Modeling

- The DtN technique as applied here, only deals with perfectly smooth conductors, and assumes their dimensions are exactly determined. It would be useful to take into account imperfections such as a surface roughness, or a statistical variation of the dimensions, due to variable parameters in the manufacturing process. A possible strategy would be, to investigate whether the deterministic surface admittance concept could be modified to take into account these effects, especially at skin effect frequencies.
- One particularly interesting possible research topic deals with *bent* conductors with a finite conductivity. Instead of immediately solving the full-wave equations, one could think of extending the 2-D quasi-TM techniques to a consistent approach for low-frequency interconnect configurations in three dimensions, starting from an equivalent situation in which the conductors are replaced by unknown surface sources in free space. This could provide a fast approximative method to calculate the scattering coefficients, or an equivalent circuit model involving transmission lines. In this way, time-consuming full-wave numerical simulations could be avoided, as they often have difficulties with a finite conductivity at skin effect frequencies and are not practical for design purposes. The strengths of such a method with respect to traditional methods like the partial element equivalent circuit (PEEC) method [11, 12], would be in the simulation of current crowding effects with a surface integral equation only, and in the simplifications that nevertheless accurately capture the current distribution.

Consider, e.g., the very simple situation of a bent conductor above a ground plane. If both the ‘transverse’ dimensions of the lines over which the fields are relevant, and the region near the bend or corner, are small as compared to the wavelength, the following strategy could be adopted. In the cross-section perpendicular to the lines in the ‘2-D’ zone, and in the region covering the bend, the surface value of the scalar electric potential could be considered a constant (as in the 2-D case) as to formulate an equivalent capacitance problem. In the ICWM algorithm, the actual 2-D current pattern is found by an iterative

method starting from the situation where the sides of a triangle do not interfere. A logical choice here would therefore be to adopt an iterative method as well, in order to determine either the equivalent surface current, or an expansion of the inside current profile in terms of waveguide modes, including the reflexion and transmission of the applied excitation. A suitable starting point for such an iterative process could be the 2-D field profiles at both sides of the corner, as if the lines would not interfere and no reflexions would occur.

Applications of the ICWM algorithm

- The ICWM algorithm, based on a superposition of modes from waveguides with a different orientation, was first developed as an alternative to using a single complete set of waveguide modes, which lacked accuracy due to unstable exponential terms. The initial purpose was however not to find an expression for the DtN operator, but to numerically determine the Dirichlet eigenfunctions and eigenvalues of an arbitrary triangle, in an attempt to extend the original Dirichlet expansion technique of [5] to triangles. Using a single complete set of modes, we managed to only determine a few hundred of Dirichlet functions with a sufficient accuracy, by far not enough for an accurate expansion of high-frequency current densities. However, as soon as the correct expansion technique became clear, based on partial sets of modes from different waveguides, the purpose was no longer to find the Dirichlet functions, but instead, to directly calculate the DtN operator, by analogy with the new calculation technique for rectangles. Regarding the accuracy of the iterative technique [3], the resulting method could probably be modified as to calculate the Dirichlet and Neumann eigenfunctions of a triangle (or convex polygon), as well as the corresponding eigenvalues.
- As presented in [3], the convergence of the ICWM is only guaranteed if only *evanescent* waveguide modes are used, and the applications are therefore restricted to, in terms of wavelengths, ‘low-frequency’ problems. It would be interesting to investigate how the expansion technique could be extended to problems with the size in the order of a wavelength or larger, especially for lossless materials. The same argumentation as in the original algorithm shows that a solution exists. Three sets of modes that are complete on one of the sides, form the exact solution inside the triangle and are zero at the opposite corner, must be sufficient to represent the overall solution (due to the uniqueness of the solution, but omitting possible resonances), even if they are not exponentially damped. The convergence of the iterative method might be an issue, as well as a good ‘initial’ expansion. A direct approach instead of an iterative procedure could present an alternative solution technique. Note that for the numerical determination of the Dirichlet eigenfunctions of a triangle as mentioned above, apart from the evanescent modes, a truncated series of these ‘propagating’ waveguide

modes is required.

- It would be possible to apply the ICWM algorithm to other geometries than just triangles (or convex polygons). One could think of geometries involving, e.g., circle segments, and an expansion using a combination of parallel-plate waveguide and circular waveguide modes. Even in three dimensions, the algorithm could hold, for geometries such as a general parallelepiped, because the Dirichlet and Neumann eigenfunctions for its sides are known. For geometries such as a tetrahadron, the numerically determined Dirichlet functions (in full-wave applications completed with the Neumann functions), of the faces would have to be used. Towards the inside, the exact behavior can then be written down in terms of complex exponential functions, by means of the Dirichlet eigenvalues of the corresponding face and the wavenumber of the material inside.

The determination of the surface admittance matrix for three-dimensional shapes would only be practical, provided not too many discretization intervals are required, otherwise the resulting matrices would be very large, as already mentioned. On the other hand, in certain cases not the projection of the expansion functions on, e.g., rooftop functions on the faces, but the expansion functions *themselves* with corresponding coefficients could be used to represent the fields. A possible application could be the following. In numerical methods with a regular grid, oblique surfaces are often difficult to model. The DtN operator of a prism, even with very few expansion functions, could for instance be used as a transition between the regular grid and an oblique material boundary, such that the boundary conditions could be enforced with greater accuracy than on the original staircase representation of the surface.

Bibliography

- [1] T. Demeester and D. De Zutter, “Quasi-TM transmission line parameters of coupled lossy lines based on the Dirichlet to Neumann boundary operator,” *IEEE Trans. Microw. Theory Tech.*, vol. 56, no. 7, pp. 1649–1660, Jul. 2008.
- [2] ——, “Modeling the broadband inductive and resistive behavior of composite conductors,” *IEEE Microw. Wireless Compon. Lett.*, vol. 18, no. 4, pp. 230–232, Apr. 2008.
- [3] ——, “Construction of the Dirichlet to Neumann boundary operator for triangles and applications in the analysis of polygonal conductors,” *IEEE Trans. Microw. Theory Tech.*, recommended for publication.
- [4] ——, “Construction and applications of the Dirichlet to Neumann operator in transmission line modeling,” *J. Elec. Eng. Comp. Sci.*, accepted for publication.
- [5] D. De Zutter and L. Knockaert, “Skin effect modeling based on a differential surface admittance operator,” *IEEE Trans. Microw. Theory Tech.*, vol. 53, no. 8, pp. 2526–2538, Aug. 2005.
- [6] T. Demeester and D. De Zutter, “Modeling the broadband resistive and inductive behavior of polygonal conductors,” in *International Conference on Electromagnetics in Advanced Applications, Torino, Italy*, Torino, Italy, Sep. 2009.
- [7] G. Lippens, “Model order reduction in the context of interconnections,” Ph.D. dissertation, 2005.
- [8] T. Demeester and D. De Zutter, “Internal impedance of composite conductors with arbitrary cross section,” *IEEE Trans. Electromagn. Compat.*, vol. 51, no. 1, pp. 101–107, Feb. 2009.
- [9] I. Bogaert, J. Peeters, and F. Olyslager, “A nondirective plane wave MLFMA stable at low frequencies,” *IEEE Trans. Antennas Propag.*, vol. 56, no. 12, pp. 3752–3767, Dec. 2008.
- [10] D. Deschrijver, M. Mrozowski, T. Dhaene, and D. De Zutter, “Macromodeling of multiport systems using a fast implementation of the vector fitting method,” *IEEE Microw. Wireless Compon. Lett.*, vol. 18, no. 6, pp. 383–385, Jun. 2008.

-
- [11] K. Coperich, A. Ruehli, and A. Cangellaris, “Enhanced skin effect for partial-element equivalent-circuit (PEEC) models,” *IEEE Trans. Microw. Theory Tech.*, vol. 48, no. 9, pp. 1435–1442, Sep. 2000.
 - [12] A. Ruehli, G. Antonini, J. Esch, J. Ekman, A. Mayo, and A. Orlandi, “Nonorthogonal PEEC formulation for time- and frequency-domain em and circuit modeling,” *Electromagnetic Compatibility, IEEE Transactions on*, vol. 45, no. 2, pp. 167–176, May 2003.

APPENDICES

APPENDIX A

Conference Papers

A.1 Design and Simulation of On-Chip Lossy Transmission Line Pairs [1]

Thomas Demeester and Daniël De Zutter

★ ★ ★

A quasi-TM reciprocity based multiconductor transmission line model is used to investigate the influence of the geometry on the performance of on-chip transmission line pairs for high-frequency differential signal transmission. It is shown that both the knowledge of the fundamental transmission line modes and of the internal impedance of both connected circuits, are essential for a good design.

A.1.1 Introduction

In the design of very large scale integration (VLSI) circuits, wave phenomena on interconnects are becoming responsible for significant signal integrity problems, due to the always increasing frequencies. Commonly used at the highest frequencies is the technique of differential signaling in order to reduce the impact of electromagnetic noise and coupling with neighboring circuits. This means long interconnects have to be modeled as multi-conductor transmission lines. Only few electromagnetic models for the determination of the fundamental propagation modes allow the combined simulation of the finite conductivity of both the signal lines and the semiconducting substrate. An accurate quasi-TM two-dimensional model has been proposed in [2], for the case of a single conductor. Based on power considerations, the current in the transmission line equivalent was proven to be a suitably weighted combination of the current in the signal line and the current through the substrate. The theory of [2] can

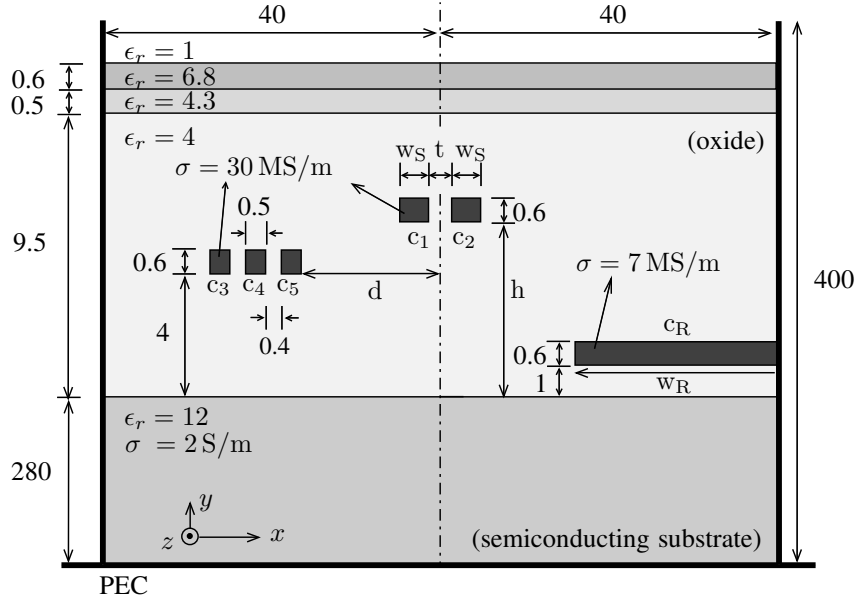


Figure A.1: On-chip transmission line structure with signal conductor pair (c_1, c_2). All dimensions are in micrometers.

be extended to the multi-conductor case, provided mode reciprocity is invoked instead of the conservation of power. A rigorous derivation of such a multi-conductor model within the quasi-TM frequency range is given in [3]. The use of the Dirichlet to Neumann boundary operator leads to a pure boundary integral equation formulation, allowing the fast simulation of complex configurations. In this paper we propose some design criteria, based on the transmission line properties of differential lines in combination with the circuit impedances of source and load. The propagation characteristics of the lines will be determined by using the model from [3].

A.1.2 Design of a Differential Pair

Consider the two-dimensional structure shown in Fig. A.1, with a conductor pair (c_1, c_2) embedded in a dielectric layer on a semiconducting substrate, above a perfect electric conducting (PEC) ground. PEC walls are used to simulate a wide slab. A reference conductor (c_R), kept on zero volt, and some neighboring conductors ($c_3 - c_5$) are also shown on Fig. A.1. The signal pair (c_1, c_2) is, e.g., needed to transmit high-frequency signals from a chip input amplifier to the output buffer. For a fixed line length of $960 \mu\text{m}$, we will optimize the geometry parameters (w_S, t, h, w_R, d) in order to minimize wave effects.

The quasi-TM modal analysis of the signal lines leads to the capacitance and con-

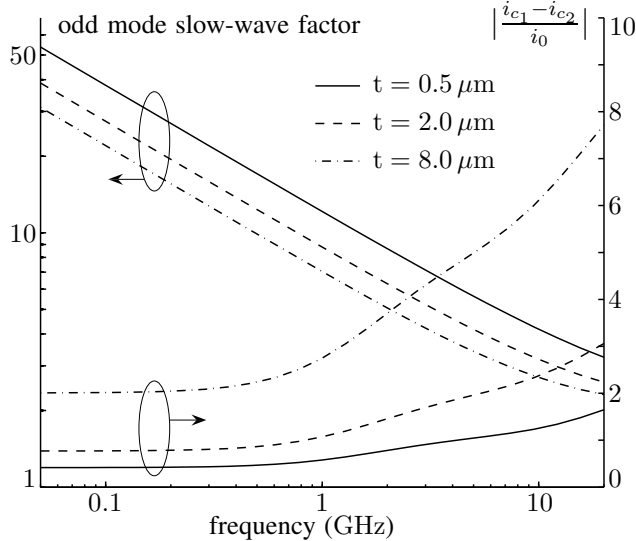


Figure A.2: Left axis: odd mode SWF, for $w_S = 0.6$, $h = 5.5$, $w_R = 16$, $d = 19.2$ (all in μm), and for different values of t . Right axis: normalized differential signal current $|(i_{c_1} - i_{c_2})/i_0|$, induced by a current i_0 through conductor c_5 .

ductance matrices (per unit length) C and G , and the inductance and resistance matrices L and R . The lines c_3 , c_4 and c_5 are, e.g., used to feed certain circuits with current. Here, we force their current to zero (which is a good approximation for high input impedance circuits), such that the 5×5 circuit matrices can be reduced to 2×2 matrices, relating voltages and currents on the signal lines only w.r.t. the reference conductor c_R (except for Fig. A.2, when the influence of line c_5 is investigated). The propagation constants are then found as the square root of the eigenvalues of $-(j\omega C + G)(j\omega L + R)$. For a perfectly symmetric configuration, the circuit matrices would have equal diagonal entries (subscript s) and equal off-diagonal entries (subscript m). The differential mode propagation constant β_d , corresponding to an $e^{-j\beta_d z + j\omega t}$ field dependence, would be given by

$$\beta_d^2 = -(j\omega(L_s - |L_m|) + (R_s - R_m)) \cdot (j\omega(C_s + |C_m|) + (G_s - G_m)) \quad (\text{A.1})$$

The configuration of Fig. A.1 is not perfectly symmetric with respect to the dashed line in Fig. A.1, but still the actual propagation constants agree with an almost entirely ‘odd’, resp. an ‘even’ mode. Hence, (A.1) can be used to explain the line properties for a differential excitation. On the one hand, we want to minimize the odd mode slow-wave factor (SWF), determined as $\text{Re}(\beta_d/k_0)$ (with k_0 the free space wave number), and the attenuation $-\text{Im}(\beta_d)$. The line then becomes electrically shorter (as the modal

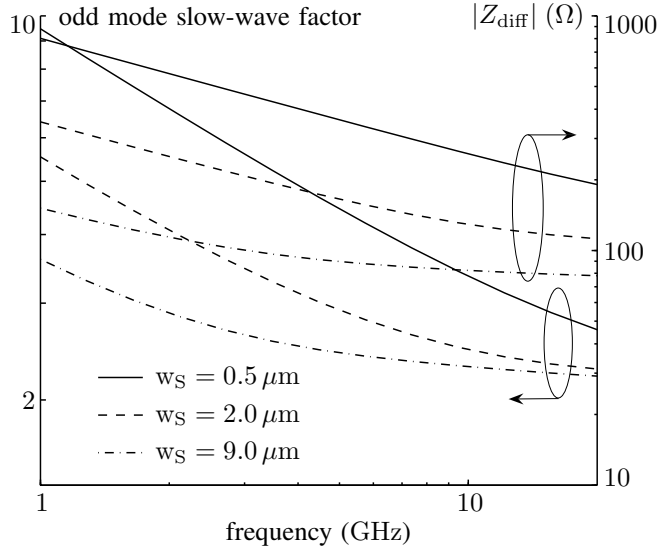


Figure A.3: Left axis: odd mode SWF, for $h = 5.5$, $w_R = 16$, $d = 19.2$, and $t = 2$ (all in micrometers), and for different values of w_S . Right axis: diff. characteristic line impedance $|Z_{\text{diff}}|$.

wave length is inversely proportional to the SWF), and wave effects are reduced. On the other hand, the differential characteristic impedance Z_{diff} of the line,

$$Z_{\text{diff}} = 2\sqrt{(j\omega(L_s - |L_m|) + (R_s - R_m)) / (j\omega(C_s + |C_m|) + (G_s - G_m))} \quad (\text{A.2})$$

should remain large enough, to prevent the input impedance seen by the source from becoming too small, which in turn would lead to an unacceptable voltage drop.

In the following, we will briefly discuss some of our results. Both the attenuation and the SWF decrease by increasing the distance t between both signal conductors (see Fig. A.2 for the SWF, the attenuation is not shown). However, t has to remain much smaller than the distance d to the nearest neighboring circuits or lines. As an illustration, we excite c_5 with a current i_0 , while keeping c_1 and c_2 on zero volt. Fig. A.2 shows the absolute value of the induced differential current component ($i_{c_1} - i_{c_2}$) through the signal conductors. An increase in t results in a higher induced current. Obviously, the effect is weaker for larger values of d . Increasing the width w_S of the signal conductors leads to a lower SWF and a lower attenuation. However, the SWF does not change much further, as soon as R_s becomes lower than $j\omega L_s$ for the highest relevant frequencies (as is the case for $w_S = 8.0 \mu\text{m}$ in Fig. A.3). Further widening the conductors only leads to a lower Z_{diff} , as shown in Fig. A.3. Fig. A.4 shows how the signal lines are used in a source-load configuration. For typical but

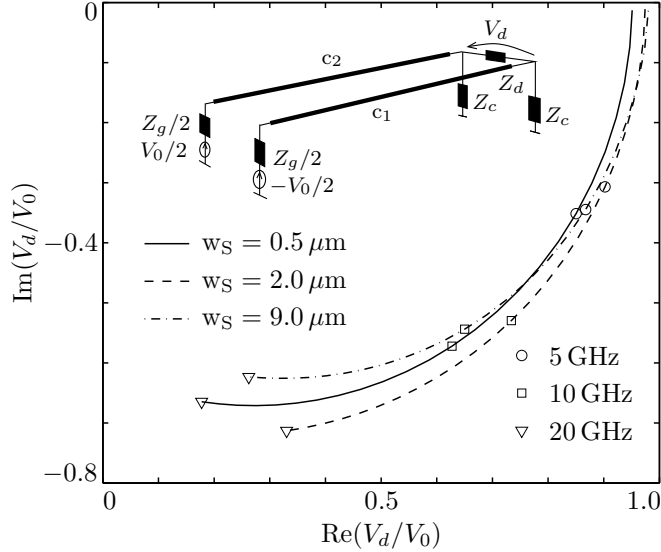


Figure A.4: Load voltage V_d (for the same geometry as Fig. A.3). Impedance values are $Z_g = 120 \Omega$, $Z_g = Z_c = 10 \text{ k}\Omega$.

simplified (frequency-independent) impedances, the complex differential load voltage V_d is shown, with the frequency as a parameter. For $w_S = 0.5 \mu\text{m}$, the SWF and attenuation are higher than for $w_S = 2 \mu\text{m}$, due to the larger line resistance. For $w_S = 8 \mu\text{m}$, V_d is again lower, due to the decreased line impedance.

Analogous considerations regarding the SWF and Z_{diff} , show that it is not recommended to increase w_R such that c_1 and c_2 become situated directly above the reference conductor, and that the height h of the signal lines above the semiconductor substrate should be as large as possible.

A.1.3 Conclusion

It is shown how the performance of an on-chip differential pair interconnect depends on its geometry, considering both the transmission line properties and the circuits, connected by the lines.

A.2 Modeling the Broadband Resistive and Inductive Behavior of Polygonal Conductors [4]

Thomas Demeester and Daniël De Zutter



This paper describes an accurate method to discretize the Dirichlet to Neumann boundary operator for a convex polygonal conductor. The technique is based on an expansion of the boundary value of the current density. Because the corresponding expansion functions exhibit the exact current behavior inside the conductor, they ensure a very good accuracy up to skin effect frequencies. In combination with a classical boundary integral method and the Method of Moments, the Dirichlet to Neumann technique allows for a direct determination of the resistive and inductive properties of transmission line configurations constructed from these conductors, as is illustrated with some numerical examples.

A.2.1 Introduction

For accurate signal integrity simulations of interconnect structures, both on the printed circuit board (PCB) level as on-chip, a good conductor model is indispensable. On the one hand, the finite conductivity, thickness and the exact conductor shape have to be rigorously modeled, in order to calculate the transmission line parameters of the considered interconnections, see [5, 6]. On the other hand, the interconnections can be treated with the quasi-TM approximations of Maxwell's equations [2, 3], which assume that the dimensions of the transverse cross-section of the considered interconnections are sufficiently smaller than the substrate wavelength, such that wave phenomena only occur in the longitudinal direction.

The current crowding effect inside a conductor, from DC to tens of GHz, can be described by means of the surface admittance operator \mathcal{Y} , introduced in [7], which is calculated by means of the Dirichlet to Neumann boundary operator of the conductor. To determine the per unit length resistance matrix R and the inductance matrix L of a particular transmission line configuration, the conductors are replaced by an equivalent surface current density on its boundary c , residing in the background medium.

Starting from the conductor's geometry and material properties, the surface admittance operator \mathcal{Y} relates the boundary value of the longitudinal electric field e_z with the equivalent surface current density j_{eq} ,

$$j_{eq}(\mathbf{r}) = \oint_c \mathcal{Y}(\mathbf{r}, \mathbf{r}') e_z(\mathbf{r}') d\mathbf{c}', \quad \mathbf{r} \in c. \quad (\text{A.3})$$

A second relationship between equivalent sources and fields is found using the Green's

function of the background medium, and allows to determine the fields with the Method of Moments.

Originally, the surface admittance matrix \mathbf{Y} (as the matrix discretization of \mathcal{Y}) could only be calculated for geometries of which the Dirichlet eigenfunctions are known [3, 7], or combinations of these [6, 8]. In [9] we introduced the Iterative Combined Waveguide Modes (ICWM) algorithm, to calculate \mathbf{Y} for triangles, for which the Dirichlet eigenfunctions are not readily available, based on an expansion of e_z in waveguide modes inside the triangle.

Section A.2.2 of the current paper shows how the ICWM method can be extended to arbitrary convex polygons, such that these no longer have to be modeled as combinations of triangles. A possible application is modeling on-chip conductors, which often have a trapezoidal cross-section, due to underetching during the manufacturing process. In Section A.2.3, some simulation results are shown, focussing on the influence of the finite conductivity and of the conductor's shape. Finally, Section A.2.4 formulates some conclusions.

A.2.2 The Dirichlet to Neumann Operator of a Convex Polygon

The surface admittance operator \mathcal{Y} of a 2-D conductor P is given by

$$\mathcal{Y}(\mathbf{r}, \mathbf{r}') = \frac{1}{j\omega\mu_0} (\mathcal{D}(\mathbf{r}, \mathbf{r}') - \mathcal{D}_0(\mathbf{r}, \mathbf{r}')) \quad (\text{A.4})$$

with the Dirichlet to Neumann (DtN) operator \mathcal{D} defined for a quantity ψ by

$$\frac{\partial\psi(\mathbf{r})}{\partial n} = \oint_c \mathcal{D}(\mathbf{r}, \mathbf{r}') \psi(\mathbf{r}') d\mathbf{c}', \quad \mathbf{r} \in c \quad (\text{A.5})$$

for ψ satisfying

$$\nabla_t^2 \psi = -k^2 \psi(\mathbf{r}), \quad \mathbf{r} \in P \quad (\text{A.6})$$

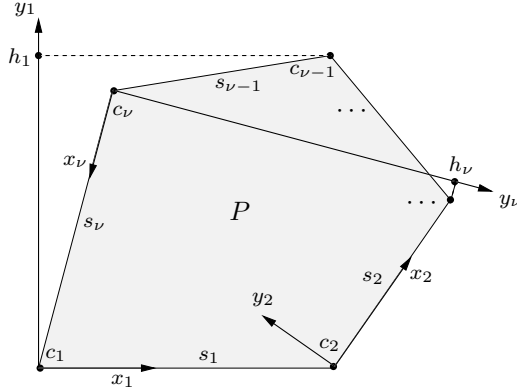
with $k^2 = -j\omega\mu_0\sigma$ and $\partial/\partial n$ the outward pointing normal derivative on c . The DtN operator \mathcal{D}_0 also satisfies (A.5) and (A.6), but with $k = 0$.

The considered conductor P is the convex polygon with boundary c shown in Fig A.5. P has ν sides s_i (with length l_i) and corners c_i ($i = 1, \dots, \nu$). A local coordinate system (x_i, y_i) is associated with each side s_i , see Fig A.5. The distance from a side s_i to its farthest corner point of P is called h_i .

In order to discretize (A.5), ψ is expanded on P as

$$\psi(\mathbf{r}) = \sum_{i=1}^{\nu} \psi^{(i)}(x_i, y_i), \quad \mathbf{r} \in P \quad (\text{A.7})$$

in which each term is expressed in terms of the coordinate system (x_i, y_i) , associated

Figure A.5: Convex polygon P .

with side s_i . The subfunctions $\psi^{(i)}$ are given by

$$\psi^{(i)}(x_i, y_i) = \sum_{n=0}^{N_i} A_{c_i, n} f_{c_i, n}(x_i, y_i) \quad (\text{A.8})$$

with

$$\begin{aligned} f_{c_i, 0}(x_i, y_i) &= (e^{j\beta_{i, 0} y_i} - e^{-j\beta_{i, 0} (y_i - 2h_i)}) \\ &\times \cos \frac{\pi x_i}{2l_i} \end{aligned} \quad (\text{A.9})$$

$$\begin{aligned} f_{c_i, n}(x_i, y_i) &= (e^{j\beta_{i, n} y_i} - e^{-j\beta_{i, n} (y_i - 2h_i)}) \\ &\times \sin \frac{n\pi x_i}{l_i}, \quad n > 0 \end{aligned} \quad (\text{A.10})$$

and

$$\beta_{i, 0}^2 = k^2 - \left(\frac{\pi}{2l_i}\right)^2 \quad (\text{A.11})$$

$$\beta_{i, n}^2 = k^2 - \left(\frac{n\pi}{l_i}\right)^2, \quad n > 0. \quad (\text{A.12})$$

with the square root of $\beta_{i, n}^2$ chosen such that $\text{Im}(\beta_{i, n}) > 0$. The number of terms N_i in $\psi^{(i)}$ should be large enough for an accurate representation of ψ on side s_i . It is observed that the expansions (A.8) all satisfy (A.6), but are overcomplete on side s_i . The ν terms for $n = 0$ are however necessary to ensure the correct value in the corners, where the sine expansion of the terms for $n > 0$ does not converge and would otherwise lead to an important Gibbs phenomenon.

First, the coefficients $A_{c_i, 0}$ are determined. Their determination is quite more

involved for a general polygon than for a triangle [9], because the functions $f_{c_i,0}$ are $(1 - e^{j\beta_{i,0}2h_i})$ in c_i and zero in c_{i+1} (or c_1 for $i = \nu$), but also non-zero in $(\nu - 3)$ of the remaining corner points, such that they interfere with one another. The superposition of the functions $f_{c_i,0}$ in each of the corners must equal the actual corner value of ψ , or

$$\left[\sum_{i=1}^{\nu} A_{c_i,0} f_{c_i,0} \right]_{c_j} = \psi_{c_j}, \quad j = 1, \dots, \nu \quad (\text{A.13})$$

which leads to a matrix relationship between the coefficients $A_{c_i,0}$ (taken together into the column vector \mathbf{A}_0) and the corner values ψ_{c_j} (in vector Ψ_0)

$$\mathbf{F}_0 \mathbf{A}_0 = \Psi_0. \quad (\text{A.14})$$

Inversion of the $\nu \times \nu$ matrix \mathbf{F}_0 yields the coefficients $A_{c_i,0}$ for an arbitrary boundary value of ψ . The matrix is well-conditioned because, at DC, the expansion functions $f_{c_i,0}$ decrease linearly inside P to reach zero at the corner the farthest away from side s_i , and they decrease exponentially when the diffusion term in (A.6) starts playing a role. In other words, the fact that \mathbf{F}_0 is well-conditioned, is analogous to the good convergence properties of the ICWM scheme, as motivated in [9].

In a second step, the remaining function “ ψ minus the contribution of the $f_{c_i,0}$ ” is expanded using the general functions $f_{c_i,n}$ ($n > 0$). The expansion is convergent everywhere, because the expanded function has identical zero corner values. The reason why instead of sine boundary functions, a cosine expansion cannot be used (although well-convergent on the corners), is that their normal derivative would not always converge (e.g., for 90° angles).

The functions $A_{c_i,n} f_{c_i,n}$ ($n > 0$) can be interpreted as modes of parallel plate waveguides, perpendicular to the sides and with the plates through the end points. Their amplitude for an arbitrary boundary value of ψ on c can be determined by means of the ICWM algorithm, as introduced in [9].

Once the expansions (A.8) are fully determined in terms of a general boundary value of ψ , the normal derivative of the subfunctions leads to $\partial\psi/\partial n$ on c , and via (A.5) to the DtN operator.

The reason why the algorithm is only robust for convex polygons, are the exponential functions in (A.10) which would increase rapidly for any $y_i < 0$, and the numerical results would no longer be accurate. However, non-convex structures can be handled by combining the DtN matrices of convex subregions, as described in [8].

In the special case of a rectangular conductor, the different subfunctions $\psi^{(i)}$ do not interfere, and the situation simplifies to the case described in [8], which uses the modes of two perpendicular parallel plate waveguides.

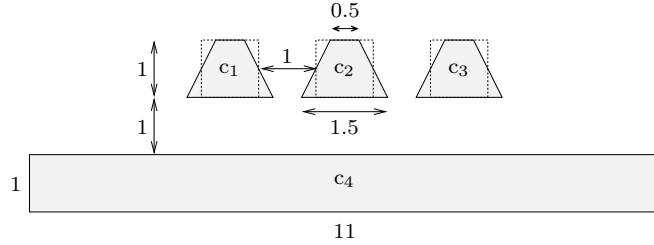


Figure A.6: Three signal lines (c_1 , c_2 , c_3) and one reference line (c_4), all Al-oxide ($\sigma = 35.7 \text{ MS/m}$). All dimensions are in micrometers.

A.2.3 Numerical Results

Consider the four line configuration shown in Fig. A.6, consisting of three trapezoidal signal conductors and a rectangular reference conductor.

Here, we concentrate on the inductance and resistance values. In the quasi-TM limit these values do not depend on the (layered) dielectric background medium in which they reside (provided this medium is not a semi-conductor with a high conductivity).

In Fig. A.7 and A.8, some of the resistance and inductance elements of the structure are presented. The solid lines are the results for the trapezoidal conductor configuration. They are compared to the analogous case with rectangular signal conductors (actually squares with a side length of $1 \mu\text{m}$, and hence the same cross-sectional area), indicated in dashed lines. The results for the rectangular conductors were taken from [7], where their calculation was based on the Dirichlet expansion of e_z in the conductors. As a verification, the transmission line parameters of the square signal lines were also calculated with the ICWM algorithm and yielded identical results, confirming the accuracy of the ICWM method.

The resistance elements are very similar for both configurations. However, a surprising result is observed for the high-frequency self-resistance. Note that only R_{11} is shown here (corresponding to the left conductor of Fig. A.6), being identical to R_{33} and comparable with R_{22} (which would overload the figure). The self-resistance of the trapezoidal conductors becomes higher than for the rectangular lines, as soon as current crowding starts to appear (the difference is about 5% at the highest shown frequency). One would expect the opposite behavior whereby the rectangular conductor with the shortest perimeter would have the highest resistance at skin effect frequencies. The reason for the observed phenomenon is the particular current distribution near the sharp corners of the trapezoidal lines, which still has an important influence on the overall behavior at the shown frequencies. A detailed current distribution will be given at the oral presentation.

The inductance elements are shown in Fig. A.8. At the highest frequencies, they are compared to the analogous configurations with perfect electric conductors, again

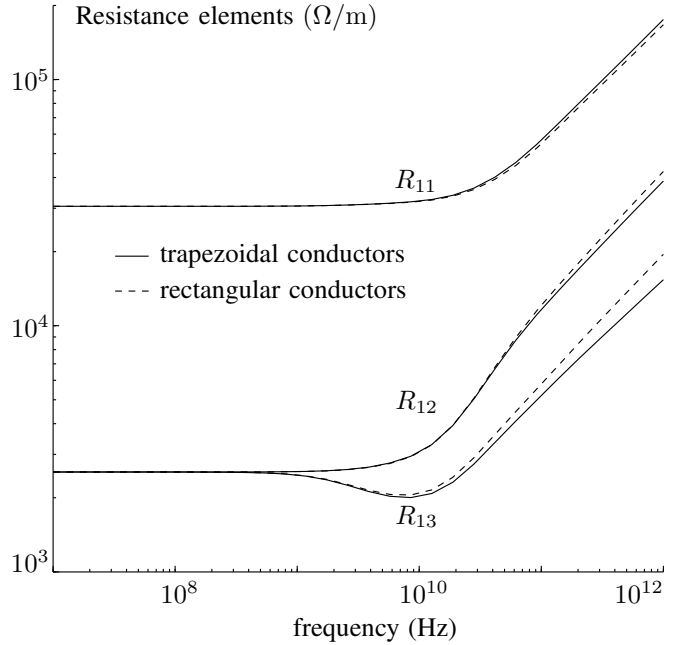


Figure A.7: Resistance elements R_{11} , R_{12} and R_{13} (in Ω/m) for the configuration of Fig. 2 with the trapezoidal signal conductors (solid lines), and with the rectangular conductors (dashed lines; data from [7]).

for both the trapezoidal and the rectangular signal lines case. The values for perfect conductors are the limiting values for their finite conductivity counterparts, when the frequency goes to infinity and they are shown as the horizontal lines at the highest frequencies in Fig. A.8. The self-inductance L_{11} is, over the whole frequency range, lower for the trapezoidal conductors. This is due to the fact that the proximity effect of the ground conductor is more dominant for the wider lower side of the trapezoidal conductor as compared to the rectangular case. A similar phenomenon leads to the slightly lower mutual inductance between the trapezoidal signal lines, but also to an increased capacitive coupling.

A.2.4 Conclusion

This paper introduces an extension of the Iterative Combined Waveguide Modes algorithm, to discretize the Dirichlet to Neumann operator on polygonal conductors, in order to calculate their surface admittance matrix. This allows to take into account their exact shape and material properties in the interconnect characterization, from DC up to skin effect frequencies. In some numerical examples, it was seen how the

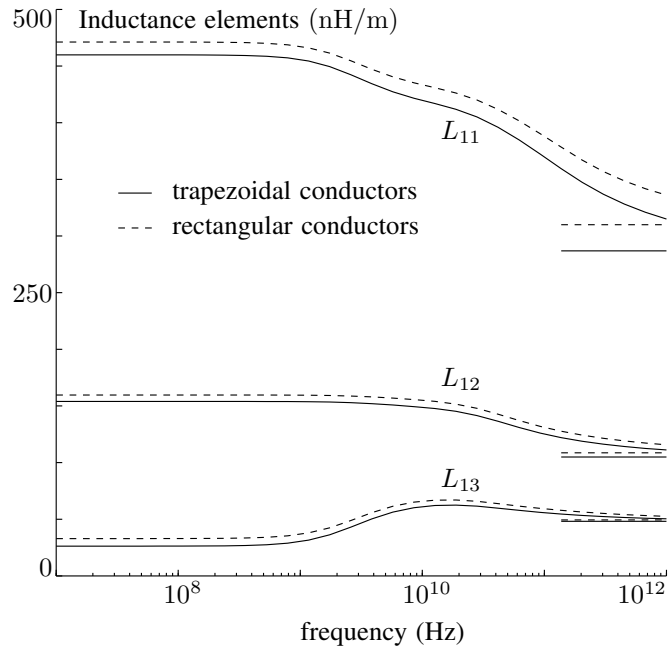


Figure A.8: Inductance elements L_{11} , L_{12} and L_{13} (in nH/m) for the configuration of Fig. 2 with the trapezoidal signal conductors (solid lines), and with the rectangular conductors (dashed lines; data from [7])

broadband behavior of trapezoidal conductors was influenced by the corner effect, with respect to rectangular conductors, or with respect to their perfectly conducting trapezoidal counterparts.

Bibliography

- [1] T. Demeester and D. De Zutter, “Design and simulation of on-chip lossy transmission line pairs,” in *12th IEEE Workshop on Signal Propagation on Interconnects*, Avignon, France, May 2008.
- [2] G. Plaza, R. Marques, and F. Medina, “Quasi-TM MoL/MoM approach for computing the transmission-line parameters of lossy lines,” *IEEE Trans. Microw. Theory Tech.*, vol. 54, no. 1, pp. 198–209, Jan. 2006.
- [3] T. Demeester and D. De Zutter, “Quasi-TM transmission line parameters of coupled lossy lines based on the Dirichlet to Neumann boundary operator,” *IEEE Trans. Microw. Theory Tech.*, vol. 56, no. 7, pp. 1649–1660, Jul. 2008.
- [4] ——, “Modeling the broadband resistive and inductive behavior of polygonal conductors,” in *International Conference on Electromagnetics in Advanced Applications, Torino, Italy*, Torino, Italy, Sep. 2009.
- [5] K. Coperich, A. Ruehli, and A. Cangellaris, “Enhanced skin effect for partial-element equivalent-circuit (PEEC) models,” *IEEE Trans. Microw. Theory Tech.*, vol. 48, no. 9, pp. 1435–1442, Sep. 2000.
- [6] T. Demeester and D. De Zutter, “Modeling the broadband inductive and resistive behavior of composite conductors,” *IEEE Microw. Wireless Compon. Lett.*, vol. 18, no. 4, pp. 230–232, Apr. 2008.
- [7] D. De Zutter and L. Knockaert, “Skin effect modeling based on a differential surface admittance operator,” *IEEE Trans. Microw. Theory Tech.*, vol. 53, no. 8, pp. 2526–2538, Aug. 2005.
- [8] T. Demeester and D. De Zutter, “Applications of the Dirichlet to Neumann boundary operator in transmission line modeling,” presented at the 20th International Zurich Symposium on Electromagnetic Compatibility, Jan. 2009.
- [9] ——, “Construction of the Dirichlet to Neumann boundary operator for triangles and applications in the analysis of polygonal conductors,” *IEEE Trans. Microw. Theory Tech.*, recommended for publication.

APPENDIX B

Analytical Calculation of Quasi-Static Interactions in Free Space

B.1 Introduction

This Appendix describes how the quasi-static Green's function's interactions in two dimensions and in free space can be calculated analytically. The considered numerical method is a boundary integral equation formulation of Maxwell's equations, using the Method of Moments with piecewise linear basis functions and a Galerkin weighting procedure (see, e.g., [1]). An analytical calculation of the interaction integrals is only required for the so-called self-patch and the neighbor-patch cases (where both required integrations cover the same, respectively, adjacent segments in space). However, it turns out that the method presented here allows a fast analytical integration of *all* interaction integrals, as compared to the traditional numerical quadrature techniques.

In [2], the special case of two segments with a common corner point (including the self-patch case) is treated analytically. However, in complex configurations where several materials have common boundaries, a more general treatment is desirable. This allows for a more straightforward discretization of the field quantities on the boundaries, in the sense that adjacent materials no longer need exactly the same discretization on their common boundary. Note that in [2], the *full wave* Green's function of free space is employed. The interactions are calculated in two steps. First, the singularity is extracted, for which the nearest interactions have to be calculated analytically. In a second step, the remaining terms can be treated numerically without any difficulties. The extracted singular term equals the quasi-static Green's function. The method given below is therefore not only relevant for quasi-TM approximative methods, but also for full-wave calculations in two dimensions.

A direct implementation of the formulas given below was used for the final simulation of Chapter 4 and for the examples given in Chapter 5.

B.2 Interaction Integrals

In order to calculate the interaction between two line segments $[\mathbf{r}_p, \mathbf{r}_{p+1}]$ and $[\mathbf{r}_q, \mathbf{r}_{q+1}]$, described by

$$\mathbf{r} \leftrightarrow \mathbf{r}_p + s(\mathbf{r}_{p+1} - \mathbf{r}_p) \quad (\text{B.1})$$

$$\mathbf{r}' \leftrightarrow \mathbf{r}_q + t(\mathbf{r}_{q+1} - \mathbf{r}_q), \quad (\text{B.2})$$

for a piecewise-linear boundary discretization of the field quantities, and with the quasi-static Green's function of free space

$$G_0(\mathbf{r}, \mathbf{r}') = \frac{1}{2\pi} \ln |\mathbf{r} - \mathbf{r}'|, \quad (\text{B.3})$$

following integrals have to be determined

$$I_{00} = \int_0^1 ds \int_0^1 \ln |\mathbf{r} - \mathbf{r}'| dt \quad (\text{B.4})$$

$$I_{01} = \int_0^1 ds \int_0^1 t \ln |\mathbf{r} - \mathbf{r}'| dt \quad (\text{B.5})$$

$$I_{10} = \int_0^1 s ds \int_0^1 \ln |\mathbf{r} - \mathbf{r}'| dt \quad (\text{B.6})$$

$$I_{11} = \int_0^1 s ds \int_0^1 t \ln |\mathbf{r} - \mathbf{r}'| dt \quad (\text{B.7})$$

in which

$$|\mathbf{r} - \mathbf{r}'| = \sqrt{(x - x')^2 + (y - y')^2} \quad (\text{B.8})$$

$$= \left[((x_p - x_q) + s(x_{p+1} - x_p) - t(x_{q+1} - x_q))^2 + ((y_p - y_q) + s(y_{p+1} - y_p) - t(y_{q+1} - y_q))^2 \right]^{\frac{1}{2}} \quad (\text{B.9})$$

Consider the following map from the two-dimensional space into the complex plane

$$\mathbf{r} = x \mathbf{u}_x + y \mathbf{u}_y \rightarrow z = x + iy \quad (\text{B.10})$$

such that $|\mathbf{r}| = |z|$. The results given here can be considered an extension of those given by Sarkar and Djordjevic in [3], based on an analogous transformation to the

complex plane, but for one special case only. (B.9) can be written as

$$|\mathbf{r} - \mathbf{r}'| = |z_0 + z_1 s + z_2 t| \quad (\text{B.11})$$

with

$$z_0 = (z_p - z_q) \quad (\text{B.12})$$

$$z_1 = (z_{p+1} - z_p) \quad (\text{B.13})$$

$$z_2 = -(z_{q+1} - z_q), \quad (\text{B.14})$$

with $z_p, z_{p+1}, z_q, z_{q+1}$ found from $\mathbf{r}_p, \mathbf{r}_{p+1}, \mathbf{r}_q$ and \mathbf{r}_{q+1} as in (B.10). Notice that $|z_1| \neq 0$ and $|z_2| \neq 0$. With

$$K_{00} \stackrel{\text{def}}{=} \int_0^1 ds \int_0^1 \ln(z_0 + z_1 s + z_2 t) dt \quad (\text{B.15})$$

$$K_{01} \stackrel{\text{def}}{=} \int_0^1 ds \int_0^1 t \ln(z_0 + z_1 s + z_2 t) dt \quad (\text{B.16})$$

$$K_{10} \stackrel{\text{def}}{=} \int_0^1 s ds \int_0^1 \ln(z_0 + z_1 s + z_2 t) dt \quad (\text{B.17})$$

$$K_{11} \stackrel{\text{def}}{=} \int_0^1 s ds \int_0^1 t \ln(z_0 + z_1 s + z_2 t) dt \quad (\text{B.18})$$

the interaction integrals (B.4)-(B.7) can be written as

$$I_{ij} = \text{Re}[K_{ij}], \quad \text{with } i, j = 0, 1 \quad (\text{B.19})$$

The complex integrals $K_{00}, K_{01}, K_{10}, K_{11}$ are determined by integration in the complex plane.

B.3 Determination of K_{00}

The function $P_{00}(s, t)$, defined by

$$P_{00}(s, t) \stackrel{\text{def}}{=} \frac{1}{2} \frac{(z_0 + z_1 s + z_2 t)^2}{z_1 z_2} \ln(z_0 + z_1 s + z_2 t) - \frac{3}{2} s t \quad (\text{B.20})$$

satisfies

$$\frac{\partial^2 P_{00}(s, t)}{\partial s \partial t} = \ln(z_0 + z_1 s + z_2 t) \quad (\text{B.21})$$

where $(z_0 + z_1 s + z_2 t) \neq 0$. Note that the logarithmic term in P_{00} becomes zero if $(z_0 + z_1 s + z_2 t) = 0$. The numerical value of K_{00} according to (B.15) can only be directly found from the function $P_{00}(s, t)$, if the logarithmic function is holomorphic

over the *complete* integration area. Consequently, if the branch cut of $\ln()$ crosses the square $S \leftrightarrow \{0 \leq s \leq 1, 0 \leq t \leq 1\}$, a correction term Q_{00} has to be introduced, such that

$$K_{00} = \left[P_{00}(s, t) \right]_{t=0, s=0}^{t=1, s=1} - Q_{00}. \quad (\text{B.22})$$

in which the following notation was introduced

$$\left[f(s, t) \right]_{t=t_1, s=s_1}^{t=t_2, s=s_2} \stackrel{\text{def}}{=} f(s_2, t_2) - f(s_2, t_1) - f(s_1, t_2) + f(s_1, t_1). \quad (\text{B.23})$$

The correct value of K_{00} can be determined by integrating over the whole square S except for an area that includes the branch cut. The branch cut of the natural logarithm is, for most numerical tools, taken on (or rather ‘just below’) the negative part of the real axis, and, for the logarithmic term in P_{00} , becomes

$$L \leftrightarrow y_0 + s y_1 + t y_2 = 0 \quad (\text{B.24})$$

$$x_0 + s x_1 + t x_2 \leq 0 \quad (\text{B.25})$$

This choice is adopted here as well. In order to calculate the correction term Q_{00} , we will exclude a region with infinitesimal thickness around the straight line L (B.24). The region where condition (B.25) is not met (corresponding to the positive part of the real axis in the complex plane) will yield no contribution to Q_{00} . Extra care is required for special cases, such as, when L passes through a corner of S . In the sequel, we will therefore carefully enumerate and consider all different geometric possibilities for L . It should be mentioned that for many applications, most of the possibilities never occur. For example, if both integration intervals have only one point in common, this point normally needs to be the end point of one of the segments, in a classical Method of Moments implementation. But, in order to give a complete solution for the proposed integrals, each possibility is treated here. The next paragraphs provide the reader with the solution for each different situation. The comprehensive calculations that led to them are omitted, as this Appendix only provides a reference for later use.

Consider the (s, t) -plane, with the horizontal axis $t = 0$ and the vertical axis $s = 0$. First, the case with a horizontal or vertical branch cut is treated. Next, the general case with L neither vertical, nor horizontal is treated. In this case, we can write

$$L \leftrightarrow t = t_0 + m s, \quad \text{with } t_0 = -\frac{y_0}{y_2} \text{ and } m = -\frac{y_1}{y_2}, \quad (\text{B.26})$$

with non-zero y_1 and y_2 , such that L intersects with the lines $s = 0$, $s = 1$, $t = 0$, and $t = 1$, in the respective (s, t) pairs $(0, t_0)$, $(1, t_1)$, $(s_0, 0)$ and $(s_1, 1)$, for

$$t_1 = -\frac{y_0 + y_1}{y_2}, \quad s_0 = -\frac{y_0}{y_1}, \quad s_1 = -\frac{y_0 + y_2}{y_1}. \quad (\text{B.27})$$

The following auxiliary functions are defined

$$B_0(s, t, y) = \frac{1}{2} \frac{(z_0 + z_1 s + z_2 t)^2}{z_1 z_2} j\pi \operatorname{sgn}(z_0 + z_1 s + z_2 t, y) \quad (\text{B.28})$$

$$\begin{aligned} B(s, y) &= \frac{1}{2} \frac{(z_0 + z_1 s + z_2 (t_0 + m s))^2}{z_2 (z_1 + m z_2)} \\ &\quad \cdot j\pi \operatorname{sgn}(z_0 + z_1 s + z_2 (t_0 + m s), y), \quad \text{if } z_1 \neq -m z_2 \quad (\text{B.29}) \end{aligned}$$

$$= \frac{z_0 + z_2 t_0}{z_2} s j\pi \operatorname{sgn}(z_0 + z_2 t_0, y), \quad \text{if } z_1 = -m z_2 \quad (\text{B.30})$$

with the introduction of the function $\operatorname{sgn}(x, y)$ with real arguments x and y , defined by

$$\operatorname{sgn}(x, y) = \begin{cases} 1 & \text{if } x < 0 \text{ and } y \geq 0 \\ -1 & \text{if } x < 0 \text{ and } y < 0 \\ 0 & \text{otherwise} \end{cases} \quad (\text{B.31})$$

Notice that $\operatorname{Im}(z_0 + z_1 s + z_2 (t_0 + m s)) \equiv 0$, such that the first argument of sgn in $B(s, y)$ is real indeed. For $B_0(s, t, y)$ as well, s and t will be chosen such, that the first argument of sgn always remains real.

B.3.1 CASE 1: branch cut horizontal or vertical

When L is horizontal ($y_1 = 0$), we find

- $t_0 = 0$

$$Q_{00} = [B_0(s, t_0, y)]_{y=0, s=0}^{y=y_2, s=1} \quad (\text{B.32})$$

- $0 < t_0 < 1$

$$Q_{00} = [B_0(s, t_0, y)]_{y=-y_2, s=0}^{y=y_2, s=1} \quad (\text{B.33})$$

- $t_0 = 1$

$$Q_{00} = [B_0(s, t_0, y)]_{y=-y_2, s=0}^{y=0, s=1} \quad (\text{B.34})$$

When L is vertical ($y_2 = 0$), we find

- $s_0 = 0$

$$Q_{00} = [B_0(s_0, t, y)]_{y=0, t=0}^{y=y_1, t=1} \quad (\text{B.35})$$

- $0 < s_0 < 1$

$$Q_{00} = \left[B_0(s_0, t, y) \right]_{y=-y_1, t=0}^{y=y_1, t=1} \quad (\text{B.36})$$

- $s_0 = 1$

$$Q_{00} = \left[B_0(s_0, t, y) \right]_{y=-y_1, t=0}^{y=0, t=1} \quad (\text{B.37})$$

B.3.2 CASE 2: L through a corner of S

The second considered case encompasses the situations in which L goes through at least one corner of S , and is neither vertical, nor horizontal.

- L through lower left corner ($t_0 = 0, s_0 = 0$)

- $t_1 < 0$ (or $m < 0$)

$$Q_{00} = \left[B_0(s_0, t_0, y) \right]_{y=y_1}^{y=0} \quad (\text{B.38})$$

- $0 < t_1 < 1$ (or $0 < m < 1$)

$$Q_{00} = \left[B_0(s_0, t_0, y) \right]_{y=y_1}^{y=0} + \left[B(s, y) \right]_{y=-y_2, s=0}^{y=y_2, s=1} \quad (\text{B.39})$$

- $t_1 = 1$ (or $m = 1$)

$$\begin{aligned} Q_{00} = & \left[B_0(s_0, t_0, y) \right]_{y=y_1}^{y=0} + \left[B(s, y) \right]_{y=-y_2, s=0}^{y=y_2, s=1} \\ & + \left[B_0(s_1, t_1, y) \right]_{y=-y_1}^{y=0} \end{aligned} \quad (\text{B.40})$$

- $t_1 > 1$ (or $0 < s_1 < 1$)

$$\begin{aligned} Q_{00} = & \left[B_0(s_0, t_0, y) \right]_{y=y_1}^{y=0} + \left[B(s, y) \right]_{y=-y_2, s=0}^{y=y_2, s=s_1} \\ & + \left[B_0(s_1, 1, y) \right]_{y=-y_1}^{y=y_1} \end{aligned} \quad (\text{B.41})$$

- L through upper right corner ($t_1 = 1, s_1 = 1$)

- $t_0 < 0$ (or $m > 1$)

$$Q_{00} = \left[B_0(s_0, 0, y) \right]_{y=y_1}^{y=-y_1} + \left[B(s, y) \right]_{y=-y_2, s=s_0}^{y=y_2, s=1} \\ + \left[B_0(s_1, t_1, y) \right]_{y=-y_1}^{y=0} \quad (\text{B.42})$$

- $0 < t_0 < 1$ (or $0 < m < 1$)

$$Q_{00} = \left[B(s, y) \right]_{y=-y_2, s=0}^{y=y_2, s=1} + \left[B_0(s_1, t_1, y) \right]_{y=-y_1}^{y=0} \quad (\text{B.43})$$

- $t_0 > 1$ (or $m < 0$)

$$Q_{00} = \left[B_0(s_1, t_1, y) \right]_{y=-y_1}^{y=0} \quad (\text{B.44})$$

• L through lower right corner ($t_1 = 0, s_0 = 1$)

- $s_1 < 0$ (or $-1 < m < 0$)

$$Q_{00} = \left[B(s, y) \right]_{y=-y_2, s=0}^{y=y_2, s=1} + \left[B_0(s_0, t_1, y) \right]_{y=0}^{y=-y_1} \quad (\text{B.45})$$

- $s_1 = 0$

$$Q_{00} = \left[B_0(s_1, t_0, y) \right]_{y=0}^{y=y_1} + \left[B(s, y) \right]_{y=-y_2, s=0}^{y=y_2, s=1} \\ + \left[B_0(s_0, t_1, y) \right]_{y=0}^{y=-y_1} \quad (\text{B.46})$$

- $0 < s_1 < 1$

$$Q_{00} = \left[B_0(s_1, 1, y) \right]_{y=-y_1}^{y=y_1} + \left[B(s, y) \right]_{y=-y_2, s=s_1}^{y=y_2, s=1} \\ + \left[B_0(s_0, t_1, y) \right]_{y=0}^{y=-y_1} \quad (\text{B.47})$$

- $s_1 > 1$

$$Q_{00} = \left[B_0(s_0, t_1, y) \right]_{y=0}^{y=-y_1} \quad (\text{B.48})$$

• L through upper left corner ($s_1 = 0, t_0 = 1$)

- $t_1 < 0$

$$Q_{00} = \left[B_0(s_1, t_0, y) \right]_{y=0}^{y=y_1} + \left[B(s, y) \right]_{y=-y_2, s=0}^{y=y_2, s=s_0} \\ + \left[B_0(s_0, 0, y) \right]_{y=y_1}^{y=-y_1} \quad (\text{B.49})$$

- $0 < t_1 < 1$

$$Q_{00} = \left[B(s, y) \right]_{y=-y_2, s=0}^{y=y_2, s=1} + \left[B_0(s_1, t_0, y) \right]_{y=0}^{y=y_1} \quad (\text{B.50})$$

- $t_1 > 1$

$$Q_{00} = \left[B_0(s_1, t_0, y) \right]_{y=0}^{y=-y_2} \quad (\text{B.51})$$

B.3.3 CASE 3: L through two opposite sides (not through corners)

- $0 < t_0 < 1$ and $0 < t_1 < 1$

$$Q_{00} = \left[B(s, y) \right]_{y=-y_2, s=0}^{y=y_2, s=1} \quad (\text{B.52})$$

- $0 < s_0 < 1$ and $0 < s_1 < 1$

$$Q_{00} = \left[B_0(s_1, 1, y) \right]_{y=-y_1}^{y=y_1} + \left[B(s, y) \right]_{y=-y_2, s=\min(s_0, s_1)}^{y=y_2, s=\max(s_0, s_1)} \\ + \left[B_0(s_0, 0, y) \right]_{y=y_1}^{y=-y_1} \quad (\text{B.53})$$

B.3.4 CASE 4: L through two adjacent sides (not through corners)

- $0 < s_0 < 1$ and $0 < t_1 < 1$

$$Q_{00} = \left[B(s, y) \right]_{y=-y_2, s=s_0}^{y=y_2, s=1} + \left[B_0(s_0, 0, y) \right]_{y=y_1}^{y=-y_1} \quad (\text{B.54})$$

- $0 < t_0 < 1$ and $0 < s_1 < 1$

$$Q_{00} = \left[B(s, y) \right]_{y=-y_2, s=0}^{y=y_2, s=s_1} + \left[B_0(s_1, 1, y) \right]_{y=-y_1}^{y=y_1} \quad (\text{B.55})$$

- $0 < t_0 < 1$ and $0 < s_0 < 1$

$$Q_{00} = \left[B(s, y) \right]_{y=-y_2, s=0}^{y=y_2, s=s_0} + \left[B_0(s_0, 0, y) \right]_{y=y_1}^{y=-y_1} \quad (\text{B.56})$$

- $0 < t_1 < 1$ and $0 < s_1 < 1$

$$Q_{00} = \left[B(s, y) \right]_{y=-y_2, s=s_1}^{y=y_2, s=1} + \left[B_0(s_1, 1, y) \right]_{y=-y_1}^{y=y_1} \quad (\text{B.57})$$

B.4 Determination of K_{01} , K_{10} , and K_{11}

For the integrals given by (B.16), (B.17), and (B.18), analogous functions P , B and B_0 can be found, such that (B.22) and (B.32)-(B.57) remain valid, with a modified subscript (respectively, ‘01’, ‘10’, and ‘11’ instead of ‘00’), because the new integrands still contain the same branch cut.

B.4.1 Auxiliary functions for K_{01}

$$\begin{aligned} P_{01}(s, t) = & -\frac{1}{6} \frac{(z_0 + z_1 s - 2 z_2 t)(z_0 + z_1 s + z_2 t)^2}{z_1 z_2^2} \ln(z_0 + z_1 s + z_2 t) \\ & + \frac{s t}{12 z_2} (2 s z_1 - 7 t z_2 + 4 z_0) \end{aligned} \quad (\text{B.58})$$

$$B_0(s, t, y) = -\frac{1}{6} \frac{(z_0 + z_1 s - 2 z_2 t)(z_0 + z_1 s + z_2 t)^2}{z_1 z_2^2} j\pi \operatorname{sgn}(z_0 + z_1 s + z_2 t, y) \quad (\text{B.59})$$

$$\begin{aligned} B(s, y) = & -\frac{1}{6} \frac{\left(z_1(z_0 + z_1 s - 2 z_2 t_0) + m z_2(2 z_0 - z_2(t_0 + m s)) \right) (z_0 + z_1 s + z_2(t_0 + m s))^2}{z_2^2(z_1 + m z_2)^2} \\ & \cdot j\pi \operatorname{sgn}(z_0 + z_1 s + z_2(t_0 + m s), y), \quad \text{if } z_1 \neq -m z_2 \end{aligned} \quad (\text{B.60})$$

$$= -\frac{1}{2} \frac{(z_0 - z_2(m s + t_0))(z_0 + z_2 t_0)}{z_2^2} s j\pi \operatorname{sgn}(z_0 + z_2 t_0, y), \quad \text{if } z_1 = -m z_2 \quad (\text{B.61})$$

B.4.2 Auxiliary functions for K_{10}

$$\begin{aligned} P_{01}(s, t) = & -\frac{1}{6} \frac{(z_0 - 2z_1 s + z_2 t)(z_0 + z_1 s + z_2 t)^2}{z_1^2 z_2} \ln(z_0 + z_1 s + z_2 t) \\ & + \frac{st}{12z_1} (-7s z_1 + 2t z_2 + 4z_0) \end{aligned} \quad (\text{B.62})$$

$$\begin{aligned} B_0(s, t, y) = & -\frac{1}{6} \frac{(z_0 - 2z_1 s + z_2 t)(z_0 + z_1 s + z_2 t)^2}{z_1^2 z_2} \\ & \cdot j\pi \operatorname{sgn}(z_0 + z_1 s + z_2 t, y) \end{aligned} \quad (\text{B.63})$$

$$\begin{aligned} B(s, y) = & -\frac{1}{6} \frac{(z_0 - 2z_1 s + z_2(t_0 - 2ms))(z_0 + z_1 s + z_2(t_0 + ms))^2}{z_2(z_1 + mz_2)^2} \\ & \cdot j\pi \operatorname{sgn}(z_0 + z_1 s + z_2(t_0 + ms), y), \text{ if } z_1 \neq -mz_2 \end{aligned} \quad (\text{B.64})$$

$$= \frac{1}{2} \frac{(z_0 + z_2 t_0)}{z_2} s^2 j\pi \operatorname{sgn}(z_0 + z_2 t_0, y), \text{ if } z_1 = -mz_2 \quad (\text{B.65})$$

B.4.3 Auxiliary functions for K_{11}

$$\begin{aligned} P_{11}(s, t) = & -\frac{1}{24} \frac{(3s^2 z_1^2 + 2z_0 s z_1 - 6t s z_1 z_2 + 3z_2^2 t^2 - z_0^2 + 2z_0 z_2 t)(z_0 + z_1 s + z_2 t)^2}{z_1^2 z_2^2} \\ & \cdot \ln(z_0 + z_1 s + z_2 t) \\ & + \frac{st}{48z_1 z_2} (-9st z_1 z_2 + 10s z_0 z_1 + 10t z_0 z_2 + 6t^2 z_2^2 + 2z_0^2 + 6s^2 z_1^2) \end{aligned} \quad (\text{B.66})$$

$$\begin{aligned} B_0(s, t, y) = & -\frac{1}{24} \frac{(3s^2 z_1^2 + 2z_0 s z_1 - 6t s z_1 z_2 + 3z_2^2 t^2 - z_0^2 + 2z_0 z_2 t)(z_0 + z_1 s + z_2 t)^2}{z_1^2 z_2^2} \\ & \cdot j\pi \operatorname{sgn}(z_0 + z_1 s + z_2 t, y) \end{aligned}$$

$$\begin{aligned} B(s, y) = & -\frac{1}{24} F(s) \frac{(z_0 + z_1 s + z_2(t_0 + ms))^2}{z_2^2 (z_1 + mz_2)^3} \\ & \cdot j\pi \operatorname{sgn}(z_0 + z_1 s + z_2(t_0 + ms), y), \text{ if } z_1 \neq -mz_2 \end{aligned} \quad (\text{B.67})$$

$$\begin{aligned} = & \frac{1}{12} \frac{(3z_2 t_0 + 4ms z_2 - 3z_0)(z_0 + t_0 z_2)}{z_2^2} s^2 \\ & \cdot j\pi \operatorname{sgn}(z_0 + z_2 t_0, y), \text{ if } z_1 = -mz_2 \end{aligned} \quad (\text{B.68})$$

with

$$\begin{aligned} F(s) = & 3(z_1 - m z_2)(z_1 + m z_2)^2 s^2 \\ & + 2(z_1 + m z_2)(z_0 z_1 - 3t_0 z_1 z_2 + 3m z_0 z_2 - t_0 m z_2^2) s \\ & -(z_0 + t_0 z_2)(z_0 z_1 - 3t_0 z_1 z_2 + 3m z_0 z_2 - t_0 m z_2^2) \quad (\text{B.69}) \end{aligned}$$

Bibliography

- [1] M. Sadiku, *Numerical Techniques in electromagnetics*. Boca Raton, Florida: CRC Press, 1992.
- [2] J. Fostier, “Parallel techniques for fast multipole algorithms,” Ph.D. dissertation, 2009.
- [3] T. Sarkar and A. Djordjevic, “Wideband analysis of finite-conductivity cylinders,” *Progress In Electromagnetic Research (PIER)*, no. 16, pp. 153–173, 1997.

APPENDIX C

Calculation of the Surface Admittance Matrix on a Rectangular 3-D Conductor

This Appendix describes how the full-wave surface admittance operator can be calculated on the surface of a rectangular parallelepiped, by expanding the internal fields into the superposition of the modal fields inside three waveguides with a different orientation. The basic field expansions are written down here, but working out the Galerkin weighting procedure with a specific type of basis functions would lead to numerous pages with formulas that are not relevant within the framework of this dissertation, and these calculations are therefore left out.

C.1 Introduction

Consider a straight 3-D conductor (or dielectric body), more specifically a homogeneous isotropic rectangular parallelepiped $P \leftrightarrow 0 \leq x \leq x_0, 0 \leq y \leq y_0, 0 \leq z \leq z_0$ with material parameters (ϵ, μ, σ) . The purpose is to find a linear relationship between the tangential electric and magnetic fields, $e_{\tan,0}$ and $h_{\tan,0}$, on its boundary ∂P , written as

$$\mathbf{u}_n \times \mathbf{h}_{\tan}(\mathbf{r}') = \iint_{\partial P} \mathcal{A}(\mathbf{r}', \mathbf{r}'') \mathbf{e}_{\tan}(\mathbf{r}'') dS'' \quad (\text{C.1})$$

with \mathbf{u}_n the outward pointing normal unit vector. The operator \mathcal{A}_0 constitutes a similar relationship for the fields on the boundary of P , but this time filled with the background material. The differential surface admittance operator \mathcal{Y} is constructed as $\mathcal{Y} = \mathcal{A} - \mathcal{A}_0$, such that

$$\mathbf{u}_n \times (\mathbf{h}_{\text{tan}}(\mathbf{r}') - \mathbf{h}_{\text{tan},0}(\mathbf{r}')) = \iint_{\partial P} \mathcal{Y}(\mathbf{r}', \mathbf{r}'') \mathbf{e}_{\text{tan}}(\mathbf{r}'') dS'' \quad (\text{C.2})$$

with $\mathbf{h}_{\text{tan},0}$ the tangential magnetic field in the case of P filled with the background medium, but corresponding to the original tangential electric field on the boundary $\mathbf{e}_{\text{tan},0} = \mathbf{e}_{\text{tan}}$.

The left-hand side of (C.1) can be constructed as the superposition of three field contributions. These are found by considering three rectangular PEC waveguides, aligned along, respectively, the z , x , and y direction. In each case two opposite sides of P form the open ends of the waveguide, while the remaining four planes constitute the PEC mantle. These waveguides are shown together with the conductor P in Fig. C.1. The field excitation of each of these waveguides corresponds to the original tangential electric field on the two opposite sides of P that correspond with the open ends of the considered waveguide. Along the mantle of the PEC waveguide itself, the tangential electric field is identically zero. Hence, by construction, the total tangential electric field on the boundary of P is the superposition of the total tangential electric fields on P , as found by analysing the three different waveguides. As a consequence, the superposition of the total tangential magnetic fields for the three waveguides constitutes the total tangential magnetic field, which leads to the surface admittance matrix.

Here, only the z -directed waveguide is considered, as both other situations are perfectly analogous. The fields are derived as an expansion in the 2-D electric and magnetic eigenvectors of the transverse (x, y) dependence and with an exact z behavior, instead of as a superposition of the 3-D eigenvectors.

C.2 Field Expansions in a PEC Waveguide

In this section, we will derive an expression for the total electric and magnetic fields inside a *general* cylindrical z -directed PEC waveguide (with known Dirichlet and Neumann eigenfunctions), from the knowledge of the transverse electric field on $z = 0$ and $z = z_0$ only. Further on, the analysis will be restricted to a rectangular parallelepiped.

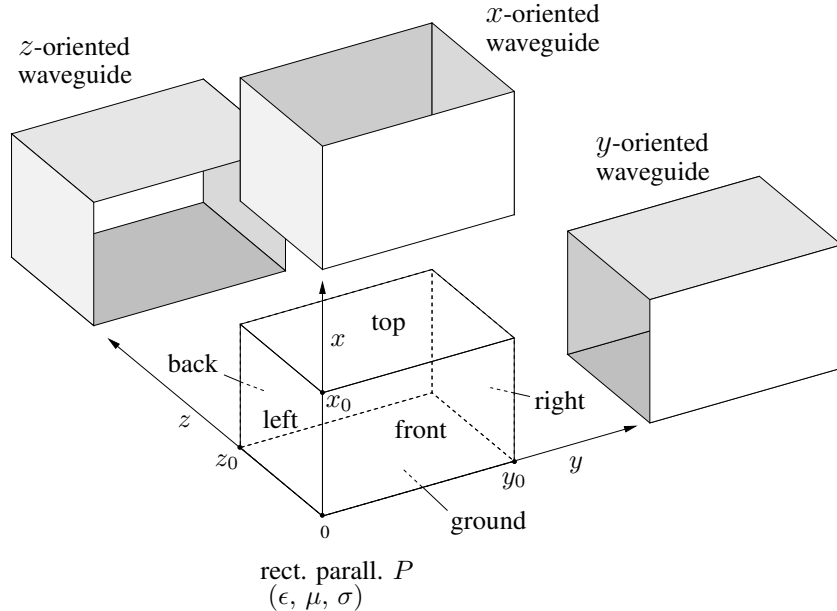


Figure C.1: Schematic presentation of the rectangular parallelepiped P , and the three rectangular PEC waveguides, of which the superposition of their inside fields forms the total fields inside P .

C.2.1 Electric and Magnetic Eigenvectors

The field expansions are based on the following eigenfunctions and eigenvectors (with S defined by $0 \leq x \leq x_0$, $0 \leq y \leq y_0$, and c its boundary):

- Orthonormal Dirichlet eigenfunctions $\xi_m(x, y)$ with eigenvalues μ_m^2 , satisfying

$$\nabla_t^2 \xi_m = -\mu_m^2 \xi_m \quad \text{on } S \quad (\text{C.3})$$

$$\xi_m = 0 \quad \text{on } c \quad (\text{C.4})$$

- Orthonormal Neumann eigenfunctions $\psi_{\dot{m}}(x, y)$ with eigenvalues $\tau_{\dot{m}}^2$, satisfying

$$\nabla_t^2 \psi_{\dot{m}} = -\tau_{\dot{m}}^2 \psi_{\dot{m}} \quad \text{on } S \quad (\text{C.5})$$

$$\partial_n \psi_{\dot{m}} = 0 \quad \text{on } c \quad (\text{C.6})$$

A dotted index \dot{m} is used to distinguish the Neumann index from the Dirichlet index m . Note that the indices m and \dot{m} in a rectangular cross-section each stand for a ‘double’ index.

- Orthogonal 2-D electric eigenvectors $\mathbf{f}_m(x, y)$ and $\mathbf{e}_{\dot{m}}(x, y)$

- irrotational: $\mathbf{f}_m = \nabla_t \xi_m$
- solenoidal: $\mathbf{e}_{\dot{m}} = \mathbf{u}_z \times \nabla_t \psi_{\dot{m}}$ (single-bounded)

satisfying

$$\iint_S \mathbf{f}_m \cdot \mathbf{e}_{\dot{n}} dS = 0, \quad \iint_S \mathbf{f}_m \cdot \mathbf{f}_n dS = \mu_m^2 \delta_{mn}, \quad \iint_S \mathbf{e}_{\dot{m}} \cdot \mathbf{e}_{\dot{n}} dS = \tau_{\dot{m}}^2 \delta_{\dot{m}\dot{n}} \quad (\text{C.7})$$

- Orthogonal 2-D magnetic eigenvectors $\mathbf{g}_{\dot{m}}(x, y)$ and $\mathbf{h}_m(x, y)$

- irrotational: $\mathbf{g}_{\dot{m}} = \nabla_t \psi_{\dot{m}}$
- solenoidal: $\mathbf{h}_m = \mathbf{u}_z \times \nabla_t \xi_m$

satisfying

$$\iint_S \mathbf{g}_{\dot{m}} \cdot \mathbf{h}_n dS = 0, \quad \iint_S \mathbf{g}_{\dot{m}} \cdot \mathbf{g}_{\dot{n}} dS = \tau_{\dot{m}}^2 \delta_{\dot{m}\dot{n}}, \quad \iint_S \mathbf{h}_m \cdot \mathbf{h}_n dS = \mu_m^2 \delta_{mn} \quad (\text{C.8})$$

C.2.2 Field Expansions

We start from the 3-D field equations, with $k^2 = -j\omega\mu(j\omega\epsilon + \sigma)$, written in terms of their transversal and longitudinal parts

$$\nabla_t e_z - \frac{\partial \mathbf{e}_t}{\partial z} = -j\omega\mu(\mathbf{u}_z \times \mathbf{h}_t) \quad (\text{C.9})$$

$$\nabla_t \times \mathbf{e}_t = -j\omega\mu h_z \mathbf{u}_z \quad (\text{C.10})$$

$$\nabla_t h_z - \frac{\partial \mathbf{h}_t}{\partial z} = -\frac{k^2}{j\omega\mu}(\mathbf{u}_z \times \mathbf{e}_t) \quad (\text{C.11})$$

$$\nabla_t \times \mathbf{h}_t = -\frac{k^2}{j\omega\mu} e_z \mathbf{u}_z, \quad (\text{C.12})$$

Longitudinal Fields

We expand e_z and h_z by separation of variables as

$$e_z(x, y, z) = \sum_m a_m(z) \xi_m(x, y) \quad (\text{C.13})$$

$$h_z(x, y, z) = \sum_{\dot{m}} b_{\dot{m}}(z) \psi_{\dot{m}}(x, y) \quad (\text{C.14})$$

because (C.11) shows that on the PEC walls, $e_z = 0$ and $\partial_n h_z = 0$ (because $\partial_n h_z = \partial_z h_n$ which is zero on the PEC), and such that

$$a_m(z) = \iint_S e_z \xi_m dS \quad \text{and} \quad b_{\dot{m}}(z) = \iint_S h_z \psi_{\dot{m}} dS \quad (\text{C.15})$$

For a careful analysis, we also need to expand $\nabla_t^2 e_z$ as

$$\nabla_t^2 e_z = \sum_m \check{a}_m \xi_m \quad (\text{C.16})$$

Because e_z and ξ_m are zero on c , we get $\check{a}_m = -\mu_m^2 a_m$, and (C.16) becomes

$$\nabla_t^2 e_z = -(\partial_{zz} + k^2) e_z = \sum_m -(\partial_{zz} + k^2) a_m \xi_m, \quad (\text{C.17})$$

due to the orthogonality of the Dirichlet functions. We find

$$\mu_m^2 a_m = (\partial_{zz} + k^2) a_m \quad (\text{C.18})$$

and analogously, since $\partial_n \psi_{\dot{m}}$ and $\partial_n h_z$ are zero on c ,

$$\tau_{\dot{m}}^2 b_{\dot{m}} = (\partial_{zz} + k^2) b_{\dot{m}}. \quad (\text{C.19})$$

Solving (C.18) and (C.19) leads to

$$a_m(z) = A_m^+ e^{-j\beta_m z} + A_m^- e^{j\beta_m z}, \quad \text{with } \beta_m^2 = k^2 - \mu_m^2 \quad (\text{C.20})$$

$$b_{\dot{m}}(z) = B_{\dot{m}}^+ e^{-j\tilde{\beta}_{\dot{m}} z} + B_{\dot{m}}^- e^{j\tilde{\beta}_{\dot{m}} z}, \quad \text{with } \tilde{\beta}_{\dot{m}}^2 = k^2 - \tau_{\dot{m}}^2 \quad (\text{C.21})$$

Obviously, β_m and $\tilde{\beta}_{\dot{m}}$ are the wave numbers of the TM, resp. the TE modes.

Transverse Electric Field

We expand the transverse electric field \mathbf{e}_t by means of the electric eigenvectors as

$$\mathbf{e}_t(x, y, z) = \sum_m \hat{a}_m(z) \mathbf{f}_m(x, y) + \sum_{\dot{m}} \hat{b}_{\dot{m}}(z) \mathbf{e}_{\dot{m}}(x, y). \quad (\text{C.22})$$

The coefficients can be calculated, using (C.7), as

$$\begin{aligned}
 \hat{a}_m(z) &= \frac{1}{\mu_m^2} \iint_S \mathbf{e}_t \cdot \mathbf{f}_m dS \\
 &= \frac{1}{\mu_m^2} \oint_c \xi_m \mathbf{e}_t \cdot \mathbf{u}_{n,t} dc - \frac{1}{\mu_m^2} \iint_S \xi_m \nabla_t \cdot \mathbf{e}_t dS \\
 &= \frac{1}{\mu_m^2} \iint_S \xi_m \partial_z e_z dS \\
 &= \frac{\partial_z a_m(z)}{\mu_m^2}
 \end{aligned} \tag{C.23}$$

$$\begin{aligned}
 \hat{b}_{\dot{m}}(z) &= \frac{1}{\tau_{\dot{m}}^2} \iint_S \mathbf{e}_t \cdot \mathbf{e}_{\dot{m}} dS \\
 &= \frac{1}{\tau_{\dot{m}}^2} \left(\oint_c \psi_{\dot{m}} (\mathbf{e}_t \times \mathbf{u}_z) \cdot \mathbf{u}_{n,t} dc - \iint_S \psi_{\dot{m}} \mathbf{u}_z \cdot (\nabla_t \times \mathbf{e}_t) dS \right) \\
 &= \frac{1}{\tau_{\dot{m}}^2} \iint_S \psi_{\dot{m}} j\omega\mu h_z dS \\
 &= \frac{j\omega\mu b_{\dot{m}}(z)}{\tau_{\dot{m}}^2}
 \end{aligned} \tag{C.24}$$

with $\mathbf{u}_{n,t}$ the unit normal vector to the boundary c of the (x, y) cross-section. Finally, we find with (C.20) and (C.21)

$$\hat{a}_m(z) = -\frac{j\beta_m}{\mu_m^2} (A_m^+ e^{-j\beta_m z} - A_m^- e^{j\beta_m z}) \tag{C.25}$$

$$\hat{b}_{\dot{m}}(z) = \frac{j\omega\mu}{\tau_{\dot{m}}^2} (B_{\dot{m}}^+ e^{-j\tilde{\beta}_{\dot{m}} z} + B_{\dot{m}}^- e^{j\tilde{\beta}_{\dot{m}} z}) \tag{C.26}$$

Transverse Magnetic Field

We expand the transverse magnetic field \mathbf{h}_t by means of the magnetic eigenvectors as

$$\mathbf{h}_t(x, y, z) = \sum_{\dot{m}} \check{a}_{\dot{m}}(z) \mathbf{g}_{\dot{m}}(x, y) + \sum_m \check{b}_m(z) \mathbf{h}_m(x, y). \tag{C.27}$$

The coefficients can be calculated in an analogous way as (C.23) and (C.24), using (C.7), as

$$\check{a}_{\dot{m}}(z) = -\frac{j\tilde{\beta}_{\dot{m}}}{\tau_{\dot{m}}^2} (B_{\dot{m}}^+ e^{-j\tilde{\beta}_{\dot{m}}z} - B_{\dot{m}}^- e^{j\tilde{\beta}_{\dot{m}}z}) \quad (\text{C.28})$$

$$\check{b}_m(z) = \frac{k^2}{j\omega\mu\mu_m^2} (A_m^+ e^{-j\beta_m z} + A_m^- e^{j\beta_m z}) \quad (\text{C.29})$$

Resulting Field Expansions

The total field expansions consist of the TE modes (with subscript \dot{m}) and the TM modes (with subscript m).

$$\begin{aligned} \mathbf{e}_t(x, y, z) &= \sum_m -\frac{j\beta_m}{\mu_m^2} (A_m^+ e^{-j\beta_m z} - A_m^- e^{j\beta_m z}) \mathbf{f}_m(x, y) \\ &\quad + \sum_{\dot{m}} \frac{j\omega\mu}{\tau_{\dot{m}}^2} (B_{\dot{m}}^+ e^{-j\tilde{\beta}_{\dot{m}}z} + B_{\dot{m}}^- e^{j\tilde{\beta}_{\dot{m}}z}) \mathbf{e}_{\dot{m}}(x, y) \end{aligned} \quad (\text{C.30})$$

$$e_z(x, y, z) = \sum_m (A_m^+ e^{-j\beta_m z} + A_m^- e^{j\beta_m z}) \xi_m(x, y) \quad (\text{C.31})$$

$$\begin{aligned} \mathbf{h}_t(x, y, z) &= \sum_{\dot{m}} -\frac{j\tilde{\beta}_{\dot{m}}}{\tau_{\dot{m}}^2} (B_{\dot{m}}^+ e^{-j\tilde{\beta}_{\dot{m}}z} - B_{\dot{m}}^- e^{j\tilde{\beta}_{\dot{m}}z}) \mathbf{g}_{\dot{m}}(x, y) \\ &\quad + \sum_m \frac{k^2}{j\omega\mu\mu_m^2} (A_m^+ e^{-j\beta_m z} + A_m^- e^{j\beta_m z}) \mathbf{h}_m(x, y) \end{aligned} \quad (\text{C.32})$$

$$h_z(x, y, z) = \sum_{\dot{m}} (B_{\dot{m}}^+ e^{-j\tilde{\beta}_{\dot{m}}z} + B_{\dot{m}}^- e^{j\tilde{\beta}_{\dot{m}}z}) \psi_{\dot{m}}(x, y) \quad (\text{C.33})$$

C.3 Discretization of \mathbf{e}_t

The tangential electric field on the ‘front’ side ($z = 0$, see Fig. C.1) is discretized as

$$\mathbf{e}_t(x, y, 0) = \sum_i e_{F,i} \mathbf{b}_i(x, y) \quad (\text{C.34})$$

in which the basis functions $\mathbf{b}_i(x, y)$ on area S_i (with boundary c_i) are, e.g., pulses or, preferably, rooftop functions. Note that the basis function \mathbf{b}_i in (C.34) represents a *double* set of vectorial basis functions, each with a corresponding set of field coefficients. One set is directed along x , corresponding to e_x , and the other along y , for the discretization of e_y . Weighting (C.34) on $z = 0$ with the electric eigenvectors and

invoking (C.22), leads to

$$\iint_S \left[\sum_i e_{F,i} \mathbf{b}_i(x, y) - \sum_{\tilde{m}} \hat{a}_{\tilde{m}}(0) \mathbf{f}_{\tilde{m}}(x, y) \right] \cdot \mathbf{f}_m dS = 0, \quad \forall m \quad (\text{C.35})$$

$$\iint_S \left[\sum_i e_{F,i} \mathbf{b}_i(x, y) - \sum_{\tilde{m}} \hat{b}_{\tilde{m}}(0) \mathbf{e}_{\tilde{m}}(x, y) \right] \cdot \mathbf{e}_{\tilde{m}} dS = 0, \quad \forall \tilde{m} \quad (\text{C.36})$$

such that

$$\hat{a}_m(0) = \frac{1}{\mu_m^2} \sum_i e_{F,i} \iint_{S_i} \mathbf{b}_i \cdot \mathbf{f}_m dS \quad (\text{C.37})$$

$$= \frac{1}{\mu_m^2} \sum_i e_{F,i} \left(\oint_{c_i} \xi_m \mathbf{b}_i \cdot \mathbf{u}_n dc - \iint_{S_i} \xi_m \nabla_t \cdot \mathbf{b}_i dS \right) \quad (\text{C.38})$$

$$\hat{b}_{\tilde{m}}(0) = \frac{1}{\tau_{\tilde{m}}^2} \sum_i e_{F,i} \iint_{S_i} \mathbf{b}_i \cdot \mathbf{e}_{\tilde{m}} dS \quad (\text{C.39})$$

$$= \frac{1}{\tau_{\tilde{m}}^2} \sum_i e_{F,i} \left(\oint_{c_i} \psi_{\tilde{m}} \mathbf{u}_n \cdot (\mathbf{b}_i \times \mathbf{u}_z) dc - \iint_{S_i} \psi_{\tilde{m}} \mathbf{u}_z \cdot (\nabla_t \times \mathbf{b}_i) dS \right) \quad (\text{C.40})$$

Discretizing \mathbf{e}_t on the ‘back’ side ($z = z_0$) with the same basis functions

$$\mathbf{e}_t(x, y, z_0) = \sum_i e_{B,i} \mathbf{b}_i(x, y). \quad (\text{C.41})$$

results in the same formulas as (C.38) and (C.40), but with the coefficients $e_{F,i}$ replaced by $e_{B,i}$.

In order to determine the magnetic field inside P , the coefficients A_m^+ , A_m^- and $B_{\tilde{m}}^+$, $B_{\tilde{m}}^-$ are required, as seen from (C.33) and (C.32). They are found as a function of $\hat{a}_m(0)$ and $\hat{a}_m(z_0)$, respectively, $\hat{b}_{\tilde{m}}(0)$ and $\hat{b}_{\tilde{m}}(z_0)$, via (C.25) and (C.26)

$$A_m^+ = -\frac{k_m^2}{j\beta_m} \frac{\hat{a}_m(z_0) e^{-j\beta_m z_0} - \hat{a}_m(0)}{e^{-j2\beta_m z_0} - 1} \quad (\text{C.42})$$

$$A_m^- = -\frac{k_m^2}{j\beta_m} (e^{-j\beta_m z_0}) \frac{\hat{a}_m(z_0) - \hat{a}_m(0) e^{-j\beta_m z_0}}{e^{-j2\beta_m z_0} - 1} \quad (\text{C.43})$$

$$B_{\tilde{m}}^+ = \frac{k_{\tilde{m}}^2}{j\omega\mu} \frac{\hat{b}_{\tilde{m}}(z_0) e^{-j\tilde{\beta}_{\tilde{m}} z_0} - \hat{b}_{\tilde{m}}(0)}{e^{-j2\tilde{\beta}_{\tilde{m}} z_0} - 1} \quad (\text{C.44})$$

$$B_{\tilde{m}}^- = -\frac{k_{\tilde{m}}^2}{j\omega\mu} (e^{-j\tilde{\beta}_{\tilde{m}} z_0}) \frac{\hat{b}_{\tilde{m}}(z_0) - \hat{b}_{\tilde{m}}(0) e^{-j\tilde{\beta}_{\tilde{m}} z_0}}{e^{-j2\tilde{\beta}_{\tilde{m}} z_0} - 1} \quad (\text{C.45})$$

C.4 Weighting of $\mathbf{u}_n \times \mathbf{h}$

The expression “ $\mathbf{u}_n \times \mathbf{h}$ ” will be concisely denoted as \mathbf{J} , as it has the dimension of a surface current density. It is shown here, how the discretized \mathbf{J} is written in terms of the magnetic field expansion coefficients.

- *Front side $z = 0$: determine $\mathbf{J}_F = -\mathbf{u}_z \times \mathbf{h}_t(x, y, 0)$*

Because of (C.27), \mathbf{J}_F can be written

$$\mathbf{J}_F = \sum_m \check{a}_m(0) \mathbf{g}_m \times \mathbf{u}_z + \sum_m \check{b}_m(0) \mathbf{h}_m \times \mathbf{u}_z \quad (\text{C.46})$$

and is expanded in basis functions $\mathbf{b}_{\bar{i}}$ as

$$\mathbf{J}_F = \sum_{\bar{i}} J_{F,\bar{i}} \mathbf{b}_{\bar{i}} \quad (\text{C.47})$$

with $S_{\bar{i}}$ on the front side the domain of basis function $\mathbf{b}_{\bar{i}}$, with boundary $c_{\bar{i}}$. The Galerkin weighting procedure (with identical test and basis functions) allows to write, $\forall i$

$$\begin{aligned} \sum_{\bar{i}} J_{F,\bar{i}} \iint_{S_i \cap S_{\bar{i}}} \mathbf{b}_{\bar{i}} \cdot \mathbf{b}_i dS &= \sum_m \check{a}_m(0) \iint_{S_i} (\mathbf{g}_m \times \mathbf{u}_z) \cdot \mathbf{b}_i dS \\ &\quad + \sum_m \check{b}_m(0) \iint_{S_i} (\mathbf{h}_m \times \mathbf{u}_z) \cdot \mathbf{b}_i dS \end{aligned} \quad (\text{C.48})$$

in which we can calculate the integrals as

$$\begin{aligned} \iint_{S_i} (\mathbf{g}_m \times \mathbf{u}_z) \cdot \mathbf{b}_i dS &= \oint_{c_i} \psi_m (\mathbf{u}_z \times \mathbf{b}_i) \cdot \mathbf{u}_{n_i} dc \\ &\quad + \iint_{S_i} \psi_m \mathbf{u}_z \cdot (\nabla_t \times \mathbf{b}_i) dS \end{aligned} \quad (\text{C.49})$$

$$\iint_{S_i} (\mathbf{h}_m \times \mathbf{u}_z) \cdot \mathbf{b}_i dS = \oint_{c_i} \xi_m \mathbf{b}_i \cdot \mathbf{u}_n dc - \iint_{S_i} \xi_m \nabla_t \cdot \mathbf{b}_i dS \quad (\text{C.50})$$

with \mathbf{u}_{n_i} the outward pointing unit vector, normal to the path c_i .

- *Ground side $x = 0$: determine $\mathbf{J}_G = -\mathbf{u}_x \times \mathbf{h}_t(0, y, z) + h_z(0, y, z) \mathbf{u}_y$*

On the one hand,

$$\begin{aligned}\mathbf{J}_G &= \sum_m -\check{b}_m(z) \partial_x \xi_m(0, y) \mathbf{u}_z \\ &\quad + \sum_{\dot{m}} -\check{a}_{\dot{m}}(z) \partial_y \psi_{\dot{m}}(0, y) \mathbf{u}_z + b_{\dot{m}}(z) \psi_{\dot{m}}(0, y) \mathbf{u}_y\end{aligned}\quad (\text{C.51})$$

and on the other hand, we discretize \mathbf{J}_G as

$$\mathbf{J}_G = \sum_{\tilde{i}} J_{G,\tilde{i}} \mathbf{b}_{\tilde{i}} \quad (\text{C.52})$$

and the Galerkin procedure leads to

$$\begin{aligned}\sum_{\tilde{i}} J_{G,\tilde{i}} \iint_{S_i \cap S_{\tilde{i}}} \mathbf{b}_{\tilde{i}} \cdot \mathbf{b}_i dS &= \sum_m \iint_{S_i} \left(-\check{b}_m(z) \partial_x \xi_m(0, y) \mathbf{u}_z \right) \cdot \mathbf{b}_i dS \\ &\quad + \sum_{\dot{m}} \iint_{S_i} \left(-\check{a}_{\dot{m}}(z) \partial_y \psi_{\dot{m}}(0, y) \mathbf{u}_z \right. \\ &\quad \left. + b_{\dot{m}}(z) \psi_{\dot{m}}(0, y) \mathbf{u}_y \right) \cdot \mathbf{b}_i dS\end{aligned}\quad (\text{C.53})$$

- For the remaining sides, the procedure is very similar and therefore not given explicitly.

C.5 Further Procedure for a Rectangular Parallelepiped

C.5.1 Eigenfunctions of the Rectangular Cross-Section

For a rectangular cross-section S , the indices m and \dot{m} are in fact, as already mentioned, double indices, and the corresponding Dirichlet and Neumann eigenfunctions are

$$\xi_{mn}(x, y) = \frac{2}{\sqrt{x_0 y_0}} \sin\left(\frac{m\pi x}{x_0}\right) \sin\left(\frac{n\pi y}{y_0}\right) \quad (\text{C.54})$$

$$\psi_{mn}(x, y) = \frac{2}{\sqrt{x_0 y_0}} \cos\left(\frac{m\pi x}{x_0}\right) \cos\left(\frac{n\pi y}{y_0}\right) \quad (\text{C.55})$$

$$\psi_{0n}(x, y) = \sqrt{\frac{2}{x_0 y_0}} \cos\left(\frac{n\pi y}{y_0}\right) \quad (\text{C.56})$$

$$\psi_{m0}(x, y) = \sqrt{\frac{2}{x_0 y_0}} \cos\left(\frac{m\pi x}{x_0}\right) \quad (\text{C.57})$$

with $m = 1, \dots, M_x$ and $n = 1, \dots, M_y$, with M_x and M_y large enough for an accurate field expansion. If the Neumann eigenfunctions are written as $\psi_{\dot{m}\dot{n}}$, in terms of the dotted (double) index, the ranges for \dot{m} and \dot{n} are $\dot{m} \in [0, M_x]$ and $\dot{n} \in [0, M_y]$, with \dot{m} and \dot{n} not zero at the same time. The corresponding Dirichlet eigenvalues μ_{mn}^2 and the Neumann eigenvalues τ_{mn} are equal, and written as k_{mn}^2

$$k_{mn}^2 = \left(\frac{\dot{m}\pi}{x_0}\right)^2 + \left(\frac{\dot{n}\pi}{y_0}\right)^2 \quad (\text{C.58})$$

$$\beta_{mn}^2 = k^2 - k_{mn}^2 \quad (\text{C.59})$$

with the only difference between the Dirichlet and the Neumann case, that k_{m0}^2 and k_{0n}^2 do not exist for the Dirichlet eigenvalues. It is however very important to take into account the lowest order Neumann eigenfunctions, given by (C.56) and (C.57) (and which do not have a counterpart in the Dirichlet functions), in order to obtain a *complete* series expansion of the fields.

C.5.2 Discretization of \mathcal{A}

The further mathematical treatment, depending on the choice of the basis functions \mathbf{b}_i , is not given in detail here. Schematically, one has to proceed as follows. The transverse electric field coefficients (C.38) and (C.40) on the front side $z = 0$ and analogous formulas for the back side $z = z_0$ are substituted in (C.42) to (C.45), which in turn are inserted into (C.28) and (C.29) to find the magnetic transverse field coefficients in terms of the discretized electric field coefficients on the front and back side. It is important to express all exponential functions such, that the real part of their exponent is negative, in order to avoid numerical problems. For the discretized form of (C.1), the resulting equations are now put into the weighting formulas for the tangential magnetic field (C.48), (C.53), and the analogous formulas for the other sides. These equations constitute a linear relationship, expressing how each coefficient in the discretized form of $\mathbf{u}_n \times \mathbf{h}$ depends on all coefficients of \mathbf{e}_t on the front and the back side. They can be cast into a matrix form. The submatrices that correspond with the contribution from either e_x or e_y on the front or the back can be written as the matrix product of three matrices. The first matrix represents the projection of the considered electric field component onto the basis of electric eigenvectors, the second one describes the map from the electric to the magnetic field, and the last matrix gives the projection onto the magnetic basis functions.

C.5.3 Discretization of \mathcal{Y}

The result as described in C.5.2, is a discretization of the *non-differential* operator \mathcal{A} , and might cause Gibbs effect problems on the boundaries. The discretization of (C.2) however, ought to be accurate, as \mathbf{e}_{\tan} and $\mathbf{e}_{\tan,0}$ are identical on P 's boundary

(with the subscript zero to denote the case in which P is filled with the background medium).

The matrix discretization of (C.2) can be readily calculated from the one of (C.1). As the projection matrices are the same, the only difference is found in the matrices that map the electric fields onto the magnetic fields, both cast in their eigenvector representation. These matrices for the conductor case and for the ‘background medium’ case need to be subtracted. This should however not be done numerically, for reasons of accuracy. Instead, the analytical expressions for the elements of these matrices can be subtracted and the result should be simplified with care. This is important in the case of a non-magnetic, non-conducting material. One of the main problems here is in the calculation of $\beta_{mn}^\Delta \stackrel{\text{def}}{=} \beta_{mn} - \beta_{mn,0}$ (with $\beta_{mn}^2 = k^2 - k_{mn}^2$), because in the mentioned case of dielectric contrast, $k_{mn}^2 \gg k^2$ and $k_{mn}^2 \gg k_0^2$ and hence $\beta_{mn} \approx \beta_{mn,0}$. It should be calculated as

$$\beta_{mn}^\Delta = \frac{k^2 - k_0^2}{\beta_{mn} + \beta_{mn}^0}, \quad (\text{C.60})$$

to obtain a good accuracy. In this case, the factor $(1 - e^{-j\beta_{mn}^\Delta z_0})$ which is required as well, should be calculated by means of

$$(1 - e^{-j\beta_{mn}^\Delta z_0}) = - \sum_{p=1}^{\nu} \frac{1}{p!} (-j\beta_{mn}^\Delta z_0)^p \quad (\text{C.61})$$

in which a low number ν of terms is typically sufficient.



This research was funded by a Ph.D. grant from the
Research Foundation - Flanders (FWO - Vlaanderen).

